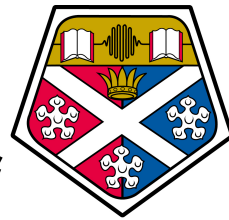


# High Contrast Measurements with a Bose-Einstein Condensate Atom Interferometer



University of  
**Strathclyde**  
**Glasgow**

Billy Ian Robertson

Experimental Quantum Optics and Photonics Group  
Department of Physics and SUPA

University of Strathclyde

A thesis presented in the fulfilment of the requirements for the  
degree of

*Doctor of Philosophy*

2016

---

This thesis is the result of the authors original research. It has been composed by the author and has not been previously submitted for examination which has led to the award of a degree.

The copyright of this thesis belongs to the author under the terms of the United Kingdom Copyright Acts as qualified by University of Strathclyde Regulation 3.50. Due acknowledgement must always be made of the use of any material contained in, or derived from, this thesis.

Signed:

Date:

# Abstract

Atom interferometry is a next-generation technique of precision measurement that can vastly outperform its optical analogue. These devices utilise the wave nature of atoms to make interferometric measurements of, for example, gravitational and magnetic fields, inertial effects, and the fine-structure constant. The main focus of this thesis is the creation of a general purpose atom interferometer in free space.

We create a Bose-Einstein condensate of  $\sim 10^5$   $^{87}\text{Rb}$  atoms in a crossed-optical dipole trap. The atomic wavefunction is coherently manipulated using highly tuned pulses comprising off-resonant light that form our atom-optical elements. These atom optics are analogous to the beam splitters and mirrors in an optical interferometer. By controlling the timing and amplitude of the pulses we demonstrate the ability to excite specific momentum states with high efficiency.

The tuned atom optics allows for the construction of an atom interferometer in free space. From this we can measure the recoil velocity of an  $^{87}\text{Rb}$  atom and calculate the value of the fine structure constant. We also demonstrate the measurement of magnetic field gradients using atom interferometry.

A second method of data readout is also demonstrated, known as contrast interferometry. This increases the rate at which information is obtained and decreases the measurement duration from a few hours to a few minutes.

Within the vacuum chamber we also have a copper ring which form the basis of an AC coupled ring trap for atoms. The long term goal is to use this as a waveguide for atom interferometry and, whilst not the main focus of this thesis, we present some proof-of-principle type data demonstrating the ring trap. In addition we show the first Kapitza-Dirac splitting of a BEC within the waveguide which forms the first part of a guided atom interferometer.

# Acknowledgements

I would like to express huge thanks to my primary supervisor, Paul Griffin. I really appreciate the time you have spent teaching and guiding me over the last few years, and how you always make time to help me. The way to can take seemingly complex physics and explain it simply and clearly is a great skill.

Erling Riis, thank you for your inspiring conversations, wise words and support. The fact you still find time to visit the offices and labs, despite being head of the department, is very much appreciated.

Thanks must go to Aidan Arnold, my unofficial third supervisor and the person who introduced me to Bose-Einstein condensates as an undergraduate student. Your expertise and suggestions in group meetings proved invaluable.

To my colleague and friend Andrew MacKellar, I have very much enjoyed your company during my PhD and you've no doubt been a hugely positive influence on my work. I have learned many things from you, physics or otherwise.

I thank greatly our previous post-doc Jonathan Pritchard and my PhD predecessor Aline Dinkelaker. Not only did you construct the excellent experiment foundation on which my work is based, but you also welcomed me into the photonics group and took the time to answer my questions and guide me in my early days.

I am pleased to see a new PhD student, James Halket, join our experiment (if nothing else, it means I didn't break it). I am excited to see what the future holds and I am confident you will produce some excellent data.

My office mates, Andrew, Vicki, Rachel, and Jan. A wise man once proclaimed "best office ever!", and I am tempted to agree. I feel very lucky that we get on so well, and I appreciate your company, advice, and support.

When I first joined the group, we were a small band of physicists, but with the expansion of the the group to become the Experimental Quantum Optics and Photonics (EQOP) Group, we have greatly increased in number. I will not try to list all EQOP members past and present; there are so many, and in truth I fear I may forget someone. Therefore I will simply thank you as a group, and say I couldn't have done it without you.

My outside-of-work thanks go to family and friends. Mum and Dad, thank you for your endless love, support and encouragement. As far as I am concerned, my PhD is as much your achievement as it is mine; I am only here because of you and I feel very fortunate.

# Contents

<b>Abstract</b>	<b>ii</b>
<b>Acknowledgements</b>	<b>iii</b>
<b>Contents</b>	<b>vi</b>
<b>List of Figures</b>	<b>vii</b>
<b>1 Introduction</b>	<b>1</b>
1.1 Research at the University of Strathclyde . . . . .	1
1.2 Atom Interferometry . . . . .	2
1.2.1 Atoms as Waves . . . . .	3
1.2.2 Advantages of Using Atoms . . . . .	4
1.2.3 Waveguides . . . . .	5
1.2.4 Cold Atoms, Bosons and Fermions . . . . .	6
1.3 Ring Traps . . . . .	7
1.3.1 Optical Ring Traps . . . . .	7
1.3.2 RF Dressed Ring Traps . . . . .	7
1.3.3 Magnetic Ring Traps . . . . .	8
1.3.4 Our AC Coupled Ring Trap . . . . .	8
1.4 Fine-Structure Constant . . . . .	8
1.4.1 Measurement of $\alpha$ . . . . .	10
1.5 Thesis Outline . . . . .	12
<b>2 Cold Atoms &amp; Quantum Gases</b>	<b>13</b>
2.1 Cooling and Trapping of Neutral Atoms . . . . .	13
2.1.1 Doppler Cooling . . . . .	14
2.1.2 Sub-Doppler Cooling . . . . .	16
2.1.3 Magneto-Optical Traps . . . . .	18
2.1.4 Magnetic Trapping . . . . .	21
2.1.5 Optical Dipole Traps . . . . .	22
2.1.6 Radio Frequency Evaporative Cooling . . . . .	23
2.1.7 Optical Evaporative Cooling . . . . .	25
2.2 Bose-Einstein Condensation . . . . .	26
2.2.1 Phase-Space Density . . . . .	26
2.2.2 Bose Gas in a Harmonic Potential . . . . .	27

2.2.3	Condensation in a Harmonic Potential . . . . .	28
2.2.4	Condensate Fraction . . . . .	29
<b>3</b>	<b>Atom Interferometry and Splitting the Wavefunction</b>	<b>31</b>
3.1	Bose-Einstein Condensates . . . . .	32
3.1.1	Coherence . . . . .	32
3.1.2	Momentum Spread . . . . .	34
3.2	Resonant Scattering . . . . .	35
3.3	Kapitza-Dirac Scattering . . . . .	36
3.3.1	Single Pulses . . . . .	37
3.3.2	Double Pulses . . . . .	39
3.4	Composite Pulses for High Efficiency Splitting . . . . .	42
3.4.1	Blackman Pulses . . . . .	44
3.4.2	Competing Methods . . . . .	45
3.5	Atom Interferometer Model . . . . .	46
3.5.1	3-arm Interferometer Model . . . . .	46
3.5.2	2-arm Interferometer Model . . . . .	48
<b>4</b>	<b>Experimental Setup</b>	<b>50</b>
4.1	System . . . . .	50
4.1.1	Vacuum System . . . . .	50
4.1.2	Glass Cells . . . . .	51
4.1.3	Atom Source . . . . .	51
4.1.4	Copper Ring . . . . .	52
4.1.5	Magnetic Coils . . . . .	52
4.1.6	ECDL Lasers . . . . .	53
4.1.7	Optics Setup . . . . .	54
4.1.8	Light-Induced Atomic Desorption . . . . .	59
4.2	Experimental Sequence . . . . .	60
4.3	Interferometry Setup . . . . .	69
4.3.1	Interferometry Laser Setup . . . . .	69
4.3.2	Optical Control of Interferometer Sequence . . . . .	71
4.3.3	Contrast Interferometer Probe Beam . . . . .	74
4.3.4	Low Light Level Detection . . . . .	75
<b>5</b>	<b>Interferometry in Free Space</b>	<b>77</b>
5.1	Optical Toolbox . . . . .	78
5.1.1	Lattice Depth Calibration . . . . .	78
5.1.2	First Order Atomic Beam Splitters . . . . .	79
5.1.3	Second Order Atomic Beam Splitters . . . . .	82
5.1.4	Atomic Mirrors . . . . .	84
5.1.5	Efficiency and Limitations . . . . .	87

## CONTENTS

---

5.1.6	Higher Order Splitting . . . . .	88
5.2	Two-Arm Interferometer . . . . .	89
5.3	Three-Arm Interferometer . . . . .	90
5.4	Magnetic Gradiometry . . . . .	92
5.4.1	Method . . . . .	95
5.4.2	Measurements . . . . .	96
<b>6</b>	<b>Contrast Interferometry</b>	<b>99</b>
6.1	Difficulty . . . . .	100
6.2	Avalanche Photodiode (APD) Detection . . . . .	101
6.2.1	First Detection . . . . .	101
6.2.2	Further Analysis . . . . .	103
6.2.3	APD Limitations . . . . .	107
6.3	Single Photon Counting Module (SPCM) Detection . . . . .	108
6.3.1	Method of Detection . . . . .	108
6.3.2	Measurements . . . . .	108
<b>7</b>	<b>AC Coupled Ring Trap</b>	<b>114</b>
7.1	Theory . . . . .	115
7.2	Thermal Atoms in the Ring Trap . . . . .	119
7.2.1	Loading from Dipole Trap . . . . .	121
7.2.2	Pendulum Modelling . . . . .	123
7.2.3	Kapitza-Dirac Splitting . . . . .	127
7.3	Limitations . . . . .	128
<b>8</b>	<b>Conclusions</b>	<b>130</b>
8.1	Conclusions . . . . .	130
8.2	Future Work . . . . .	131
8.2.1	Magnetic Gradiometry using CI . . . . .	131
8.2.2	Measurements of Gravity . . . . .	131
8.2.3	Higher Order Interferometry . . . . .	131
<b>A</b>	<b>Appendix</b>	<b>132</b>
A.1	Shutter Circuit Diagram . . . . .	132
A.2	LIAD Circuit Diagram . . . . .	133
A.3	Magnetic Levitation . . . . .	134
A.4	AOM Driver Circuit Diagram . . . . .	135
A.5	Thermal Size Calculation . . . . .	136
A.6	Calculation of $\alpha$ . . . . .	137
A.7	BEC Reflectivity . . . . .	139
A.8	Gravitational Phase Calculation . . . . .	140
	<b>Bibliography</b>	<b>141</b>

# List of Figures

<b>List of Figures</b>	<b>x</b>
1.1 Ring traps at the University of Strathclyde . . . . .	2
1.2 BEC interference fringes . . . . .	4
1.3 Sagnac interferometer . . . . .	5
1.4 Ultra-cold atoms, Bosons, and Fermions . . . . .	6
1.5 Fine-structure constant measurements . . . . .	11
2.1 Doppler cooling. . . . .	14
2.2 Scattering force. . . . .	15
2.3 3D molasses. . . . .	16
2.4 Sisyphus cooling. . . . .	17
2.5 Polarisation gradient cooling. . . . .	18
2.6 3D magneto-optical trap. . . . .	19
2.7 1D magneto-optical trap. . . . .	20
2.8 RF cooling diagram . . . . .	24
2.9 Optical evaporation. . . . .	25
2.10 Bose-Einstein condensation. . . . .	26
2.11 Bose-Einstein distribution. . . . .	27
2.12 BEC fraction. . . . .	30
3.1 Young's double slits. . . . .	33
3.2 Correlation in BECs and Ultra-cold gasses. . . . .	34
3.3 Resonant scattering. . . . .	35
3.4 Resonant Raman transition. . . . .	36
3.5 Kapitza-Dirac scattering. . . . .	37
3.6 Momentum population evolution using Bessel functions. . . . .	39
3.7 Double pulse on Bloch sphere. . . . .	41
3.8 Double pulse surface plot. . . . .	42
3.9 Splitting pulse diagram. . . . .	43
3.10 Blackman window spectra. . . . .	45
3.11 3-arm interferometer scheme. . . . .	46
3.12 2-arm interferometer scheme. . . . .	49

## LIST OF FIGURES

---

4.1	Vacuum system. . . . .	51
4.2	Ring cross section & photo. . . . .	52
4.3	Magnetic coil side view diagram. . . . .	53
4.4	ECDL diagram. . . . .	54
4.5	Cooling optics setup. . . . .	56
4.6	Optics around vacuum chamber. . . . .	58
4.7	MOT coil current. . . . .	60
4.8	Magnetic transport atomic motion schematic. . . . .	61
4.9	Magnetic transport coil currents. . . . .	61
4.10	Magnetic transport atomic motion. . . . .	62
4.11	RF evaporation trajectory. . . . .	63
4.12	Evaporation efficiency. . . . .	64
4.13	Dipole evaporation trajectory. . . . .	65
4.14	Dipole trap frequency at 0.4 W. . . . .	66
4.15	Dipole trap frequencies. . . . .	66
4.16	QP coil current. . . . .	67
4.17	BEC expansion . . . . .	68
4.18	Interferometer laser setup. . . . .	69
4.19	GaussianBeam program screen shot. . . . .	70
4.20	Interferometer beams with ring diagram. . . . .	71
4.21	Interferometry optical control diagram. . . . .	72
4.22	LabVIEW interferometry control. . . . .	73
4.23	Interferometry AOM response. . . . .	74
4.24	APD detection setup. . . . .	75
4.25	SPCM detection setup. . . . .	76
5.1	Optical and atom interferometers. . . . .	77
5.2	$26\hbar k$ diffraction. . . . .	78
5.3	Lattice depth calibration. . . . .	79
5.4	Composite splitting pulse. . . . .	80
5.5	$\pm 2\hbar k$ split image. . . . .	81
5.6	$\pm 2\hbar k$ split population evolution. . . . .	82
5.7	$\pm 2\hbar k$ split integrated profile. . . . .	83
5.8	$\pm 4\hbar k$ split population evolution. . . . .	84
5.9	$\pm 2\hbar k$ reflection - integrated profile. . . . .	85
5.10	$\pm 2\hbar k$ reflection - duration scan. . . . .	86
5.11	$\pm 2\hbar k$ reflection - amplitude scan. . . . .	86
5.12	3-arm interferometer output. . . . .	87
5.13	2-arm interferometer scheme. . . . .	89
5.14	2-arm interferometer output. . . . .	90

## LIST OF FIGURES

---

5.15	3-arm interferometer scheme. . . . .	91
5.16	3-arm interferometer output. . . . .	92
5.17	Gradient coil schematic . . . . .	93
5.18	Magnetic field contour plot. . . . .	94
5.19	Magnetic field profiles. . . . .	94
5.20	Gradiometry pulse scheme. . . . .	95
5.21	Simulated interferometer output. . . . .	95
5.22	Gradiometry output - $T_1 = T_2 = 1.4$ ms. . . . .	97
5.23	Gradiometry output - $T_1 = T_2 = 2.0$ ms. . . . .	98
5.24	Gradiometry - current to magnetic field gradient calibration. . . . .	98
6.1	Contrast interferometry scheme. . . . .	100
6.2	First CI signal . . . . .	102
6.3	CI sequence with thermal atoms. . . . .	102
6.4	CI probe with BEC. . . . .	103
6.5	APD Filter. . . . .	104
6.6	Contrast interferometry pulses. . . . .	104
6.7	CI signal on APD. . . . .	105
6.8	Atoms after CI . . . . .	106
6.9	DC vs strobed CI probe. . . . .	107
6.10	CI with SPCM detection . . . . .	109
6.11	CI with early probe. . . . .	110
6.12	CI: peak contrast as a function of expansion duration. . . . .	111
6.13	Short CI scheme. . . . .	111
6.14	Short CI with SPCM detection. . . . .	112
6.15	Phase fluctuations with temperature. . . . .	113
7.1	Magnetic field around a current carrying wire . . . . .	115
7.2	Ring trap driving, induced and combined magnetic fields . . . . .	116
7.3	Ring trap potential . . . . .	117
7.4	Ring trap potentials - shifting the zeros . . . . .	118
7.5	Thermal atoms in ring trap. . . . .	120
7.6	Ring trap lifetime. . . . .	120
7.7	Ultra-cold atoms in ring trap. . . . .	122
7.8	Ring artefact shift. . . . .	123
7.9	Pendulum modelling example images. . . . .	124
7.10	Pendulum modelling. . . . .	125
7.11	Pendulum lifetime. . . . .	127
7.12	KD split in ring trap. . . . .	128
A.1	Homemade shutter circuit diagram . . . . .	132

*LIST OF FIGURES*

---

A.2	LIAD circuit diagram . . . . .	133
A.3	AOM driver circuit diagram . . . . .	135

# Chapter 1

## Introduction

### 1.1 Research at the University of Strathclyde

In 2002, Arnold and Riis started the construction of an apparatus at the University of Strathclyde to investigate the behaviour of a Bose-Einstein condensate (BEC) of  $^{87}\text{Rb}$  atoms in a large (10 cm diameter) toroidal magnetic waveguide [1]. The motivation for such an experiment was that the use of a waveguide to confine a BEC would allow for the study of “persistent currents, Josephson effects, phase fluctuations and Sagnac or gravitational interferometry”. The first experimental realisation of a BEC in this large ring trap (figure 1.1a), along with data showing the complete revolution of the atoms around the ring, was reported in 2006 [2]. In 2010, the same apparatus was used to show the interference fringes between two initially spatially separated condensates [3, 4], in an atomic analogue of a Young’s double slit type experiment. Further investigation of these interference fringes, including their phase stability, formed the basis of the work by Carson [5], who reported single-shot contrasts of  $\geq 95\%$ . The large ring experiment continues to operate and at the time of writing, further publications are in preparation regarding phase fluctuations and the Talbot effect.

In parallel to the large ring trap, the group at Strathclyde have been investigating AC coupled ring traps. First proposed by Griffin *et al.* in 2008 [6], the idea is to use an induced current to generate the trapping magnetic field potential and thus eliminating the ‘end-effects’ produced in conventional coils of wire that use input and output wires. These input and output wires can cause unwanted deviations in an otherwise smooth trapping potential. The first experimental demonstration of such a ring trap was reported in 2012 by Pritchard *et al.* [7] using ultra cold  $^{87}\text{Rb}$  atoms in a proof-of-principle type experiment, with the accompanying thesis written by Dinkelaker in 2013 [8] (figure 1.1b). Following the success of the first generation AC coupled ring trap, the second generation experiment was started involving the construction of a new, vertically orientated AC coupled ring trap of 4 mm diameter, this time for the confinement of a BEC of  $^{87}\text{Rb}$ . It is this experiment that is the focus of this thesis. Recent success has lead to the preparation of a paper reporting on the optical control of our

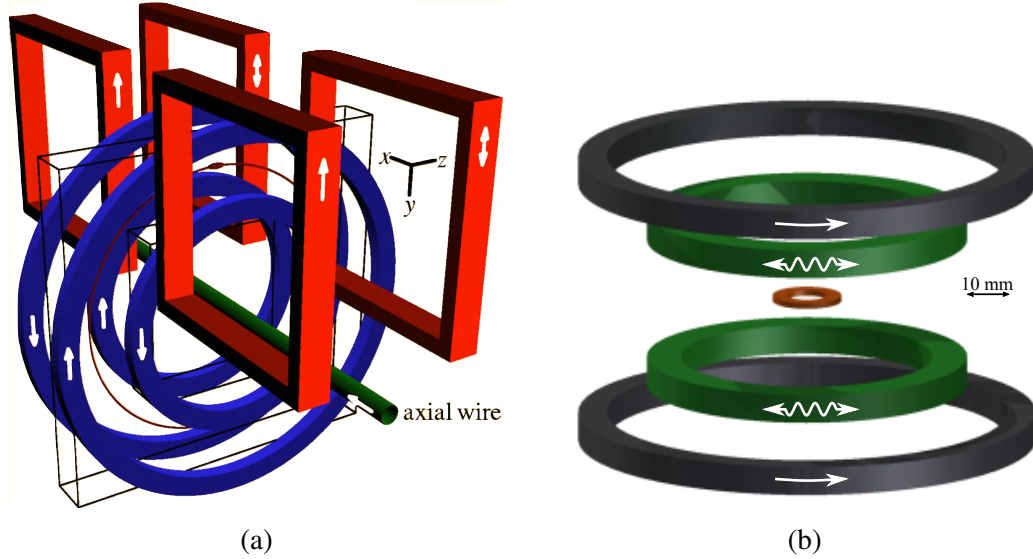


Figure 1.1: (a): Schematic of large (10 cm diameter) magnetic ring trap for a Bose-Einstein condensate, where the ‘y’ axis points downwards in the lab frame. Figure from [2]. (b): Horizontally orientated AC coupled ring trap for ultra-cold  $^{87}\text{Rb}$  atoms.

BEC [9], and further findings will be published in due course, including measurements using our contrast interferometer.

## 1.2 Atom Interferometry

Interferometry, in general, offers the ability to make precision measurement by observing the constructive and destructive interference effects of waves. For example, an optical interferometer uses the wave nature of light to produce interference patterns from which it is possible to make measurements, such as differences in optical path length [10]. Using this it is possible to make accurate measurements of external influences that cause a change in phase at the interferometer output, for example, rotations [11, 12].

Wave-like properties are not exclusive to light, and indeed matter can also be assigned a wave-like nature known as the de Broglie wavelength, described in section 1.2.1. For everyday, macroscopic objects this wavelength is tiny. A golf ball driven off the tee at 180 mph has a de Broglie wavelength of just  $1.8 \times 10^{-34}$  m, but for ultra-cold atoms this wavelength lengthens to hundreds of nanometres. With precise manipulation of ultra-cold atoms, it is possible to construct interferometers that use the wave nature of matter to produce constructive and destructive interference effects. In ad-

dition to rotations [13, 14, 15, 16, 17], atoms can also be used to measure magnetic fields [18], gravity [19, 20, 21], and ac Stark shifts [22]. This leads to many practical applications such as gravimetry, inertial sensing and magnetometry.

It is widely known that light can be manipulated by matter as demonstrated by the interaction of light with mirrors, lenses, beamsplitters, and diffraction gratings. The inverse of this is also possible; matter can be directed by the application of light and this fact is key in atom interferometry. Throughout this thesis we will draw the analogy between optical and atomic interferometers, and we begin here by mentioning beam splitters and mirrors. For an optical interferometer the beam splitters and mirrors are made of matter: glass and dielectric slabs. Conversely, standing and travelling waves of light can be used to coherently split and reflect atomic wavefunctions. This forms the basis of an atom interferometer.

The first proposal of the coherent manipulation of matter waves by a standing wave of light was made by Kapitza and Dirac in 1933 [23]. Here they proposed an experiment where a beam of electrons is partially reflected from a standing wave of light by stimulated Compton scattering. Although it took until 2001 for this to be conclusively demonstrated experimentally [24], experimental atom interferometers have been around since 1991 [25, 26] where gratings made of matter were used to diffract an atomic beam. The first experiments to use standing waves of light for the diffraction of atoms were demonstrated in 1995 [27, 28], although matter-wave interferometers using electrons [29, 30] and neutrons [31, 32] pre-date this. Whilst early interferometers were ‘proof-of-principle’ type experiments, today the technology has progressed such that it is possible to use atom interferometers to make measurements of external influences. Applications include inertial force and rotation sensing [33, 34, 16, 35], gradiometry [20, 21], tests of fundamental physics [36], and measurements of the fine-structure constant [37, 38].

### 1.2.1 Atoms as Waves

Atom interferometry utilises the wave-like nature of matter. In 1923 de Broglie assigned matter a wave-like nature [39] where the wavelength of a particle can be expressed by the well known equation

$$\lambda_{\text{dB}} = \frac{h}{p}, \quad (1.1)$$

where  $\lambda_{\text{dB}}$  is known as the de Broglie wavelength,  $h$  is the Planck constant and  $p$  is the momentum of the particle. Just as the wave nature of light causes interference effects, so can the wave nature of particles. The simplicity of a Young’s double slit type experiment provides an ideal example of this interference effect in atoms as shown in figure 1.2 [3, 5, 26].

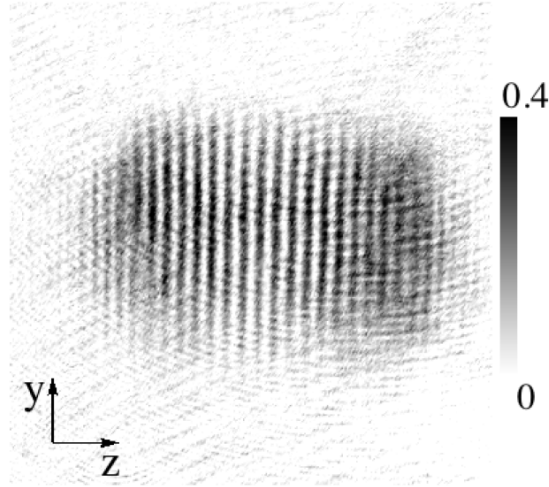


Figure 1.2: Two condensates of  $^{87}\text{Rb}$  are allowed to expand such that they overlap and interference fringes are observed in absorption imaging (figure from [5]). Scale shows optical density.

## 1.2.2 Advantages of Using Atoms

There are two main advantages of atoms over photons for interferometric measurements: increased phase accumulation in certain situations such as Sagnac interferometry, and atoms are sensitive to effects that photons are not such as electromagnetic fields. The increased phase accumulation, and therefore sensitivity, can be demonstrated by considering the Sagnac effect [14, 40], illustrated in figure 1.3. The phase accumulation of a Sagnac interferometer is given by

$$\Delta\Phi = \frac{4\pi A \Omega_{\text{rot}}}{\lambda v}, \quad (1.2)$$

where  $A$  is the enclosed area,  $\Omega_{\text{rot}}$  is the rotational velocity,  $\lambda$  is the wavelength, and  $v$  is the propagation velocity. If we compare the optical and atomic versions of this scheme, the sensitivity per particle has a ratio of

$$\frac{\Delta\Phi_{\text{atom}}}{\Delta\Phi_{\text{photon}}} = \frac{\lambda_{\text{photon}} c}{\lambda_{\text{dB}} v} = \frac{mc^2}{\hbar\omega_{\text{photon}}}. \quad (1.3)$$

For example, by comparing an atom interferometer using  $^{87}\text{Rb}$  to an optical interferometer using laser light of 780 nm, the sensitivity ratio  $\frac{\Delta\Phi_{\text{atom}}}{\Delta\Phi_{\text{photon}}} \approx 5 \times 10^{10}$ . This increase in sensitivity can also be illustrated by considering the ratio of the velocities of the interfering particles. Photons travel at  $c = 3 \times 10^8 \text{ ms}^{-1}$ , while atoms in an interferometer typically travel at  $v \approx 10^{-2} \text{ ms}^{-1}$ . The ratio  $c/v \sim 3 \times 10^{10}$ , and the low atomic velocity gives a de Broglie wavelength on the order of an optical wavelength,  $\lambda_{\text{dB}} \approx \lambda_{\gamma}$ . Given the comparable wavelengths, and therefore frequencies, atoms typically have more time to accumulate phase than photons do due to their lower velocities.

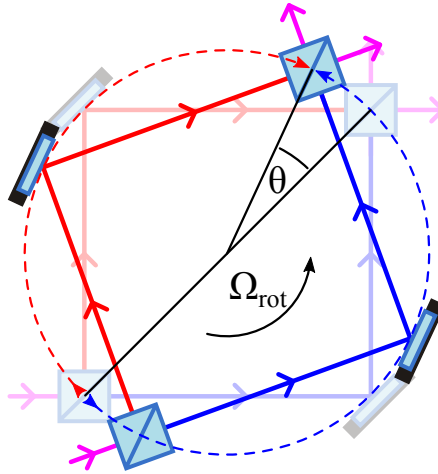


Figure 1.3: A schematic of a Sagnac interferometer. Each arm of a rotating interferometer has an interfering field that travels a different path length due to the finite propagation speed and thus the phase at the output will vary. From this, a measurement of the rotation can be made.

In the interest of transparency, it's worth pointing out that this increased sensitivity is per particle, and it's normally easier to get more photons than it is atoms. However, with the potential for such large gains in using atoms, they are still favourable for many applications.

The other advantage of atoms over photons is that atoms have a strong sensitivity to electromagnetic fields. This makes them excellent measurement devices for magnetometry [41], and an example of such a measurement is demonstrated in chapter 5.4.

### 1.2.3 Waveguides

The use of waveguides in atomic (and optical) interferometry allows for the construction of compact devices with long interaction times and minimal dispersion transverse to the propagation direction. This then leads to an increased sensitivity of the apparatus, albeit with an increased cost in terms of complexity. For example, a laser ring gyroscope can measure rotations via the Sagnac effect and uses coiled optical fibres that direct the photons around the enclosed area multiple times which increases the sensitivity (equation 1.2). By directing the interfering particles around the same region of space multiple times, the size of the device can be reduced whilst the sensitivity can be increased, with no additional cost in terms of size. Moreover, the transverse confinement provided by a waveguide reduces divergence, which increases the signal strength at longer interferometer durations.

The first demonstration of an interferometer using a BEC in a waveguide was by Wang *et al.* in 2005 [18], followed the next year by Garcia *et al.* [42]. Both are

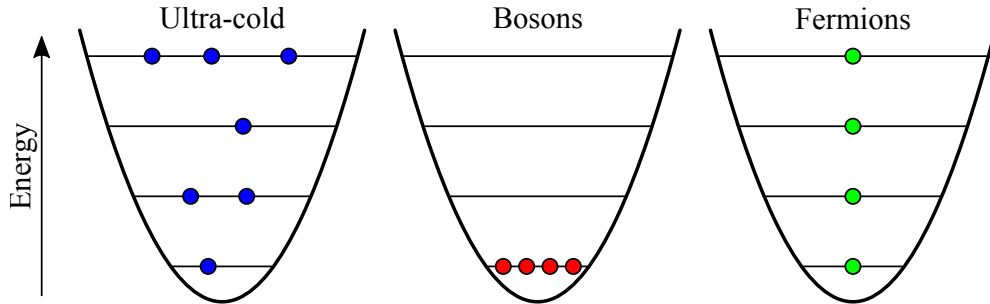


Figure 1.4: *Ultra-cold atoms fill up the trapping potential with a Maxwell-Boltzmann distribution. Once cold enough, bosons can all fall into the ground state of a trapping potential, while fermions cannot occupy the same state due to the Pauli exclusion principle and therefore fill the energy levels from the bottom up.*

examples of Michelson interferometers. The first Mach-Zehnder interferometer using a BEC was demonstrated by Horikoshi *et al.* [43].

Waveguides can be described as quasi-one-dimensional systems because the atoms are confined in the two dimensions orthogonal to the propagation direction. By considering these waveguides to be 1D, analysis and modelling becomes simpler. However, in reality there can be 3D dynamics such as sloshing within the waveguide, as well as thermal or mean field expansion of the atomic ensemble.

### 1.2.4 Cold Atoms, Bosons and Fermions

We can define three classes of atoms used in atom interferometry: ultra-cold thermal atoms, Bose-Einstein condensates (BEC), and Degenerate Fermi gasses (DFG) (see figure 1.4). Each class has advantages and, depending on the application, one may be more suited than another.

Ultra-cold thermal atoms have the advantage that experimentally they are easier and faster to produce. The repetition rate of the apparatus can be very high compared to the often lengthy process required to create a BEC or DFG. For example, the group of Tino [20] use thermal atoms with a cycle time of  $<400$  ms and the group of Biedermann [19] use a recapture method to increase their cycle rate to 60 Hz. BEC production is typically slower and the apparatus in this thesis requires  $\sim 30$  s to create a BEC. However, thermal atoms do not have the high coherence of a BEC. This can be likened to performing optical interferometry with white light; it works, but only a few fringes are visible. Coherence will be discussed further in section 3.1.1.

Temporal and spatial coherence (given by the  $g^{(1)}$  correlation function) is a key argument for using a BEC and will be discussed in section 3.1.1. It is analogous to using a laser for optical interferometry instead of white light. As a result the signal-to-noise ratio can be much greater and the contrast of the signal is increased. However, a BEC suffers from self-interactions which can result in a loss of phase coherence [44]. Also, upon releasing a BEC from a trapping potential, it expands due to mean field

effects [45]. If this expansion rate is sufficiently high, the density of the cloud will decrease rapidly which can lead to a reduced interferometry signal. The expansion of our BEC is discussed in section 4.2.

The non-interacting nature of a DFG [46] makes it an attractive choice for atom interferometry. The Pauli-exclusion principle implies that atoms in the same internal state cannot interact and therefore the ultra-cold fermions of a DFG do not have the self interactions of a BEC. This ultimately means there is less noise from uncontrolled phases in the system. However, a reduction of phase coherence can lead to a reduced contrast in the interferometry signal. In [47], an interferometry signal from fermions and bosons in an optical lattice are compared. In this specific case, the experiment “proves the superiority of noninteracting fermions with respect to bosons for precision interferometry”. This is due to the mean field expansion of the BEC in the optical lattice which “tends to wash out the contrast of the Bloch oscillations”.

## 1.3 Ring Traps

As mentioned above, waveguides can improve the performance of an atom interferometer. One commonly used geometry is a ring or toroidal trap. If the interfering particles are split such that they counterpropagate around the ring with an integer number of rotations, phase noise common to both arms is equal and opposite so it can be cancelled out. In addition, since the atoms will return to their initial position, a reflection pulse is not required so systematic noise can be reduced.

### 1.3.1 Optical Ring Traps

One method of creating a ring trap for BECs is to use optical potentials. These traps are typically small in size and as such the BEC may fill the entire ring, which means they are suited to the study of superflow [48, 49, 50, 51], although interferometry is still possible [52]. It is also possible to create arbitrary static potentials by using specially engineered diffraction gratings [53], or static and dynamical potentials by using an AOM to control a fast moving laser beam that ‘paints’ the trap [54]. The BEC can then be confined to the time averaged optical potential. Small ring traps can also be used to simulate other physical phenomena such as the sonic analogue of black holes [55].

### 1.3.2 RF Dressed Ring Traps

First proposed by Zobay and Garraway in 2006 [56], the application of radio-frequency (RF) radiation to a magnetic trap modifies the potential and can be used to create ring traps. The atomic sub-levels shift in the presence of an RF field, and the combined magnetic and RF energy, the dressed state, varies adiabatically in space giving rise to a trapping potential. This allows for the smooth, adiabatic transformation to different trap shapes, and the construction of novel trap geometries such as ring traps [57, 58, 59]

and double-well potentials that can be used as beam splitters for atom interferometry [60, 61].

### 1.3.3 Magnetic Ring Traps

The first magnetic ring trap for neutral atoms was demonstrated in 2001 [62]. Since then there have been various publications regarding magnetic ring traps for cold atoms [62, 63, 64], and many experiments have successfully demonstrated the confinement of BECs in magnetic waveguides (eg. [2, 65]). Hybrid ring traps combining magnetic and optical potentials have also been demonstrated [66]. Ring traps, both for BECs and thermal atoms, are of great interest commercially for compact rotation sensing.

### 1.3.4 Our AC Coupled Ring Trap

The apparatus presented in this thesis has a vertically-orientated, AC-coupled magnetic ring trap for a BEC, and is based on a previous generation AC coupled ring trap involving a horizontally orientated ring trap for thermal atoms [6, 7, 8]. Typically a magnetic ring trap would require current-carrying input and output wires to the coils that produce the magnetic field (eg. [2]). This results in deviations to the smooth magnetic field profile, often referred to as end effects, which can lead to an asymmetry in the system [63]. The AC coupled ring trap design does not require these input and output wires to be near the atoms and therefore results in a smoother trap geometry [6]. Moreover, the alternating current has the effect of smoothing any roughness in the crystal structure of the copper ring which further smooths the trapping potential [67].

## 1.4 Fine-Structure Constant

The fine-structure constant is given by

$$\alpha = \frac{e^2}{(4\pi\epsilon_0)\hbar c} \approx \frac{1}{137}, \quad (1.4)$$

where  $e$  is the charge of an electron,  $\epsilon_0$  is the permittivity of free space,  $\hbar$  is the reduced Planck constant, and  $c$  is the speed of light. Originally introduced by Sommerfeld in 1916, its purpose was to describe the splitting of degenerate energy levels in a Bohr atom [68]. It is a dimensionless parameter that characterises the strength of electromagnetic interactions [38], and as a result determines the structure of atoms and molecules, as well as the propagation of electromagnetic waves [69]. It has been described in Kolachevsky *et al.* [69] as “the electromagnetic force between two electrons at a distance of one meter measured in units where the speed of light  $c$  and Planck’s constant  $\hbar$  are set to unity” and is also the key parameter of calculations in quantum electrodynamics (QED) [70]. Interestingly, equation 1.4 combines three areas of

physics into one value: the charge of an electron  $e$  from particle physics, the reduced Planck constant  $\hbar$  from quantum physics, and the speed of light  $c$  from relativity. Another, perhaps more philosophical, question is why does  $\alpha$  have the value it does? If it was just slightly different, the universe as we know it would not have formed the way it has; atomic structure would be different leading to the alteration of star formation and the carbon chemistry on which life is based would not exist.

One argument for  $\alpha$  having the value it does is the anthropic principle, which states that we observe the value we do because if it was different we would not be here to make the observation in the first place, i.e.  $\alpha \approx 1/137$  because we exist to measure it.

Despite  $\alpha$  being described as a constant, there exists the possibility that it varies very slightly over time and space. In 1937 Dirac formulated his “large number hypothesis” [71] where he used known physical constants to construct small dimensionless numbers. For example, the age of the universe in atomic units divided by the electromagnetic force between a proton and electron in units of gravitational force, which in 1937 was calculated to be  $\xi \approx 3$  [69]. This is demonstrated below.

Cosmological theories in 1937 predicted the age of the universe to be around  $2 \times 10^9$  years old [71]. If we express this age in units of  $e^2/(m_e c^3)$ , where  $e$  is the charge of an electron,  $m_e$  is the mass of an electron, and  $c$  is the speed of light in a vacuum, with all constants taking their values in c.g.s units, we obtain a value of  $6.7 \times 10^{39}$ .

The electromagnetic force between a proton and an electron, in c.g.s units can be written as

$$F_{\text{em}} = \frac{q_p q_e}{r^2}, \quad (1.5)$$

where  $q_p$  and  $q_e$  are the proton and electron charges respectively, and  $r^2$  is their separation. The gravitational force, again in c.g.s units, is given by

$$F_g = \frac{G m_p m_e}{r^2}, \quad (1.6)$$

where  $m_p$  and  $m_e$  are the proton and electron masses respectively, and  $G$  is the gravitational constant. By taking the ratio  $F_{\text{em}}/F_g$  we obtain  $(q_p q_e)/(G m_p m_e)$ , and when calculated, this returns a value of  $2.3 \times 10^{39}$ . Thus, the age of the universe in atomic units,  $6.7 \times 10^{39}$ , divided by the electromagnetic force between a proton and an electron in units of the gravitational force,  $2.3 \times 10^{39}$ , is  $\approx 3$ .

It is worth pointing out that this calculation is based on information from 1937 and the current estimate of the age of the universe is  $13.8 \times 10^9$  years. Also, if SI units are used instead of c.g.s units with the current estimate of the age of the universe, we obtain a value of  $\xi \approx 1.5 \times 10^{14}$ .

From calculations such as this, Kolachevsky *et al.* state “the gravitational constant,  $G$ , or any other constant that appears in the construction of these small numbers should vary in time as the Universe expands”. A review of the possible variation in  $\alpha$  during different universe epochs is given in [72].

At the time of writing the best constraint on the temporal variation of  $\alpha$  was determined by Godun *et al.* [73] who reported  $\dot{\alpha}/\alpha = -0.7(2.1) \times 10^{-17} \text{yr}^{-1}$ . This

was achieved by comparing two ultra-narrow optical transition frequencies of  $^{171}\text{Yb}^+$ . However, it is possible that  $\alpha$  has varied in the past even if it is shown to be stable today [72].

It is worth noting that  $\alpha = \alpha(E)$ , which means that the value of  $\alpha$  actually changes depending on what energy scale is being considered, and equation 1.4 is only valid in the low energy limit. Physically, this low energy  $\alpha$  describes the interaction of electrons that are infinitely separated. If the electrons are close together, then there is a screening effect and the interaction energy increases, corresponding to an increase in  $\alpha$ . The variation of  $\alpha$  across differing energy scales is known as the running value and can be expressed by [74]

$$\alpha(E) = \frac{\alpha(0)}{1 - \Delta\alpha(E)}, \quad (1.7)$$

where  $\alpha(0)$  is the fine-structure constant value at zero energy (equation 1.4), and  $\Delta\alpha(E)$  is a measured deviation in  $\alpha(0)$  at a given energy.

The running value of  $\alpha$  is important in particle physics and has implications when considering the standard model. As mentioned in [75], the value of  $\alpha(E)$  is needed for precise standard model calculations, and interestingly  $\alpha(E)$  for  $E > 1$  GeV is the “least precisely known of the fundamental parameters of the standard model”. Also, it is expected that if the four forces (strong, weak, electromagnetic, and gravity) are unified,  $\alpha(E)$  and other running constants will converge at a high energy [76].

### 1.4.1 Measurement of $\alpha$

There are various ways in which  $\alpha$  has been measured [68]. For example, it can be determined by the measurement of the ‘anomalous’ electron magnetic moment (g-factor) and QED calculations [77]. The g-factor is the ratio of the magnetic moment to the angular momentum of a rotating charge. The part-per-thousand level corrections to the calculated g-factor value of 2, which arise due to the interaction of electrons with virtual particles in a vacuum, requires the input of  $\alpha$  [76, 70].

Another method is to measure the ratio  $h/m_a$ . The fine-structure constant can be written as [38]

$$\alpha^2 = \frac{2R_\infty}{c} \frac{m_a}{m_e} \frac{h}{m_a}, \quad (1.8)$$

where  $R_\infty$  is the Rydberg constant,  $m_a$  is the mass of a test atom,  $m_e$  is the mass of an electron, and  $h$  is Planck’s constant. The  $h/m_a$ , for alkali atoms, is the least well known part in the expression above and therefore if the precision of this was to increase, the precision of  $\alpha$  would be improved. Currently the uncertainty of  $R_\infty$  is  $1.6 \times 10^{-12} \text{ m}^{-1}$  [78]. The uncertainty in the  $^{87}\text{Rb}$ -electron mass ratio  $m_{\text{Rb}}/m_e$  is  $4.4 \times 10^{-10}$  [38, 79],  $c$  is defined as 299,729,458 m/s [80], and  $h/m_a$  is measured to  $5 \times 10^{-9} \text{ m}^2\text{s}^{-2}$  by [38].

The ratio  $h/m_a$  is often measured by using atom interferometry to determine the

#### 1.4. FINE-STRUCTURE CONSTANT

recoil frequency,  $\omega_r$ , of a test atom. The recoil frequency can be written as

$$\omega_r = \frac{1}{2} \frac{\hbar}{m_a} k^2, \quad (1.9)$$

where  $k$  is the wavevector of the interferometry beams. The wavelength, and therefore  $k$ , can be measured very accurately by use of, for example, a frequency comb. Therefore by measurement of  $\omega_r$ , a value of  $\hbar/m_a$  can be obtained and by substitution in equation 1.8, a value of  $\alpha$  can be calculated.

The current best estimate of  $\alpha$  from a single measurement was reported by Hanneke *et al.* [77]. They determined  $\alpha^{-1} = 137.035999084(51)$  by measurement of the electron magnetic moment. The current best estimate by measurement of  $\hbar/m_a$  was reported by Bouchendiria *et al.* [38] who found  $\alpha^{-1} = 137.035999037(91)$ . The CODATA database combines many different measurements and calculates an accepted value of  $\alpha^{-1} = 137.035999139(31)$  [81].

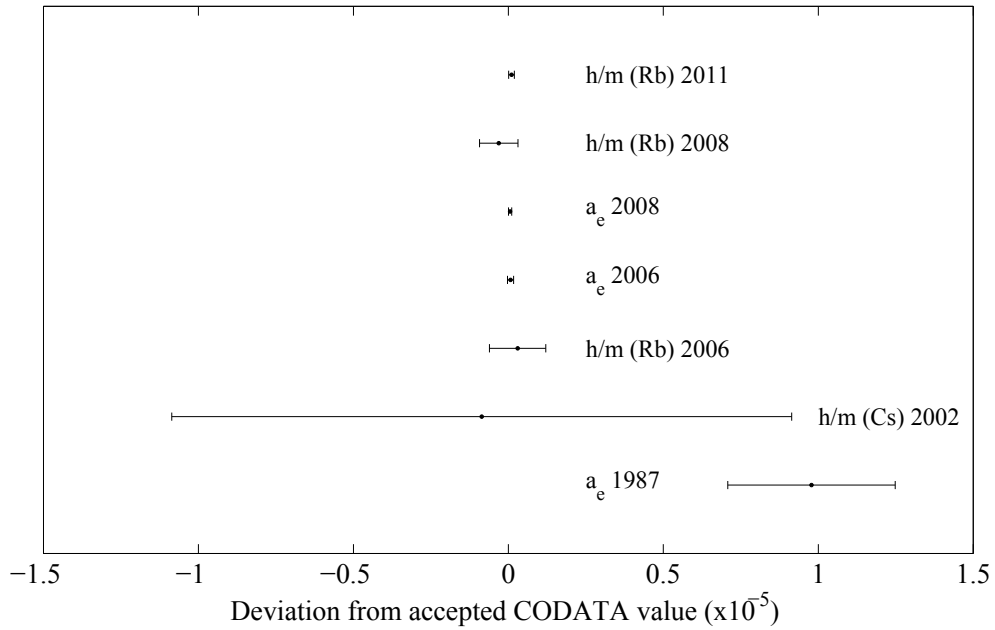


Figure 1.5: Measurements of  $\alpha$  relative to the accepted value reported by the CODATA database [81]. There are two types of measurement displayed: ‘h/m’ and electron anomaly measurements denoted by ‘ $a_e$ ’. From bottom to top: Van Dyck *et al.* 1987 [82], Wicht *et al.* 2002 [83], Cladé *et al.* 2006 [84], Odom *et al.* 2006 [70], Hanneke *et al.* 2008 [77], Cadoret *et al.* 2008 [85], and Bouchendiria *et al.* 2011 [38]. Note the values determined from ‘ $a_e$ ’ include the re-evaluation of the “eighth-order contribution” in QED calculations [86, 87].

## 1.5 Thesis Outline

This thesis reports on initial measurements of a Bose-Einstein condensate (BEC) atom interferometer, the progress towards performing atom interferometry in an AC coupled ring trap, and the initial measurement of the fine-structure constant. After motivating my work and the advantages of atom interferometry as a general technique, I give a brief description of the theory involved in creating a source of ultra-cold atoms in chapter 2. Then, in chapter 3, I describe the theory of the atom interferometer and describe how to achieve high efficiency optical control of a BEC using tuned pulses of light.

The experimental apparatus is described in chapter 4. The experiment reported here is a second generation AC coupled ring trap system and as such some of the optical setup remains the same [8]. With this in mind more emphasis is given to the newer apparatus including the interferometry laser and low light level detection. The experimental sequence used to create a BEC of  $^{87}\text{Rb}$  is also outlined.

Chapter 5 presents results from an atom interferometer performed in free space. I first demonstrate our beam splitter and mirror pulses described in chapter 3, then results from a full atom interferometer sequence and a preliminary measurement of the fine-structure constant are presented. The interferometer is then used to measure magnetic field gradients generated by an electromagnet

In chapter 6 I report on contrast interferometry. At the time of writing there are only two reported examples of this method [37, 88] and this is the first using a BEC of  $^{87}\text{Rb}$ . This technique allows atom interferometry to be performed with a greatly increased data readout rate.

Finally, a description of the AC coupled ring trap is given in chapter 7. This second generation, vertically orientated ring trap works on the same principle as the first generation. Whilst most of my PhD work was focussed on performing interferometry, the ring trap was used briefly as a proof of principle and thus the results will be reported here.

# Chapter 2

## Cold Atoms & Quantum Gases

In this chapter we consider the cooling and trapping of neutral atoms using magnetic and optical fields, with the goal being to create a Bose-Einstein condensate (BEC) that can be used for atom interferometry. The production of an atomic BEC<sup>1</sup> relies on capturing and cooling a large number of atoms.

We start in section 2.1 by considering the cooling of atoms from room temperature down to sub-Kelvin temperatures by the application of photons. Then we discuss magnetic trapping of these cold atoms and the creation of a magneto-optical trap (MOT). Optical trapping is then presented, followed by evaporative cooling techniques used in the creation of a BEC. Finally, in section 2.2 we outline the formation and properties of a BEC in a harmonic potential and introduce some key parameters.

### 2.1 Cooling and Trapping of Neutral Atoms

Atoms at room temperature have a speed of a few hundreds of meters per second ( $\approx 240$  m/s in the case of Rb). In order to achieve sufficient control of the atoms for our experiments we must first reduce their temperature and, therefore, their speed. A typical atom trap has a trap depth ranging from a few mK to a few hundred  $\mu$ K, or less, and any atoms that are hotter than this will have sufficient energy to escape the trap. Efficient cooling and trapping of atoms is key both in the experiment presented in this thesis and many others (eg. [5, 8, 90, 91]).

In order to cool atoms from room temperature laser cooling can be used. The idea, first proposed by Hänsch and Schawlow in 1975 [92], is to make fast moving atoms absorb many oncoming photons, and the momentum kick from these photons will reduce the velocity of the atoms and thus reduce temperature. Each absorption event transfers a very small amount of momentum ( $\hbar k$ , where  $k$  is the wavevector of the photon) to the atom, and therefore many absorption events are needed. A laser provides an ideal source of photons for this, due to the high photon flux and well

---

<sup>1</sup>A BEC of photons has been made by Klaers *et al.* [89]

defined wavelength.

### 2.1.1 Doppler Cooling

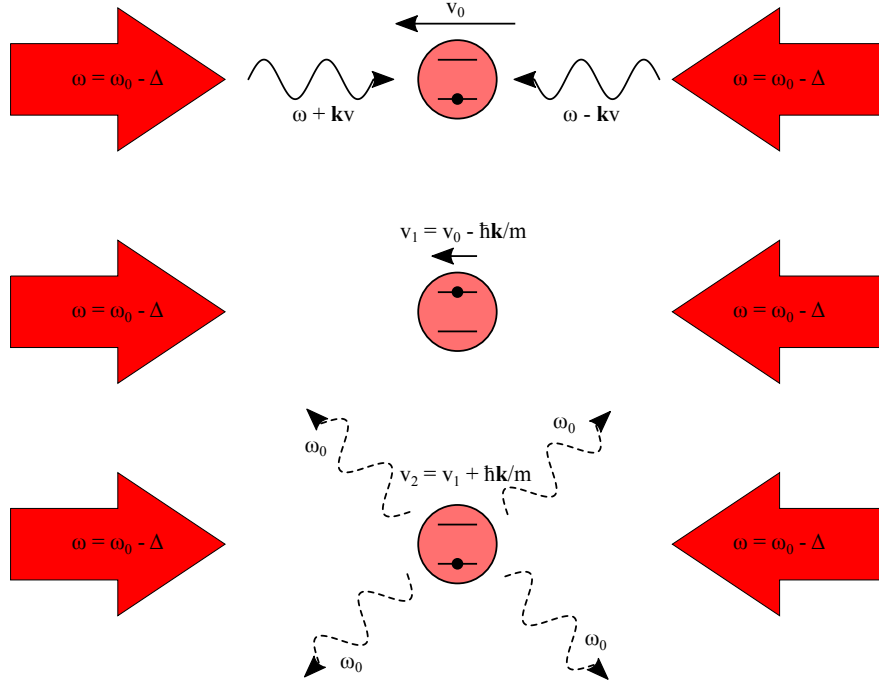


Figure 2.1: *Doppler cooling diagram. An atom moving to the left preferentially absorbs a photon from the left beam. This causes a momentum kick opposing the direction of travel and therefore a reduction in velocity due to the conservation of momentum. The atom, now in the excited internal state, can emit a photon by spontaneous emission in a random direction, which results in a second momentum kick.*

For simplicity we consider a two-level atom moving in 1D. We apply two counter-propagating laser beams of frequency  $\omega$  that are red detuned from the atomic resonance, as shown in figure 2.1. As an atom moves along the axis of the beams it ‘sees’ the frequency of one beam increase and the other decrease. This Doppler shift results in the increased frequency laser becoming closer to the atomic transition resonance and therefore photons from this beam are preferentially absorbed by the atom. This photon absorption rate for a single laser beam, also known as the scattering rate, can be expressed as

$$\gamma_{sc} = \frac{\Gamma}{2} \frac{I/I_{sat}}{1 + I/I_{sat} + 4(\frac{\Delta + \vec{k} \cdot \vec{v}}{\Gamma})^2}, \quad (2.1)$$

where  $\Gamma$  is the linewidth of the atomic transition,  $I$  is the laser intensity,  $I_{sat}$  is the saturation intensity,  $\delta$  is the laser detuning from the atomic transition,  $\vec{k}$  is the wavevector

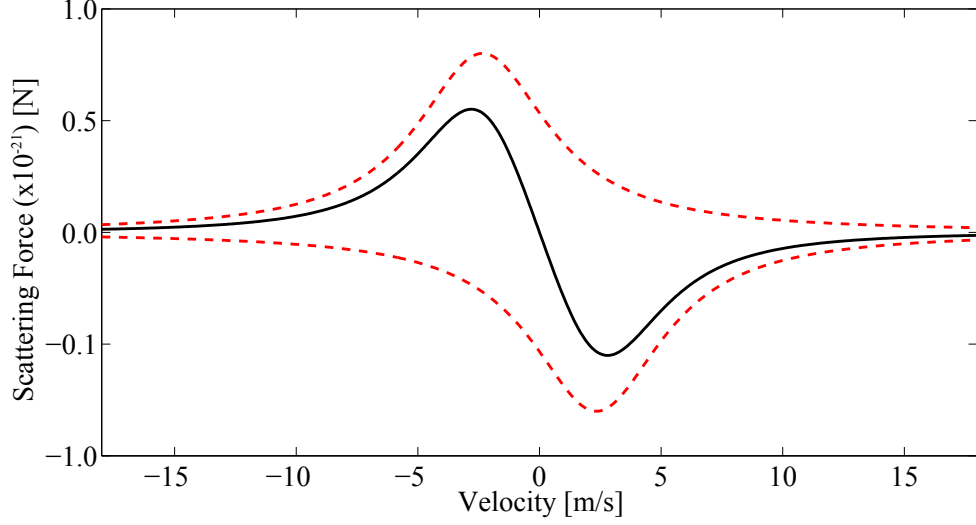


Figure 2.2: Scattering force as a function of atomic velocity (equation 2.2). The red dashed lines indicate the forces from a single laser beam while the solid black line is the sum of the two forces. Here,  $I/I_{\text{sat}} = 1$  and  $\Delta = -\Gamma/2$ .

of the laser, and  $\vec{v}$  is the velocity of the atom. The fact that there are two counter-propagating beams gives rise to a viscous, or restoring force, acting upon the atoms that is often referred to as optical molasses. The force from a single laser beam is given by

$$\vec{F}_{\text{scatt}} = \hbar \vec{k} \frac{\Gamma}{2} \frac{I/I_{\text{sat}}}{1 + I/I_{\text{sat}} + 4\left(\frac{\Delta + \vec{k} \cdot \vec{v}}{\Gamma}\right)^2}. \quad (2.2)$$

Figure 2.2 plots the force on an atom as a function of velocity in the presence of two counter-propagating laser beams. This force implies that it would be possible for the atom to reach a temperature of 0 K, however in reality this is not the case as described below.

The lower temperature limit for the mechanism described above, the Doppler limit, arises due to the random direction in which the absorbed photon is emitted, and in fact this emission increases the temperature of the atom slightly. The Doppler limited temperature (for a six beam molasses) can be expressed as [93]

$$T_D = \frac{\hbar \Gamma}{4k_B} \frac{1 + (2\Delta/\Gamma)^2}{2|\Delta|/\Gamma}, \quad (2.3)$$

where  $k_B$  is the Boltzmann constant. This is minimised at  $\Delta = -\Gamma/2$  giving  $T_{D\text{min}} = \hbar\Gamma/2k_B$  (146  $\mu\text{K}$  for  $^{87}\text{Rb}$ ).

If the atoms are moving sufficiently fast the laser frequency will remain far from resonance and the atomic motion will not be impeded. This gives rise to a maximum velocity that an atom can have if it is to be impeded by the molasses beams such that it

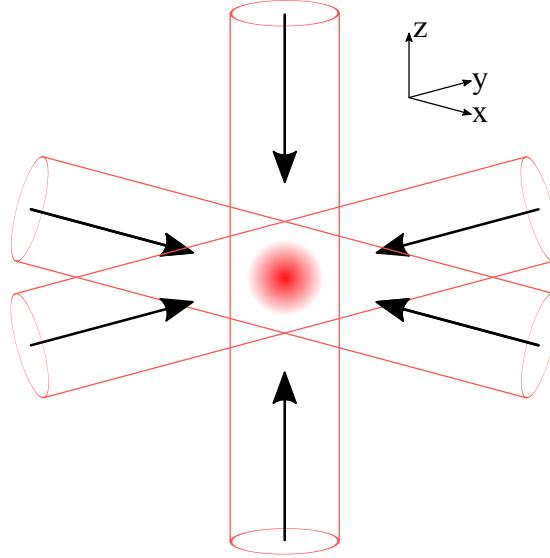


Figure 2.3: *Six beam 3D molasses. By expanding the mechanism described in figure 2.1, cooling in three spatial dimensions can be achieved.*

is ‘captured’ in velocity space and settles at the point (0,0) in figure 2.2. An estimate of this capture velocity is given by  $v_c \simeq \Gamma/k$  [93], which for  $^{87}\text{Rb}$  is  $\approx 5 \text{ ms}^{-1}$ .

To create a 3D optical molasses the above description can be expanded to include six laser beams (figure 2.3) and atomic velocity components in three directions [94, 95].

### 2.1.2 Sub-Doppler Cooling

Using the model outlined above, the minimum achievable temperature is limited to the Doppler temperature (equation 2.3). However, experimentally lower temperatures can be achieved as observed by Lett *et al.* in 1988 using sodium atoms [96]. Below we outline the two common models explaining this sub-Doppler cooling.

The two types of sub-Doppler cooling at play in a 3D molasses are Sisyphus cooling, involving two counter-propagating laser beams of orthogonal linear polarisation, and polarisation gradient cooling using laser beams of opposite circular polarisation [97, 95]. Experimentally, circularly polarised beams are used but due to the interference between the (typically six) beams, the polarisation gradients are complex and both effects contribute to the cooling, hence both methods are described below.

**Sisyphus cooling:** Consider an atom with two ground states:  $m_J = +1/2$  and  $m_J = -1/2$ , and an excited state  $J' = J + 1$ . The interference of two counter-propagating, orthogonally linearly polarised laser beams, red detuned from the atomic resonance produces a periodic modulation in the AC stark shift of the ground states [93]. In figure 2.4, an atom entering from the left in the  $m_J = -1/2$  state, sees an increasing

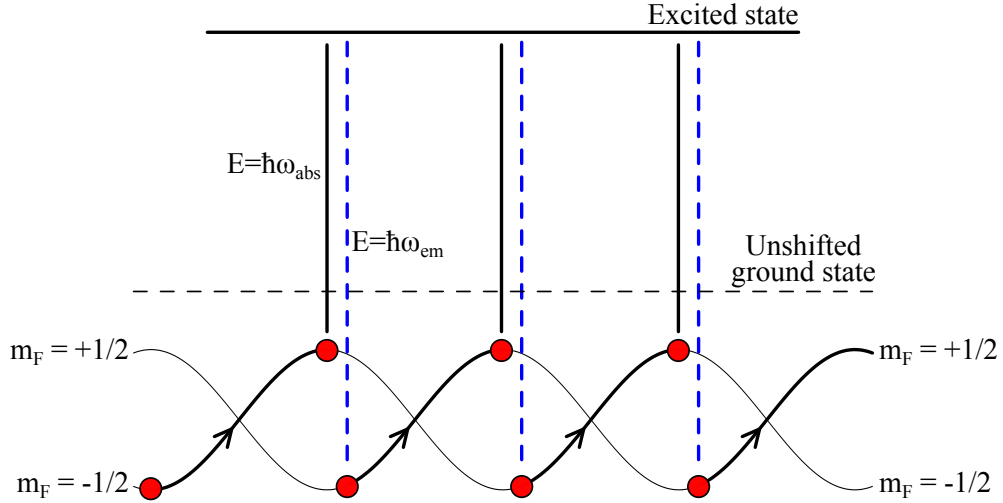


Figure 2.4: A periodic AC stark shift is generated by the interference of two counter-propagating, red detuned laser beams whose polarisation is linear and orthogonal. An atom entering from the left gains potential energy as it travels, shifting it closer to resonance. It absorbs a photon, then by spontaneous emission emits a photon such that it transitions to the other ground state. The net effect is it dissipates an energy of  $E = \hbar(\omega_{\text{em}} - \omega_{\text{abs}})$  per cycle, resulting in cooling.

potential. As it travels up the ‘hill’ its transition is shifted closer to the frequency of the laser and the possibility of absorbing a photon increases. It can then spontaneously decay by emitting a photon which transfers it to either the  $m_J = +1/2$  state or the  $m_J = -1/2$  state. If the atom transitions to the  $m_J = -1/2$  state, the absorption process repeats, but if it transitions to the  $m_J = +1/2$  state the atom now has a lower potential energy than before the absorption-emission event and thus energy is dissipated from the system, resulting in cooling. This cycle can then be repeated many more times to provide further energy dissipation of  $E = \hbar(\omega_{\text{em}} - \omega_{\text{abs}})$  per cycle.

**Polarisation gradient cooling:** Two red detuned, counter-propagating laser beams are circularly polarised. The laser beams interfere to give a standing wave of linearly polarised light, the polarisation of which rotates along the beam axis with period  $\lambda/2$  [97]. We consider a two-level atom with ground states  $m_F = -1, 0, 1$  and excited states  $m_F = -2, -1, 0, 1, 2$  (figure 2.5).

If the atom is at rest, the distribution of states is symmetric around  $m_F = 0$ , and it is energetically favourable for the atom to be in the  $m_F = 0$  ground state. If the atom starts moving, the local polarisation direction changes, which causes the  $m_F$  states skew and become asymmetric as a result of the light-shift. It also causes the oncoming  $\sigma^+$  beam to shift closer to resonance and the atoms start to get optically pumped toward the most light-shifted  $m_F$  level. Moreover, the Clebsch-Gordon coefficients of the most light-shifted transitions increase.

The dipole of the atom has minimum energy when aligned with the polarised field.

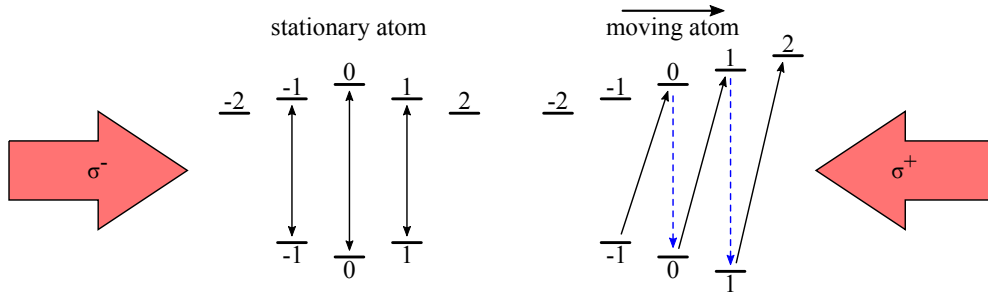


Figure 2.5: A stationary atom sees a linearly polarised light field. If it starts moving to the right the  $\sigma^+$  beam becomes closer to resonance and the atom is optically pumped into the positive  $m_F$  states. The difference in energy between the absorbed and emitted photons leads to the dissipation of energy and therefore cooling. Numbers in figure denote the  $m_F$  states of the atom

This dipole cannot instantly change direction to align itself with a new polarisation direction, but instead takes some finite time to do so via the scattering of photons. Much like Sisyphus cooling, the kinetic energy of the atom is converted to potential energy during the absorption and emission of photons, which allows the dipole to realign with the new polarisation direction. Thus, as before, the energy of the system is dissipated via spontaneously emitted photons, but unlike the Doppler limited case, the energy loss is the *difference* in energy between the absorbed and emitted photons.

The mechanisms above are known as polarisation gradient cooling and are limited by the recoil momentum of the atom,  $\hbar k$ , which is the momentum one atom gets from absorbing one photon. This lower temperature can be written as

$$T_{\text{rec}} = \frac{\hbar^2 k^2}{mk_B}, \quad (2.4)$$

where  $m$  is the atomic mass and  $k_B$  is the Boltzmann constant. For  $^{87}\text{Rb}$  this is 362 nK [98] although experimentally the lowest temperatures are typically several  $T_{\text{rec}}$  [99]. This can be intuitively understood because as the atom cools and loses kinetic energy, its de Broglie wavelength increases such that it is compatible in length to the periodicity of the polarisation lattice. Therefore its position is poorly defined, the variation in energy between the  $m_F$  states washes out and the cooling mechanism becomes less efficient.

### 2.1.3 Magneto-Optical Traps

The application of laser light onto atoms can reduce their temperature as described above. It does not, however, provide spatial trapping as atoms will eventually diffuse out of the laser cooling volume. The trapping of atoms can be achieved by the application of magnetic fields combined with light. A magneto-optical trap (MOT) can be constructed that both cools and traps the atoms by adding a spatially varying magnetic

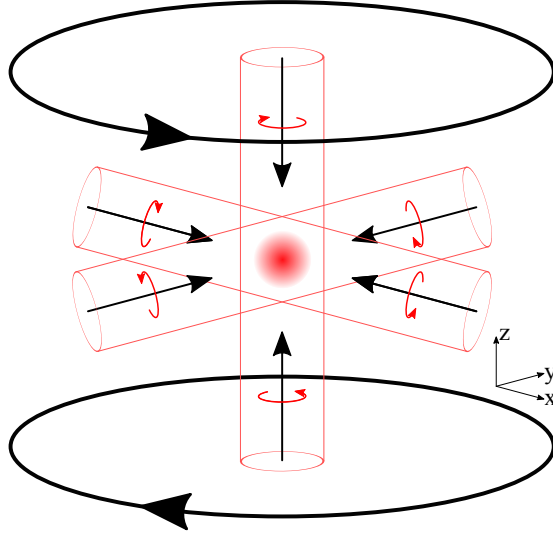


Figure 2.6: *Six beam 3D MOT. By expanding the mechanism described in figure 2.7, cooling and trapping in three spatial dimensions can be achieved.*

field. Here the light provides the velocity trapping whilst the magnetic field provides the spatial trapping. This atom trapping scheme was first demonstrated in 1987 by Raab *et al.* [100] using a six beam configuration. This is the most commonly used configuration although in principle only  $n + 1$  beams are needed to trap atoms in  $n$  dimensions, and thus only 4 beams are needed for 3D trapping [101].

To construct a (six beam) MOT a quadrupole magnetic field is applied to the overlap region of the six circularly polarised molasses beams. This is typically done with two magnetic coils in an anti-Helmholtz configuration as shown in figure 2.6. The quadrupole field gives a zero magnetic field at the centre of the trap and a linearly increasing field going outwards. The trapping mechanisms can be described by considering the 1D case (figure 2.7) and then expanding into 3D as done previously, however, here we must consider the  $m_F$  states.

In figure 2.7, we label the polarisation of the laser beam as  $\sigma^+$  and  $\sigma^-$ , not to indicate handedness of the polarisation but the atomic transitions that they drive. The accessible atomic transitions for each handedness changes depending on what direction the magnetic field gradient is (the quantisation axis), and hence the direction of optical pumping flips as an atom crosses the centre of the trap. This is why a single beam is labelled as  $\sigma^+$  on one side of the magnetic field and it is labelled  $\sigma^-$  on the other.

We start with a two-level atom in the ground state  $|F = 0, m_F = 0\rangle$ , and two counter-propagating laser beams detuned from the atomic resonance. The atom can be excited into the  $|F' = 1, m_{F'} = -1, 0, +1\rangle$  state depending on the polarisation of the incident light. Right hand circularly polarised light drives  $\Delta m_F = +1$  transitions where the quantisation axis is collinear with the incident photon and similarly left hand circularly polarised light drives  $\Delta m_F = -1$  transitions. If the atom moves to the right

## 2.1. COOLING AND TRAPPING OF NEUTRAL ATOMS

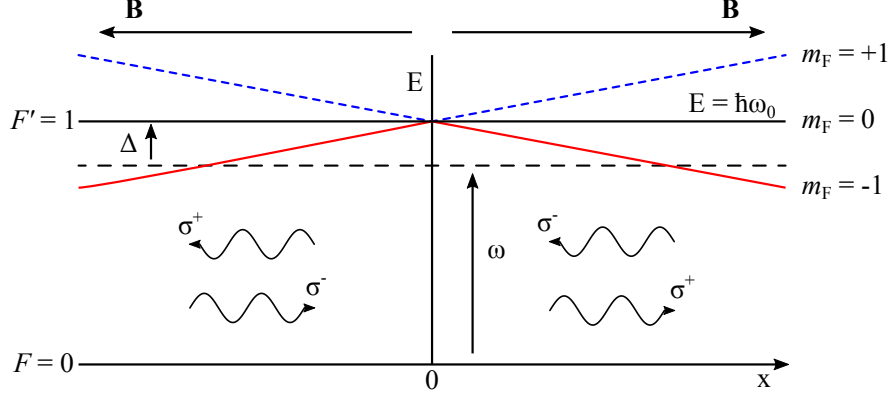


Figure 2.7: 1D MOT schematic. An atom in the  $|F = 0, m_F = 0\rangle$  ground state sees a Zeeman shift of its  $|F = 1, m_F = -1, 0, 1\rangle$  magnetic sub-levels which is proportional to its position (due to the magnetic field). This shifts the relative detunings of the incoming laser beams, and therefore the atom preferentially absorbs a photon of the appropriate polarisation. For example, an atom at a position of positive  $x$  has its  $|F = 1, m_F = -1\rangle$  state shifted closer to resonance and so is more likely to absorb a  $\sigma^-$  photon and get kicked towards negative  $x$ .

of centre ( $x > 0$  in figure 2.7), it sees a Doppler shift in the light beam due to its velocity as well as a change in  $m_{F'}$  level energy, due to the Zeeman splitting. In our case we set  $g_F > 0$  and hence  $m_F = -1$  is shifted closer to resonance. The atom therefore preferentially absorbs a photon from the counter-propagating ( $\sigma^-$  beam) which results in a momentum kick towards the centre of the trap. An atom moving to the left of centre experiences the same phenomena and the  $m_F = -1$  is again shifted closer to resonance but here the magnetic field gradient is the opposite direction and therefore it preferentially absorbs a photon from the counter-propagating beam.

The detuning of the  $\sigma^-$  laser beams decreases as the distance from the centre of the trap increases due to the increasing B-field. Therefore the restoring force that the atoms experience increases as they drift further from the centre. This force can be written as [8]

$$\vec{F} = -\beta\vec{v} - \kappa\vec{r}, \quad (2.5)$$

where  $\beta$  is the damping coefficient and  $\kappa$  is the spring constant (when the laser detuning is large compared to the Doppler and Zeeman shifts). This force leads to damped harmonic motion of the atoms [95]. Note that for a quadrupole field the trapping force is not spherically symmetric and the force is double along the coil axis compared to the radial directions due to the increased field gradient.

The system described above is a one dimensional case but if it is expanded into three dimensions using six orthogonal beams and a quadrupole magnetic field, it is possible to trap atoms in three spatial dimensions.

The maximum atomic velocity (temperature) of an atom that a MOT can capture is known as the capture velocity  $v_c$ . It is given by “the incoming velocity for which

atoms are completely stopped when they reach the opposite edge of the MOT region” and is typically  $\sim 100 \text{ m s}^{-1}$  [95].

### 2.1.4 Magnetic Trapping

In order to obtain control over, and interact with atoms, it can be useful to confine them to a specific location in space. One method of achieving this is to use magnetic trapping.

The potential energy of an atom in a magnetic field can be written as

$$U_B = -\vec{\mu} \cdot \vec{B}, \quad (2.6)$$

where  $\vec{B}$  is the external magnetic field and  $\vec{\mu}$  is the magnetic moment of the atom [97]. This magnetic moment varies with  $m_F$  level and as such the atomic energy can increase or decrease depending on the  $m_F$  value. Magnetic trapping works by the fact that for a given  $m_F$  state, the potential energy of the atom  $U_B$  can be written as

$$U_B = g_F m_F \mu_B |\vec{B}|, \quad (2.7)$$

where  $g_F$  is the Landé g-factor and  $\mu_B$  is the Bohr magneton. Thus for  $g_F m_F > 0$ , atoms are low-field seeking and can be magnetically trapped in a static magnetic field. High-field seeking atoms ( $g_F m_F < 0$ ) cannot be trapped<sup>2</sup>, due to Earnshaw’s theorem which states there cannot be any local DC field maxima in free space [103, 104].

In order for neutral atoms to remain trapped, they must remain in a low field seeking state. Therefore the magnetic moment of the atom  $\vec{\mu}$  must be able to follow the magnetic field lines as it moves around within the trap. The precession of the magnetic moment is known as the Larmor precession frequency  $\omega_L$  and is given by

$$\omega_L = \frac{g_F m_F \mu_B |\vec{B}|}{\hbar}. \quad (2.8)$$

To avoid the atoms ‘spin-flipping’ into an untrapped  $m_F$  state, the rate of change of the magnetic field in the reference frame of the moving atom must be significantly less than  $\omega_L$  [95]. If this condition is met, the atom will maintain its  $m_F$  state and it is said to follow the magnetic field adiabatically. The first observation of magnetically trapped neutral atoms was made by Migdall *et al.* in 1985 [105] using a quadrupole trap.

A quadrupole trap can be created by two coils of wire aligned axially along the z axis. A current is passed through them in opposite directions which is known as an anti-Helmholtz configuration. The resultant magnetic field gives a trapping potential that, for a ground state atom, can be written as [90]

$$U(x, y, z) = \mu_B g_F m_F B'(\vec{r}) \sqrt{\frac{x^2}{4} + \frac{y^2}{4} + z^2}, \quad (2.9)$$

---

<sup>2</sup>The group of Schmiedmayer actually successfully trapped high-field seeking atoms using a single current-carrying wire [102].

where  $B'(\vec{r})$  is the magnitude of the spatially varying magnetic field. This magnetic field geometry has been described as a “three dimensional ‘conical’ potential” [90].

The simplicity of the quadrupole trap is attractive for experiments. However, there exists a point of zero magnetic field at the very centre of the trap. At this position, the  $m_F$  states of the atom become degenerate and therefore there is a possibility that the atom will fall into an untrapped or antitrapped  $m_F$  state. This results in the atom leaving the trap. These losses are known as Majorana losses [106].

It is possible to avoid Majorana losses by removing the point of zero magnetic field from the trap. This can be achieved using repulsive blue detuned light to ‘plug’ the bottom of trapping potential and was essential for the production of the first BEC of sodium [107]. Another method to reduce Majorana losses is to use a time orbiting potential (TOP) [108], which involves applying a time varying bias field of angular frequency  $\omega_B$  to make the magnetic zero point orbit around the atoms such that the atoms see the averaged potential which contains no zeros. For this scheme to work, the varying magnetic field must meet the condition

$$\omega_L > \omega_B > \omega_A, \quad (2.10)$$

where  $\omega_A$  is the frequency of the atomic motion [8].

### 2.1.5 Optical Dipole Traps

Optical dipole traps for neutral atoms work due to the AC Stark shift. This is the variation of atomic energy levels in the presence of a light field and is analogous to the Zeeman shift in magnetic fields. If the light field is red detuned from the atomic resonance, it is energetically favourable for the atoms to remain in a region of maximum intensity, whilst blue detuned light will repel atoms. It is therefore possible to trap atoms in a red detuned beam and the spatially varying Gaussian beam profile will provide 3D confinement at a beam focus. A blue detuned beam can also provide confinement if more complex beam shapes are used. For example, a cylindrical beam with two sheets capping the ends can produce a uniform cylindrical trap for a BEC [109]. Note that these potentials are conservative for far detuned beams so in order to retain the atoms in the trapping volume, the atomic temperature must be less than the trap depth.

In order for the confining dipole force  $U_{\text{dip}}$  to dominate over the force from scattering photons  $\Gamma_{\text{sc}}$ , the laser must be sufficiently detuned. However, if we assume that the detuning from atomic resonance of the trapping laser,  $\Delta$ , is much less than the atomic resonance itself, such that  $\Delta \ll \omega_0$ , then the rotating-wave approximation ( $\omega/\omega_0 \approx 1$ ) expression for these two phenomena are [110, 111]

$$U_{\text{dip}} = \frac{3\pi c^2}{2\omega_0^3} \frac{\Gamma}{\Delta} I, \quad (2.11a)$$

$$\Gamma_{\text{sc}} = \frac{3\pi c^2}{2\hbar\omega_0^3} \left(\frac{\Gamma}{\Delta}\right)^2 I, \quad (2.11b)$$

where  $\omega_0$  is the optical transition frequency and  $I$  is the laser intensity. Note that these equations assume a single atomic transition. The important thing to note here is that  $U_{\text{dip}}$  scales as  $1/\Delta$  while  $\Gamma_{\text{sc}}$  scales as  $1/\Delta^2$  and therefore it is advantageous to have a far detuned trapping laser. However, an increased intensity would then be needed to provide the same trap depth.

It is worth noting that in our experiment we use  $^{87}\text{Rb}$  which has a  $D_1$  and a  $D_2$  transition of 795 nm and 780 nm respectively. Therefore we drive multiple transitions with our 1070 nm trapping laser, and a more complete expression for the trap depth would be the incoherent sum of equation 2.11a, [110]

$$U_{\text{dip}}(r) = \frac{\pi c^2 \Gamma}{2\omega_0^3} \left( \frac{2 + \mathcal{P} g_F m_F}{\Delta_{2,F}} + \frac{1 - \mathcal{P} g_F m_F}{\Delta_{1,F}} \right) I(r), \quad (2.12)$$

where  $\mathcal{P}$  indicates the polarisation of the laser (0 or  $\pm 1$  for linear and circular  $\sigma^\pm$  respectively), and  $\Delta_{2,F}$  and  $\Delta_{1,F}$  are the detunings from the transitions between the ground state  $5^2S_{1/2}$  and the  $5^2P_{3/2}$  and  $5^2P_{1/2}$  excited states respectively.

### 2.1.6 Radio Frequency Evaporative Cooling

The laser cooling techniques described previously can cool and trap atoms down to a temperature of a few recoil energies (equation 2.4). This puts a hard limit on the minimum achievable temperature and in order to decrease the temperature further other methods must be used. Such a method is radio frequency (RF) evaporative cooling. Simply put, we remove the hottest atoms and allow the remaining atoms to rethermalise, thus reducing the temperature.

Ideally we would use a mechanism, such as an RF field, to remove only the hottest atoms from the trap, and indeed we can selectively target the hottest atoms by the application of a spatially varying magnetic field in conjunction with an RF field. The atoms in the high magnetic field have their  $m_F$  states Zeeman shifted onto resonance with an otherwise detuned RF field. This selected velocity group of atoms then transition from one spin state to another, e.g. from  $|F = 1, m_F = 1\rangle$  to  $|F = 1, m_F = -1\rangle$  via the  $|F = 1, m_F = 0\rangle$  state, and are left untrapped or anti-trapped.

The application of an RF field targets one 'position', or more generally, atoms at one particular magnetic field value. This gives rise to an evaporation surface; the surface from which the atoms are lost from the trap.

To evaporatively cool an ensemble of atoms, we must remove the hottest atoms, then allow time for the system to rethermalise via inter-atomic collisions, which narrows the velocity distribution of the atoms and the atoms are cooled. This technique is then repeated, and if we make the time step increasingly small, we can use a smooth RF field ramp of decreasing frequency to apply an 'RF knife' to the system that progressively targets the hottest remaining atoms in the ensemble. The average temperature of the remaining atoms is therefore decreased as the frequency of the RF field is decreased.

## 2.1. COOLING AND TRAPPING OF NEUTRAL ATOMS

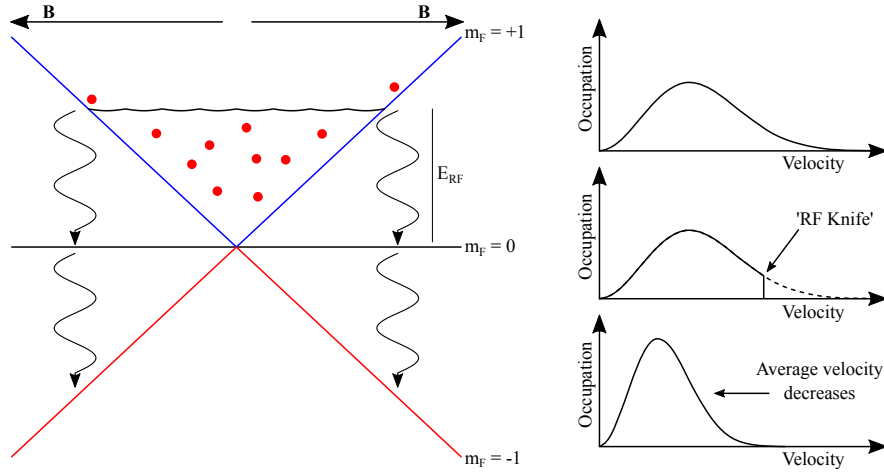


Figure 2.8: *RF cooling scheme. Atoms in the  $|F = 1, m_F = 1\rangle$  state are trapped in a quadrupole field. When an RF photon becomes resonant, it causes the atom to ‘spin flip’ and it becomes untrapped or anti-trapped. The hotter atoms have more energy and can reach higher RF frequencies, therefore the RF field is swept from high to low frequency such that the hotter atoms are addressed first. With rethermalisation, the average temperature of the ensemble decreases. Note that the effects of gravity are neglected here.*

The maximum speed at which the RF sweep can be applied whilst still achieving efficient cooling is determined by the scattering rate, which is the number of inter-atomic collisions per second. The higher the scattering rate the faster the rethermalisation and therefore the RF sweep can be applied faster. If the RF sweep is too fast, there will be very few remaining atoms at the end, albeit very cold, and whilst a slow ramp in principle would work, experimental factors such as trap lifetime start to come into play that make a slow ramp less than optimal. In producing a BEC, the figure of merit during the evaporation stage is phase-space density, discussed in section 2.2.1, which should increase throughout the sequence. This requires a high atom number and a low temperature and as a result RF sweep parameters are often experimentally tuned.

It is worth noting that the trap described in figure 2.8 is a quadrupole magnetic field. Therefore there exists a point of zero magnetic field at the centre. At this point the  $m_F$  states of the atom become degenerate and Majorana losses can occur (section 2.1.4). This is a limiting factor in our experiment; as we cool the atoms a point is reached where the atoms are lost without a reduction in temperature. Also, the quadrupole trap is not harmonic. As a result the rethermalisation dynamics during the RF knife technique are altered slightly from the typical example of atoms in a harmonic trap.

Given an appropriate trap geometry and RF ramp, it is possible to cool bosons to a Bose-Einstein condensate using this method (eg. [2, 5, 90]).

### 2.1.7 Optical Evaporative Cooling

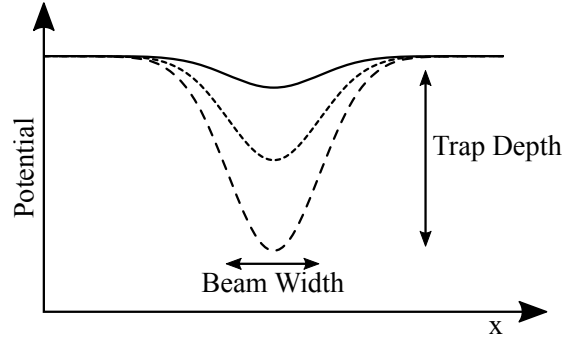


Figure 2.9: *Optical evaporative cooling. As the power of the laser beam is reduced, the trap depth is also reduced. This allows the hottest atoms to escape the trap. With the correct temporal power sweep, the remaining atoms rethermalise and the mean temperature of the ensemble decreases. Note that the effects of gravity are neglected here.*

The general idea of evaporative cooling in optical potentials is the same as for RF cooling in magnetic potentials; the most energetic atoms escape thus lowering the average temperature of the remaining atoms. As described in section 2.1.5, for a red detuned trapping beam the atoms see a potential minimum at the point of maximum intensity and, for a Gaussian beam, the potential will have a Gaussian profile. Any atoms with energy greater than the trap depth will be able to escape the confining potential (equation 2.11a) and this fact is used to control the evaporative cooling.

To achieve optical evaporative cooling the optical power of the trapping beam will initially be high in order to have a deep trapping potential and capture a large number of atoms. The power can then be ramped down allowing the hot atoms escape and the remaining atoms rethermalise and reduce the average temperature of the ensemble. As in RF cooling this ramp is typically approximately exponential in shape, which allows sufficient time for the atoms to rethermalise.

A key difference from RF cooling is the varying trap frequency. In this case the trap frequency, and therefore atomic collision rate, scales with the square root of optical power [112]. Therefore, as the power is reduced so does the collision rate and rethermalisation takes longer [113]. To account for this the power ramp can be drawn out in time such that the exponential is effectively stretched, or a magnetic field can be added to provide additional confinement and recover some of the reduced trap frequency [114, 115]. The application of both optical and magnetic trapping potentials is referred to as a hybrid trap. It is this type of trap that is used in this thesis to create a BEC.

## 2.2 Bose-Einstein Condensation

The de Broglie wavelength of a particle of mass,  $m$ , at temperature,  $T$ , is written as

$$\lambda_{\text{dB}} = \frac{h}{\sqrt{2\pi m k_B T}}. \quad (2.13)$$

At room temperature, atoms can be considered as particles due to their short de Broglie wavelength. It can be seen that as temperature decreases, the de Broglie wavelength increases. When the wavelength becomes greater than the inter-atomic spacing of an ensemble, the particles overlap and become indistinguishable. Providing the particles are bosons, they preferentially condense into the ground state of a trapping potential and Bose-Einstein condensation can occur.

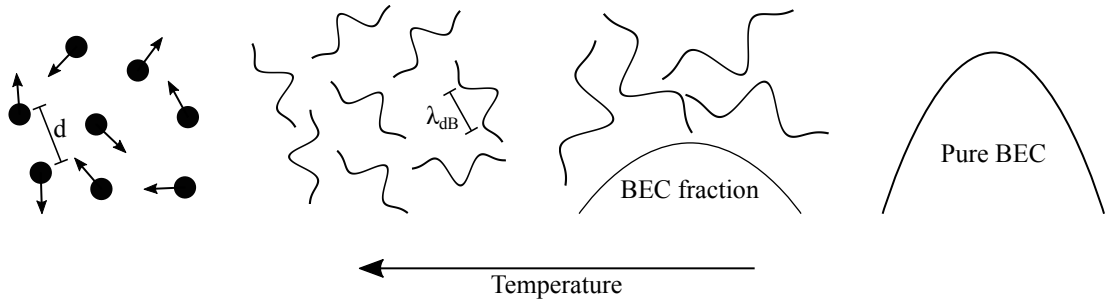


Figure 2.10: As the temperature of a cloud of bosons decreases, their de Broglie wavelength becomes comparable to the inter-atomic separation. At this point the bosons start to overlap and they condense into the ground state of the trapping potential. As temperature decreases further, the fractional population of atoms in the condensed fraction increases until a pure BEC remains. Figure adapted from [108].

### 2.2.1 Phase-Space Density

Phase-space density,  $\Lambda$ , is a critical parameter in creating a BEC. It is defined as “the number of particles contained within a volume equal to the cube of the thermal de Broglie wavelength” [104], and is written as

$$\Lambda = n\lambda_{\text{dB}}^3, \quad (2.14)$$

where  $n$  is the number density. Therefore if it is greater than one, the particles can be considered as overlapping. Phase-space density is dependent on atom density and temperature, and we will now show that a large number and low temperature are required to create a BEC.

The minimum phase-space density needed to achieve condensation is in fact more complicated than above, and this critical phase-space density has a value of 2.612 regardless of the trapping potential [116].

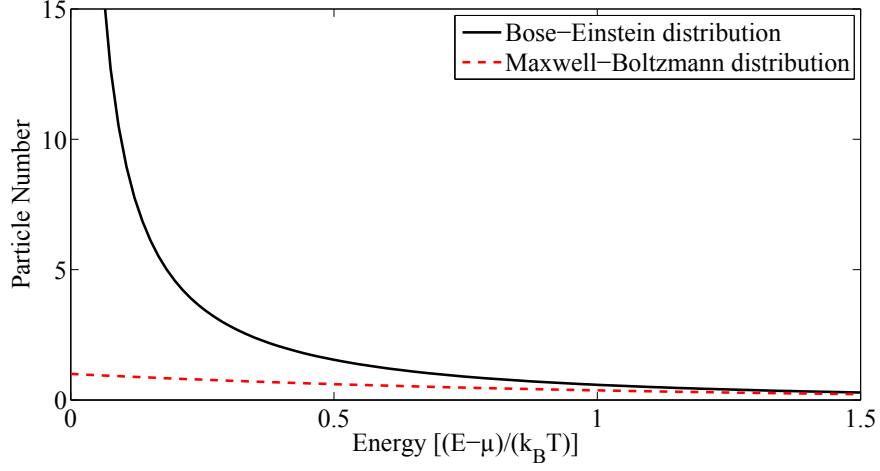


Figure 2.11: *Bose-Einstein distribution (black solid line) and a Maxwell-Boltzmann distribution (red dashed line) describing the occupation of energy levels of a system in thermal equilibrium.*

### 2.2.2 Bose Gas in a Harmonic Potential

The following describes the properties of an ideal Bose gas in a harmonic potential and follows the formalism of [117]. We start by considering a system of  $N$  non-interacting bosons in a harmonic potential. At thermal equilibrium the particles will exist in a Bose-Einstein distribution over the energy levels (figure 2.11):

$$N_{n_x, n_y, n_z} = \frac{1}{\exp[\beta(E_{n_x, n_y, n_z} - \mu)] - 1}, \quad (2.15)$$

where  $n_x, n_y, n_z = 0, 1, 2, \dots$  are the energy levels of the trapping potential,  $\beta = 1/(k_B T)$ ,  $E$  is energy, and  $\mu$  is the chemical potential. The total number of particles  $N$  is then

$$N = \sum_{n_x, n_y, n_z=0}^{\infty} \frac{1}{\exp[\beta(E_{n_x, n_y, n_z} - \mu)] - 1}. \quad (2.16)$$

If  $k_B T$  is larger than the energy level spacing in the harmonic potential, the sum in equation 2.16 can be replaced with an integral:

$$N = N_0 + \int_0^{\infty} dE D(E), \quad (2.17)$$

where  $N_0$  is the population number of the lowest energy state,

$$N_0 = \frac{1}{\exp[\beta(E_0 - \mu)] - 1}, \quad (2.18)$$

and  $D(E)$  is the density of states for a harmonic trap given by [118]

$$D(E) \simeq \frac{1}{2} \frac{E^2}{(\hbar\bar{\omega})^3} + \gamma \frac{E}{(\hbar\bar{\omega})^2}, \quad (2.19)$$

where  $\bar{\omega} = (\omega_x\omega_y\omega_z)^{1/3}$  is the geometrical mean trap frequency and

$$\gamma = \frac{\omega_x + \omega_y + \omega_z}{2\bar{\omega}}. \quad (2.20)$$

For an isotropic trap  $\gamma = 3/2$  [118]<sup>3</sup>.

By substitution of equation 2.19 into 2.17, the total number can be written as

$$N = N_0 + \frac{1}{2(\hbar\bar{\omega})^3} \int_0^\infty \frac{E^2 dE}{e^{\beta(E+E_0-\mu)} - 1} + \frac{\gamma}{(\hbar\bar{\omega})^2} \int_0^\infty \frac{E dE}{e^{\beta(E+E_0-\mu)} - 1}. \quad (2.21)$$

We now introduce the polylogarithmic function  $g_n(z)$  and the fugacity of the ensemble

$$z = \exp[\beta(\mu - E_0)], \quad (2.22)$$

which lies in the range  $0 < z < 1$ . This allows equation 2.21 to be written as

$$N = N_0 + \left(\frac{k_B T}{\hbar\bar{\omega}}\right)^3 g_3(z) + \gamma \left(\frac{k_B T}{\hbar\bar{\omega}}\right)^2 g_2(z). \quad (2.23)$$

At the transition temperature  $z=1$ , giving

$$g_n(1) = \sum_{l=1}^{\infty} \frac{1}{l^n} = \zeta(n), \quad (2.24)$$

where

$$\zeta(2) = \frac{\pi^2}{6}, \quad \zeta\left(\frac{3}{2}\right) = 2.612, \quad \text{and} \quad \zeta(3) = 1.202\dots \quad (2.25)$$

The function  $\zeta(n)$  is known as the Riemann zeta function. It is from the value of this function that the critical phase-space density for condensation to occur in a given potential is determined.

### 2.2.3 Condensation in a Harmonic Potential

At low temperature where the number of bosons in the ground state is large such that  $N_0 \gg 1$  and  $z=1$ , equation 2.23 can be rearranged to

$$N_0 = N - \left(\frac{k_B T}{\hbar\bar{\omega}}\right)^3 \zeta(3) - \gamma \left(\frac{k_B T}{\hbar\bar{\omega}}\right)^2 \zeta(2). \quad (2.26)$$

---

<sup>3</sup>If the trap is anisotropic,  $\gamma$  must be determined numerically [118, 119].

To obtain an expression for the transition temperature  $T_c$ , we say that it is the temperature where  $N_0=0$ . With  $T=T_c$ ,

$$T_c = \frac{\hbar\bar{\omega}}{k_B} \left( \frac{N}{\zeta(3)} \right)^{\frac{1}{3}} \left[ 1 - \gamma \frac{\zeta(2)}{N} \left( \frac{k_B T_c}{\hbar\bar{\omega}} \right)^2 \right]^{\frac{1}{3}}. \quad (2.27)$$

As the total number of bosons,  $N$ , approaches infinity, the terms in the square brackets approach 1, giving the transition temperature in the limit of infinite boson number

$$T_{N \rightarrow \infty} = \frac{\hbar\bar{\omega}}{k_B} \left( \frac{N}{\zeta(3)} \right)^{\frac{1}{3}}. \quad (2.28)$$

If the number of bosons is low enough such that this approximation becomes invalid,  $T_c$  decreases. This modification leads to

$$T_c \simeq T_{N \rightarrow \infty} \left[ 1 - \frac{\gamma \zeta(2)}{3 \zeta(3)^{2/3}} \frac{1}{N^{1/3}} \right], \quad (2.29)$$

To put this in perspective, for  $N = 10,000$ , the shift in  $T_c$  is about 3 % (see figure 2.12).

Experimentally, the transition temperature of a harmonically trapped Bose gas decreases further due to inter-atomic repulsions which reduces the peak density [90, 120].

## 2.2.4 Condensate Fraction

The classic signature of a BEC created in a 3D harmonic trap is a bimodal distribution comprised of a Gaussian distribution of thermal atoms and an inverted, approximately<sup>4</sup> parabolic distribution of condensed atoms. The parabolic density distribution of the BEC fraction results from the parabolic trap shape; the condensed atoms fill up the trap starting from the bottom [108]. Below  $T_c$  the BEC fraction increases as the temperature of the system  $T$  is decreased. By rearranging equation 2.26 we obtain

$$\frac{N_0}{N} = 1 - \left( \frac{k_B T}{\hbar\bar{\omega}} \right)^3 \frac{\zeta(3)}{N} - \gamma \left( \frac{k_B T}{\hbar\bar{\omega}} \right)^2 \frac{\zeta(2)}{N}, \quad (2.30)$$

then by substitution of equation 2.28 the condensate fraction can be written as

$$\frac{N_0}{N} = 1 - \left( \frac{T}{T_{N \rightarrow \infty}} \right)^3 - \gamma \frac{\zeta(2)}{\zeta(3)^{2/3}} \left( \frac{T}{T_{N \rightarrow \infty}} \right)^2 N^{-\frac{1}{3}}. \quad (2.31)$$

This is shown in figure 2.12.

---

<sup>4</sup>In the Thomas-Fermi approximation, which ignores the kinetic energy of the atoms. See eg. [108].

## 2.2. BOSE-EINSTEIN CONDENSATION

---

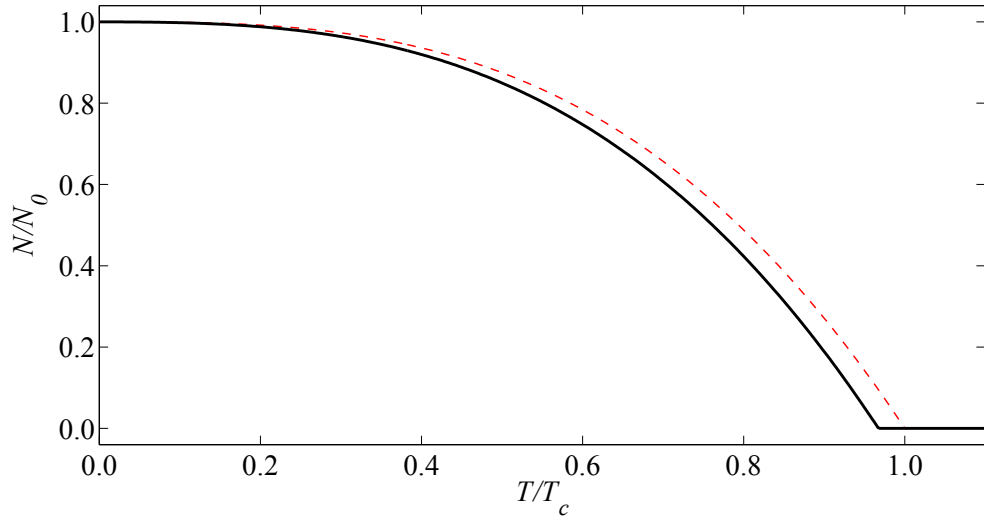


Figure 2.12: Fractional ground state population as temperature is decreased. Solid black line is for  $N=10,000$  bosons using equation 2.31 while the dashed red line is for the infinite boson limit meaning the last term of equation 2.31 is ignored.

## Chapter 3

# Atom Interferometry and Splitting the Wavefunction

Atom interferometry utilises the wave-like nature of particles to make precision measurements. The de Broglie wave nature of the particles causes interference effects, which are analogous to light interfering in an optical interferometer. The advantage of atom interferometers over optical ones is the increased sensitivity as discussed in section 1.2.2.

A ‘back-of-the-envelope’ type calculation demonstrates the difference in sensitivity: A 1 W laser of frequency 400 THz has an energy per photon of  $\sim 3 \times 10^{-19}$  J and an output of  $4 \times 10^{18}$  photons per second. A typical BEC in our experiment has an atom number of  $\sim 10^5$ , and, if we assume a cycle time of 25 s we obtain a particle flux of  $4 \times 10^3$  atoms per second. This gives a difference of  $\sim 10^{15}$  in terms of particle flux. However, we must also consider the sensitivity in the phase of the interferometer which scales as  $1/\sqrt{N}$ , where  $N$  is particle number. Thus the ratio of sensitivities is given by

$$\frac{\text{photon}}{\text{atom}} = \frac{\sqrt{4 \times 10^{18}}}{\sqrt{4 \times 10^3}} \approx 10^7. \quad (3.1)$$

Comparing this to the  $5 \times 10^{10}$  increase in particle energy (equation 1.3) gives a  $10^3$  improvement for atoms compared to photons.

We can generally describe two types of atom interferometer. The first uses the internal electronic state of the atom to make interferometric measurements, for example, atomic clocks [121, 122]. The other type uses momentum states which is the type that is described here. The momentum state version typically uses the absorption and emission of photons to transfer momentum to the atoms which allows them to trace out a path in space. This allows for the measurement of spatial magnetic fields and gravity gradients [18, 20], as well as inertial sensing [35], including Sagnac effects [16, 34].

The construction of an atom interferometer requires the coherent control of atomic states. This is achieved by the application of light fields in the form of standing waves. Just as beam splitters create coherent superpositions of photonic states, it is possible to

use light to create coherent superpositions of atomic states. Similarly, light can also be used to coherently redirect matter much like a mirror. The following sections describe these phenomena and the methods used for the coherent control of atoms.

## 3.1 Bose-Einstein Condensates

### 3.1.1 Coherence

Coherence is a key factor in obtaining high contrast interferometry data, as is well understood in classical optics [10]. Hence, we show why a BEC is a good choice for interferometry [123]. We start by considering the coherence length of a laser

$$L_{\text{laser}} = \frac{c}{\Delta f} = \frac{\lambda^2}{\Delta \lambda}, \quad (3.2)$$

where  $c$  is the speed of light in a vacuum,  $\Delta f$  and  $\Delta \lambda$  quantify the spectral width, and  $\lambda$  is the laser wavelength. By drawing the analogy between light waves and matter waves, we write the coherence length of matter as

$$L_{\text{matter}} = \frac{\lambda_{\text{dB}}^2}{\Delta \lambda_{\text{dB}}}, \quad (3.3)$$

where  $\lambda_{\text{dB}}$  is the de Broglie wavelength given by

$$\lambda_{\text{dB}} = \frac{h}{p} = \frac{h}{mv}. \quad (3.4)$$

To increase the coherence length one can therefore increase  $\lambda_{\text{dB}}$  by reducing the particle velocity, i.e. cooling in the laboratory reference frame. In addition, this also decreases the spread of velocities  $\Delta v$ . The spread in de Broglie wavelength,  $\Delta \lambda_{\text{dB}}$ , can be obtained by differentiation of equation 3.4, with respect to  $v$ , to give

$$\Delta \lambda_{\text{dB}} = \frac{h}{mv^2} \Delta v. \quad (3.5)$$

By substitution of equations 3.4 and 3.5 into 3.2, the coherence length of an ensemble of cold particles then becomes

$$L_{\text{matter}} = \frac{h}{m \Delta v}. \quad (3.6)$$

Ultra-cold atoms, particularly BECs have a narrow velocity distribution corresponding to a large coherence length. This spectral coherence and a narrower velocity distribution are analogous to having a laser of narrower linewidth.

**First order correlations:** The normalised first-order correlation function,  $g^{(1)}$ , parameterises the level of first-order coherence in a system. A  $g^{(1)} = 1$  indicates a perfectly

### 3.1. BOSE-EINSTEIN CONDENSATES

coherent system, while a value of 0 indicates a fully incoherent system, with all values between indicating partial coherence [124]. A fully coherent system would give an interference signal of 100% contrast while a fully incoherent system would give 0% contrast. From this it is obvious that a system with  $g^{(1)}=1$  would be the ideal case when performing interferometry.

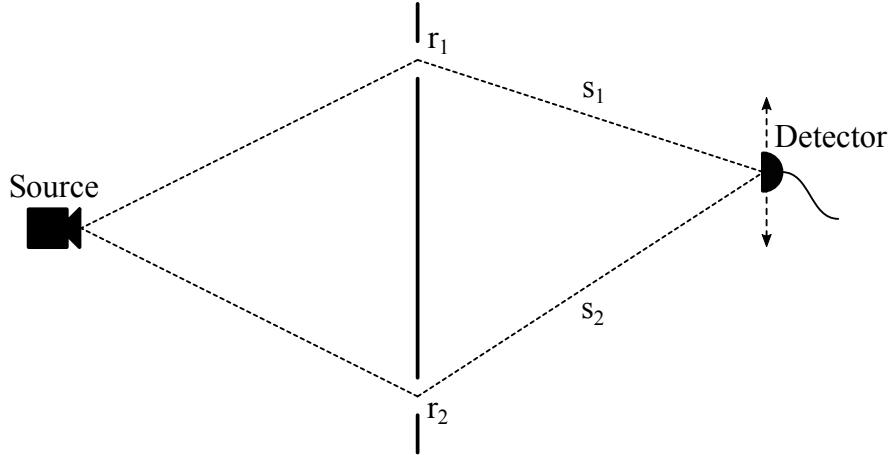


Figure 3.1: *Young's double slit experiment.*

An explanation of the physical origins of  $g^{(1)}$  is given by considering a Young's double slit type experiment. Figure 3.1 shows a source of monochromatic waves, for example light, two slits labelled  $r_1$  and  $r_2$  and a detector at some position after the slits which can be scanned in the detection plane parallel to the plane of the slits. The signal from  $r_1$  will arrive at the detector after time  $t_1$ , and similarly that from  $r_2$  after time  $t_2$ . We define  $x_i = (r_i, t_i)$  as a point in both space and time. From [124], the normalised first-order correlation function can be written as

$$g^{(1)}(x_1, x_2) = \frac{G^{(1)}(x_1, x_2)}{\sqrt{G^{(1)}(x_1, x_1)G^{(1)}(x_2, x_2)}}, \quad (3.7)$$

where  $G^{(1)}(x_i, x_i)$  is the amplitude of a signal at the detector and  $G^{(1)}(x_1, x_2)$  is a measure of the correlation, or contrast, of the signal arriving at the detector from  $x_1$  and  $x_2$ .  $G^{(1)}(x_i, x_i)$  can be measured by scanning the detector and observing the signal from one slit at a time.  $G^{(1)}(x_1, x_2)$  is measured by scanning the detector and observing the interference pattern with both slits unblocked. Thus we see that  $g^{(1)}$  is a measure of both spatial and temporal coherence.

In principle, the  $g^{(1)}$  value of a pure BEC is 1, and therefore a BEC can give high contrast when performing interferometric measurements. Figure 3.2 shows the difference in the first order correlation for ultra-cold atoms and a BEC, which has been shown experimentally by Bloch *et al.* [125]. Here they investigate the visibility of interference fringes produced by a double slit type experiment performed with atoms for

varying slit separation. The  $g^{(1)}$  value for ultra-cold atoms approaches zero for varying time and/or separation, while for a BEC it approaches the condensate fraction [126]. This is a strong reason for using a BEC in our experiments.

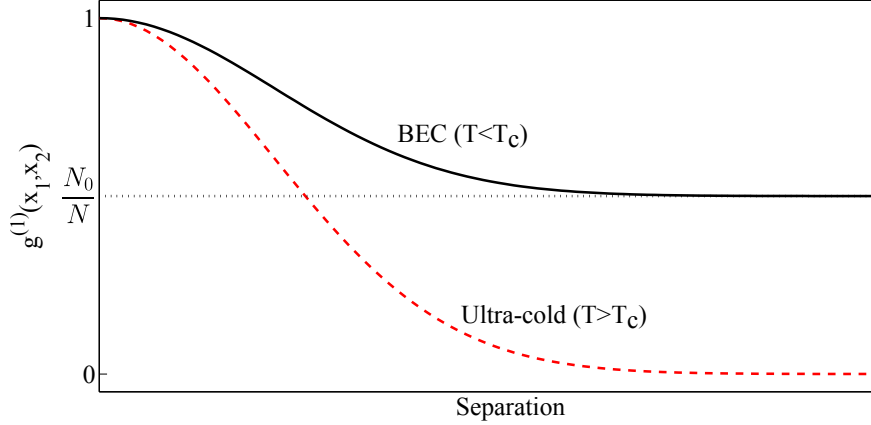


Figure 3.2: Normalised first-order correlation function of ultra-cold atoms (red dashed line) and a BEC (black solid line) as a function of initial separation of the two ensembles. In the Young’s double slit analogy this is equivalent to the slit separation. This was shown experimentally in [125].

### 3.1.2 Momentum Spread

In the experiment to be described in this thesis we use a BEC as the interfering medium, not just for its coherence properties but also for its low momentum distribution. We interfere the momentum states of the BEC, and typically we use the  $p = \pm 2\hbar k$  momentum states which, in our setup, correspond to a velocity of 10.6 mm/s. Ideally the BEC would have zero initial velocity, however, experimentally it has a velocity distribution determined by the trapping frequency of the trap in which it was created, which for our experiment is  $\sim 1.6$  mm/s along the interferometer axis<sup>1</sup>. Additional initial velocity results in a momentum of  $p = \pm 2\hbar k \pm \delta$  where  $\delta$  is the initial momentum. This extra momentum is then carried through the interferometer and therefore an initial momentum causes a perturbation in the interferometer output frequency. If the initial momentum distribution is centred around zero, then the output frequencies of all the momentum classes will be centred around the ‘zero-momentum’ frequency and any initial distribution will simply cause a reduction in signal contrast.

Since the experiment to be described in this thesis uses momentum states as the interfering medium, a low momentum distribution of atoms in the ensemble is advantageous for increased signal contrast. More specifically, the velocity of the atoms that are used in the interferometer should ideally be sub-recoil, and a BEC provides us with

<sup>1</sup>This is determined from the gradient of figure 4.17.

a narrow velocity spread atoms<sup>2</sup>, in addition to increased coherence. However, it is also possible to have ultra-cold thermal atoms with sub-recoil velocities [34], and even atoms with a velocity distribution larger than the recoil-velocity can be used to make measurements. For example, the group of Kasevich [15] measure rotation using a colimated Cs beam with a transverse velocity of 10 cm/s to which they impart a velocity of 7 mm/s, although in this case not all the atoms are used to make the measurement.

## 3.2 Resonant Scattering

When an atom absorbs (or emits) a photon, it recoils with some energy. This recoil energy,  $E_r$ , is given by

$$E_r = \hbar\omega_r = \frac{\hbar^2 k^2}{2m}, \quad (3.8)$$

where  $\omega_r$  is the recoil frequency,  $k$  is the wavevector of the photon, and  $m$  is the mass of the atom. This leads to a momentum,  $p$ , associated with the photon absorption (or emission) given by  $p = \hbar k$ .

Consider an atom with momentum  $p = +\hbar k$  in the reference frame of the laboratory. Two counter-propagating laser beams of frequency  $\omega$  detuned from an atomic transition,  $\omega_0$ , by  $\Delta$  (figure 3.3) interfere to produce an optical lattice. It is possible to drive a two-photon Raman transition, shown in figure 3.4, such that the atom receives two ‘recoils’ of momentum. These two momentum recoils come from the absorption of a photon from one beam and the stimulated emission of a photon into the other beam. The scattering process has the effect of changing the momentum of the atom from  $p = +\hbar k$  to  $p = -\hbar k$ .

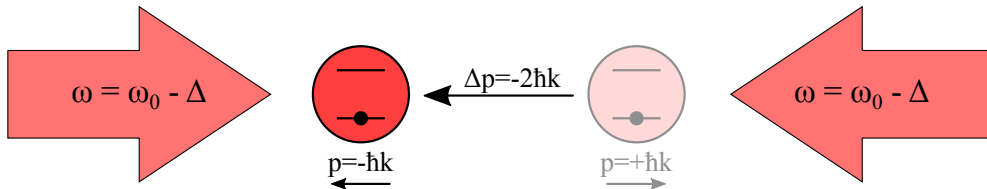


Figure 3.3: An atom with initial momentum  $p = +\hbar k$  undergoes a two-photon Raman transition such that it then has momentum  $p = -\hbar k$ .

We describe these Raman transitions as ‘resonant’ because the total energy of the atom, shown on the dispersion curve of figure 3.4, does not change, i.e. the energy levels are degenerate. If one laser beam is detuned relative to the other, the previously stationary optical lattice will become a moving optical lattice. It is then possible to transition between momentum states that are not degenerate in the lab reference frame but degenerate in the reference frame of the optical lattice.

<sup>2</sup>The velocity distribution of a BEC is dependant on the trapping frequency of the trap in which it was created, and for our experiment is  $\sim 1.6$  mm/s along the interferometer axis

### 3.3. KAPITZA-DIRAC SCATTERING

These resonant scattering processes using laser beams of equal frequency form the basis of our reflection pulses, which will be discussed further in section 3.4. In order to impart a momentum *change* onto the atoms with laser beams of the same frequency, Raman transitions can still be used, but since the momentum states are no longer degenerate there is a detuning that results from the difference in energy making the transition off-resonant. This is discussed in the following section.

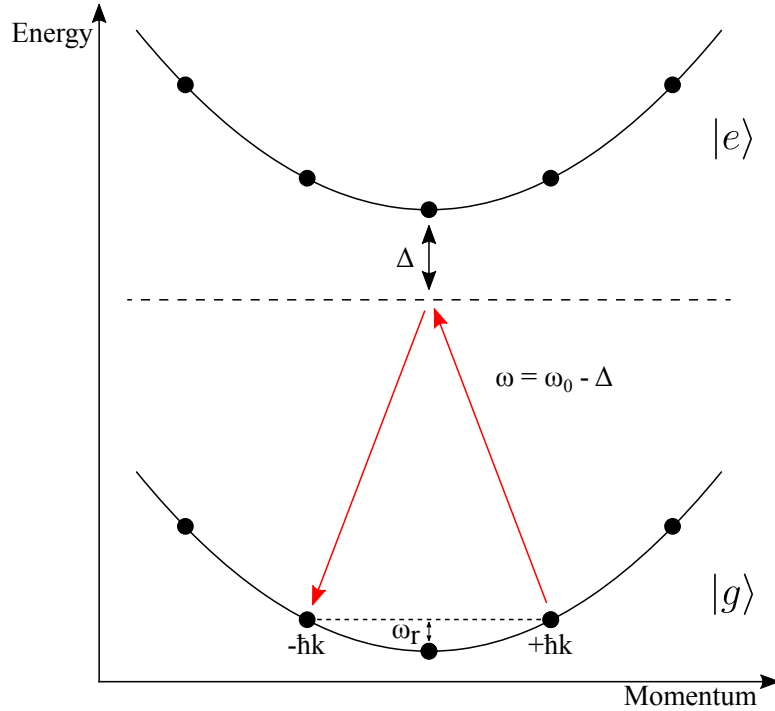


Figure 3.4: *Dispersion curve of energy and momentum. An atom with initial momentum  $p = +\hbar k$  can undergo a two-photon Raman transition, transferring it to the  $p = -\hbar k$  state. The reverse is also possible and this scheme can be extended to higher orders by driving  $2n$ -photon Raman transitions, for example  $p = +2\hbar k \rightarrow p = -2\hbar k$  using a four-photon transition.*

### 3.3 Kapitza-Dirac Scattering

In the creation of an atomic interferometer we first need to engineer beam splitters. This involves taking a stationary BEC and imparting momentum on to it such that the wavefunction splits in to positive and negative momentum states. Here we introduce the idea of Kapitza-Dirac scattering, which is a method of splitting the BEC by applying pulses of light from two laser beams of the same frequency. They create a stationary optical lattice which can excite the  $\pm 2n\hbar k$  momentum states of the BEC.

The complete transfer of the atomic population cannot be achieved with a single off-resonant pulse because the kinetic energy introduced by the pulse leads to an ef-

### 3.3. KAPITZA-DIRAC SCATTERING

fective detuning. To explain this we introduce the ‘Bloch sphere’ picture in figure 3.5, where the south pole represents the  $|g, 0\hbar k\rangle$  momentum state and the north pole represents the  $|g, \pm 2\hbar k\rangle$  momentum state. When the state vector lies in a position somewhere inbetween the two pole, the system is in a superposition state. A state vector starting at the south pole will never reach the north pole because the detuning of the off-resonant pulse applies an additional torque which causes the path of the state vector to deviate from its ‘on-resonance’ trajectory. Therefore, a single Bragg pulse with beams of equal detuning will not allow 100% transfer from  $|g, 0\hbar k\rangle$  to  $|g, \pm 2\hbar k\rangle$ , or any other transfer where the total atomic energy changes. In Kapitza-Dirac splitting the energy of the wavefunction changes which makes it an off-resonant process.

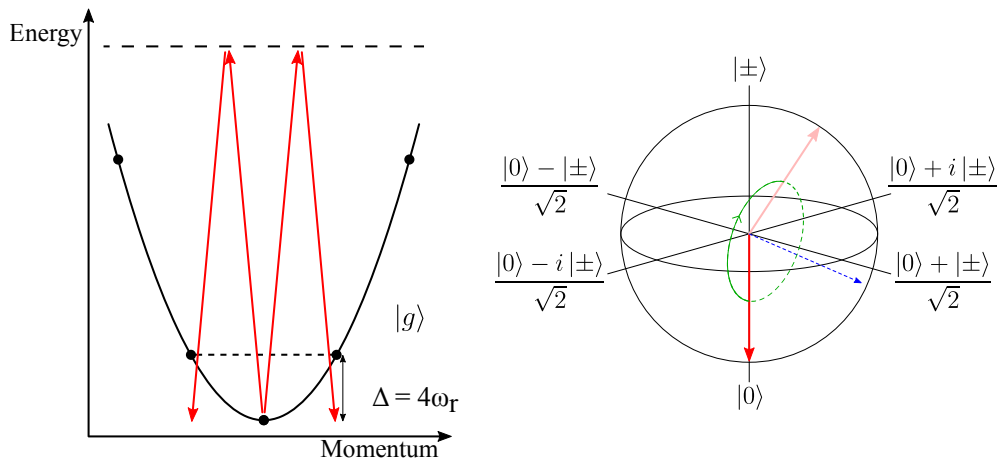


Figure 3.5: A two-photon Raman transition imparts a momentum of  $\pm 2n\hbar k$  on to an atom. This leads to an effective detuning  $\Delta$  (left). Therefore a single pulse will not give 100% population transfer from  $0\hbar k$  to  $\pm 2\hbar k$  as the state vector never reaches the top of the Bloch sphere (right).

In the following sections we first describe the excitation of momentum states using single pulses of light. Then we look at a double pulse technique for controlled excitation of only the  $\pm 2\hbar k$  momentum states.

#### 3.3.1 Single Pulses

Kapitza and Dirac, in 1933, predicted that a beam of electrons would undergo Compton scattering when incident on an appropriate standing wave of light [23]. Providing the light field is on for a short enough period of time,  $\tau \ll 1/\omega_r$ , the atoms can be considered to be at rest for the duration of the pulse. This pulse can therefore be said to operate within the Raman-Nath regime, which is analogous to the thin lens approximation in optics [127].

In our experiment, the reality is that we operate somewhere just outside the Raman-Nath regime, and therefore the kinetics of the atom are included here for a more ac-

### 3.3. KAPITZA-DIRAC SCATTERING

---

curate model. The mathematical description below follows the formalism of Gadway *et al.* [128]. The Hamiltonian of a BEC in a standing wave of light can be given as

$$\hat{H} = -\frac{\hbar^2}{2m} \frac{d^2}{dz^2} + V_0 \cos^2(kz), \quad (3.9)$$

where  $V_0$  is the amplitude of the light field, often referred to as the lattice depth,  $k$  is the wavevector of the light, and  $z$  is the axis of propagation. The first and second terms describe the kinetic and potential components, respectively. The atomic wavefunction can be written as the sum of all modes:

$$\Psi(t) = \sum_n C_n(t) e^{i2nkz}, \quad (3.10)$$

where  $C_n$  is the complex amplitude coefficient of the  $n$ -th momentum state given by  $p = \pm 2n\hbar k$ . By substitution of equation 3.10 into the time-dependent Schrödinger equation we obtain a set of coupled differential equations

$$i \frac{dC_n}{dt} = \frac{\alpha n^2}{\tau} C_n + \frac{\beta}{4\tau} (C_{n-1} + 2C_n + C_{n+1}), \quad (3.11)$$

where  $\alpha = (E_r^{(2)}/\hbar)\tau$ ,  $\beta = (V_0/\hbar)\tau$ ,  $E_r^{(2)}$  is the 2-photon recoil energy, and  $\tau$  is pulse duration. Here  $\alpha$  and  $\beta$  are dimensionless parameters that describe pulse duration and pulse area respectively. From the second term in equation 3.11 we see that any given momentum state,  $n$ , is coupled to its nearest neighbours, namely the  $n + 1$  and  $n - 1$  momentum states.

We temporarily ignore the kinetics and operate entirely within the Raman-Nath regime. This requires the pulse duration,  $\tau$ , to be much shorter than the period of the harmonic oscillation given by  $\omega_{\text{ho}} = (V_0 E_r^{(2)})^{1/2}/\hbar$ , or  $\alpha\beta \ll 1$ . This means the  $\alpha n^2$  term in equation 3.11 is ignored and the standing wave can be treated as a “thin phase grating” [129], or to link it back to optics, it is the equivalent to the thin lens approximation. Assuming a stationary initial population such that  $|C_0|^2 = 1$ , the solution then becomes

$$C_n(t) = (-i)^n e^{-i\beta t/2\tau} J_n(\beta t/2\tau), \quad (3.12)$$

where  $J_n$  are Bessel functions of the first kind. The population of the  $n$ -th momentum state then becomes

$$P_n = |C_n|^2 = J_n^2\left(\frac{\beta}{2}\right). \quad (3.13)$$

Figure 3.6 shows the population evolution for a varying  $\beta$ , which physically equates to varying the pulse area.

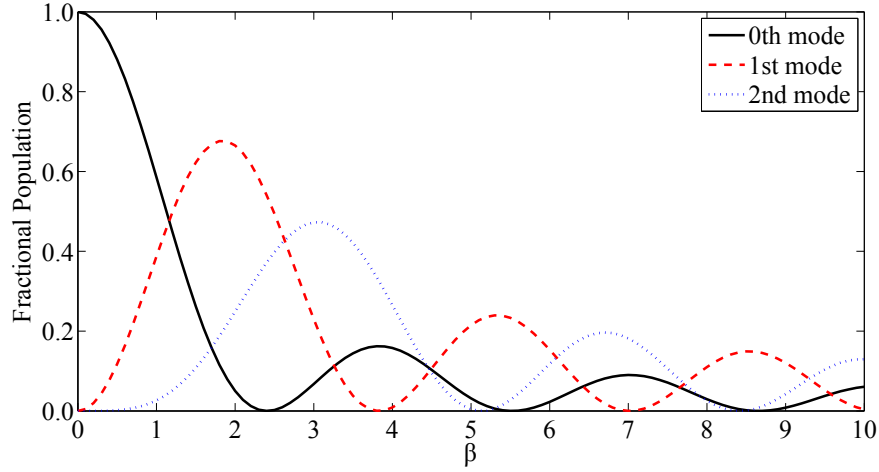


Figure 3.6: Population evolution for a varying pulse area  $\beta$ . Note that as  $\beta$  increases, the total populations plotted do not sum to unity. This is due to the negation of higher order terms. We assume a initial popouion of 100% in the 0th mode and plot the modes such that they are the sum of the positive and negative momentum sates.

As the duration of the pulse,  $\tau$ , is increased the negation of the kinetics becomes invalid and we must include them for the model to be accurate. Also, the Fourier width narrows and the excitation of higher orders is suppressed. This leads to a more general form of equation 3.13:

$$P_n = |C_n|^2 = J_n^2 \left( \frac{\beta}{2} \text{sinc} \frac{\alpha}{2} \right). \quad (3.14)$$

The above is valid in the weak-pulse regime where only the lowest momentum states are populated ( $\pm 2\hbar k$ ) and the optical lattice depth  $V_0 \lesssim 4E_r$ . For pulses of greater amplitude, this expression does not hold and numerical integration of equation 3.11 is required.

### 3.3.2 Double Pulses

The single pulse method of splitting a BEC can populate many momentum states. To perform atom interferometry it would be advantageous to target only specific momentum states, for example,  $|\pm 2\hbar k\rangle$ . Double pulse techniques allow this to be achieved (or at least very nearly) [18, 130].

Here we base our mathematical description on the work of Wu *et al.* [130]. By using equation 3.9, the Schrödinger equation for an atom in a standing wave of light can be written as

$$i\dot{\psi}(z, t) = \left( -\frac{\hbar}{2m} \frac{d^2}{dz^2} + V_0(t) \cos^2(kz) \right) \psi(z, t). \quad (3.15)$$

### 3.3. KAPITZA-DIRAC SCATTERING

---

The wavefunction of the atomic ensemble can be written as the sum of all the individual quantised momentum state components

$$\psi(z, t) = \int d\mathbf{k} \sum_n C_{2n}(\mathbf{k}, t) e^{i(2n\mathbf{k} + k_0)z}, \quad (3.16)$$

where  $k_0$  describes the initial momentum of the atom. Note that equation 3.16 is equivalent to equation 3.10 but here we allow for non-zero initial momentum and multiple wavevectors. We assume that each momentum state is only coupled to the adjacent momentum states and by substitution into equation 3.15 we obtain coupled Raman-Nath equations<sup>3</sup>:

$$i\dot{C}_{2n} = \frac{\hbar}{2m}(2nk + k_0)^2 C_{2n}(k_0, t) + \frac{V_0(t)}{2}(C_{2n-2}(k_0, t) + C_{2n+2}(k_0, t)). \quad (3.17)$$

This shows that the strength of the coupling between adjacent states is determined by the amplitude of the standing wave. Equation 3.17 comprises an infinite set of coupled equations. For simplicity we truncate them to include only the zeroth and first order modes such that  $n = -1, 0, 1$ .

If we shift into the reference frame of the atoms via a Lorentz transformation to get rid of the  $k_0$  terms, equation 3.17 becomes

$$i\dot{C}_0(k_0, t) = \frac{V_0(t)}{\sqrt{2}} C_+, \quad (3.18a)$$

$$i\dot{C}_+(k_0, t) = 4\omega_r C_+ + \frac{V_0(t)}{\sqrt{2}} C_0 + 4\omega_r \frac{k_0}{k} C_-, \quad (3.18b)$$

$$i\dot{C}_-(k_0, t) = 4\omega_r C_- + 4\omega_r \frac{k_0}{k} C_+, \quad (3.18c)$$

where  $C_+ = (1/\sqrt{2})(C_2 + C_{-2})$  and  $C_- = (1/\sqrt{2})(C_2 - C_{-2})$ . Since  $k_0 = 0$ , we can also neglect the  $k_0/k$  terms. Furthermore, an initial population of  $|C_0|^2 = 1$  means there are no atoms in the  $C_-$  state. From above we see there is no coupling to this state from the  $C_0$  state and therefore  $C_-$  remains a dark state. By setting the above equations in a different rotating frame, the resultant two-state system is described by

$$i\dot{C}_0 = -2\omega_r C_0 + \frac{V_0(t)}{\sqrt{2}} C_+, \quad (3.19a)$$

$$i\dot{C}_+ = \frac{V_0(t)}{\sqrt{2}} C_0 + 2\omega_r C_+. \quad (3.19b)$$

This two level system is conveniently visualised using state vectors on the Bloch sphere (figure 3.7), where the ‘south pole’ is the  $|C_0|^2 = 0$   $\hbar k$  momentum state and the

---

<sup>3</sup>Note that equation 3.17 is equivalent to equation 3.11 but in the reference frame of the  $C_0$  state.

### 3.3. KAPITZA-DIRAC SCATTERING

‘north pole’ is the  $|C_+|^2 = \pm 2\hbar k$  state. The goal is to find a sequence of pulses that transfers the population from the  $0\hbar k$  state to the  $\pm 2\hbar k$  state. In [130], a double pulse technique is proposed where each pulse should have an amplitude of  $\Omega = 2\sqrt{2}\omega_r$ , a duration of  $\tau_1 = (2n_1 + 1)\pi/4\sqrt{2}\omega_r$ , and a separation of  $\tau_2 = (2n_2 + 1)\pi/4\omega_r$ , where  $n_1$  and  $n_2$  are integers. These integers can be interpreted as the number of rotations around the Rabi vector during each pulse;  $n = 1$  is a  $1/2$  rotation while  $n = 2$  is  $3/2$  rotation etc. In figure 3.7,  $n_1$  and  $n_2$  are set to one.

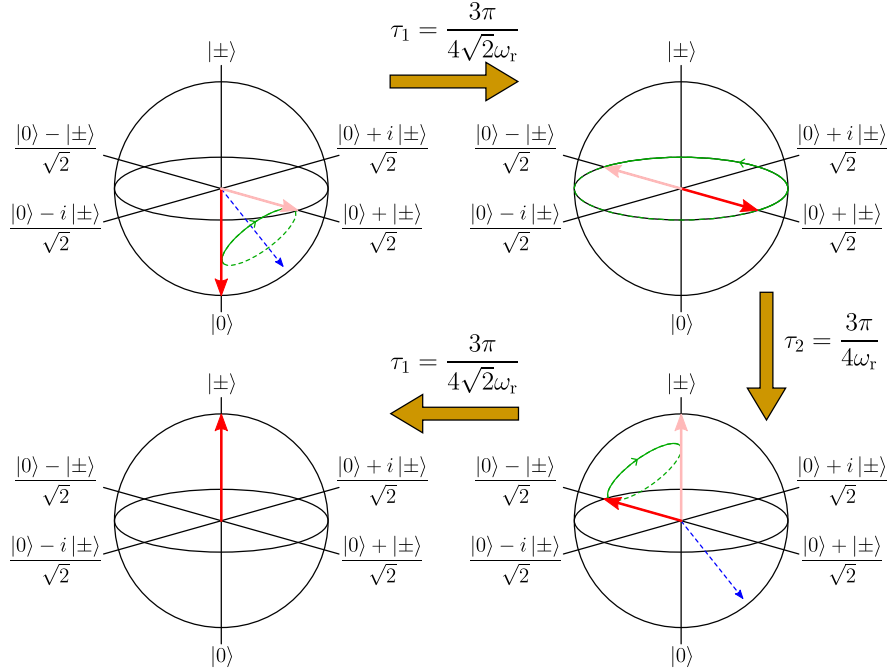


Figure 3.7: *The double pulse splitting scheme as represented on the Bloch sphere. The red arrow represents the state vector while the blue dashed arrow is the Rabi vector that is applied during the pulses.*

In figure 3.8 we plot equations 3.18 for varying pulse duration  $\tau_1$  and pulse separation  $\tau_2$  with pulse amplitudes of  $2\sqrt{2}\omega_r$ . This simulation suggests that 100 % population transfer from  $|0\hbar k\rangle$  to  $|\pm 2\hbar k\rangle$  is possible using a double pulse.

In the above model the higher order momentum states have been ignored which is an approximation. Moreover, this does not allow for the optimisation of higher order splitting pulses. We also assumed a stationary atom cloud and therefore this description would not allow for the modelling of a reflection pulse. While Kapitza-Dirac scattering is an off-resonant process, a reflection pulse is a resonant process.

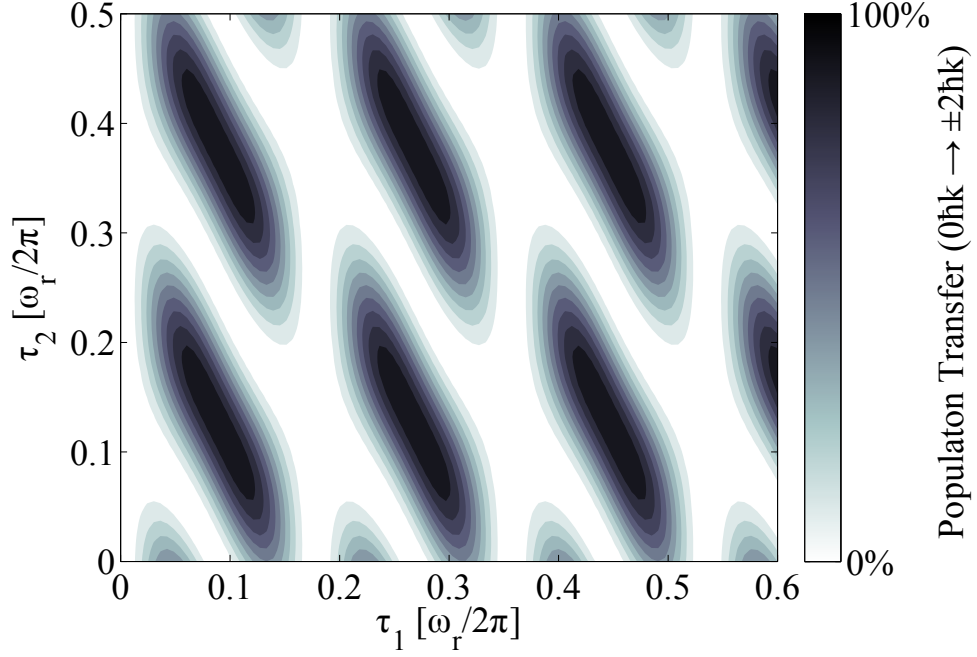


Figure 3.8: Surface plot of double pulse splitting model (equation 3.18) for varying pulse duration  $\tau_1$  and pulse separation  $\tau_2$ . Pulse amplitudes are  $2\sqrt{2}\omega_r$ .

### 3.4 Composite Pulses for High Efficiency Splitting

Ideally we would have a mathematical description of both the splitting and reflection pulses. Section 3.3.1 describes single pulses while section 3.3.2 describes double pulses for splitting into only the  $\pm 2\hbar k$  momentum states with higher orders ignored. In both sections we assumed a stationary cloud of atoms, and therefore using this description we cannot model a reflection pulse. Below we include initial momentum in the mathematical description and show how the model can be used to predict high efficiency splitting and reflection pulses.

We start by rewriting equation 3.11 with the  $\alpha$  and  $\beta$  terms substituted:

$$i\frac{dC_n}{dt} = \frac{E_r^{(2)}n^2}{\hbar}C_n + \frac{V_0}{4\hbar}(C_{n-1} + 2C_n + C_{n+1}), \quad (3.20)$$

where  $E_r^{(2)} = 4\hbar^2k^2/2m$  is the two-photon recoil energy and  $m$  is the mass of the atom. We include initial momenta by altering the value of  $k$  such that  $k = k + k_0$  where  $k_0$  is the initial momentum. This then gives

$$i\frac{dC_n}{dt} = \frac{4\hbar(k + k_0)^2n^2}{2m}C_n + \frac{V_0}{4\hbar}(C_{n-1} + 2C_n + C_{n+1}). \quad (3.21)$$

Equation 3.21 is then used to generate coupled differential equations, which are numerically solved in MATLAB. We truncate these equations at  $|\pm 12\hbar k|$ ; we only

### 3.4. COMPOSITE PULSES FOR HIGH EFFICIENCY SPLITTING

observe a population of  $10^{-18}$  in these modes from our simulations. Light shift potentials corresponding to arbitrary pulse shapes can be simulated, such that  $V_0 = V_0(t)$ , and the final population of the momentum states can be calculated<sup>4</sup> [9]. This allows us to predict the resultant state populations for arbitrary pulse shapes. By using a genetic algorithm in MATLAB we can also calculate a composite pulse sequence to generate any arbitrary final state.

We use a combination of square pulses for our composite splitting pulse. This is convenient to model because of the low resolution required compared to a smooth curve, and square pulses are also easier to implement experimentally. Smooth curves are possible although a higher resolution is required for an accurate simulation. We describe our pulse shapes with an amplitude in terms of light shift potential in units of the recoil energy  $E_r$ .

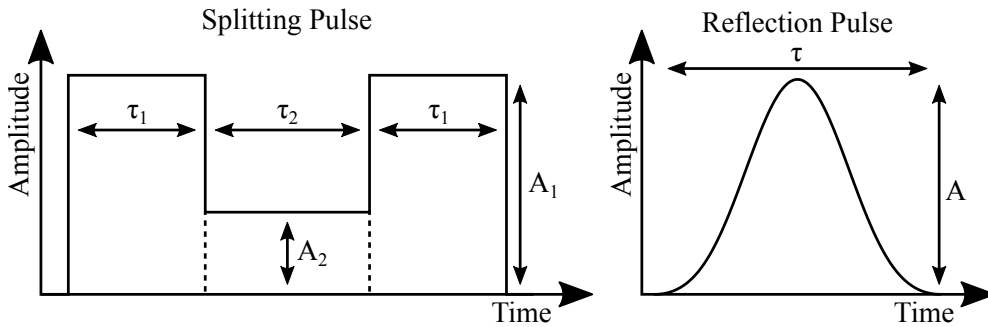


Figure 3.9: Composite light pulse for high efficiency splitting (left) and reflection pulse with a Blackman shape (right).

If the population of only the  $\pm 2\hbar k$  states is required, we find that a simple double pulse technique is not optimum. We calculate (and demonstrate in figures 5.5 and 5.6) that a small light potential between the two pulses provides a higher fidelity split. This is consistent with the data presented in [123]. The reason for this is to account for the excitation of higher order modes. By applying this extra amplitude, the  $|\pm 4\hbar k\rangle$  ‘re-phase’ such that when the second large amplitude is applied the untargeted ( $n \neq \pm 1$ ) modes tend back to zero.

Our optimised parameters are two pulses of  $\tau_1 = 26.6 \mu s$  duration and  $A_1 = 6.07 E_r$  in amplitude with a spacing of  $\tau_2 = 45.6 \mu s$  during which an amplitude of  $A_2 = 0.52 E_r$  is applied. From our model we predict a split efficiency of 100.00%, and in section 5.1.2 we experimentally observe an efficiency of  $99.97 \pm 0.03 \%$  (figure 5.5).

The population of higher order states using this technique is also possible. Indeed, we have demonstrated its efficacy in populating only the  $\pm 4\hbar k$  states in figures 5.7 and 5.8. We find optimised parameters of  $\tau_1 = 53.3 \mu s$ ,  $A_1 = 23.7 E_r$ ,  $\tau_2 = 39.0 \mu s$ , and  $A_2 = 3.59 E_r$ . Pulses designed to populate higher order states are much more

<sup>4</sup>The pulse shapes must be discretised with a finite resolution due to the MATLAB algorithm.

susceptible to intensity noise. This is due to increased rate at which the phase evolves and their increased sensitivity to amplitude noise. From our model we predict a split efficiency of 99.30 %, and experimentally we observe an efficiency of  $88 \pm 4$  %.

Our numerical model also aids us in the optimisation of the reflection pulses. In principle this is a resonant transfer of momentum and hence a single Blackman shaped pulse is used as it has a better defined frequency than a square pulse. Our pulse parameters are  $\tau = 164 \mu\text{s}$  and  $A = 12.2 E_r$  for an optimal  $\pm 2\hbar k$  reflection<sup>5</sup>. Our model predicts a reflection efficiency of 99.88 %. Experimentally this is difficult to observe due to the low velocity in which the momentum state separate, as discussed in section 5.1.4, but we place a lower bound of 86 % by analysis of the contrast of a full interferometer sequence (figure 5.12).

**A note on momentum state coupling:** Previously it was pointed out that any single momentum state is coupled only to its nearest neighbour, and this holds true for equation 3.21. However, for the reflection pulses and higher order splitting we can target and excite momentum states that aren't adjacent to the input state, so how is this possible? One can think of the atomic wavefunction sweeping through the momentum states sequentially until the final state is reached, for example, a reflection pulse applied to the  $+2\hbar k$  momentum state causes the wavefunction to sweep through the  $0\hbar k$  state before reaching the  $-2\hbar k$  state.

#### 3.4.1 Blackman Pulses

A Blackman shaped pulse was selected for our mirror pulse for a few reasons, not least of which it is relatively easy to program. A Blackman pulse has the form [131]

$$y(t) = \frac{7938}{18608} - \frac{9240}{18608} \cos\left(\frac{2\pi t}{\tau - 1}\right) + \frac{1430}{18608} \cos\left(\frac{4\pi t}{\tau - 1}\right), \quad (3.22)$$

where  $\tau$  is pulse width. A second reason is that the amplitude goes to zero at the wings. This suppresses higher frequencies that would be introduced by a discontinuous step function. Lastly, the higher frequency components have a much lower amplitude in Fourier space compared to a square pulse (figure 3.10). This means that it targets only resonant atomic transitions which is exactly what is wanted for a mirror pulse. Kasevich and Chu [132] report an improvement of “at least 3 orders of magnitude” when using a Blackman pulse compared to a square pulse to drive Raman transitions in sodium.

---

<sup>5</sup>It is worth noting that what is often referred to as a ‘mirror’ pulse is actually the addition or subtraction of  $\pm 2n\hbar k$

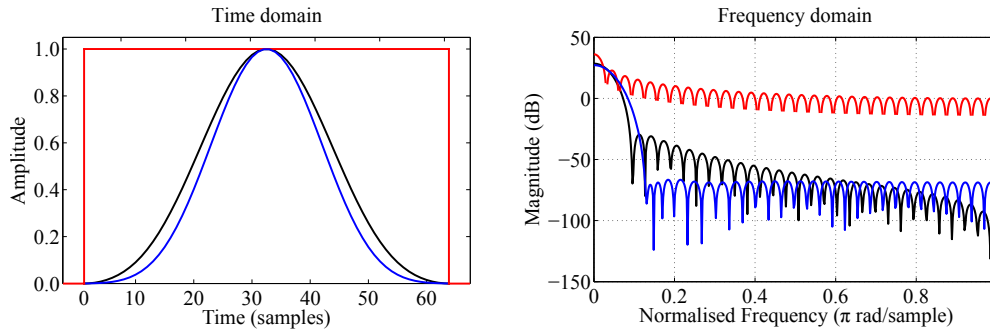


Figure 3.10: Using the window visualisation tool in MATLAB we plot the spectral density of a Blackman (black), rectangular (red), and Blackman-Nuttall (blue) window function.

However, other pulse shapes are expected to work, for example, a Blackman-Nuttall window (blue line in figure 3.10). These shapes, in theory, can further suppress higher frequency components. It is also possible to simply use a single square pulse of longer duration as demonstrated in [18].

### 3.4.2 Competing Methods

A recent paper by Berg *et al.* [133] discusses a “Composite-Light-Pulse Technique” to construct a Mach-Zehnder type interferometer. These pulses operate in the Bragg regime and require the use of blow-away pulses to remove atoms in unfavourable electronic states (these pulses are used in other atom interferometers as well [134]). Whilst Berg *et al.* demonstrate excellent levels of sensitivity, these blow-away pulse mean that not all atoms contribute to the interferometer signal.

An interferometer comprised of the pulse types described in this thesis does not require blow-away pulses as the atoms remain in the same internal state throughout. Therefore all the atoms, in principle, contribute to the output signal and the system can be regarded as more efficient, although experimentally we observe less than 100% splitting and reflection efficiency (99.77% and 82% respectively) which mean that small fraction of the atoms are still lost.

By keeping the atoms in the same internal state our type of interferometer has an inherent insensitivity to non-inertial perturbations such as phase from spatially flat magnetic fields for the entire duration of the interferometer sequence, and not just during the free evolution time as reported in [133]. Furthermore, our method requires fewer pulses and a single laser detuning making the system easier to implement, and therefore is an attractive method for the miniaturisation of atomic interferometers.

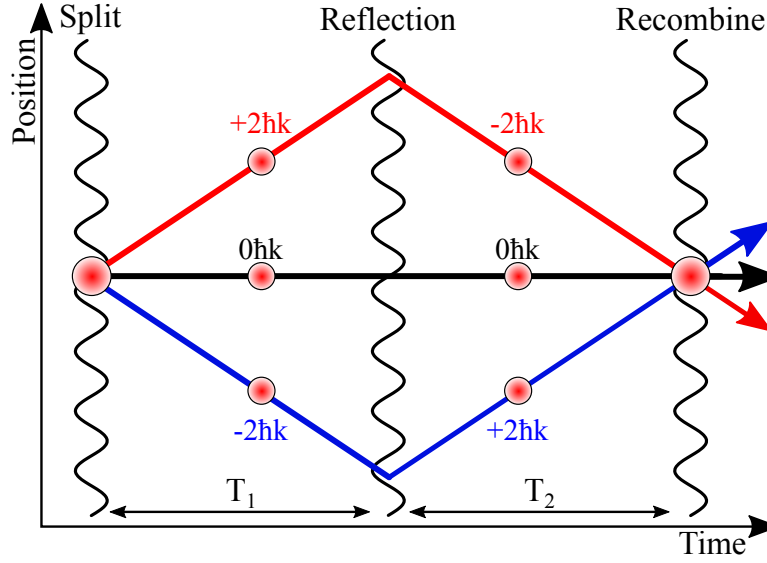


Figure 3.11: Three arm interferometer scheme.

### 3.5 Atom Interferometer Model

For the majority of our experiments the wavefunction is split into three separate wavepackets. This allows for the construction of a 3-arm interferometer using  $|p = 0, \pm 2\hbar k\rangle$ , as shown in figure 5.15, which can be likened to two Mach-Zehnder interferometers with a common arm. A 3-arm configuration allows for the measurement of  $\omega_r$  due to the central arm acting as a common phase reference.

When the interferometer is closed it is the phase *difference* between the arms that manifests itself as variation in mode population. If only two symmetrical arms are used (eg.  $\pm 2\hbar k$ ) the phase velocity of each is the same and therefore, providing there are no external perturbations, the populations will fold back into the  $0\hbar k$  state when the interferometer is closed. Using 3 arms means the phase *difference* between the  $0\hbar k$  and  $\pm 2\hbar k$  states is observed at the output and the rate of change of phase is  $\omega_r$ .

#### 3.5.1 3-arm Interferometer Model

The mathematical description here of the 3-arm interferometer (figure 3.11) tracks the phases of the arms and follows a similar formalism to [91]. After the initial splitting pulse, the phases of the three modes are

$$\Phi_0 = 0, \quad (3.23a)$$

$$\Phi_+ = \phi_1, \quad (3.23b)$$

$$\Phi_- = \phi_1, \quad (3.23c)$$

where  $\Phi_0$ ,  $\Phi_+$ , and  $\Phi_-$  refer to the phases of the middle, upper, and lower arms of the interferometer in figure 3.11 respectively, and  $\phi_1$  is a phase introduced by the op-

### 3.5. ATOM INTERFEROMETER MODEL

---

tical lattice during splitting pulse. After time  $T_1$  (time between splitting and reflection pulses) the phases are

$$\Phi_0 = 0 , \quad (3.24a)$$

$$\Phi_+ = \phi_1 - 4\omega_r T_1 , \quad (3.24b)$$

$$\Phi_- = \phi_1 - 4\omega_r T_1 , \quad (3.24c)$$

where the  $-4\omega_r T_1$  terms are due to the kinetic energy. The reflection pulse adds the spatial phase  $2\phi_2$  from the optical lattice, and after  $T_2$  we have

$$\Phi_0 = 0 , \quad (3.25a)$$

$$\Phi_+ = \phi_1 + 2\phi_2 - 4\omega_r T_1 - 4\omega_r T_2 , \quad (3.25b)$$

$$\Phi_- = \phi_1 + 2\phi_2 - 4\omega_r T_1 - 4\omega_r T_2 . \quad (3.25c)$$

Finally, after a closing pulse there are nine possible paths. At the  $|0\hbar k\rangle$  port we have

$$\Phi_0 = 0 , \quad (3.26a)$$

$$\Phi_+ = \phi_1 + 2\phi_2 + \phi_3 - 4\omega_r T_1 - 4\omega_r T_2 , \quad (3.26b)$$

$$\Phi_- = \phi_1 + 2\phi_2 + \phi_3 - 4\omega_r T_1 - 4\omega_r T_2 . \quad (3.26c)$$

At the  $|+2\hbar k\rangle$  port we have

$$\Phi_0 = \phi_3 , \quad (3.27a)$$

$$\Phi_+ = \phi_1 + 2\phi_2 + 2\phi_3 - 4\omega_r T_1 - 4\omega_r T_2 , \quad (3.27b)$$

$$\Phi_- = \phi_1 + 2\phi_2 - 4\omega_r T_1 - 4\omega_r T_2 , \quad (3.27c)$$

and at the  $|-2\hbar k\rangle$  port we have

$$\Phi_0 = \phi_3 , \quad (3.28a)$$

$$\Phi_+ = \phi_1 + 2\phi_2 - 4\omega_r T_1 - 4\omega_r T_2 . \quad (3.28b)$$

$$\Phi_- = \phi_1 + 2\phi_2 + 2\phi_3 - 4\omega_r T_1 - 4\omega_r T_2 , \quad (3.28c)$$

A full analysis of the resulting wavefunction would require the nine terms multiplied by their complex conjugate, which would give 81 terms. Therefore for simplicity we consider only at the  $|0\hbar k\rangle$  output port. From the thesis of Gupta [91], the output population is given by

$$P_{0\hbar k} \propto \cos \left( \Phi_0 - \frac{\Phi_+ + \Phi_-}{2} \right) , \quad (3.29)$$

then by substitution of equations 3.26 we obtain

$$P_{0\hbar k} \propto \cos (\phi_1 + 2\phi_2 + \phi_3 - 4\omega_r T_1 - 4\omega_r T_2) . \quad (3.30)$$

Therefore if we probe the momentum state populations as a function of  $T_2$ , we observe a frequency proportional to  $4\omega_r$ . This is demonstrated experimentally in chapter 6 and the data is shown in figure 5.16.

The output populations of the interferometer depend on the phases accumulated during the interferometer sequence. Above we assume a perfectly symmetric system such that the phase contributions from  $\Phi_+$  and  $\Phi_-$  at the  $|0\hbar k\rangle$  output port are equal. If a differential phase shift is introduced into one of the arms, there would be an additional phase terms in  $\Phi_+$  and  $\Phi_-$  that would break the symmetry. For example, if a phase difference,  $\phi_\delta$ , was introduced into  $\Phi_+$  such that at the  $|0\hbar k\rangle$  port

$$\Phi_+ = \phi_1 + 2\phi_2 + \phi_3 - 4\omega_r T_1 - 4\omega_r T_2 + \phi_\delta , \quad (3.31)$$

then

$$P_{0\hbar k} \propto \cos \left( -4\omega_r T_1 - 4\omega_r T_2 + \frac{\phi_\delta}{2} \right) . \quad (3.32)$$

This additional phase term manifests in a phase shift in the interferometer output, which makes this type of interferometer sensitive to gravitational fields, and rotations. We demonstrate in section 5.4 its sensitivity to magnetic field gradients.

In the case of contrast interferometry, where a laser beam is Bragg reflected off the matter-wave grating (see chapter 6), the intensity,  $I$ , of the reflected light becomes the square of the population modulation giving

$$I = \cos^2 (-4\omega_r T_1 - 4\omega_r T_2) . \quad (3.33)$$

When we perform contrast interferometry, we are effectively varying  $T_2$ , and therefore the frequency of the intensity modulation is  $8\omega_r$ , as will be demonstrated in chapter 7.

#### 3.5.2 2-arm Interferometer Model

By a similar analysis of a 2-arm interferometer (figure 3.12), the phases at the  $|0\hbar k\rangle$  output port are

$$\Phi_+ = \phi_1 + 2\phi_2 + \phi_3 - 4\omega_r T_1 - 4\omega_r T_2 , \quad (3.34a)$$

$$\Phi_- = \phi_1 + 2\phi_2 + \phi_3 - 4\omega_r T_1 - 4\omega_r T_2 . \quad (3.34b)$$

Since the output populations depends on the interference between the two modes, it is the relative phase difference that we must consider:

$$\Phi_+ - \Phi_- = 0 , \quad (3.35)$$

which shows that the recoil frequency does not manifest itself in the output as it does in the 3-arm interferometer scheme. However, as before, a differential phase shift,  $\phi_\delta$ , introduced into one of the arms would cause a phase shift in the output port population as in this case  $\Phi_+ - \Phi_- = \phi_\delta$ .

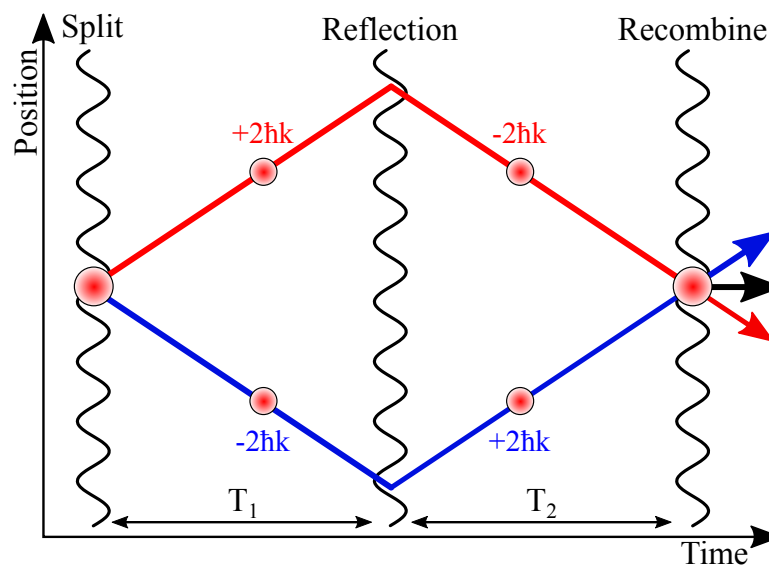


Figure 3.12: Two arm interferometer scheme.

# Chapter 4

## Experimental Setup

The current apparatus was designed as a second generation inductively coupled ring trap experiment. Given the success of the first generation, involving a horizontally orientated ring trap [7, 8], we constructed a smaller, vertically-orientated ring trap. This can act as a waveguide for an atom interferometer. By positioning the ring trap vertically, atoms originating at the bottom of the ring and travelling up the potential will return to the bottom as a result of gravity. This allows for the ‘reflection’ of the atoms without the need for laser pulses that can add experimental noise to the system.

The following sections will outline experimental apparatus used to create a BEC of  $^{87}\text{Rb}$  in the  $|F = 2, m_F = 2\rangle$  state, the interferometry laser and detection systems, and the experimental sequence.

### 4.1 System

Part of the system was already constructed upon my arrival to the group and as such I will give a brief overview of this apparatus. More details, including the construction of the vacuum system can be found in chapter 6 of the thesis of Aline Dinkelaker [8].

#### 4.1.1 Vacuum System

We use double-chamber vacuum system comprising of two glass cells at different pressures connected via a differential pumping tube (figure 4.1). Each cell has a corresponding valve allowing them to be pumped down to different pressures. The first cell, held at a higher pressure of  $\sim 10^{-7}$  Torr, contains our 2D MOT, while the second chamber is held at a lower pressure of  $\approx 2 \times 10^{-10}$  Torr, and contains the 3D MOT and ring trap. Rubidium dispensers fill up the high pressure chamber where the atoms are cooled along two axes by the 2D MOT. The cooled atoms are then pushed by a laser beam through the differential pumping tube, orientated along the third axis, into the low pressure chamber where we load the 3D MOT. Throughout this thesis, we assign axis labels of X to the direction of the differential pumping tube, Y is the other

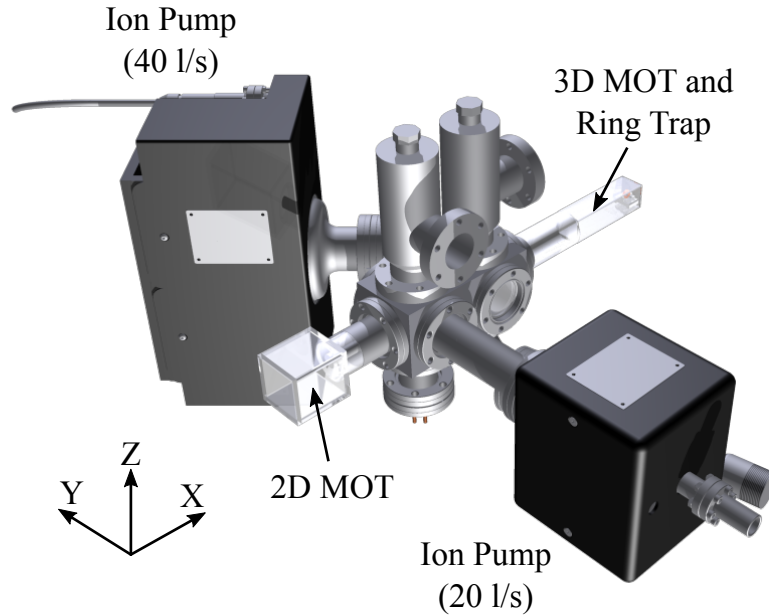


Figure 4.1: *Vacuum system comprising of two glass cells and two vacuum pumps.*

horizontal axis, and Z is the vertical axis.

### 4.1.2 Glass Cells

The 2D MOT chamber is homemade using anti reflection (AR) coated glass from SLS Optics. Each glass plate is 4 mm thick and an epoxy resin (EPO-TEK 353ND) is used to glue them together. The assembled chamber measures 5 cm in X, Y, and Z across the outside surfaces.

The science chamber housing the 3D MOT and ring trap is sourced from an external supplier (Precision Glass Blowing). Its elongated shape makes it less trivial to construct in-house. It measures 10.2 cm long, has a 27.5 mm square cross section, and is AR coated on the outside.

### 4.1.3 Atom Source

Within our vacuum chamber we have a source of Rb, although we also have a source of potassium in the system. This is for future experiments with degenerate Fermi gasses but we have yet to use this. With regards to the Rb dispensers, we have two (natural abundance)  $^{87}\text{Rb}$  dispensers from SAES with a common ground pin and a separate single (enhanced abundance)  $^{87}\text{Rb}$  dispenser from Alvatec.

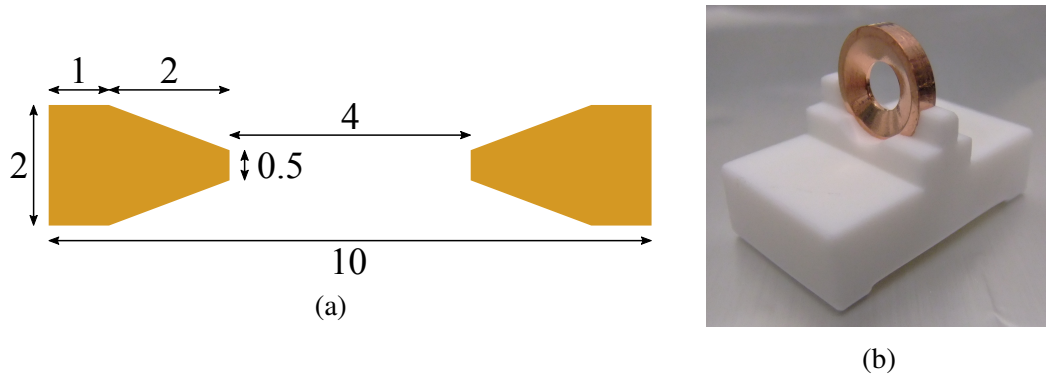


Figure 4.2: (a): Cross section of the copper ring with dimensions in millimetres. (b): Copper ring in Macor mount.

Initially we used the two SAES dispensers at a current of around 3 A. Over time this current was increased to get sufficient pressure, and after 3 years a current of 4.5 A was applied. More recently we have switched over to using the single Alvac source at a current of 2.2 A. We run the experiment with the dispensers on continuously and switch them off at the end of the day.

#### 4.1.4 Copper Ring

This second generation experiment features an oxygen-free high thermal conductivity copper ring mounted vertically and positioned within the science chamber. Its dimensions are given in figure 4.2a. A mount is machined from Macor which is non-conductive and importantly does not outgas under vacuum (figure 4.2b). The ring is machined to have a tapered inside edge which allows optical access for both the dipole trapping beams and the interferometry beams. The copper ring, in its Macor mount, was placed inside the chamber before the system was sealed.

#### 4.1.5 Magnetic Coils

To achieve the necessary magnetic fields we use several sets of coils (figure 4.3). Starting at the 2D side of the chamber we firstly have two sets of rectangular quadrupole (QP) coils aligned along the Y and Z axes. These produce a cylindrically symmetric QP field. We also have three pairs of shim coils (one per axis) to give us control over the position of the QP centre. All these coils are wrapped tightly around coil holders surrounding the glass cell.

Above and below the low pressure science chamber we have machined Perspex moulds which hold the 3D MOT, quadrupole, and the AC drive coils which induce the current in the copper ring. This form allows the coils to be held in a low form factor housing, which increases optical access. The transport coils are clamped to the outside of the Perspex forms. The aforementioned coils are made from hollow

## 4.1. SYSTEM

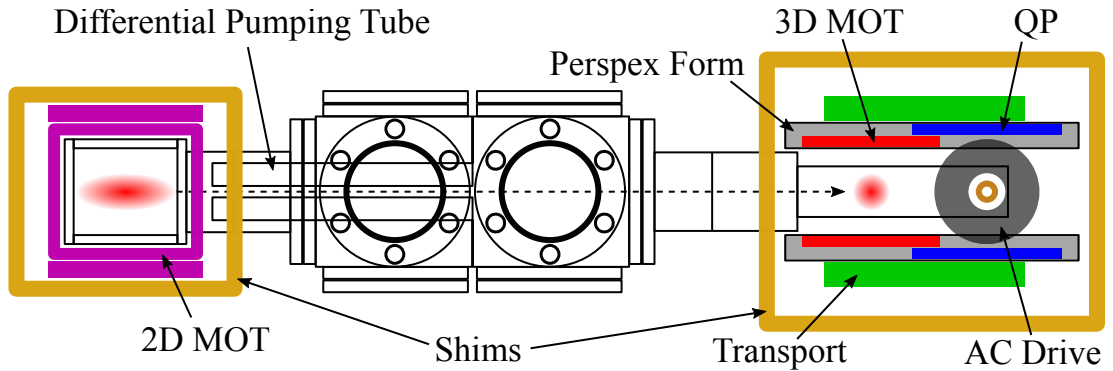


Figure 4.3: Side view schematic of the vacuum cells and magnetic coils. Atoms are initially loaded and cooled in the high pressure chamber containing the 2D MOT. They then pass through a differential pumping tube to the 3D MOT located in the low pressure chamber. They are then magnetically transported to the ring region.

copper pipe encased in electrically insulating heat shrink tubing. This allows them to be water cooled and therefore higher magnetic field gradients are achievable and for longer durations compared to if no active cooling was used.

The MOT coils are wound two layers deep and produce a measured gradient of 1.57 G/cm/A [8]. The transport coils are five layers deep and produce 0.53 G/cm/A. The uniformity of these coils is less crucial due to them being further from the chamber. The QP coils are again two layers deep, and from these we achieve 1.21 G/cm/A. Finally we mount the AC drive coils orthogonally to the other coils and on axis with the copper ring. These are wound in a Helmholtz configuration. By placing them as close to the ring as possible we achieve maximum AC coupling and therefore increased trap depth.

Surrounding these four sets of coils and the low pressure chamber, we position shim coils to cancel out stray magnetic fields in all axes. These are wound around an alloy form and are made from enamelled copper wire. They provide 3.4 G/A, 4.0 G/A, and 7.6 G/A along X, Y, and Z respectively at both the MOT position and ring position.

### 4.1.6 ECDL Lasers

The cooling and repump lasers in our system are homebuilt external cavity diode lasers (ECDLs) in a Littrow configuration [135] with 780 nm laser diodes (figure 4.4). These have the advantage of being fairly inexpensive, compact, and tunable.

The housing of the laser is machined from a single aluminium block. This main body, which holds the laser diode and collimation lens, is bolted to a thermoelectric cooler, allowing for temperature stabilisation. In addition to this there is a front plate onto which is attached a grating and mirror on a single mount. We attach the front plate and feedback control mount to the main body via stiff springs. This allows for the adjustment of the cavity which is needed for feedback and locking the laser.

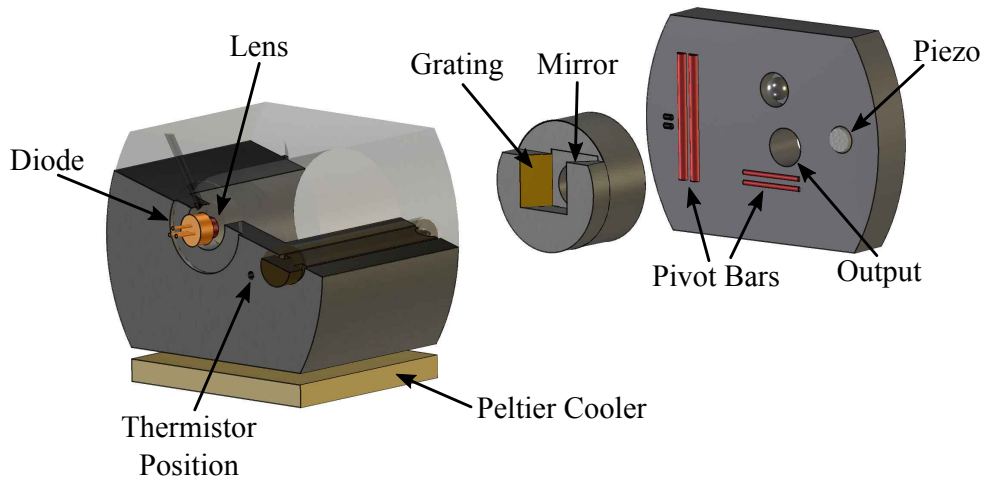


Figure 4.4: *Diagram of the Strathclyde ECDL design (adapted from [8]).*

The ‘external cavity’ is created between the diode and the diffraction grating (1800 lines/mm). This is positioned at approximately  $45^\circ$  to the incident beam with the lines vertically orientated. As a result the grating diffracts the  $-1^{\text{st}}$  order beam back towards the diode while the  $0^{\text{th}}$  order is reflected at  $90^\circ$  to the incident beam. This  $0^{\text{th}}$  order diffracted beam is then reflected off a mirror to give the output. Without this additional mirror, as the cavity is modulated the beam angle will change, resulting in misalignments later in the optical setup. By including this mirror, the modulation of the cavity leads to a small lateral shift of the beam that is favourable over an angular displacement as it results in less misalignment in the rest of the system.

Control of the lasers is achieved via a laser diode controller (MOGbox DLC-202). As well as temperature stabilisation, it also modulates the frequency of the laser by modulating the current to the laser diode, which allows us to lock the laser to the hyperfine structure of the saturation absorption spectroscopy signal [8]. The controller allows for fast locking via current feedback and slow locking via the piezoelectric crystal that controls the cavity length.

#### 4.1.7 Optics Setup

The beam preparation optics are quite complex, so it’s probably best illustrated by figure 4.5. Both lasers (cooling and repump) are locked via frequency-modulated saturation absorption spectroscopy. The repump laser is locked to the  $F = 1 \rightarrow F' = 1, 2$  crossover then frequency shifted by  $+77.210$  MHz on to resonance with a single pass AOM. This AOM also acts as a switch and allows us to turn off the repump beam. To further exclude any leakage light, we also place a homemade shutter at the focus of the telescope. Our homemade shutters comprise of a Sunex SHT934 mechanical shutter and a simple electronic control circuit, shown in appendix A.1. After this the beam is

#### 4.1. SYSTEM

---

split into the 2D and 3D paths and coupled into the appropriate optical fibres.

The laser from which the cooling beam is derived acts as the source for our imaging, optical pumping, and push beam. Again, we lock the laser via frequency-modulated saturated absorption spectroscopy to the  $F = 2 \rightarrow F' = 1, 3$  crossover, but this time we use a single pass AOM positioned in the spectroscopy beam path to shift the frequency by +200 MHz. This means that the frequency of the laser output is -200 MHz from the spectroscopy light. We take the ECDL output and pass it through a tapered amplifier (New Focus TA-7600). From  $\approx 18$  mW fibre input power we measure  $\approx 470$  mW fibre output power. A PBS after the output cleans the polarisation; it's from the reflected port that we derive the readout beam for our contrast interferometer. The transmitted beam is then further split into the 2D and 3D cooling beams and we use double pass AOMs (both operating at +200 MHz) to control the power in each beam. Finally the 2D and 3D cooling beams are mode matched to the repump beams via PBSs and fibre coupled into the appropriate fibres. In the 3D beam we use a shutter (Uniblitz LS2T2) at the focus of a telescope to block any stray resonant light from reaching the science chamber. This is not necessary in the 2D beam because the fibre output is at the other side of the vacuum system and away from the science chamber.

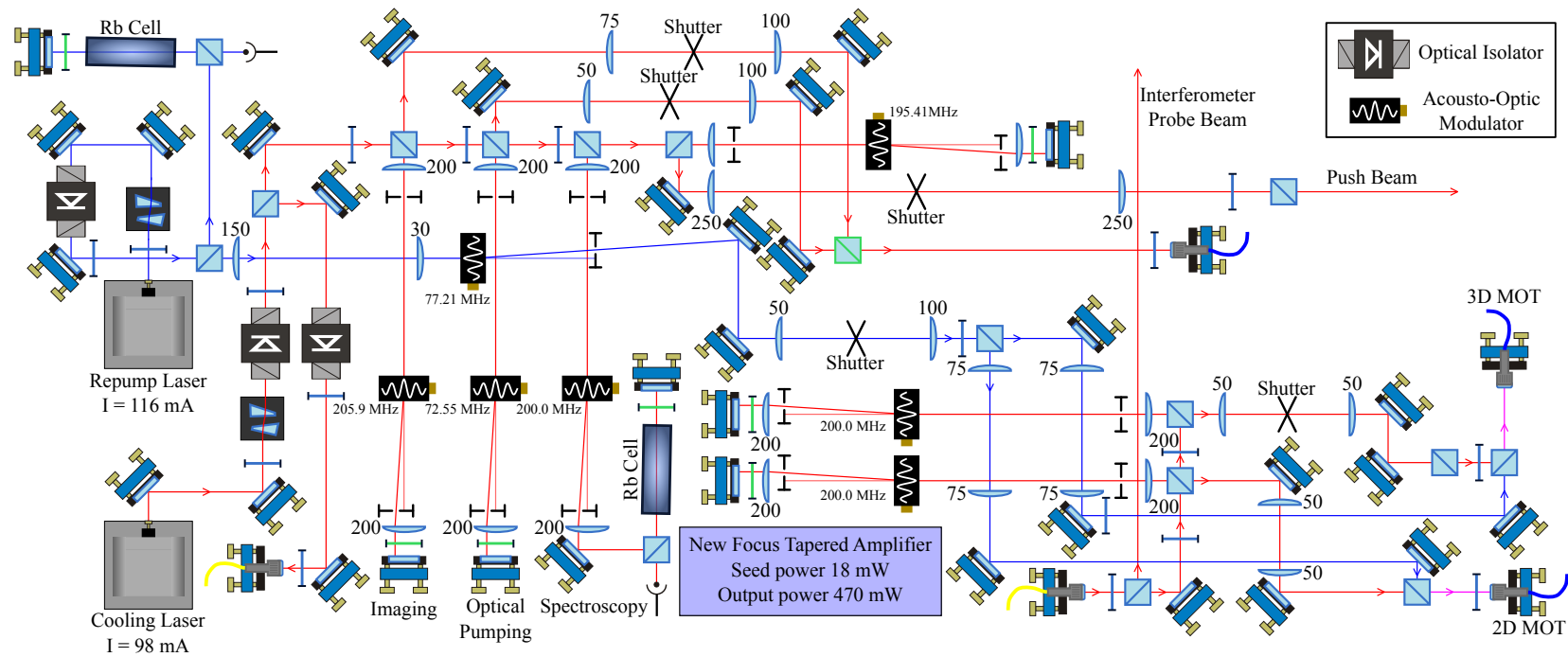


Figure 4.5: Setup of the cooling laser (red) and the repump laser (blue) preparation optics. The cooling laser is also used for imaging, optical pumping and as the push beam. The reject port of the PBS at the TA output becomes the contrast interferometer readout beam. The values next to the acousto-optic modulators denote operating frequency. The values next to lenses denote the focal length in millimetres. Blue waveplates are  $\lambda/2$  while green waveplates are  $\lambda/4$ . Numbers by ECDLs refer to typical drive currents.

#### 4.1. SYSTEM

---

The imaging beam, which drives the  $F = 2 \rightarrow F' = 3$  transition is double passed through an AOM, goes through a telescope with a homemade shutter at the focus, and is then fibre coupled into a fibre that takes the light to the main chamber. The optical pumping beam, which drives the  $F = 2 \rightarrow F' = 2$  transition follows a similar setup to that of the imaging beam. It is then mode matched to the imaging beam and fibre coupled. However, for this beam we use a fast Uniblitz LS2T2 shutter at the telescope focus. The beam cube used to mode match these beams is an NPBS which allows both beams to have the same linear polarisation upon entering the fibre.

Finally the push beam is generated by double passing an AOM then sent toward the 2D MOT by propagation in free space. We also use a homemade shutter at the telescope focus to block any leakage light. An optimum detuning of -9.18 MHz from the  $F = 2 \rightarrow F' = 3'$  transition and a power of 500  $\mu\text{W}$  is used.

The second half of our table comprises the vacuum chamber with raised breadboards for the placement of optics (figure 4.6). Starting at the high pressure chamber side we construct our 2D MOT optics. Both the vertical and horizontal beams are expanded through cylindrical lenses which increase the beam waist from  $\approx 12$  mm to  $\approx 36$  mm in one axis while the other axis remains unchanged. They are then retro-reflected back along the same beam path. The push beam is aligned using 2 mirrors to direct it through the differential pumping tube and optimised for maximum 3D MOT load rate.

#### 4.1. SYSTEM

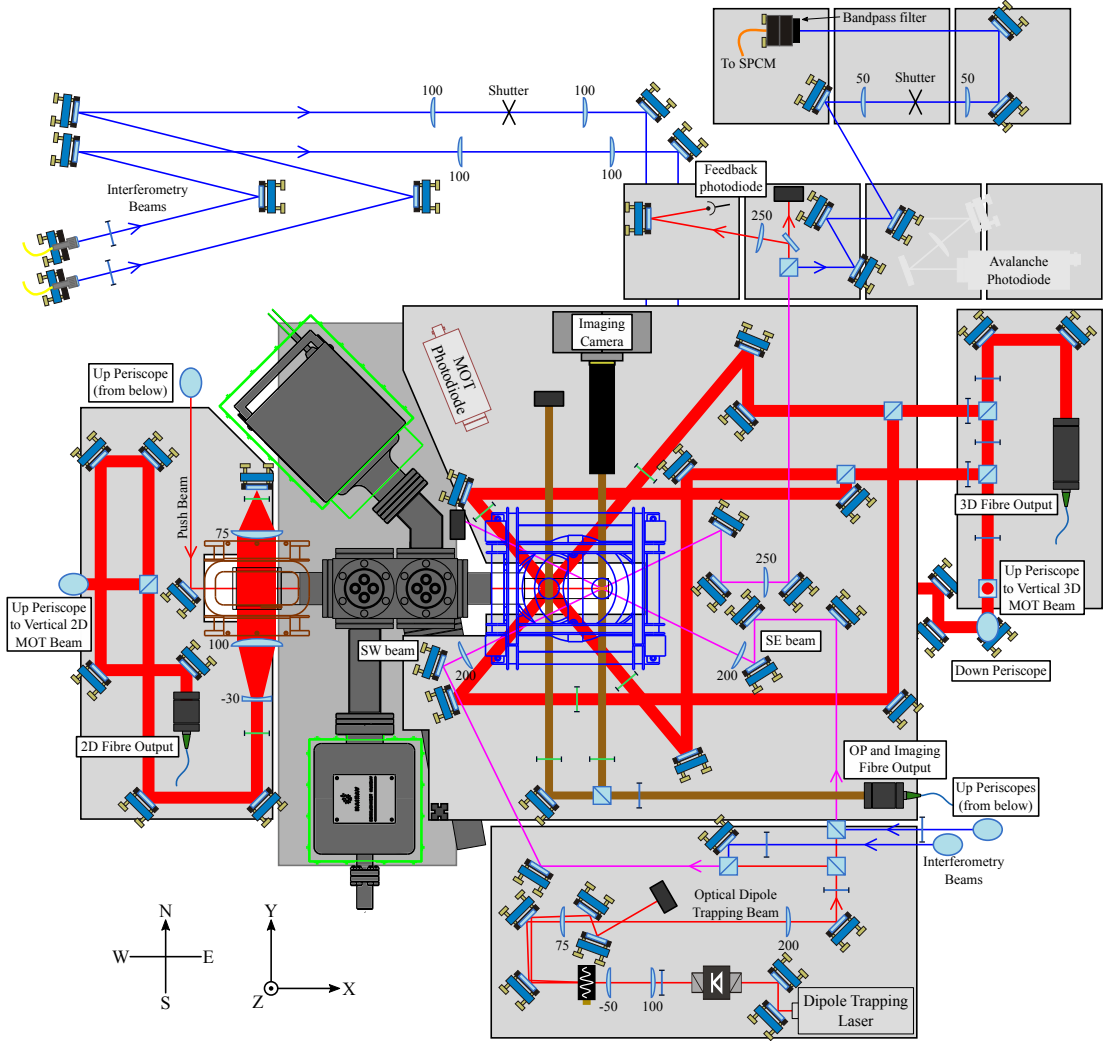


Figure 4.6: *Diagram of optics setup around the vacuum chamber. The 2D MOT (left side) loads a 3D MOT (right side). The interferometry beams (blue) pass under the breadboard and up a periscope to the level of the chamber. The values next to lenses denote the focal length in millimetres. Blue waveplates are  $\lambda/2$  while green waveplates are  $\lambda/4$ .*

Around the low pressure science chamber we firstly have the 3D MOT beams, which are collimated at the fibre output with a 12 mm waist. The beam is split into 3 pairs of beams via PBSs and  $\lambda/2$  waveplates, which allows for each pair to be made counterpropagating. The polarisation of the beams are made circular with the use of  $\lambda/4$  waveplates positioned before the cell.

The optical pumping (OP) and imaging light emerge from the same fibre and are immediately collimated. A PBS splits the beams such that both beams pass through the 3D MOT and ring sections of the cell, although the OP beam is only used in the 3D

MOT section while the imaging is only used in the ring section<sup>1</sup>. The beams are made circularly polarised by  $\lambda/4$  waveplates after the PBS.

**Optical Dipole Trap:** The crossed optical dipole trap (ODT) is derived from a 1070 nm, 20 W Ytterbium fibre laser (IPG YLM-20-LP-SC) running at an output power of 10 W. We control the power in the beam via a SRS DS345 arbitrary function generator connected to an AOM of which we use the first order (see more details in section 4.3). A PBS splits the beam into the two beams that form the crossed ODT. We refer to the beams as the South East (SE) beam and the South West (SW) beam from the direction that they ‘hit’ the atoms. Both beams are focused to a waist of  $\approx 86 \mu\text{m}$  with  $f=200 \text{ mm}$  lenses.

As indicated in figure 4.6, the optical power of the SE beam is terminated on a beam block. Around 90 % of the SW beam power is terminated on a beam block while 10 % is directed onto a photodiode using a pick-off plate. This is then used in a feedback loop for power stabilisation via the AOM.

### 4.1.8 Light-Induced Atomic Desorption

In order to temporarily increase the background pressure of rubidium in the 2D MOT chamber, we employ a Light-Induced Atomic Desorption (LIAD) scheme [136]. We apply ultraviolet light to the chamber during the MOT loading stage which causes atoms that are stuck to the inside of the chamber to be “kicked off” (desorbed). This increases the local pressure of rubidium, which increases the MOT load rate. When the light is turned off, the atoms can return to the chamber walls and the previous vacuum pressure is maintained.

We use two 5W LEDs (part no. LZ1-00UA00) with an emission wavelength centred at 400 nm and powered by 12 V, 275 mA (see appendix A.2 for circuit diagram). They are toggled on via the main experiment control during the MOT load stage. We find an increase in load rate of around 50 %.

A heat sink is attached to the LEDs and a thermal cut-off is implemented to trigger at 70 °C. Despite this we find the stable temperature with the LEDs on continuously to be around 40 °C.

---

<sup>1</sup>The imaging beam was used in the 3D MOT section for initial diagnostics and quadrupole trap alignment.

## 4.2 Experimental Sequence

The exact experimental sequence will of course depend on what type of experiment we wish to perform, however the initial stages are common to all.

**Initial Stages:** The MOT coil currents for the first stages of the experimental sequence are shown in figure 4.7. We start by loading a MOT of  $\sim 5 \times 10^8$  atoms. The load rate is  $\sim 5 \times 10^7$  atoms per second. The MOT is then compressed for 5 ms during which we increase the magnetic field gradient from 11 G/cm to 16 G/cm and change the detuning of the light from -14 MHz to -25 MHz. After 4 ms of optical molasses we optically pump our atoms into the  $|F = 2, m_F = 2\rangle$  state over a duration of 1.2 ms by using  $\sigma^+$  light on the  $|F = 2\rangle \rightarrow |F' = 2\rangle$  transition.

The atoms are then loaded into a magnetic quadrupole (QP) trap. We want to have a rapid turn on of the QP field but the inductance of the coils gives a slow rise time to the requested current. Therefore we ‘snap’ on the coils by initially requesting a high current of 330 A then, after just 180  $\mu$ s we change the requested value to 40 A, which gives us 63 G/cm. This has the effect of decreasing the rise time of the current in the coils. After 5 ms, the field is ramped linearly to 100 G/cm over 95 ms.

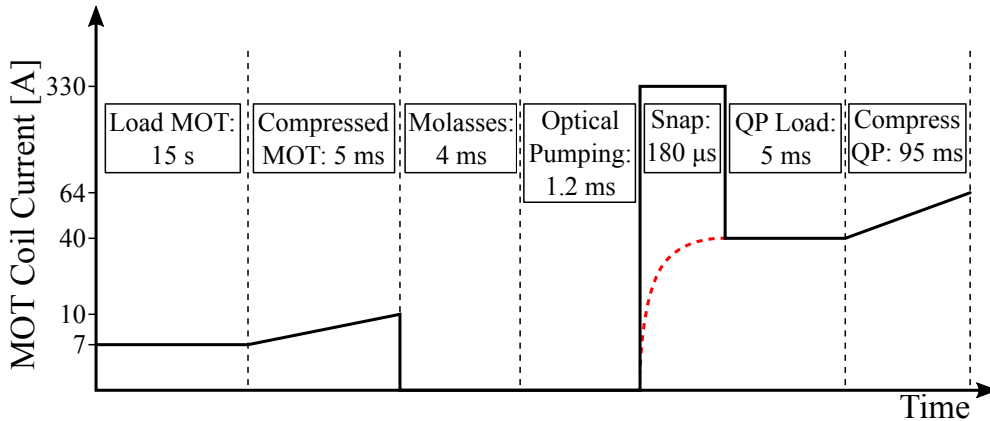


Figure 4.7: *The requested MOT coil current up to the start of the magnetic transport stage. Note that the ‘Load MOT’ stage is typically 15 s and the time axis does not vary linearly. The coils produce 1.67 G/cm/A. The red dashed line during the ‘snap’ stage indicates the actual coil current*

**Magnetic Transport:** We need to transport the cold atoms to the centre of the ring region, located 62 mm from the centre of the MOT. To do this we use a magnetic transport system [8, 137] which utilises dedicated transport coils as well as the MOT and quadrupole trap coils. The transport coil current is ramped up whilst the MOT coil current is reduced, thus shifting the centre of the trapping potential in the horizontal direction. The same is then repeated for the quadrupole trap coils and the transport

## 4.2. EXPERIMENTAL SEQUENCE

coils to further move the trap centre to the ring region. By using three pairs of coils we can maintain a constant aspect ratio across the atom cloud [137].

The magnetic transport stage takes 389 ms for the atoms to travel from the MOT region to the ring region, shown in figure 4.8. In order to avoid the atoms colliding with ring, we apply a Y bias field for the final 250 ms of the transportation. The atoms are now displaced from the plane of the ring, and so we relax the bias field and the atom cloud moves to centre of the ring.

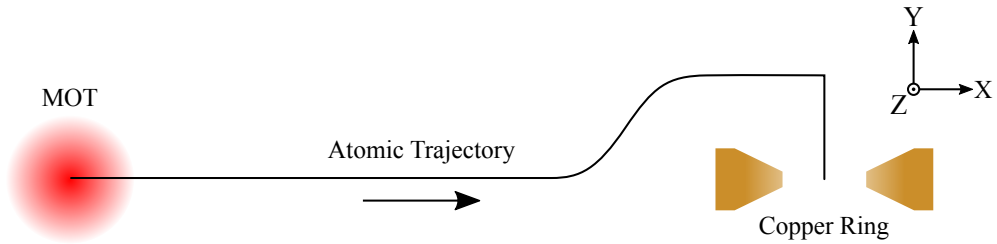


Figure 4.8: A top-down view of the trajectory of the atoms during magnetic transport.

The required coil currents for the magnetic transport stage, excluding the relaxation of the QP to the ring centre, are calculated by LabVIEW for a specified maximum velocity of 20 cm/s and a maximum acceleration of  $4 \text{ m/s}^2$ , whilst keeping the magnetic field gradient at 100 G/cm for the entire stage. The coil currents are shown in figure 4.9 and the calculated atomic trajectory is shown in figure 4.10.

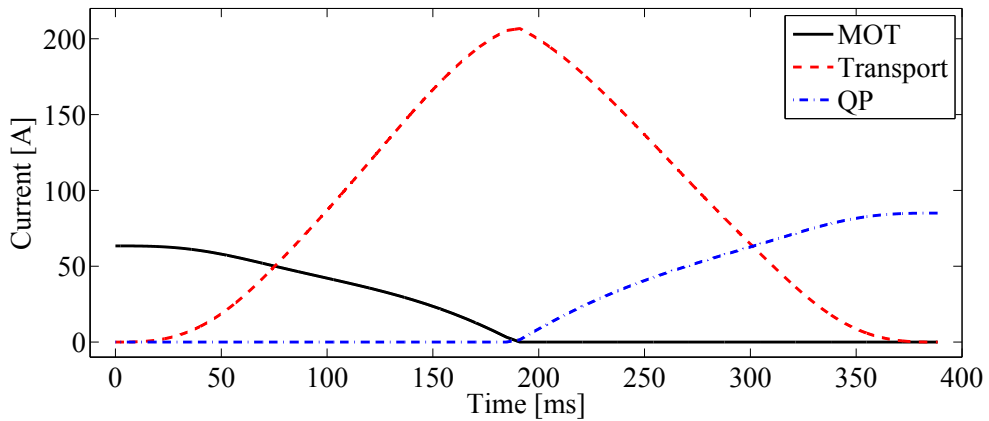


Figure 4.9: Currents applied to the MOT, transport, and quadrupole trap coils during magnetic transport.

## 4.2. EXPERIMENTAL SEQUENCE

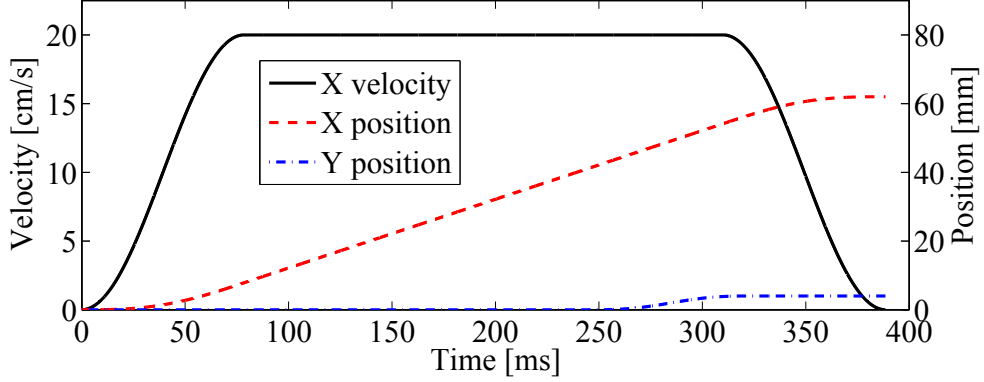


Figure 4.10: *Atomic motion during the magnetic transport stage. Velocity is in the X direction. The zero in the X direction is defined to be the centre of the MOT and the zero in Y is the MOT centre and plane of the ring.*

**RF Evaporation:** We perform RF evaporation by using an Agilent 33522A arbitrary function generator with a peak-to-peak output voltage of 10 V to apply a varying RF frequency over a total of 4.133 s, with the ‘main’ evaporation stage lasting for 3 s whilst the atoms are in a quadrupole trap of 206 G/cm. Each of the 4 different RF ramps shown in figure 4.11 can be calculated from:

$$f(t) = f_{\text{base}} + (f_{\text{start}} - f_{\text{base}}) \times e^{(-t/\tau)}, 0 < t < \tau \ln \left( \frac{f_{\text{start}} - f_{\text{base}}}{f_{\text{stop}} - f_{\text{base}}} \right), \quad (4.1)$$

where  $f_{\text{base}}$  is the frequency that the exponential asymptotically approaches,  $f_{\text{start}}$  is the initial frequency,  $f_{\text{stop}}$  is the frequency after time  $t$ , and  $\tau$  is the time constant of the ramp.

The evaporation parameters are experimentally tuned for optimum phase-space density (see below) and the ‘linear’ regions are generated using  $f_{\text{base}} = -500$  MHz. We apply an RF field during the magnetic transport stage to decrease the size of the atom cloud such that it fits into the ring region without colliding with the copper, which would result in atom loss. After the main evaporation stage, lasting 3 s, we typically have  $\approx 4 \times 10^7$  atoms at a temperature of  $\approx 35$   $\mu\text{K}$ .

The figure of merit in optimising the evaporation trajectory is the phase-space density,  $\Lambda$ , of the atomic ensemble, which can be calculated by

$$\Lambda = \lambda_{\text{dB}}^3 n_0, \quad (4.2)$$

where  $\lambda_{\text{dB}}$  is the de Broglie wavelength and  $n_0$  is the peak density of the atoms. Using this we can then calculate the efficiency,  $\gamma$ , of our evaporation stages using [114, 138]

$$\gamma = -\frac{\ln(\Lambda)}{\ln(N)}, \quad (4.3)$$

## 4.2. EXPERIMENTAL SEQUENCE

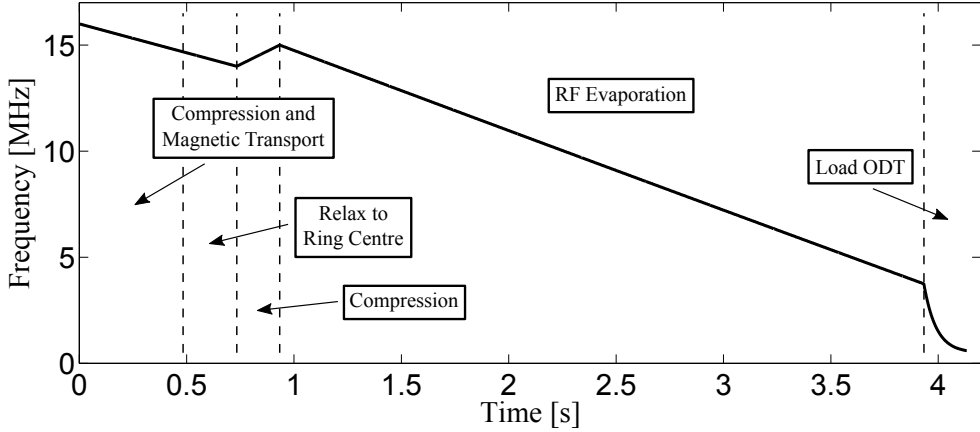


Figure 4.11: *RF evaporation frequency ramp. We start by applying 16 MHz ramped linearly to 14 MHz as we compress the MOT QP field and perform magnetic transport. We then linearly ramp the frequency to 15 MHz during the relaxation of the QP bringing the atoms into the centre of the ring. A linear ramp from 15 MHz to 3.75 MHz over 3 s is then applied as our main RF cooling stage. Finally, the frequency is ramped exponentially to 0.6 MHz in 200 ms as we load the optical dipole trap.*

where  $N$  is the number of atoms. For RF and optical evaporation we calculate  $\gamma$  to be 2.6 and 3.1 respectively (figure 4.12). To put this in perspective, using a similar apparatus, the group of Hadzibabic [114] calculate an efficiency of 2.1 and 3.1 for RF and optical evaporation respectively.

In order to estimate the phase-space density of the atoms in our trap we need to determine the number of atoms and the size of the ensemble. However, we cannot directly determine this from absorption imaging as the high density of the atoms leads to lensing of the imaging beam and results in a negative measured optical density at the edges of the cloud. Moreover, the magnetic field of the trapping potential gives the atoms the wrong quantisation axis for the imaging beam. We therefore release the atom cloud from the trap and observe the thermal expansion as a function of time. From this expansion we infer the initial size of the atom cloud as well as the atom number and temperature.

The data points in figure 4.12 are calculated by measuring the expansion rate of the atom cloud during free fall. The width of the atom cloud as a function of time is then plotted and the initial size determined by extrapolation. The final data point in figure 4.12 is measured close to the BEC transition temperature at  $\sim 130$  nK. For this data point only we infer initial cloud size from the measured trap frequency (figure 4.15).

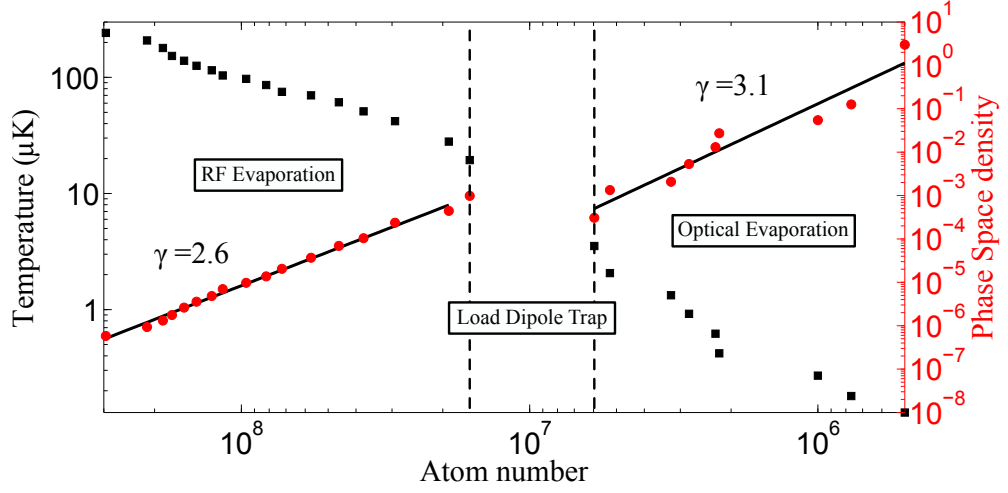


Figure 4.12: Temperature and phase-space density as a function of atom number during evaporation stages. Efficiency of the evaporation stages calculated using equation 4.3.

**Loading the Optical Dipole Trap:** After the main RF evaporation stage, we load the atoms into the crossed optical dipole trap (ODT). Our method is partly based on the scheme of Lin *et al.* [115] and Hung *et al.* [138]. The beams are aligned slightly ( $\sim$  a beam waist) below the QP centre and the magnetic field gradient is lowered such that the atoms are adiabatically transferred into the hybrid trap. The vertical alignment is determined by optimising the position of a single beam for maximum atom number, then aligning the other beam to the same height. The loading stage takes 200 ms during which the QP field is ramped from 206 G/cm to 15 G/cm. The final magnetic field gradient effectively cancels the gravitational field such that the atoms are levitated (see appendix A.3). To minimise magnetically induced atomic motion, the magnetic field gradient is ramped in a s-curve of the form

$$y(t) = \frac{y_{\max}}{1 + \exp[-(t - t_0)]}, \quad (4.4)$$

where  $y_{\max}$  is the maximum value of the curve (the new magnetic field gradient), and  $t_0$  is the centre of the curve (half the duration of the ramp).

At the end of this stage we can release the magnetic trap completely and image the number of atoms in the crossed ODT region, which we find to be  $\approx 6 \times 10^6$ . Note that in the complete sequence there will be more atoms than this contributing to the optical evaporation as the QP is held on to create a hybrid trap. The approximate phase-space density and temperature of the atoms at this point is  $3 \times 10^{-4}$  and 3.5  $\mu$ K respectively.

**Optical Evaporation:** The atoms are now held in a hybrid trap in which we perform evaporative cooling to produce a BEC. Each beam has an initial power of 2.6 W focused to a waist of  $\approx 86 \mu$ m with a crossing angle of  $128^\circ$ , giving an optical trap depth

## 4.2. EXPERIMENTAL SEQUENCE

of  $\approx 15 \mu\text{K}$ . Using an SRS DS345 arbitrary function generator, the dipole power is ramped exponentially to 0.26 W over 4 s, with a base value of 0.15 W (figure 4.13), and follows the form of equation 4.1. We also reduce the B-field gradient to 7.5 G/cm in an s-curve ramp in the first 100 ms. This is similar to the scheme in [115]. By reducing the magnetic field the trap is effectively tilted in the Z axis such that evaporation surface is at the bottom and the hot atoms are poured out.

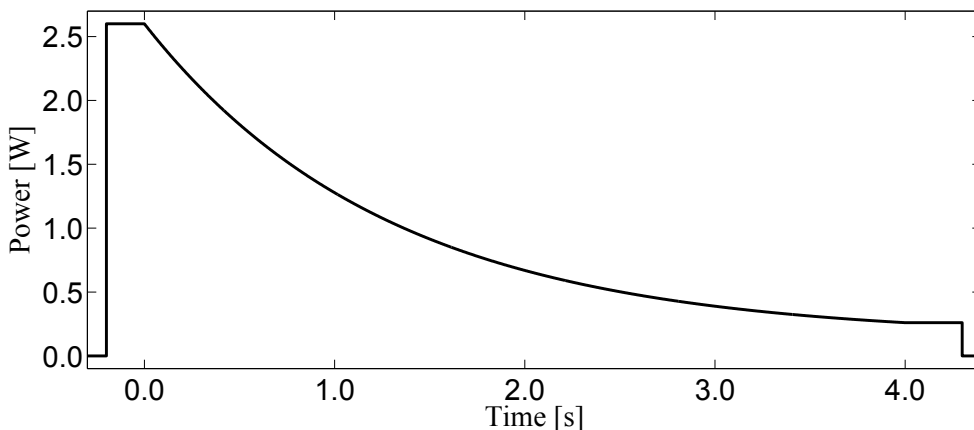


Figure 4.13: *Dipole evaporation trajectory.* The power in each beam is held at 2.6 W for 200 ms during the loading stage. The power is ramped according to equation 4.1 to final power of 0.26 W during the evaporation and is held at the final power for 300 ms. Zero is defined as the start of the dipole evaporation stage.

Half way through the power ramp we ramp up a large vertical magnetic shim which moves the QP centre upwards to  $\approx 2.7$  cm above the ODT centre. The reason for this is that we typically apply a levitation field later in the sequence, which requires the QP centre to be high such that the atoms see a magnetic field gradient with minimal curvature. By moving the QP centre at this point before the atoms condense, we minimise sloshing motion of the BEC. In addition, we no longer require the extra confinement that we did during the dipole trap loading stage and the first 2 s of dipole evaporation.

We measure the trap frequency of the hybrid magneto-optical trap by loading it with ultra-cold thermal atoms and inducing a sloshing motion using a magnetic kick via the displacement of the quadrupole trap. The vertical position of the atoms after some time of flight is then plotted against ODT duration. To these data we fit a sinusoid to extract the frequency and an exponential decay to account for the anharmonicity of the trapping potential. An example of such a measurement is shown in figure 4.14. This is repeated multiple times to obtain the data in figure 4.15. A power relationship of  $y = A \times P^B$  is also fitted to the data, where P is the optical power per beam. The fitted parameters have a value of  $A = 140$  and  $B = 0.57$ . In a purely optical trapping potential we would expect  $B = 0.5$  as the trap frequency scales as the square root of optical power [110], however in this case we are using a hybrid trap and the extra trapping potential of the magnetic field gradient alters this scaling.

## 4.2. EXPERIMENTAL SEQUENCE

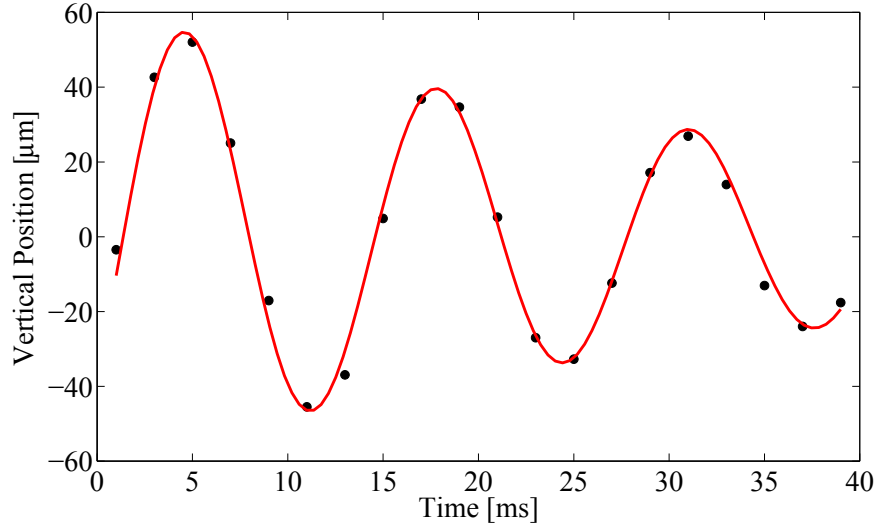


Figure 4.14: The hybrid trap is held with an optical power of 0.4 W per beam and a magnetic field gradient of 7.5 G/cm. A magnetic kick is used to induce sloshing in the vertical direction. Position as a function of time is used to measure the trap frequency for the given dipole power.

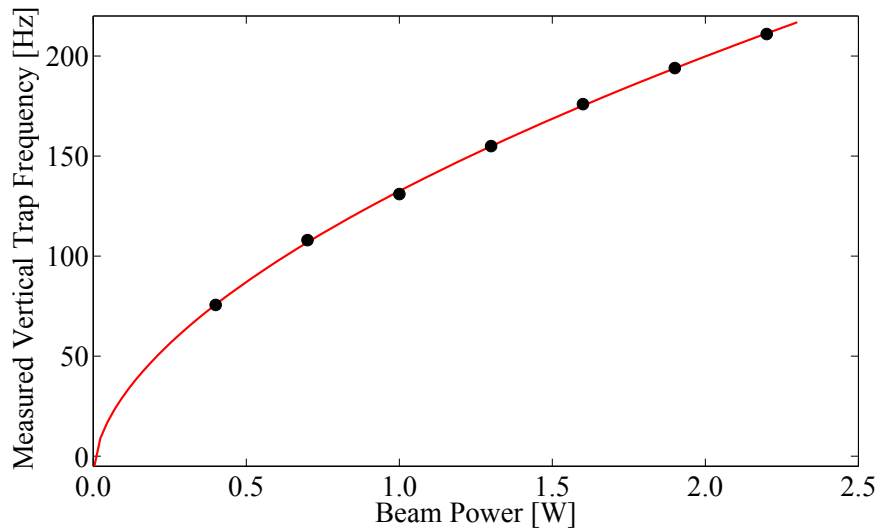


Figure 4.15: Vertical trap frequency of the hybrid trap as a function of beam power. The magnetic field gradient is 7.5 G/cm for all data points. A power relationship of  $y = A \times P^B$  is fitted to the data, where  $P$  is the optical power per beam, and  $A = 140$  and  $B = 0.57$  are constants.

The data plotted in figure 4.15 are the vertical (radial) trap frequencies. Due to the geometry of the crossed ODT, the frequencies in the other axes differ from these values but an estimate can be obtained from a simulation of the trapping potential.

## 4.2. EXPERIMENTAL SEQUENCE

This is done in MATLAB by combining the optical and magnetic potentials (equations 2.12 and 2.7). The lowest beam power of 0.4 W returns a trap frequency of 76 Hz, from which we calculate an X and Y trap frequency of 35 Hz and 74 Hz respectively. Trap frequencies for lower powers are difficult to measure due to the slow oscillation frequency, but can be inferred from the fit to the data in figure 4.15.

After 4 s of evaporation we hold the dipole power constant for 306.5 ms whilst ramping the QP field in an s-curve to 14.3 G/cm in 300 ms which we find experimentally to increase the BEC fraction of the remaining atoms<sup>2</sup>.

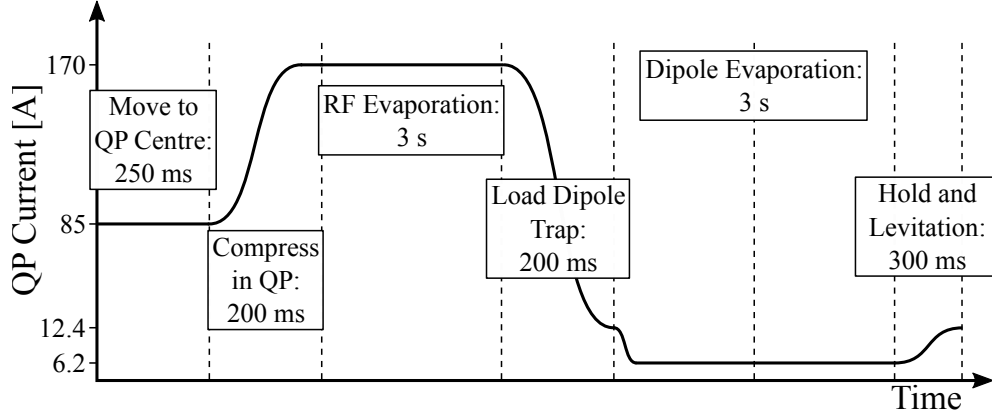


Figure 4.16: *QP coil current during last stages of creating a BEC. All ramps are S-curves to maximise adiabacity.*

We are now left with a BEC of  $\approx 10^5$  atoms with a BEC fraction of  $\gtrsim 80\%$ . From here the exact sequence varies depending on what experiment we are performing and therefore details can be found in the specific chapters.

**BEC Size:** The size of the BEC in a harmonic trap can be quantified by the Thomas-Fermi radius. The energy of a quantum harmonic oscillator can be written as

$$U(r) = \frac{1}{2}mr_{\text{TF}}^2\omega^2 = k_{\text{B}}T, \quad (4.5)$$

where  $m$  is the mass of the atom,  $r_{\text{TF}}$  is the Thomas-Fermi radius,  $\omega$  is the trap frequency,  $k_{\text{B}}$  is the Boltzmann constant and  $T$  is temperature. By rearranging we obtain

$$r_{\text{TF}} = \sqrt{\frac{k_{\text{B}}T}{\frac{1}{2}m\omega}}. \quad (4.6)$$

The typical final evaporation power is 0.26 W, which gives trap frequencies of 28 Hz, 60 Hz, and 66 Hz in the X, Y, and Z axes respectively and the Thomas-Fermi radii are

<sup>2</sup>The extra 6.5 ms is to account for opening time of the interferometry shutters

## 4.2. EXPERIMENTAL SEQUENCE

calculated to be 13  $\mu\text{m}$ , 6  $\mu\text{m}$ , and 5  $\mu\text{m}$  for a transition temperature of 172 nK (using equation 2.29).

When the BEC is released from the trapping potential it expands due to inter-atomic interactions. An estimation of the expansion of our condensate of  $1 \times 10^5$  atoms can be obtained by approximating the trapping potential to a cylinder with an axial trap frequency of 28 Hz and a radial trap frequency of 63 Hz. Equation 103 of [45] gives

$$\frac{d^2}{d\tau^2} b_{\perp} = \frac{1}{b_{\perp}^3 b_z} \text{ and } \frac{d^2}{d\tau^2} b_z = \frac{\lambda^2}{b_{\perp}^2 b_z^2}, \quad (4.7)$$

where  $\tau = \omega_{\perp} t$ ,  $\omega_{\perp}$  is radial trap frequency,  $t$  is time, and  $b_{\perp}$  and  $b_z$  are radial and axial scaling parameters respectively that define the trap dimensions. This is solved numerically in MATLAB and figure 4.17 is produced. This shows that the rate of expansion initially varies then becomes constant for long durations. When performing our atom interferometer experiments we typically allow 2 ms of free expansion before applying the initial beam splitter pulse. This duration is chosen as ideally the BEC would have a constant expansion rate but if we wait for too long the atoms can fall out of the interrogation region (if no levitation field is applied).

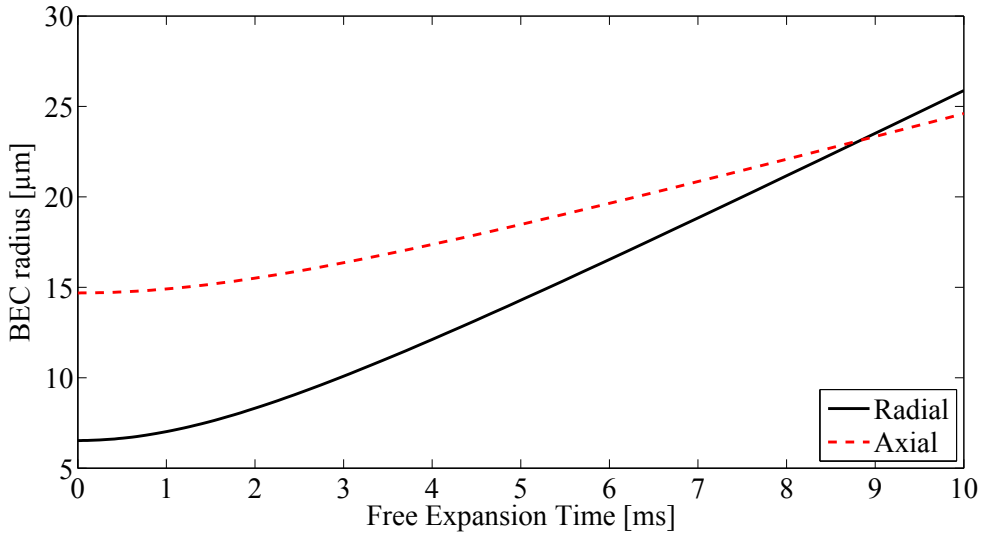


Figure 4.17: Expansion of a BEC of  $1 \times 10^5$  atoms created in an axially symmetric trapping potential with radial and axial trap frequencies of 28 Hz and 63 Hz respectively.

## 4.3 Interferometry Setup

### 4.3.1 Interferometry Laser Setup

The interferometer light (red beam of figure 4.18) that forms our beam splitter and mirror pulses is produced by an external cavity diode laser (ECDL) of 780 nm wavelength (figure 4.4). It is locked to the  $F = 2 \rightarrow F' = 2, 3$  crossover  $^{85}\text{Rb}$  repump transition using saturation absorption spectroscopy. When we apply the interferometer light to the atoms we typically apply a 20 G bias field which gives the laser a detuning of 4.18 GHz from the  $F = 2 \rightarrow F' = 2$  transition and 3.92 GHz from the  $F = 2 \rightarrow F' = 3$  transition of  $^{87}\text{Rb}$ .

The beam then passes through an acousto-optic modulator (AOM) operating at 84 MHz driven by a homemade circuit (appendix A.4). This circuit uses an RF mixer (Minicircuits ZP-3LH-S+) and an RF source (Keysight N5138B) to convert a DC input voltage to a change in amplitude of the 84 MHz output, which allows us control of the power in the  $-1^{\text{st}}$  order diffracted beam and forms the basis of our interferometer beams. The control mechanism will be discussed further in the following section 4.3.2.

The frequency shifted beam is then split using a polarising beam-splitter (PBS) with the power balance controlled by the  $\lambda/2$  waveplate beforehand. We target an even power balance in the science chamber, but each beam has different power loss mechanisms along their path lengths (eg. the NPBS in figure 4.18) and therefore the power balance after the PBS is an experimentally tuned parameter. Each beam is then coupled into separate single mode optical fibres.

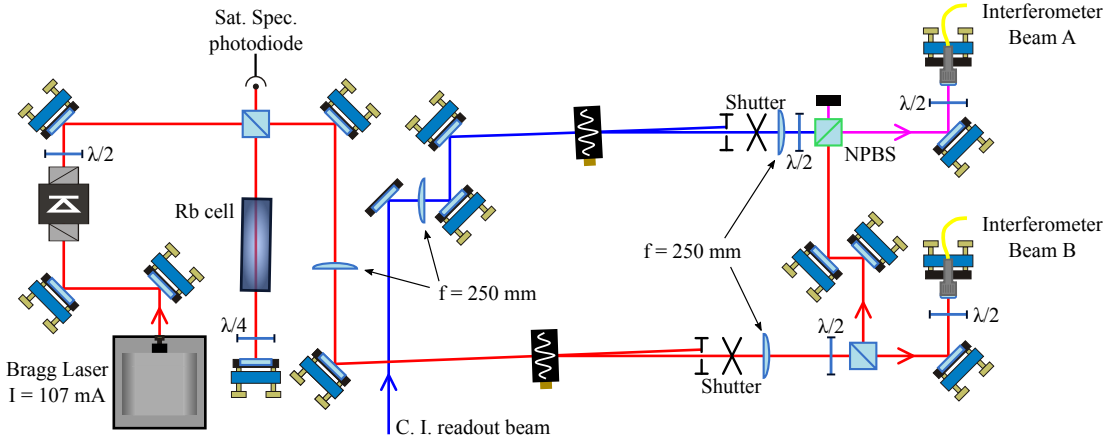


Figure 4.18: Schematic of interferometer laser setup. The red beam indicates the beams used for splitting and reflection pulses. The blue beam indicates the contrast interferometer probe beam which is drawn from the MOT cooling system and is mode matched into fibre A along with the interferometer beam A.

The aim is to spatially overlap the interferometer beams with the dipole trapping beams. This means that when we create a BEC, the interferometer beams are already

### 4.3. INTERFEROMETRY SETUP

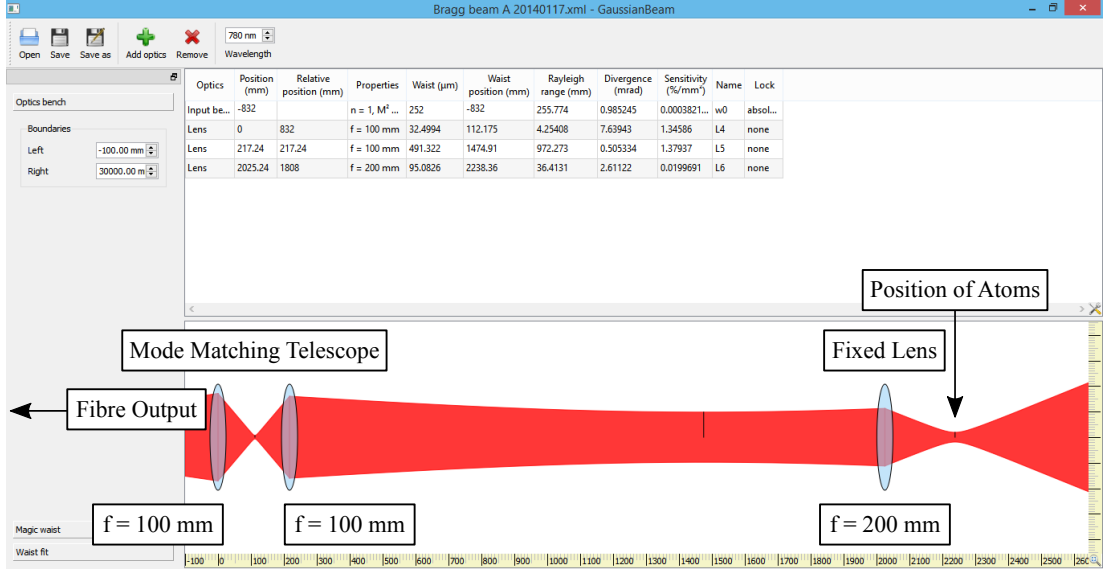


Figure 4.19: *GaussianBeam* program used in mode matching the interferometry beams to the dipole trapping beams. This example shows the predicted profile of beam A.

aligned with the atoms, and it also ensures that the interferometer beams pass through the copper ring. In addition, we want the focus of the interferometer beams to be at the position of the atoms such that the wavevectors of the beams are parallel. To do this we can use ABCD matrices to model the propagation of the beam (see eg. [139]), and do so via a freeware program called ‘*GaussianBeam*’ [140].

In order to model the interferometer beams, we first needed to profile the output of the optical fibres. The fibre of beam A is a Thorlabs PM306341 and the fibre of beam B is an Oz Optics PMJ-3A3A-780 and we use fibre collimation lenses at both fibre outputs. Profiling was done primarily with a CCD camera, providing the beam waist was significantly larger than the pixel size of  $5.5 \mu\text{m}$ . To measure the small beam waist ( $\approx 53 \mu\text{m}$ ) at the focus of the telescope, a knife edge measurement was used. A knife edge measurement was also used to confirm some of the CCD measurements to ensure accuracy.

From the beam profiling measurements we determine an  $M^2$  value of 1.05 for both beams A and B [141]. The final lenses, of focal lengths  $f=200 \text{ mm}$ , in the interferometer beam paths have a fixed position as they focus the dipole trapping beam. Therefore we use a telescope comprising two  $f=100 \text{ mm}$  lenses in each interferometer beam to set the waist size and position, as well as a long path length of  $\approx 3 \text{ m}$ .

The beam and lens parameters were used with *GaussianBeam* to determine the telescope lens position and path length for optimal spatial overlap with the dipole trapping beams at the position of the atoms (figure 4.19). The waist of the interferometer beams at the atoms is predicted to be  $95 \mu\text{m}$ . To overlap the interferometer beams with the dipole trapping beam a PBS was used in each arm (see figure 4.6). These are trans-

### 4.3. INTERFEROMETRY SETUP

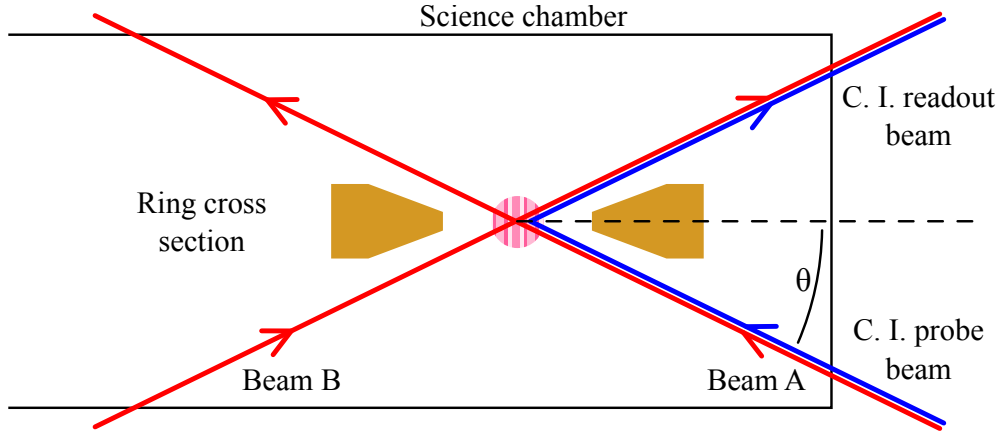


Figure 4.20: Top view cross section diagram of the copper ring and interferometer beams. Beam splitter and mirror pulses are applied with beams A and B (red). The contrast interferometer probe beam (blue) is applied via beam A only, and the Bragg reflection causes the signal to emerge along the path of beam B.

missive at 1070 nm and allow the dipole trap beam to pass through but are reflective to the 780 nm interferometer beams.

The interferometer beams are vertically polarised as they reach the science chamber. However the angle of incidence on the chamber is different for beams A and B (figure 4.20), therefore the fractional loss due to Fresnel reflections is different for each beam. Using a duplicate cell we measure a transmission of 96 % for beam A and 85 % for beam B. This difference in transmission is compensated for by the tuning the waveplate before the PBS that splits the single interferometer beam to balance the powers inside the chamber (figure 4.18).

We note that these measured transmission values differ from the theoretical values for beam A and B, which we calculate to be 95% and 78% respectively, assuming zero reflection from the air-glass interface due to the anti-reflection coating and a refractive index of 1.51 for the borosilicate glass. However, this is not of major concern as the optical lattice formed during our interferometer pulses does not require exact power balance.

#### 4.3.2 Optical Control of Interferometer Sequence

Most of the experiment timing is done by the computer with a time-step of 20  $\mu$ s, however this resolution is not sufficient for some of the stages. Therefore we use arbitrary function generators for stages requiring higher resolution. This includes the interferometer pulses sequences and timings.

The intensity control of the interferometer beams is crucial in our experiment. We use LabVIEW to trigger an SRS DS535 which in turn triggers an SRS DS345 signal generator which controls the voltage to an AOM driver circuit which in turn controls

### 4.3. INTERFEROMETRY SETUP

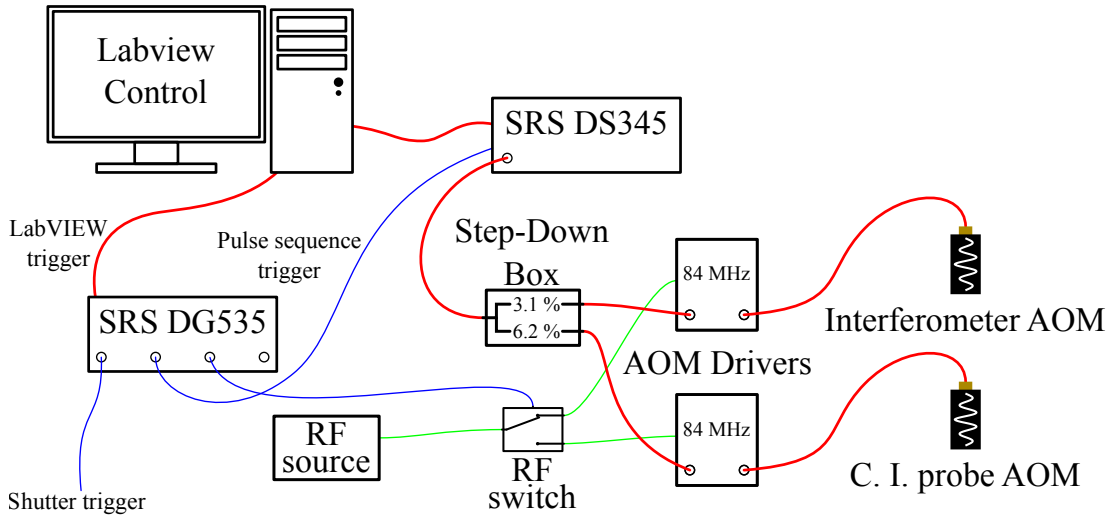


Figure 4.21: Schematic of optical control system. Red denotes pulse sequence path, blue denotes trigger signals, and green denotes RF signal path. The pulse sequence is generated by LabVIEW then sent to the arbitrary function generator (SRS DS345). The SRS DG535 timing box is triggered by the LabVIEW experiment control, and after opening the shutter it triggers the pulse sequence to be sent to the AOM via the AOM driver. The ‘step-down’ box reduces the voltage which gives us an effective increase in bit depth when specifying pulse amplitudes. The RF switch controls the path of the RF signal and effectively turns off the interferometer AOM and turns on the contrast interferometer probe AOM such that the remaining pulse sequence goes to this AOM.

the AOM. The SRS DG535 pulse delay generator, when triggered firstly opens the shutters that block the interferometer beams. Secondly it triggers the SRS DG345 arbitrary function generator that outputs a time varying voltage to drive the AOM via the driver circuit (appendix A.4). Lastly, it controls the timing of an RF switch used in contrast interferometry (see chapter 6). A schematic of this is given in figure 4.21.

We use a custom LabVIEW program to generate the pulse sequences required for interferometry (figure 4.22). This includes single and triple square pulses, and Blackman pulses. We can vary the timing and amplitudes of each pulse and can vary the duration between pulses. The SRS DS345 arbitrary function generator, to which we write our pulse train, has a maximum sampling frequency of 40 MHz and a maximum sample number of 16,299. For our high efficiency splitting pulses we use a resolution of  $0.1 \mu\text{s}$  and therefore use a sampling frequency of 10 MHz. For full interferometer sequences, specifically 3-arm interferometers, we find a resolution of  $1 \mu\text{s}$  is sufficient to give a good splitting pulse, and with a sampling frequency of 1 MHz, we can program longer interferometer sequences.

### 4.3. INTERFEROMETRY SETUP

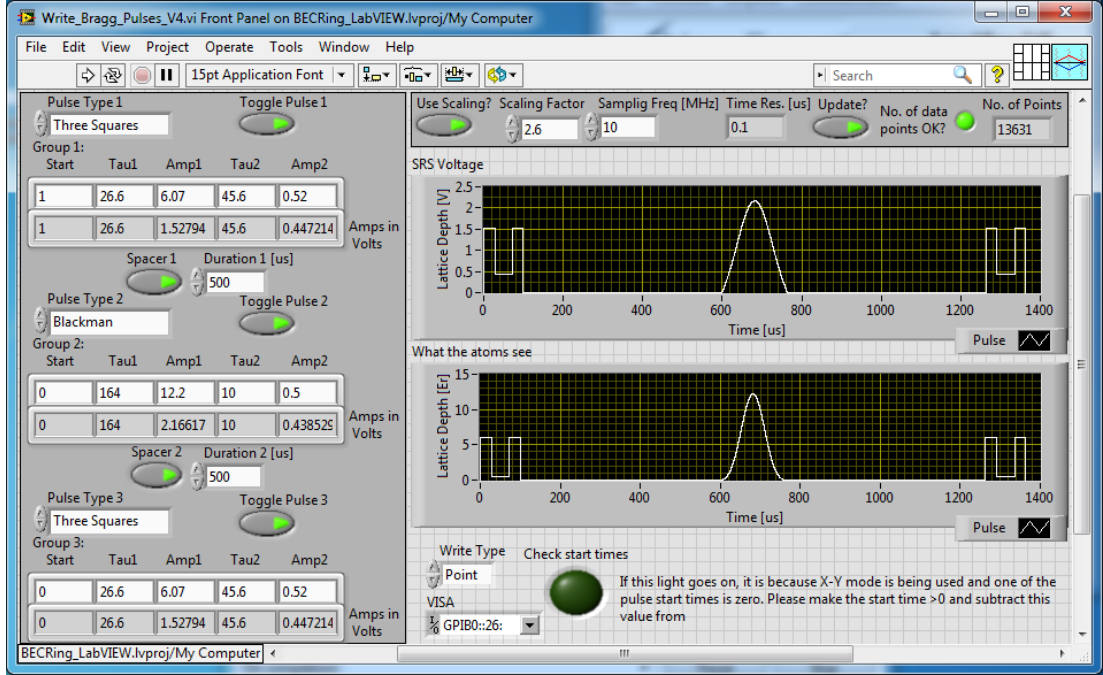


Figure 4.22: LabVIEW program GUI for writing interferometer pulses sequences to the Stanford Research Systems DS345 arbitrary function generator

Due to the finite bit-depth of the SRS DG345, it has a voltage resolution of 10 mV across the  $\pm 5$  V range. Since we operate the AOM at low voltages we don't require the full voltage range and it would be advantageous to have a higher voltage resolution, particularly for our highly tuned pulses. Therefore we use a potential divider to reduce the SRS voltage by a factor of 0.031 for the interferometer pulses and 0.062 for the contrast interferometer probe beam, which gives us an effective voltage resolution of 0.31 mV and 0.62 mV respectively.

Within the AOM driver circuit there is a double-balanced mixer that allows for the amplitude control of the 84 MHz output via a DC control voltage. In order to ensure that when we request zero amplitude (0 V from the SRS DG345) we do not have any residual 84 MHz signal coming from the AOM driver, we use a potentiometer to trim the output to zero by applying a small offset voltage to the input.

We introduce a 'scaling factor' which is a calibration between voltage output at the SRS and the optical lattice depth at the atoms. The AOM response is parabolic in the low power regime that we operate (figure 4.23) and therefore the scaling factor

$$\eta = \frac{V_0}{V_{\text{AOM}}^2}, \quad (4.8)$$

where  $V_0$  is the lattice depth and  $V_{\text{AOM}}$  is the voltage to the AOM driver. Note that the voltage offset has already been accounted for. The advantage of this system is that we can specify pulse amplitudes in units of recoil energies,  $E_{\text{r}}$ , which is a convenient unit

### 4.3. INTERFEROMETRY SETUP

---

of lattice depth. In order to calibrate the scaling factor we use a single square pulse and perform a sweep of either pulse amplitude (in Volts) or pulse duration and fit the model outlined in section 3.4 to the data [9]. The lattice depth calibration is outlined further in section 5.1.1 along with example data.

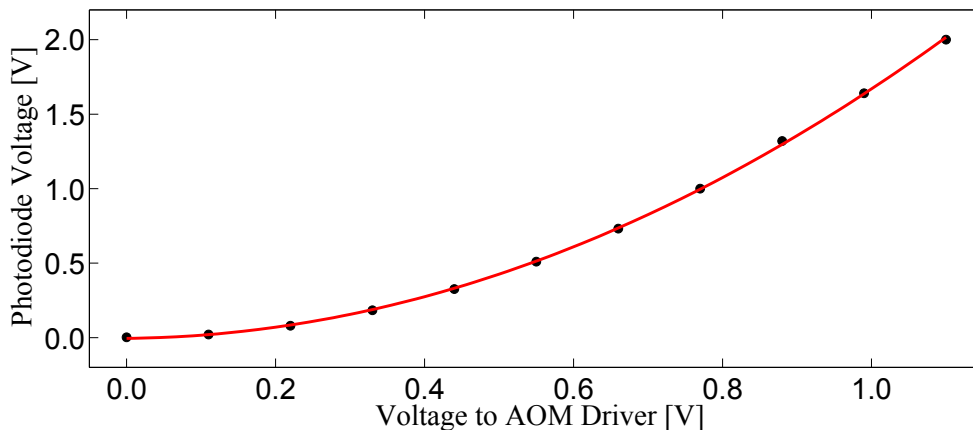


Figure 4.23: *The response curve of the AOM used for the control of the interferometer beams. Diffracted power was measured on a photodiode (Thorlabs PDA8A/M), and a the curve is a fitted parabola.*

Once we have generated our pulse sequence it is sent to the SRS DS345. The voltage output of this box is held at the starting value of the pulse sequence until triggered, at which point it outputs the entire sequence. The output is fed into a homemade AOM driver circuit (appendix A.4) which utilises an RF mixer (Minicircuits ZP-3LH-S+) and an RF source (Keysight N5138B) to convert the DC voltage to a change in amplitude of the 84 MHz output signal, which in turn gives a modulation in the optical power of the -1<sup>st</sup> diffracted order.

Figure 4.21 shows a single RF source driving both AOMs. This is because, in a previous version of our setup we used one AOM per interferometer beam and a single RF source allowed both AOMs to be phase locked. In the latest setup we found no reason to connect another RF source.

#### 4.3.3 Contrast Interferometer Probe Beam

A readout beam is required to probe our matter-wave grating to perform contrast interferometry. We derive this from the reject port of a PBS in our MOT cooling beam system (figure 4.5). This PBS is at the output of the TA and is used to clean the polarisation. The probe beam is then passed through an AOM operating at 84 MHz and the -1<sup>st</sup> diffracted order is then mode matched to interferometer beam ‘A’ before the optical fibre input (figure 4.18). Given that we typically apply a 20 G bias field during our interferometer sequence, the detunings of this probe beam are 238 MHz

### 4.3. INTERFEROMETRY SETUP

from the  $F = 2, m_F = 2 \rightarrow F' = 2, m_{F'} = 2$  transition and 505 MHz from the  $F = 2, m_F = 2 \rightarrow F' = 3, m_{F'} = 2$  transition.

We use the same LabVIEW program to control the readout AOM by using an RF switch to ‘redirect’ the 84 MHz RF signal to the readout AOM instead of the AOM used to control the splitting (and reflection) beams. The timing of the RF switch is controlled by the SRS DG535 timing box and is set to occur between the reflection and readout pulses (figure 4.21).

#### 4.3.4 Low Light Level Detection

In order to perform contrast interferometry, we need to detect the Bragg reflected light from the BEC which is very low in power ( $<100$  pW). We first used an avalanche photodiode (APD) to obtain a signal, and more recently have used a single photon counting module (SPCM). Data from both methods are reported in chapter 6. Another way to detect our signal would be to use a photomultiplier tube (PMT) [37, 142] which gives a high gain and bandwidth, however these are more expensive and are easily damaged.

The nature of the contrast interferometer scheme is such that if the matter wave grating is probed with beam A, the signal will be mode matched along the path of beam B (see figure 4.20). Therefore alignment of our APD (Hamamatsu C12703-01) is fairly straight forward. A PBS suited for 780 nm light is used to separate the signal beam from the optical dipole trap beam at 1070 nm; the 780 nm light is reflected whilst the 1070 nm is transmitted. To further reduce any stray 1070 nm light, a bandpass filter was placed in front of the APD. An aperture was placed in the beam to help eliminate stray light. The probe beam produced a reflection off the outer surface science chamber. This was approximately collinear with the signal beam but the aperture helped to reduce this offset signal as seen by the APD.

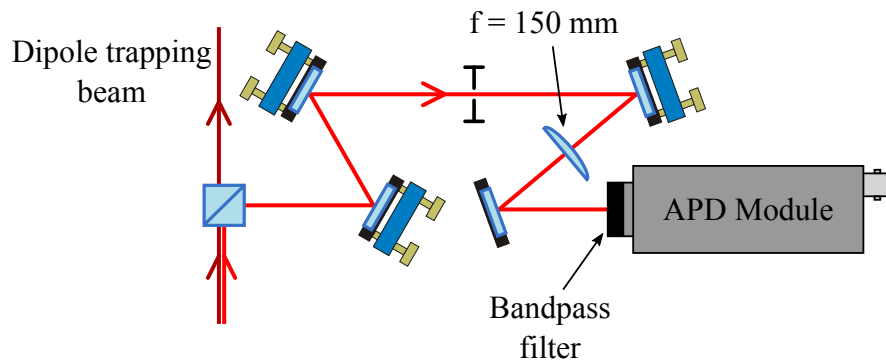


Figure 4.24: Schematic of APD signal acquisition setup. The PBS separates the signal from the optical dipole trapping beam. The aperture reduces the signal from stray light on the APD. A bandpass filter further reduces any light from the dipole trapping beam.

As will be outlined in section 6.2, the APD system has some limiting factors,

### 4.3. INTERFEROMETRY SETUP

mainly the bandwidth of 100 kHz and the low signal-to-noise ratio. Therefore, a single-photon counting module (SPCM) (Excelitas SPCM-AQRH-14-FC) was used as an upgrade to the APD as it has increased sensitivity as well as the ability to detect higher frequency signals. As shown in figure 4.25 the optics setup for this is slightly more complex than that of the APD. As before, a PBS and bandpass filter are used to separate the signal from the optical dipole trap beam. Due to the sensitivity of the SPCM, a protection shutter is kept closed until the probe beam is applied and we obtain our signal. Another protection shutter is used in beam B. This closes during the C. I. readout process and stops leakage light from the interferometry AOM travelling through beam path B and into the SPCM. Both these shutters are placed at a focus of the beams for fast switching times. We use Uniblitz LS2T2 shutters which give switching times of  $\approx 30 \mu\text{s}$ . The SPCM has a multimode fibre input to which we couple  $\approx 80\%$  of the signal.

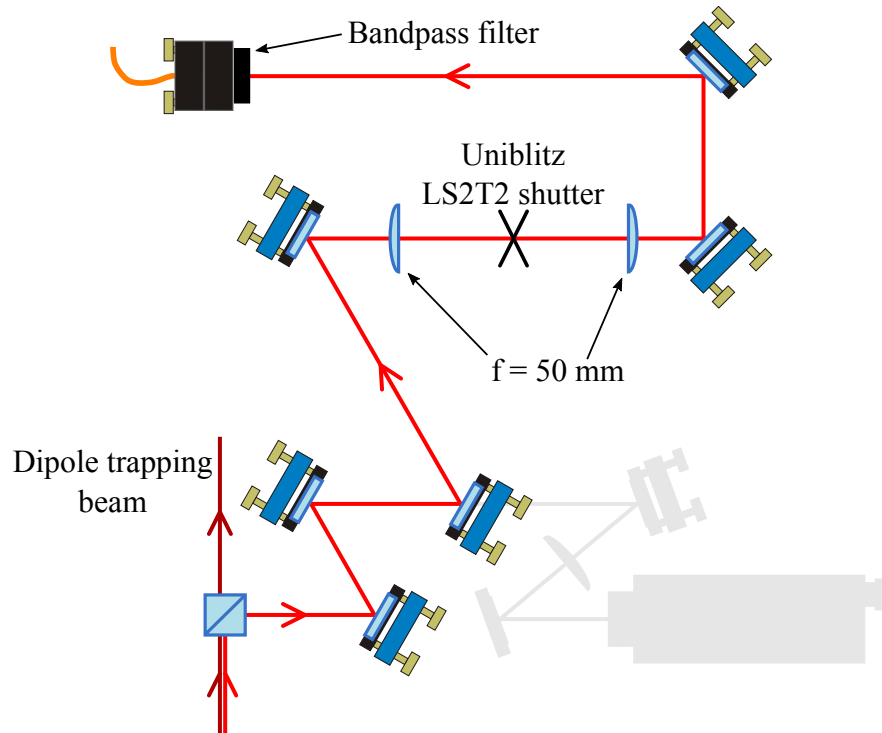


Figure 4.25: Schematic of SPCM signal acquisition setup. We remove the APD and replace it with an SPCM system. The beam is focused through a shutter to enable fast switching times. A bandpass filter further reduces any light from the dipole trapping beam.

## Chapter 5

# Interferometry in Free Space

Optical interferometers are widely used for precision measurements of rotation, distance, and recently gravitational waves [143]. Just as these systems exploit the wave nature of light, atom interferometers use the wave nature of matter to make measurements. In order to create the analogue of beam splitters and mirrors, pulses of light are used to coherently control the atoms. These pulses allow the atomic wavefunction to be split into different momentum states which then track out different spatial paths, thus making the interferometer sensitive to spatial variations in external fields and inertial forces.

In this chapter we demonstrate the coherent control of the momentum states of a BEC, and use these techniques to construct free space atom interferometers.

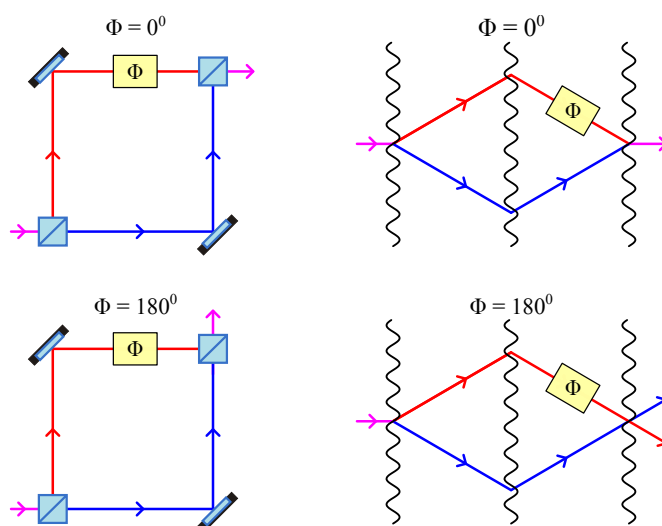


Figure 5.1: Analogy between an optical and an atom interferometer. Just as an optical interferometer (left) can return information about a phase difference  $\Phi$  introduced in one arm, so can an atom interferometer (right). This can be done by observing the relative momentum state populations after the closing pulse.

## 5.1 Optical Toolbox

All the splitting and mirror pulses are crafted using a standing wave of light that creates an optical lattice at the atoms. This then causes diffraction of the BEC into varying momentum states (see chapter 3). Figure 5.2 shows the resultant momentum states if a single strong pulse is applied. This is one of our first beam splitters and the uncalibrated pulse excited many modes and is somewhat uncontrolled. However, it would be good to be able to closely control which momentum states are populated and the relative populations of the states in order to perform interferometry. By careful application of the optical lattice we can achieve the coherent control of the diffraction and target specific momentum states. In this section we explain and demonstrate this control.

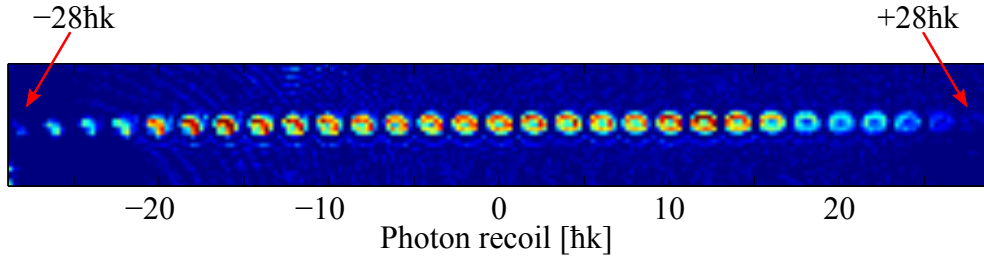


Figure 5.2: An early example of an attempt at splitting the BEC. A single intense pulse is used to Bragg diffract the BEC into many momentum states up to  $28\hbar k$ . Note that the apparent ring shape of the different momentum states is due to lensing of the imaging light as a result of the high atomic density.

### 5.1.1 Lattice Depth Calibration

The optical lattice is applied in pulses and a convenient unit of amplitude is recoil energies  $E_r$ . This is a measure of the optical lattice potential the two interferometer beams make. By using this metric, the pulse parameters are directly transferable to other atomic species.

To generate the optical pulses needed to manipulate the atoms, we use an AOM driven by an arbitrary function generator. Since the response of the AOM is parabolic in the low voltage regime that we operate (figure 4.23), it is possible to convert volts into lattice depth via equation 4.8.

To calibrate this scaling factor we apply a single square pulse of  $20\ \mu\text{s}$  duration and vary the amplitude. The absorption images of the resultant  $0\hbar k$ ,  $\pm 2\hbar k$  and  $\pm 4\hbar k$  modes then give us the fractional populations<sup>1</sup>. We then plot the fractional population as a function of pulse amplitude squared (since the AOM response is squared). Since we also know the predicted mode evolution from our model discussed in section 3.4, we rescale voltage to trap depth and extract the scaling factor,  $\eta$ , from the fitted curve. An example of such a data run is shown in figure 5.3. With the known calibration

<sup>1</sup>The analysis code actually includes up to  $\pm 12\hbar k$  modes

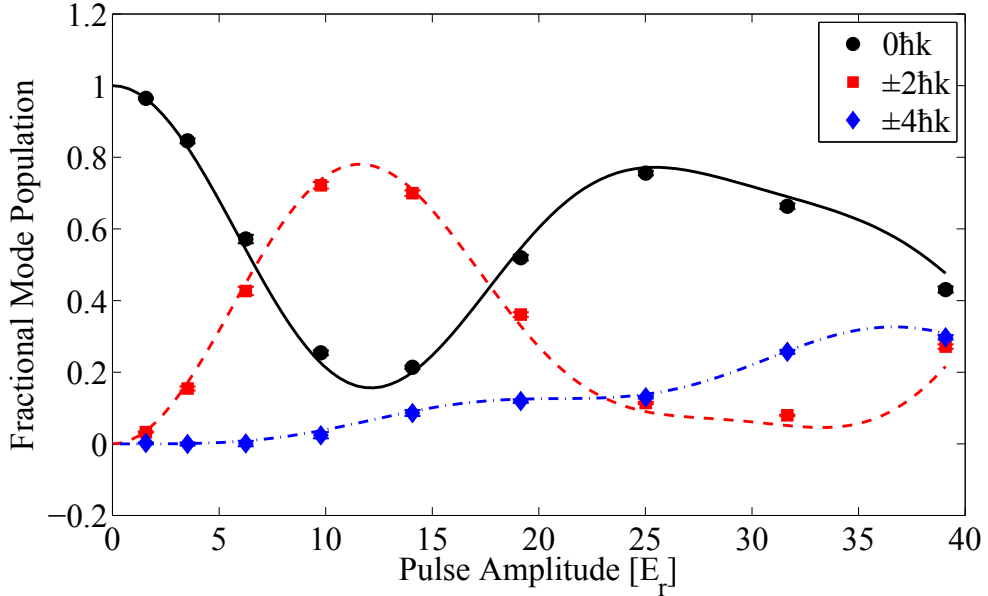


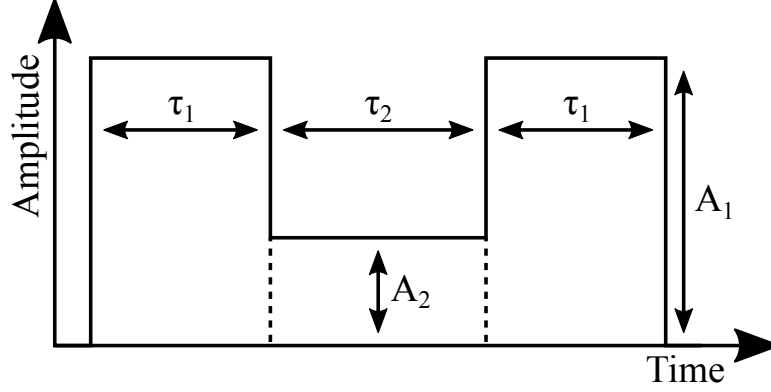
Figure 5.3: An example of how we calibrate the scaling between AOM driver voltage and lattice depth. A square pulse of  $20 \mu\text{s}$  duration and varying amplitude is applied. Equation 3.11 is fitted to the data and the pulse voltage is rescaled to lattice depth. From this we extract the fitted scaling parameter  $\eta$ .

between voltage and lattice depth we can then input all our pulse parameters in terms of lattice depth.

We find that the optical power of the interferometer beams can drift day-to-day, and therefore performing these scaling factor measurements are more reliable than using a look-up table of measured optical powers for given voltages. Moreover, this method uses the atoms as the diagnostic and as such it is a more direct measurement of lattice depth than a look-up table of inferred values calculated from measured powers.

### 5.1.2 First Order Atomic Beam Splitters

In optics, a beam splitter would split the incoming light into 2 arms. The atomic analogue is what we demonstrate here, where we perform the operation  $|0\hbar k\rangle \rightarrow |\pm 2\hbar k\rangle$ . We refer to this as our  $\pm 2\hbar k$  splitter. Using our model (see section 3.4) we predict an optimum pulse to give us a high efficiency split [9]. This composite pulse is of the form shown in figure 5.4 with values  $\tau_1 = 26.6 \mu\text{s}$ ,  $A_1 = 6.07 E_r$ ,  $\tau_2 = 45.6 \mu\text{s}$  and  $A_2 = 0.52 E_r$ . We then experimentally test the accuracy of our prediction.

Figure 5.4: *Composite splitting pulse.*

We create a BEC and following release from the dipole trap we allow 2 ms for mean field expansion during which we apply a magnetic levitation field. We then apply the splitting pulses with the levitation field on. After a further 64 ms time of flight to allow the different momentum states to spatially separate, we use absorption imaging to image the atoms (inset of figure 5.5). During the first 60 ms we apply a levitation field to cancel out the force of gravity and during the final 4 ms we align the magnetic field for absorption imaging. We then create an integrated line profile and fit Thomas-Fermi profiles to the  $|0, \pm 2\hbar k\rangle$  states plus a Gaussian to the original BEC position to account for thermal atoms that have not been split (figure 5.5). The width of the Gaussian,  $\sigma$ , is fixed and is determined from A.5

$$\sigma(t) = \sqrt{\frac{2k_B T}{m}t} + \sigma_0, \quad (5.1)$$

where the temperature,  $T$ , is an estimated 50 nK,  $m$  is the atomic mass,  $t$  is the expansion time, and the initial width,  $\sigma_0$ , is the Thomas-Fermi radius which we estimate to be 15  $\mu\text{m}$ . From the fitted profile we extract the fractional population of each momentum state.

Figure 5.5 shows the final momentum state populations and demonstrates our ability to perform a highly efficient  $\pm 2\hbar k$  splitter. These data return a split efficiency of  $99.97 \pm 0.03\%$ .

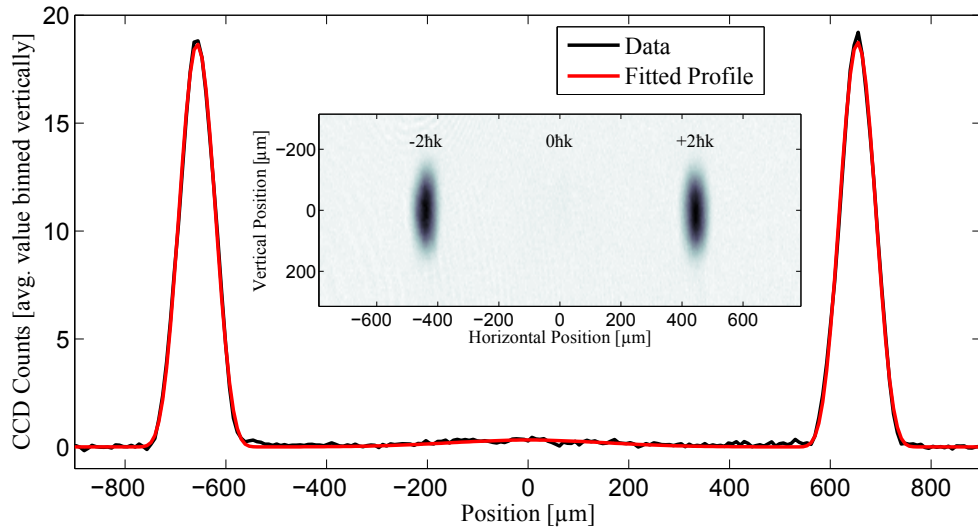


Figure 5.5: *Integrated profile of absorption image of BEC after  $\pm 2\hbar k$  splitting pulse. From the fitted Thomas-Fermi profiles, we infer the split efficiency of  $99.97 \pm 0.03$  %. Inset: absorption image of BEC after  $\pm 2\hbar k$  splitting pulse.*

To further test the accuracy of the model, we apply the above  $\pm 2\hbar k$  splitting pulse but cut it short such that we can track the evolution of the momentum states through the pulse. These data are shown in figure 5.6 where the lines are the *predicted* state evolutions for the given pulse parameters. We emphasise that the curves are not fitted to the data.

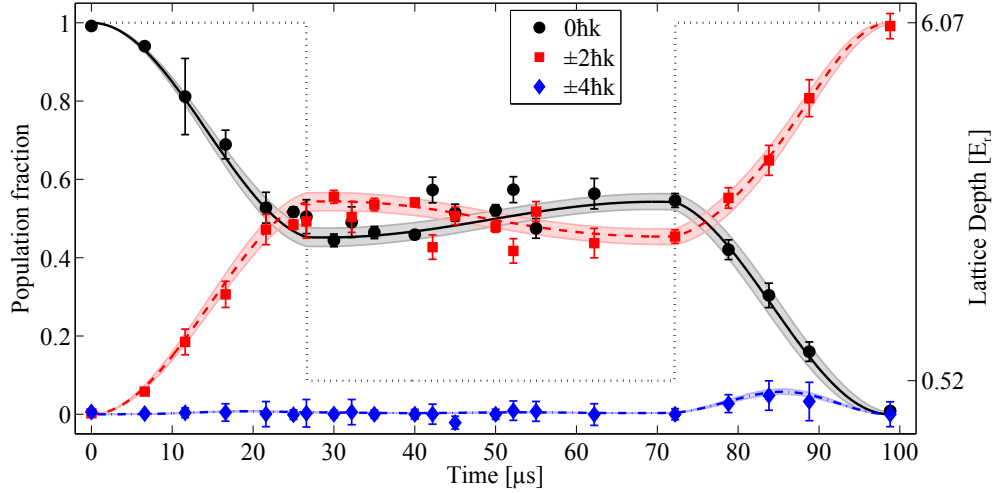


Figure 5.6: Evolution of momentum states through a  $\pm 2\hbar k$  splitting pulse. The curves are the predicted state evolutions generated by numerical simulation for the optimum pulses parameters. Shading around these lines are the 4% error bands which we estimate to be the level of error in our experiment. The black dashed line indicates the timing and amplitude of the splitting pulse.

### 5.1.3 Second Order Atomic Beam Splitters

We also investigate a second order beam splitter. Higher order momentum states offer increased sensitivity to the photon recoil frequency  $\omega_r$  which is attractive when measuring the fine-structure constant. Since the scaling goes as  $k^2$ , an interferometer using the  $\pm 4\hbar k$  momentum states offers 4x the sensitivity of an interferometer using the  $\pm 2\hbar k$  states.

The simulated pulse parameters of  $\tau_1 = 53.3 \mu\text{s}$ ,  $A_1 = 23.7 E_r$ ,  $\tau_2 = 39.0 \mu\text{s}$  and  $A_2 = 3.59 E_r$  predict an efficiency of 99.30 %. This is tested in figure 5.7 using the same method as section 5.1.2. The width of the central Gaussian is fixed, and determined using equation 5.1. From these data we obtain a split efficiency of  $88 \pm 4 \%$ .

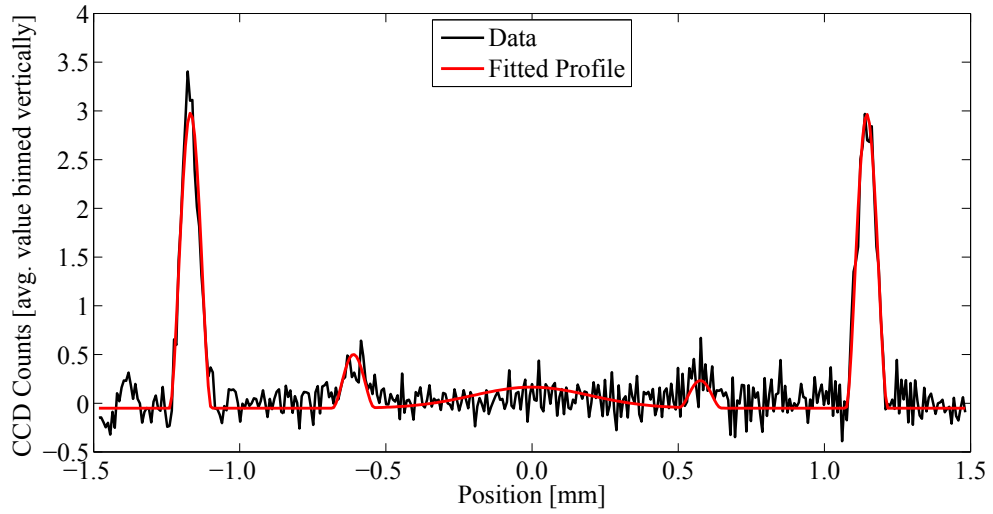


Figure 5.7: *Integrated profile of absorption image of BEC after  $\pm 4\hbar k$  splitting pulse. From the fitted Thomas-Fermi profiles, we infer the split efficiency of  $88 \pm 4$  %.*

We also track the mode populations through the optimised pulse and show the data in figure 5.8. This shows an excellent agreement with the model despite the highly non-trivial evolution of the modes. Again, we emphasise that the curves are not fitted to the data.

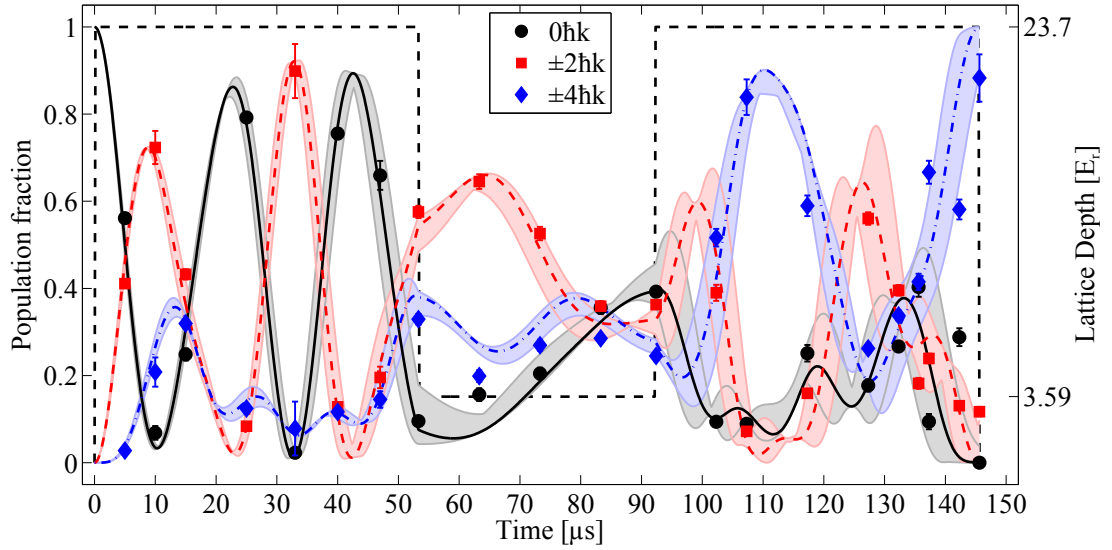


Figure 5.8: *Evolution of momentum states through a  $\pm 4\hbar k$  splitting pulse. The final data point gives a splitting efficiency of  $88 \pm 4$  %. The curves are the predicted state evolutions generated by numerical simulation for the optimum pulses parameters. The shading around these lines are the 4% error bands which we estimate to be the level of error in our experiment. The black dashed line indicates the timing and amplitude of the splitting pulse.*

The dynamics of this pulse are a lot faster than the  $\pm 2\hbar k$  splitting pulse. This is due to the higher intensity pulses and therefore deeper optical lattice potential. As a result, higher order pulses are more susceptible to noise in the system. The main source of noise in our system is laser intensity noise at the atoms.

#### 5.1.4 Atomic Mirrors

Having demonstrated efficient beam splitters, it is now necessary to perform ‘mirror’ pulses to reverse the momentum states in order to close the interferometer. Characterising our mirror pulses is more difficult than characterising our splitting pulses. The reason for this is that we would typically perform a reflection after  $\approx 1$  ms, at which time the different momentum states aren’t spatially separated much ( $\approx 10$   $\mu\text{m}$  for  $\pm 2\hbar k$ ). If we then image the atoms we cannot distinguish which atoms were reflected from  $+2\hbar k$  to  $-2\hbar k$  and which atoms were always in the  $-2\hbar k$  state. A workaround for this is to increase the time between the split and reflection pulses, and we find that we can distinguish the reflected and non-reflected atoms after 4.5 ms. An example of an integrated line profile fit to an absorption image is shown in figure 5.9. However this introduces some issues, including whether or not the atoms remain in the centre of the interferometer beams, which have a waist of 95  $\mu\text{m}$ .

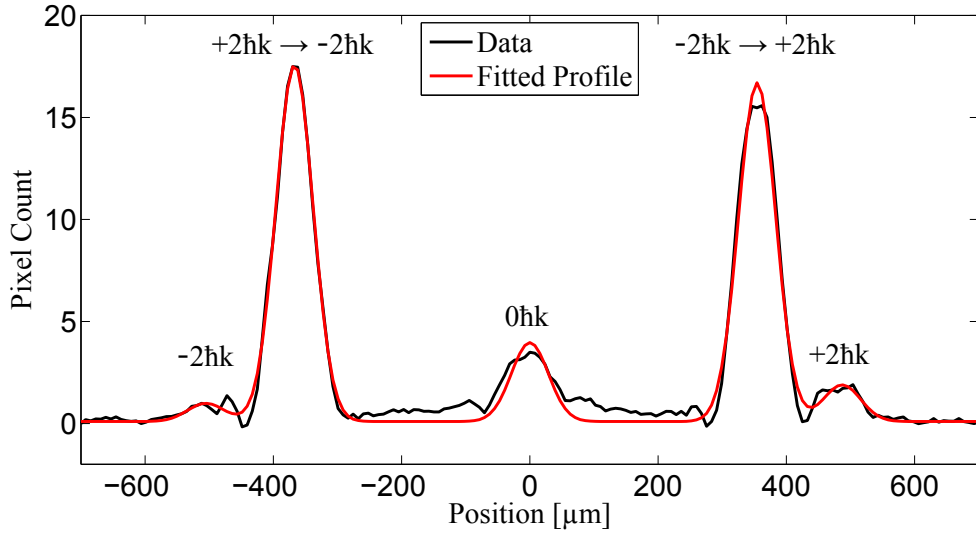


Figure 5.9: Measurement of reflection efficiency. We Split the BEC such that there is a significant fraction of the atoms in the  $\pm 2\hbar k$  state then after 4.5 ms we perform a mirror pulse. From the Gaussian fits to the reflected and unreflected atoms we infer reflection efficiency. Note: the fit to the central mode is unused in the calculation.

We nonetheless attempt to characterise the mirror pulse, and the results show reasonably good agreement with our model. We create our BEC and after 2 ms of free expansion we apply a pulse to excite the  $\pm 2\hbar k$  modes. After 4.5 ms we apply a reflection pulse, then image the atoms after some time of flight. A levitation field is applied from the creation of the BEC until the end of the pulses which cancels the force of gravity thus keeping the atoms in the interferometer beam region. We apply our mirror pulse in the form of a Blackman (see section 3.4) pulse, and vary either duration or amplitude. Integrated profiles of the absorption images (eg. figure 5.9) allow us to determine the fractional population of each state. We then fit our model to these data with pulse amplitude as the fit parameter.

The reflection parameters, duration and amplitude, can be pictured as lying on a two dimensional parameter space. To test the model we perform parameter scans in the form of straight lines through the parameter space, varying either pulse duration or amplitude. It is not necessary to scan through the optimum point to test the model, and therefore in figure 5.10 we apply a mirror pulse with an *approximate* amplitude of  $12.2 E_r$  (the predicted optimum). The duration of this pulse is then scanned and the mode populations plotted. Since we know the pulse duration for each point, we fit our model with pulse amplitude as the free parameter and in this instance we fit an amplitude of  $13.03 \pm 0.06 E_r$ .

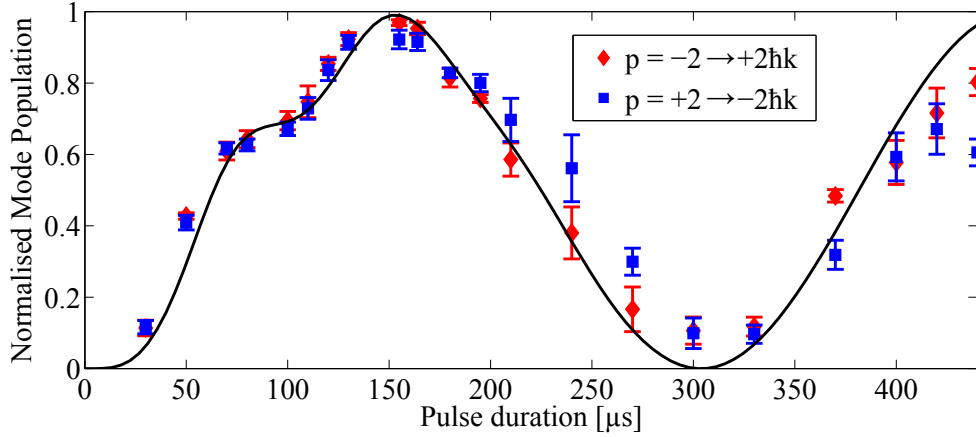


Figure 5.10: We excite  $\pm 2\hbar k$  momentum states of the BEC then apply a Blackman pulse of approximately  $12.2 E_r$  in amplitude with variable duration after 4.5 ms. We then fit our model to the data with the pulse amplitude as the free parameter. The fitted pulse amplitude is  $13.03 \pm 0.06 E_r$ .

Figure 5.11 shows data from a similar experiment but this time the pulse amplitude is scanned. We apply pulses of the predicted optimum pulse duration of  $164 \mu\text{s}$ . The pulse amplitude, with a fixed estimate of the scaling factor, is then varied and mode populations determined. By fitting our model we effectively determine the actual scaling factor, which in this instance we determine to be  $\eta = 34.83 \pm 0.18$ . This method is essentially the same as the lattice depth calibration method outlined in section 5.1.1.

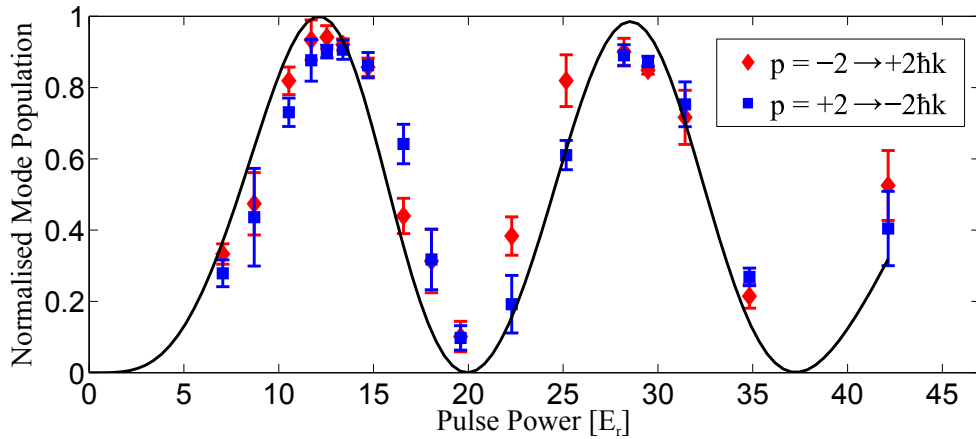


Figure 5.11: We split the BEC into the  $\pm 2\hbar k$  momentum states then apply a Blackman pulse of  $164 \mu\text{s}$  in duration and vary the pulse amplitude with an approximate, but fixed, voltage to lattice scaling factor. We then fit the data with our model with the scaling factor as a free parameter. The fit returns a scaling factor of  $34.83 \pm 0.18$ . The fitting can be regarded as the scaling of the x axis to get the best fit.

Another method of estimating the efficiency of our mirror pulse is to perform a full 3-arm interferometer sequence and infer efficiency from the contrast of the output signal. The BEC is split into a 25%, 50%, 25% superposition of the  $-2\hbar k$ ,  $0\hbar k$ , and  $+2\hbar k$  modes. After  $T_1=700 \mu\text{s}$ , the  $|\pm 2\hbar k\rangle$  are reflected using a mirror pulse and the splitting pulse is then applied to close the interferometer. The time at which the closing pulse is applied is varied and the resultant populations plotted in figure 5.12. A perfect 3-arm interferometer, with a perfect reflection, would output a maximum fractional population in the  $|0\hbar k\rangle$  of 1, and a maximum contrast of 100%. Therefore we attribute any less than this to a reduction in reflection efficiency. From these data, a lower limit on the reflection efficiency is determined to be 86%, which is calculated from the maximum - minimum of the data.

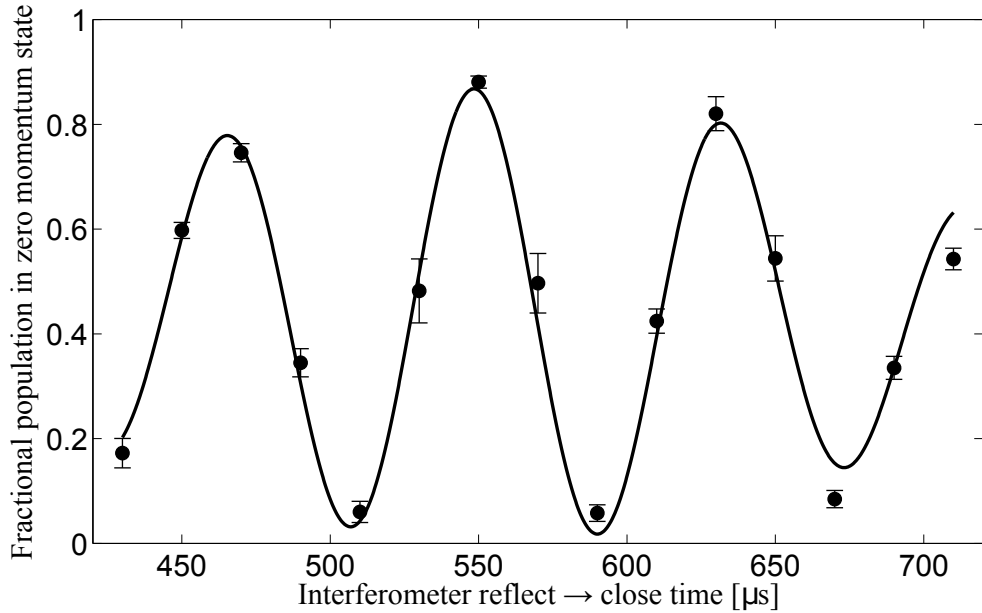


Figure 5.12: We perform a 3-arm interferometer pulse sequence using the predicted optimum mirror pulse with an 'arm length' of  $T_1=700 \mu\text{s}$ . We place a lower limit on our reflection efficiency of 86 % by maximum - minimum of the data

### 5.1.5 Efficiency and Limitations

An important consideration regarding high efficiency splitting, as well as full interferometer sequences, is the wavevectors of the laser beams creating the optical lattice. Ideally the wavevectors across the beam waist would be parallel; the phase fronts at the position of the atoms would be parallel and orthogonal to the direction of beam propagation. This occurs in a collimated beam (approximately) or at a focus. It is at a focus that we perform our atom optics.

In our model we assume that the atoms are at the focus such that the wavevectors are parallel. Experimentally this is difficult to prove, and a lot of effort has been made

to get the focus position as close as possible to the atoms. However, even if the focus was in the exact position, the angle of the interferometry beams means that across the BEC the wavevectors change slightly. Since the beams are angled at  $26^\circ$  to the X axis, a position change in the Y axis of say  $10\ \mu\text{m}$  is equivalent to moving out of the focal plane of the interferometer beams by  $4.4\ \mu\text{m}$ .

### 5.1.6 Higher Order Splitting

We have demonstrated high efficiency splitting pulses for  $|\pm 2\hbar k\rangle$  and  $|\pm 4\hbar k\rangle$  momentum states. In principle, pulses that can efficiently split a BEC into higher orders is also possible. This, however, would require excellent laser intensity control and pulse timing as well as potentially more complex pulse shapes. In addition very well defined wavevectors are also needed.

In our case the main limiting factor is laser intensity, for which the r.m.s. variation is measured to be  $0.4\%$  with a range of  $2\%$ . To put things in perspective, we can still achieve a  $98\%$  efficient split into the  $|\pm 2\hbar k\rangle$  with a  $\pm 10\%$  lattice depth variation, while for the  $|\pm 4\hbar k\rangle$  split a variation of only  $1\%$  is acceptable. A  $|\pm 6\hbar k\rangle$  would require lattice depth control of  $\pm 0.5\%$ , and this becomes even smaller for higher orders. Note that we make some assumptions here such as perfect pulse timings and arbitrarily well defined wavevectors. We also do not include mean field and density effects, which are currently under investigation.

We are optimistic that with better laser control and more constraints on system parameters, it would be possible to demonstrate higher order splitting and arbitrary state population, although this would likely require more complex pulse shapes. For example, we predict an efficiency of  $\sim 60\%$  if we target the  $|\pm 6\hbar k\rangle$  state using a pulse comprising three squares such as those demonstrated in this chapter. By comparison, our simulation predicts an efficiency of  $\gtrsim 90\%$  if we use a pulse comprising five squares.

## 5.2 Two-Arm Interferometer

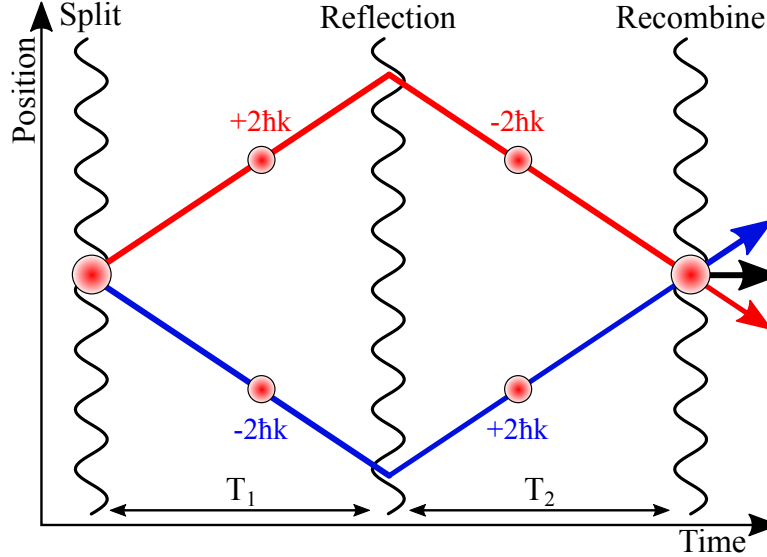


Figure 5.13: *Two arm interferometer scheme.*

As shown in section 5.1, we can split the BEC into  $|\pm 2\hbar k\rangle$  with very high efficiency. We have also demonstrated mirror pulses to reflect the atoms. This allows us to perform a simple Mach-Zehnder type interferometer (figure 5.13). In a perfect experiment, free from noise, the recombining pulse would cause all the atoms to return to the  $|0\hbar k\rangle$  state (see section 3.5). Indeed, in figure 5.14 we show that this is the case, albeit with reduced efficiency due to experimental noise and reflection pulses that are less than 100% efficient.

We create a BEC and apply our optimised splitting and reflection pulses. For the duration of the interferometer we apply a levitation field to cancel out the acceleration due to gravity. This prevents the atoms from falling out of the atom-light interaction region. Figure 5.14 shows the fractional central mode population as a function of interferometer duration. The observation of a constant central population fraction indicates that the interferometer has no inherent bias and importantly shows no oscillations, which makes it a good measurement device. The data points settle at 0.69 which is attributed to the efficiency of the reflection pulses and experimental noise; in this case there was a slight asymmetry in the mode populations which was attributed to a residual velocity.

The maximum interferometer duration tested here is 8 ms. The maximum possible time is limited by the size of the interferometer beams; when the atoms are split they begin to travel outwards and out of the interferometer region, therefore if the interferometer duration is increased sufficiently, it is possible that the atoms will have left the beams before the reflection pulses are applied.

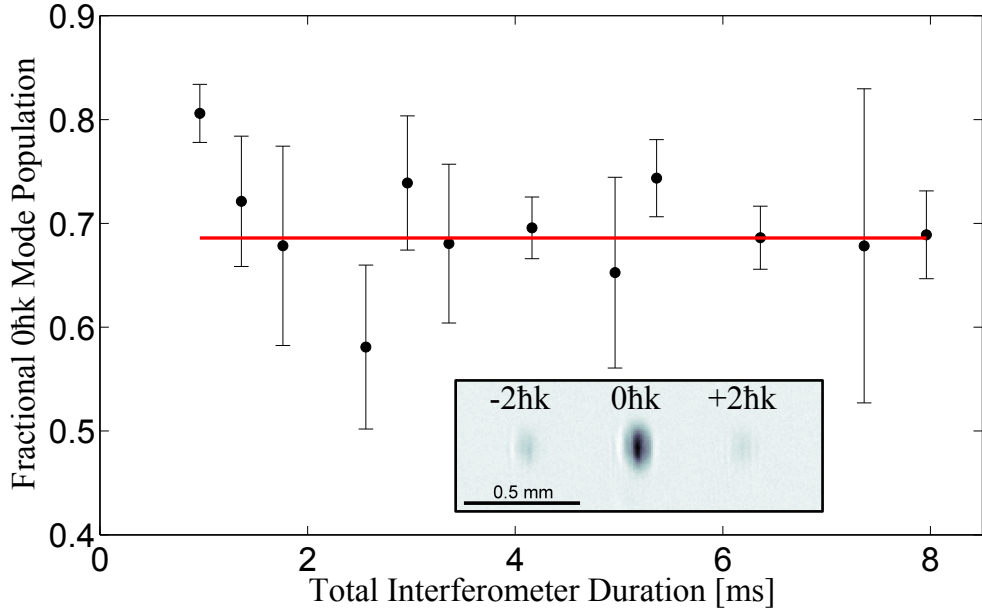


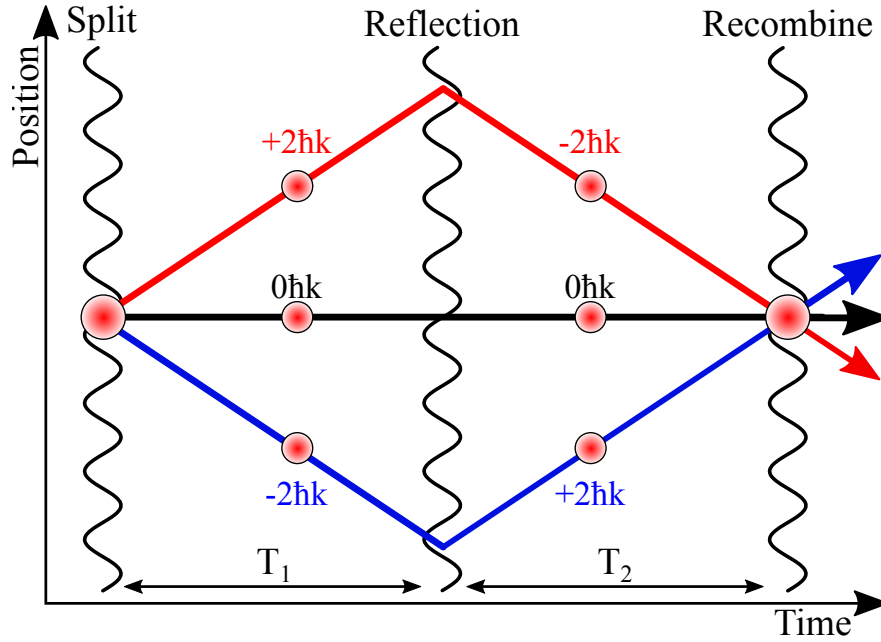
Figure 5.14: We perform a two arm interferometer for varying durations. The relative populations are determined by analysis of absorption images taken after the interferometer sequence (see inset). We fit a horizontal straight line of 0.69 to all but the left-most data point.

### 5.3 Three-Arm Interferometer

The two-arm Mach-Zehnder interferometer scheme does not allow for the measurement of the recoil frequency  $\omega_r$  (see section 3.5). In order to get this information from the system we add a third arm in the form of the  $|0\hbar k\rangle$  state (figure 5.15). This gives the two outer arms a stationary phase reference to which they ‘beat’ against. If only the  $|\pm 2\hbar k\rangle$  state are present, their phases evolve together (assuming no external influences). When they are recombined their phases always ‘match’ so the frequency does not manifest itself in the output. By adding the third arm as a reference, the relative phases between the  $|0\hbar k\rangle$  state and the  $|\pm 2\hbar k\rangle$  states vary as a function of time and this results in a frequency at the output. This frequency is  $4\omega_r$ , where the factor of 4 is a result of the  $p^2$  scaling of energy on the dispersion curve:

$$E = \hbar\omega_r = \frac{p^2}{2m} = \frac{(2\hbar k)^2}{2m}. \quad (5.2)$$

We perform the 3-arm interferometer as described in section 3.5.1 and make a measurement of the recoil frequency. We split the BEC into thirds ( $\sim 33\%$  in  $|+2,0,-2\hbar k\rangle$ ); a superposition of 25%, 50%, 25% in the  $-2\hbar k$ ,  $0\hbar k$ , and  $+2\hbar k$  modes is predicted to be the optimum but we deliberately overpopulate the  $\pm 2\hbar k$  modes to account for the less than perfect reflection pulse discussed in section 5.1.4. A single square pulse of

Figure 5.15: *Three arm interferometer scheme.*

$30 \mu\text{s}$  and amplitude  $\sim 8 E_r$  is typical, although other pulse parameters are also sufficient such as shorter pulses of increased amplitude. We then let the system evolve for some time  $T_1$  before applying a mirror pulse. The system is allowed to evolve further and we vary the timing of the recombination pulse. An absorption image is recorded and the populations of the momentum states determined by fitting Gaussians to the integrated line profiles

Figure 5.16 shows an example of a typical interferometer data set with  $T_1=1 \text{ ms}$ , to which we fit a sine curve with a Gaussian envelope to account for the wave-packets travelling through each other. The point of maximum overlap of the wave-packets is at approximately the symmetrical interferometer time<sup>2</sup>. The decay of the signal either side of this is due to the wave-packets only being partially overlapped, thus the width of the signal is given by the width and velocity of the wave-packet.

A frequency of  $12.18 \pm 0.04 \text{ kHz}$  is fitted to these data, which corresponds to a recoil frequency of  $3.77 \pm 0.6 \text{ kHz}$ , given an uncertainty in the beam angle of  $0.5^\circ$ . This gives a  $h/m$  value of  $4.6 \pm 0.7 \times 10^{-9} \text{ m}^2 \text{ s}^{-1}$  from equation 1.9 and  $\alpha^{-1} = 137 \pm 10$  from equation 1.8 (see also appendix A.6). From the CODATA database,  $\alpha^{-1} = 137.035999139(31)$  [81].

The main source of uncertainty in our measurement is the angle of the interferometer beams. As explained in section 4.3, the beams are angled in order to align with the copper ring used for our inductive ring trap. This angle is measured to be  $26.0 \pm 0.5^\circ$  relative to the plane of the copper ring, which gives a corresponding error in  $k$  of  $0.4 \%$ .

<sup>2</sup>The wave-packets may not be ‘perfectly’ overlapped at the symmetrical interferometer time due to mean-field interactions [88]

In future, the plan is to set the beams to be counter propagating. This is expected to greatly reduce the uncertainty in the measurement of the recoil frequency.

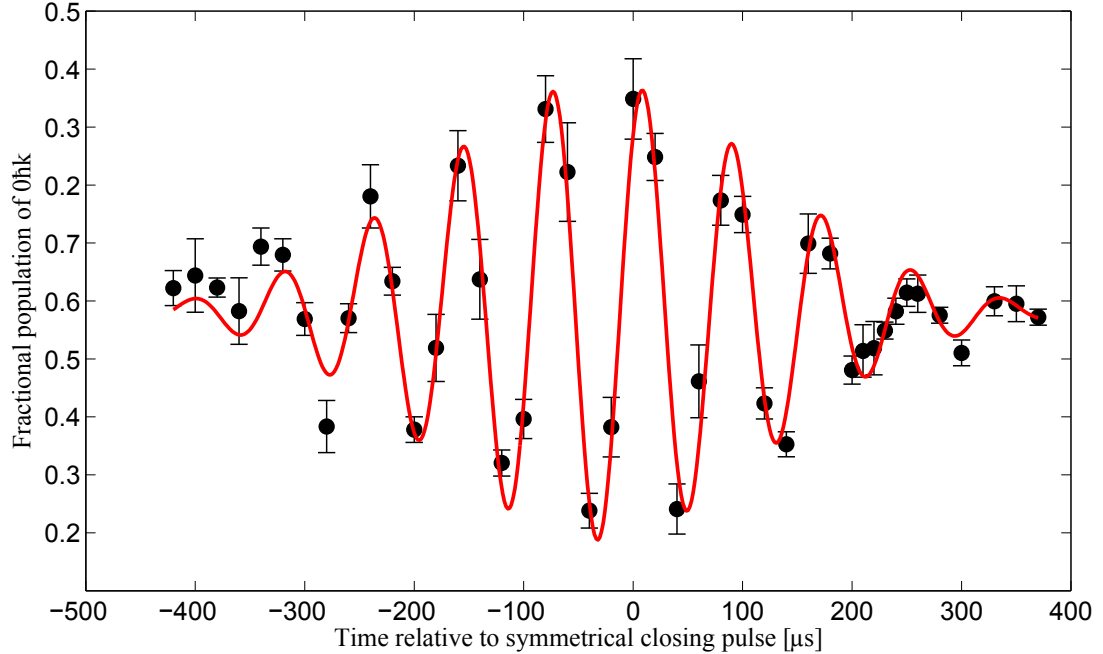


Figure 5.16: *Three arm interferometer with  $T_1 = 1$  ms. The  $|0\hbar k\rangle$  acts as a phase reference and the output frequency contains the recoil frequency. We fit a sine curve of frequency  $12.18 \pm 0.04$  kHz with a Gaussian envelope from which we determine the value of the fine-structure constant to be  $\alpha^{-1} = 137 \pm 10$ .*

## 5.4 Magnetic Gradiometry

An advantage to using atoms over photons is their sensitivity to magnetic fields, which will be harnessed in this section. We install a coil of wire in the Y-Z plane at the end of the glass science chamber. It is constructed from enamelled cooper wire with 5 turns and 2.5 cm in diameter. When a current is passed through the coil, a magnetic field gradient is produced inside the chamber and the positioning is such that the interferometer operates parallel to the axial magnetic field gradient to give maximum sensitivity.

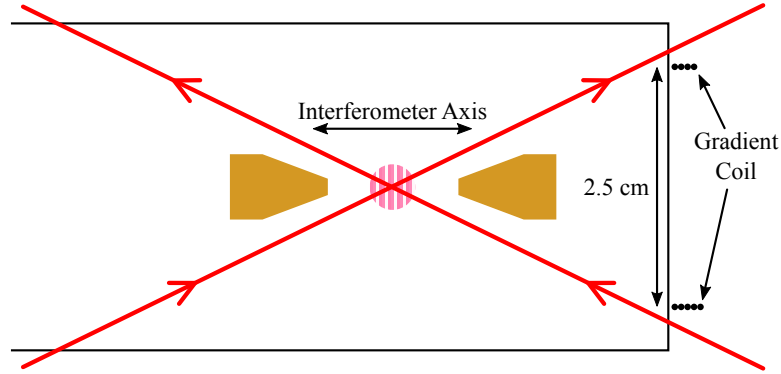


Figure 5.17: Diagram of the gradient coil positioned at the end of the science chamber in the  $Y$ - $Z$  plane such that the generated magnetic field gradient is perpendicular to the interferometer axis.

We first calculate what the expected phase shift is as a result of a gradient field. The potential energy  $U_B$  from a magnetic field is given by

$$U_B = g_F m_F \mu_B \left| \vec{\mathbf{B}}(x) \right| , \quad (5.3)$$

where  $g_F$  is the Landé  $g$ -factor,  $m_F$  is the magnetic sub-level of the atoms, and  $\mu_B$  is Bohr magneton. The phase accumulation over time  $T$ , resulting from the magnetic field gradient, can be written as [18]

$$\phi(x, t) = \int_0^T \frac{U_B(x)}{\hbar} dt , \quad (5.4a)$$

$$= \frac{g_F m_F \mu_B}{\hbar} \int_0^T \left| \vec{\mathbf{B}}(x) \right| dt . \quad (5.4b)$$

The atoms are moving in the field,  $\left| \vec{\mathbf{B}}(x) \right| = \frac{dB}{dx} vt + B_0$ , where  $v$  is the velocity of the atoms,  $t$  is the time spent in the gradient field, and  $B_0$  is the magnetic field at the initial position, and therefore

$$\phi(t) = \frac{g_F m_F \mu_B}{\hbar} \frac{vt^2}{2} \frac{dB}{dx} + B_0 t . \quad (5.5)$$

This can be thought of as the phase accumulation for one wave-packet travelling out to a point in space and the sign of the phase is determined by the direction of the gradient field.

During our interferometer sequence we apply a levitation field. This is produced by our QP coils and a large bias field. As a result the magnetic field the atoms probe is a little more complex than a simple gradient field. To get an appreciation for what's going on we model the field in MATLAB (figures 5.18 and 5.19).

## 5.4. MAGNETIC GRADIOMETRY

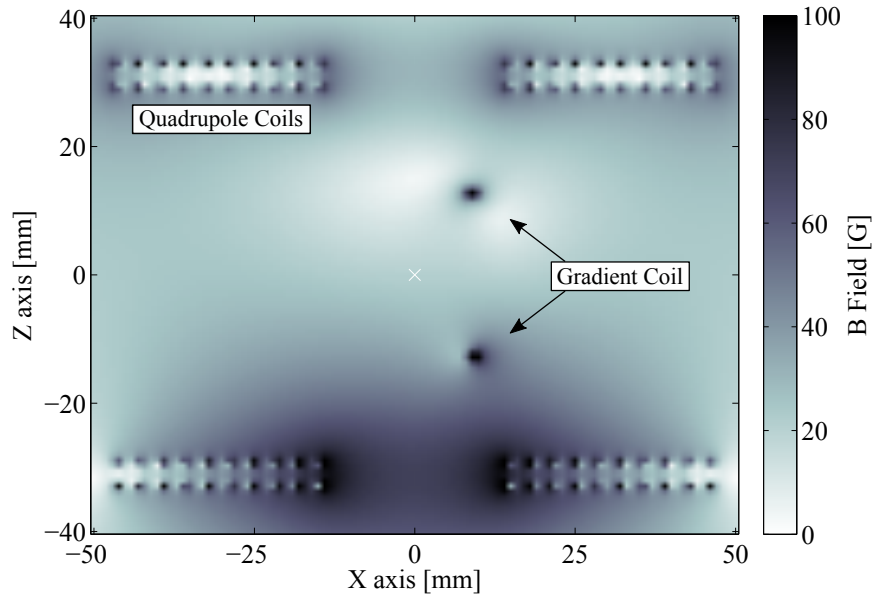


Figure 5.18: Simulation of combined quadrupole, gradient and levitation magnetic fields. Centre of interferometer indicated with white cross. Both the gradient coil and the quadrupole coils are orthogonal to the plane of the figure. Note: the gradient coil is modelled as single wire, and quadrupole coils modelled as multiple wires including wire separation.

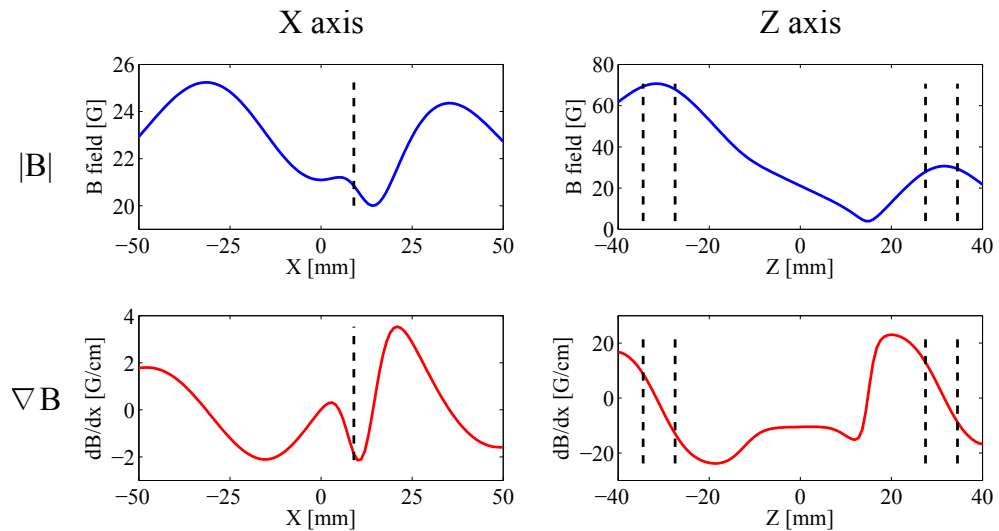


Figure 5.19: We model the magnetic field in MATLAB and plot the magnitudes (blue) and gradients (red) in the X (left) and Z (right) directions. The interferometer is located at the zeros and aligned along X. The dashed lines indicate the gradient coil position in the left-hand graphs and the quadrupole coil boundaries in the right-hand graphs.

## 5.4. MAGNETIC GRADIOMETRY

For this simulated magnetic field we can also simulate a two-arm interferometer and the effect of applying short pulses of magnetic field gradient by numerical integration of equation 5.4b. Our simulated interferometer parameters follow the form of figure 5.20 with  $T_1 = T_2 = 1.4$  ms and the magnetic field gradient applied for  $260 \mu\text{s}$  either side of the reflection. We scan the gradiometer coil current and produce figure 5.21 and observe that the symmetry is not centred around 0 A. This is due to the levitation field that we apply during the interferometer. If only the gradient field was applied, the fringes would be centred around 0 A.

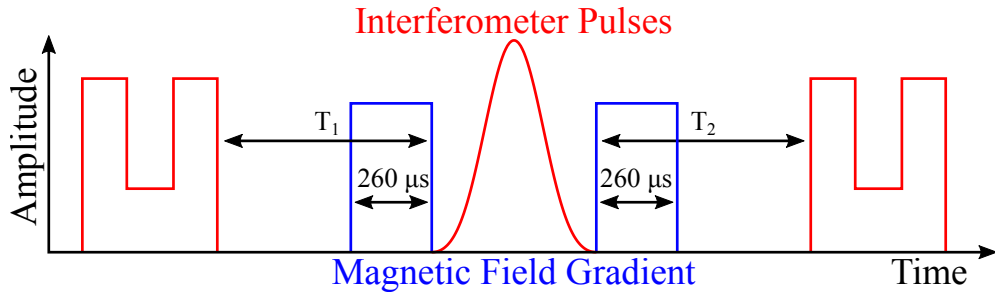


Figure 5.20: Pulse scheme for gradiometry. Beam splitter and mirror pulses (red) manipulate the atomic momentum while a magnetic field gradient (blue) is applied at the point of maximum atomic spatial separation.

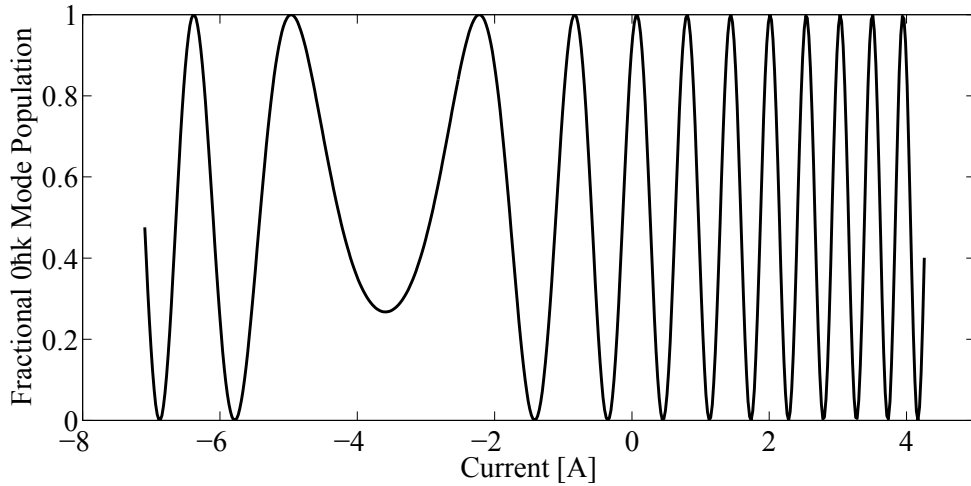


Figure 5.21: Simulated interferometer output for  $T_1=1.4$  ms. A simulated levitation field is applied which shifts the symmetry point to  $-3.6$  A.

### 5.4.1 Method

We create a BEC following the usual method, outlined in section 4.2. After release from the dipole trap we keep a levitation field on for the duration of the interferometer

in order to keep the atoms within the interferometry region.

The BEC is split into the  $|\pm 2\hbar k\rangle$  states only using the optimised pulses outlined previously (section 5.1.2). Our optimised mirror pulse reverses the velocity of the atoms (section 5.1.4) and we close the interferometer with a second splitting pulse.

Either side of the reflection pulse we apply a magnetic field gradient of varying amplitude for 260  $\mu\text{s}$ , as indicated in figure 5.20. By applying the gradient at this point in time we maximise the sensitivity of our system as this is when the two momentum states are maximally separated in space. In principle we could apply the gradient field for the entire duration, however if this was done the atoms would accelerate such that the mirror pulse would no longer be optimal. Essentially the  $|\pm 2\hbar k\rangle$  states would become  $|\pm 2\pm\delta\hbar k\rangle$  and therefore our mirror pulse would be targeting the ‘wrong’ states. By applying the gradient field for 260  $\mu\text{s}$  the change in velocity is minimal and we still obtain an interference signal. We did not apply the gradient during the reflection pulse in case it reduced the reflection efficiency, although we later determined that this was not a problem.

The magnetic field gradient is applied by varying the current passed through the coil. Negative currents are applied by simply switching the polarity of the coil and as such we obtain two data points at 0 A. We find these data give the same mode populations within the error bars. Note that we ignore the switching time of the coil which we calculate to be on the order of 1  $\mu\text{s}$ .

### 5.4.2 Measurements

We use the pulse sequence described above and in figure 5.20 for a variety of coil currents and hence magnetic field gradients and for  $T_1 = T_2$  times of 1.4 ms and 2.0 ms. After the interferometer pulses, we allow the momentum states to spatially separate before taking an absorption image. From this we determine the fractional population of each mode and plot the data in figures 5.22 and 5.23.

To each data set we fit a sine of varying frequency. For a given current value we can then extract a phase. From equation 5.5 we determine what magnetic field gradient this corresponds to and therefore we can map magnetic field gradient to coil current (figure 5.24). We note that the symmetry point in the simulated gradiometer output (figure 5.21), which is at -3.6 A, is not observed in the data of figures 5.22 and 5.23. We attribute this to the fact that the simulation is sensitive to positional changes in the placement of the gradient coil. We estimate the positional uncertainty in coil placement to be 3 mm experimentally, and if we displace the coil by 3 mm vertically in our simulation, the symmetry point in the gradiometer output occurs at -4.8 A.

From figures 5.22 and 5.23 we can calculate the sensitivity of the gradiometer. This varies depending on the applied current since the curves in figure are nonlinear. In the case where no current is applied to the gradient coil we find a resolution of 0.10  $\mu\text{T/m}$  and 0.07  $\mu\text{T/m}$  for the  $T_1 = T_2 = 1.4$  ms and 2.0 ms data respectively. This is determined functionally from the uncertainty in the fitted phase at  $I=0$  A. Given that for both cases

#### 5.4. MAGNETIC GRADIOMETRY

the magnetic field gradient is applied for  $2 \times 260 \mu\text{s}$ , for the  $T_1 = T_2 = 1.4 \text{ ms}$  and  $2.0 \text{ ms}$  data, we find sensitivities of  $4.4 \mu\text{T/m}/\sqrt{\text{Hz}}$  and  $3.0 \mu\text{T/m}/\sqrt{\text{Hz}}$  respectively.

The experiment performed here is a demonstration of the effect of a magnetic field gradient on our interferometer output, and should not be considered competitive in terms of sensitivity compared to reported values where magnetometry was the primary objective. For example, the group of Romalis achieve a maximum sensitivity of  $0.54 \text{ fT}/\sqrt{\text{Hz}}$  using thermal potassium atoms [144].

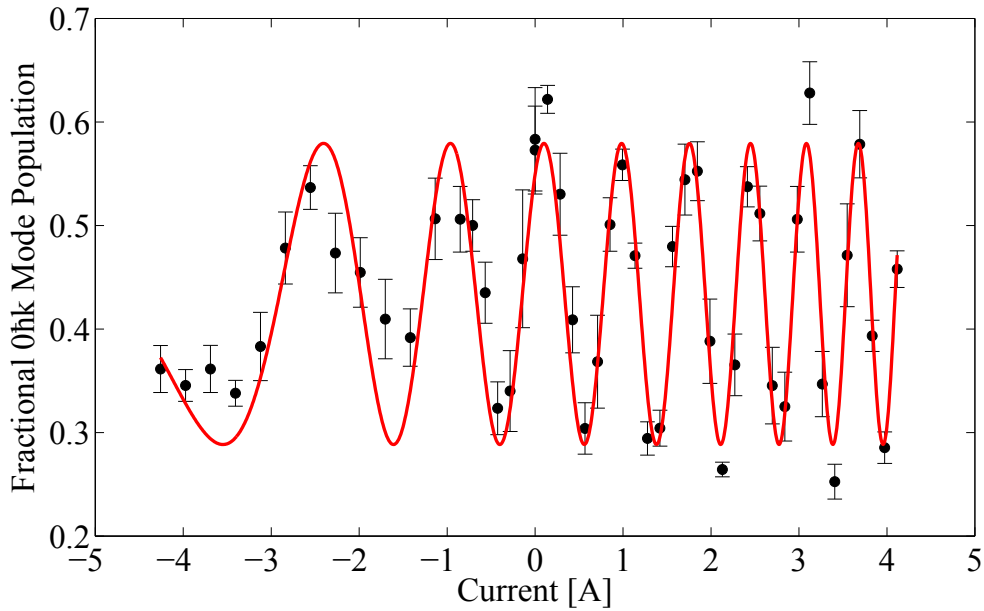


Figure 5.22: Magnetic gradiometry with  $T_1 = T_2 = 1.4 \text{ ms}$ . We fit a chirped sine curve to the data and extract the phase.

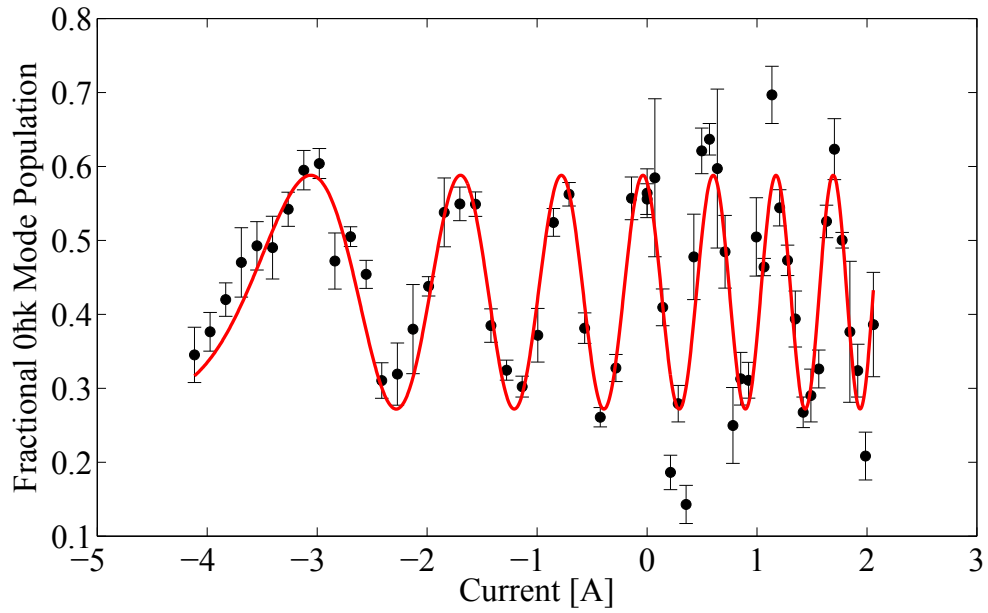


Figure 5.23: Magnetic gradiometry with  $T_1 = T_2 = 2.0$  ms. We fit a chirped sine curve to the data and extract the phase.

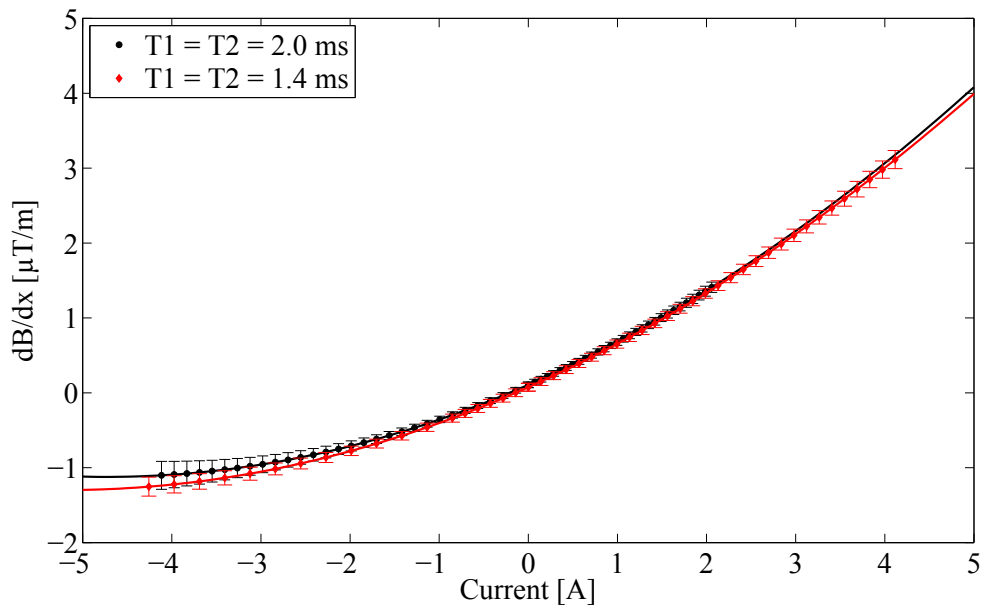


Figure 5.24: Using the data in figures 5.22 and 5.23, we determine the applied magnetic field gradient for a given current by modelling the magnetic fields in MATLAB (figure 5.19).

## Chapter 6

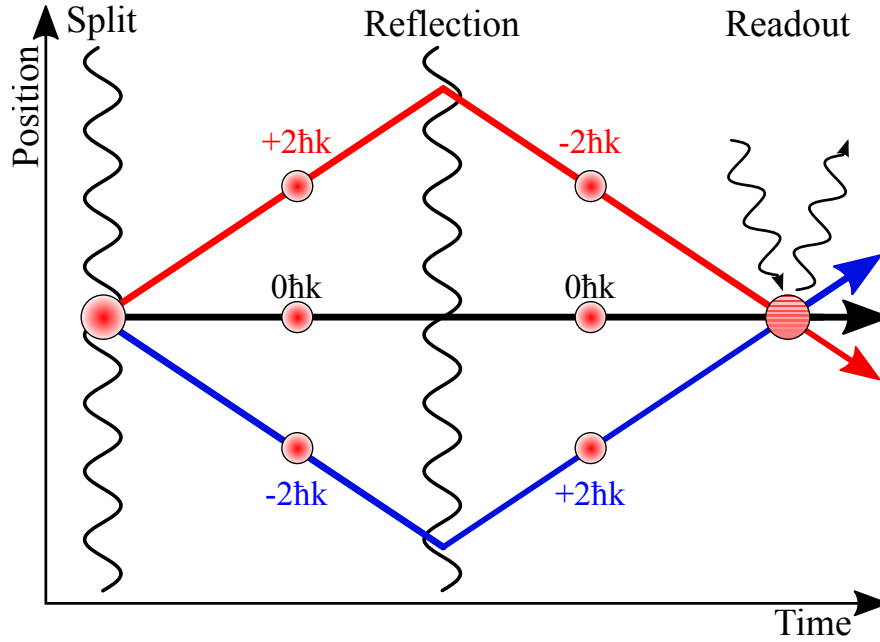
# Contrast Interferometry

The unique selling point of contrast interferometry (CI) is the method by which the information is read out of the system. Whilst in the previous chapter (5.3) absorption images were used to determine fractional momentum state mode populations, here we apply a single probe beam and observe the reflection from the atoms.

Applying a closing pulse at the end of the sequence, then taking absorption images and determining populations can be a time consuming process; the data in figure 5.16 was recorded over many hours and many experiment cycles. Contrast interferometry offers the ability to get this type of data but in only a few experiment cycles (as low as one) corresponding to a few minutes in the case of our system.

Consider three separate wave-packets ( $0\hbar k, \pm 2\hbar k$ ) as they overlap in space. Each wave-packet has an associated wavelength. Therefore the  $0\hbar k$  state and the  $+2\hbar k$  state will interfere to produce a travelling wave, and similarly the  $0\hbar k$  state and the  $-2\hbar k$  state will interfere to produce a travelling wave in the opposite direction. The combination of these two travelling wave will produce a standing wave of time varying contrast, sometimes referred to as a Moiré pattern.

The standing wave, when at non-zero contrast, can act like a Bragg reflector. If a laser is directed onto this matter-wave grating, it will be reflected back as if it had struck a grating. Since the contrast of the matter-wave grating evolves at  $8\omega_r$  (for  $0\hbar k, \pm 2\hbar k$  states), if a laser is shone onto it, the reflected signal will be modulated at this frequency. With the detection of this signal, it is possible to make a measurement of  $\omega_r$ , as well as detect magnetic fields and gravity gradients.

Figure 6.1: *Contrast interferometry scheme.*

## 6.1 Difficulty

Simply put, constructing a contrast interferometer is difficult. Given that there are only two examples [37, 88] of contrast interferometers to date, the range of literature is limited and it is a fairly unknown technique. With this in mind, outlined below are some of the crucial factors with regards constructing such a device.

**Signal detection:** The initial plan was to simply use an amplified photodiode for detection. However after further calculations it was determined that the reflected signal would likely be too low in power for this to work. The predicted reflection from the matter-wave grating is only  $\sim 0.02\%$  of the probe power incident on the BEC (see appendix A.7). Therefore an avalanche photodiode (APD) was purchased to provide the required sensitivity: a Hamamatsu C12703-01 with a sensitivity of  $1.5 \times 10^8$  V/W. It was on this device that we detected our first CI signal.

In later experiments we use a single photon counting module (SPCM) for further sensitivity and increased bandwidth. These experiments are discussed at the end of this chapter.

**Signal filtering:** Using first-order momentum states the expected signal frequency is  $\approx 25$  kHz, and therefore the APD signal could be filtered before being viewed on the oscilloscope. Whilst this could be done in post-processing, real-time filtering helped the signal emerge from the noise as the experiment was running and we were observing

the cumulative average, which was useful in initial experiments when we were still optimising the system.

**Probe Beam:** This was final hurdle in obtaining a signal. Initially the C.I. probe beam was simply one of the splitting beams (beam A) which has a detuning of 4 GHz, however no signal was detected on the APD. It was then decided to use light derived from the cooling laser instead as it is closer to the atomic resonance and the scattering rate is increased (see optics diagram in figure 4.5). It is passed through an AOM operating at 84 MHz and the -1<sup>st</sup> order goes to the atoms (figure 4.18). The BEC is created in the  $|F = 2, m_F = 2\rangle$  state and we apply light of linear polarisation, and typically a levitation field of 20 G is applied. As a result we drive the  $|F = 2, m_F = 2\rangle \rightarrow |F' = 2, m_{F'} = 2\rangle$  and the  $|F = 2, m_F = 2\rangle \rightarrow |F' = 3, m_{F'} = 2\rangle$  transitions with a detuning of 238 MHz and 505 MHz respectively.

**Atom number:** More atoms results in a higher signal amplitude since the scattering of the probe laser increases linearly with atom number. We typically use a BEC of around  $1 \times 10^5$  atoms. A smaller BEC still gives a signal but reduced in amplitude.

## 6.2 Avalanche Photodiode (APD) Detection

### 6.2.1 First Detection

The readout signal from our interferometer is detected on an APD (setup shown in figure 4.24). A signal of  $\approx 25$  kHz is expected and therefore we filter the APD output with a 50 kHz low-pass Bessel filter operating at 12 dB/octave (Stanford Research Systems SIM965 Analog Filter). Note that this filter was later changed to 100 kHz low-pass.

In figure 6.2 the first CI signal is shown. To ensure this ‘blip’ was indeed due to the matter-wave grating, data was recorded where the MOT beams were blocked during the MOT load stage. This meant at the point of applying the probe beam all experimental conditions were the same except for the presence of atoms. From the peak voltage we estimate a peak optical power of  $\sim 10$  pW.

## 6.2. AVALANCHE PHOTODIODE (APD) DETECTION

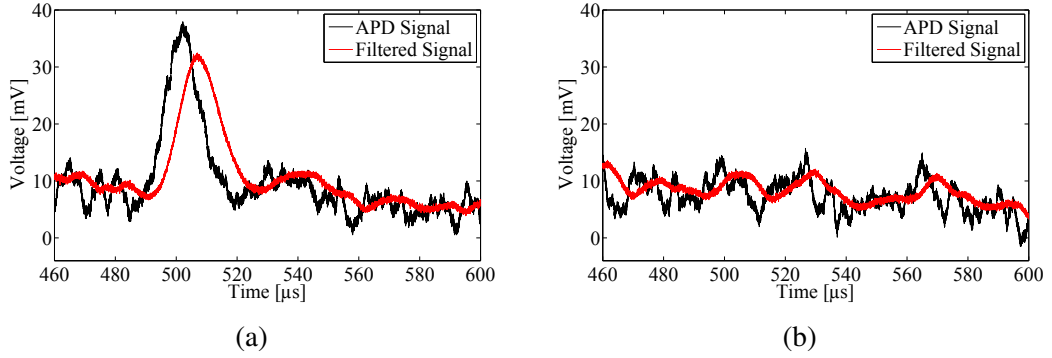


Figure 6.2: *First CI signal (a). To check the signal was from the atoms, in (b) the same experimental sequence was performed but with no atoms.*

We now ask some questions of our system. Firstly, what do we detect if we perform the CI sequence on ultra-cold thermal atoms just above  $T_c$ ? Figure 6.3 shows the average of 16 shots and we observe a pedestal in the signal for the duration of the CI probe beam. However, no discernible CI signal is observed. In principle it should be possible to perform CI with ultra-cold atoms but in this instance we assume that the signal-to-noise ratio of the detection system is too low<sup>1</sup>. The pedestal here is assumed to be fluorescence.

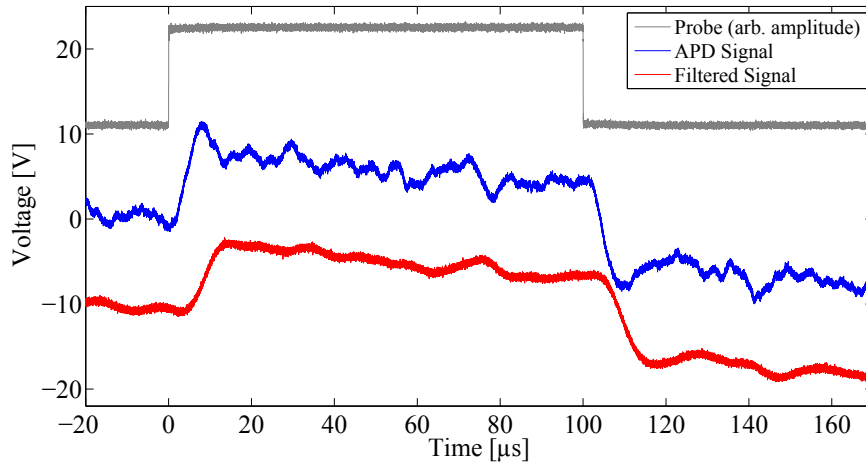


Figure 6.3: *Contrast interferometry with thermal atoms just above  $T_c$  (no BEC). Clean oscillations are not observed and the pedestal is assumed to be fluorescence. Note the grey probe pulse is for a timing reference only and the amplitude is arbitrary.*

Next, what signal would we observe if the probe beam is applied to a stationary BEC? In this instance there are no splitting or mirror pulses, and therefore no matter-

<sup>1</sup>We have yet to attempt this with the recently installed single photon counting module, which has a larger signal-to-noise ratio.

wave grating. The obtained signal (figure 6.4) shows a pedestal but no peaks that we attribute to a CI signal. As before, the pedestal this is assumed to be fluorescence.

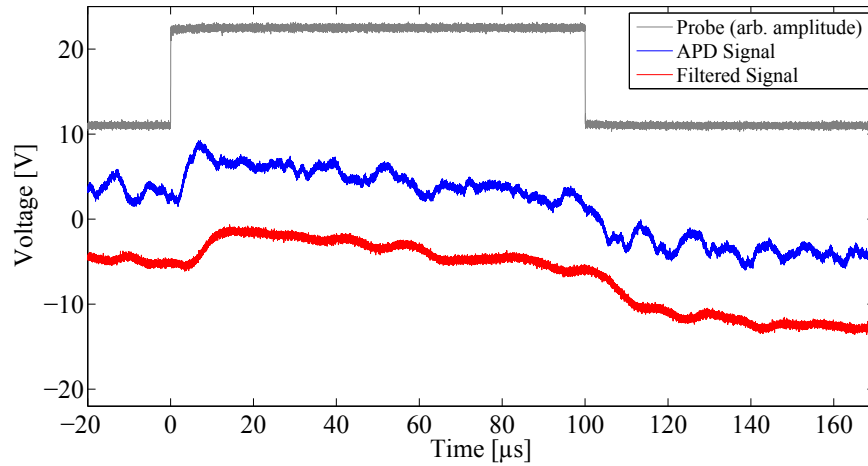


Figure 6.4: *CI probe beam applied to a stationary BEC with no split or mirror pulses. No oscillations are observed and the pedestal is assumed to be fluorescence. Note the grey probe pulse is for a timing reference only and the amplitude is arbitrary.*

### 6.2.2 Further Analysis

**Signal Filtering:** Given that using a 50 kHz low-pass filter results in a small attenuation at 25 kHz the filtering frequency is increased to 100 kHz. The effect of this filter is tested in figure 6.5. We find that without the filter, the power at 25 kHz is 7 mVs and with the filter it reduces by an order of magnitude to 0.8 mVs.

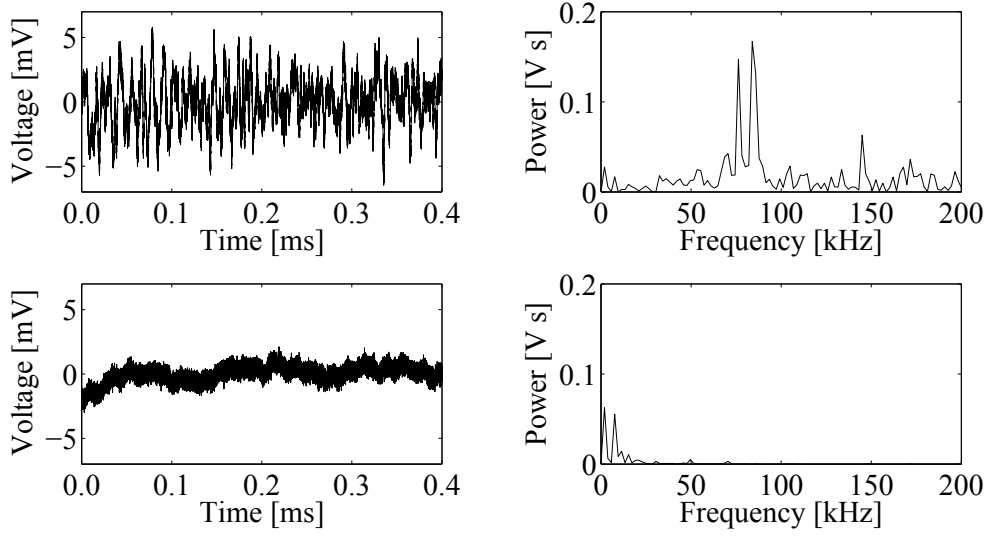


Figure 6.5: The effect of applying a 100 kHz low-pass Bessel filter to the APD signal background signal. Upper left plot is raw APD signal. Lower left plot is filtered signal. Plots on the right are FFTs of the signals. (We expect a signal of  $\approx 25$  kHz).

**APD Detection:** We prepare our BEC of  $1.2 \times 10^5$  atoms as described previously. After 1.87 ms free expansion we apply our interferometer pulses. The splitting pulse is  $11.5 \mu\text{s}$  with an amplitude of  $12.2 E_r$ . This splits the BEC into the  $|0, \pm 2\hbar k\rangle$  states with  $\approx 60\%$  in the  $\pm 2\hbar k$  modes and a negligible amount in higher order modes. After  $T_1 = 700 \mu\text{s}$  we apply a Blackman mirror pulse of  $164 \mu\text{s}$  duration, and  $12.2 E_r$  amplitude. Then we apply the probe beam  $480 \mu\text{s}$  after the reflection. The probe is applied before the symmetrical time in an effort to increase the duration of our signal.

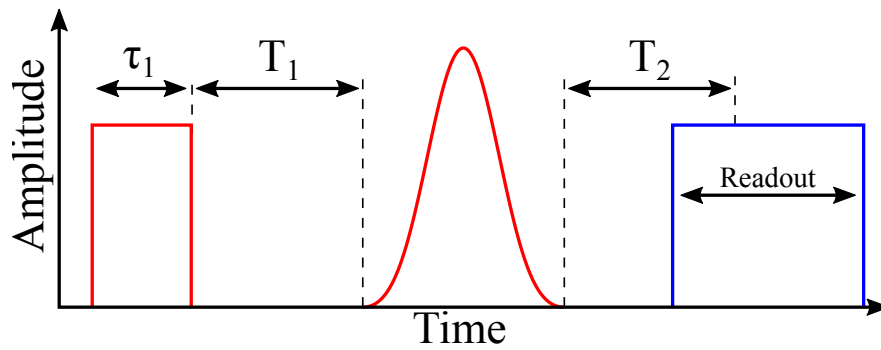


Figure 6.6: We apply a splitting and mirror pulses (red) as previously. The contrast interferometry probe beam (blue) is applied slightly before the symmetrical time in order to increase the signal duration.

We perform the experiment and view the APD signal on an oscilloscope. The data is then saved and processed in MATLAB. Figure 6.7 shows data from a 10 shot

## 6.2. AVALANCHE PHOTODIODE (APD) DETECTION

average where the averaging is done on the oscilloscope. We fit an exponentially decaying sinusoid using the curve fitting toolbox in MATLAB (‘cftool’). A frequency of  $24.349 \pm 0.003$  kHz obtained where the uncertainty is the 68 % confidence bounds. This returns a value of  $\alpha^{-1} = 137 \pm 5$  following the calculation outlined in appendix A.6.

We attribute the decay of the signal to the loss of atoms from the grating. In the particle picture, for every photon reflected by the grating, an atom has absorbed then emitted a photon which causes a momentum kick of  $2\hbar k$ . As a result, that particular atom no longer contributes to the matter-wave grating. The reading out of data could therefore be described as a destructive process.

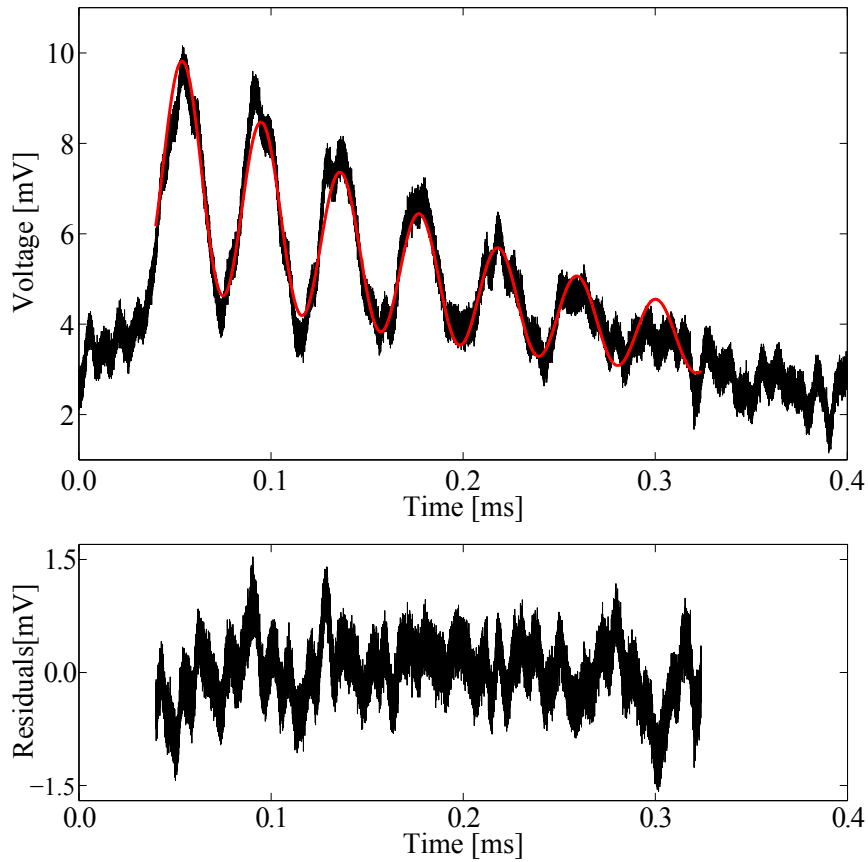


Figure 6.7: *Top: Average of 10 single shot contrast interferometry measurements.  $T_1 = 700 \mu\text{s}$  and probe beam applied  $480 \mu\text{s}$  after reflection. A exponentially decaying sinusoid is fitted to the data with a frequency of  $24.349 \pm 0.003$  kHz. Bottom: Residuals of fit.*

This hypothesis is backed up by figure 6.8 showing the absorption images of the atoms after a weak CI probe. Up until the probe is applied, the system is symmetric, however after the sequence (with a low probe power) the integrated profile is asymmetric as shown in figure 6.8. The probe is applied from the left hand side so some of the

## 6.2. AVALANCHE PHOTODIODE (APD) DETECTION

$-2\hbar k$  atoms have transferred to the  $0\hbar k$  state while some of the  $0\hbar k$  state have transferred to the  $+2\hbar k$  state. This is also reported in figure 2-10 of [91] and it is pointed out that this is a good indication that the CI system is working even before a signal is observed.

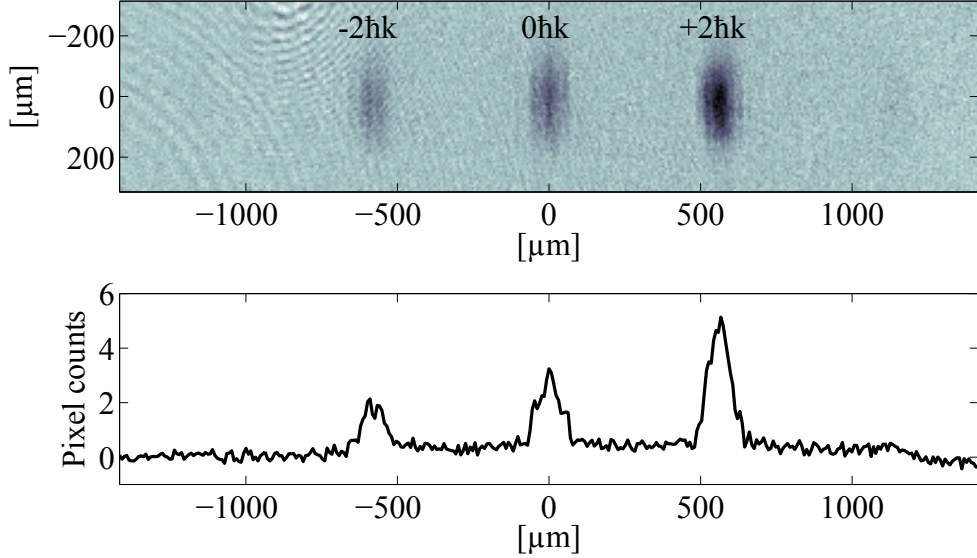


Figure 6.8: Absorption image and profile of atoms after a weak CI probe beam is applied. Image acquired after 64 ms time-of-flight. Asymmetric distribution is characteristic of a successful CI probe and readout.

Assuming the exponentially decaying signal is indeed due to effective atom ‘loss’ from the matter-wave grating, we should be able to observe a signal for longer if we reduce the probe power. This however has the issue that it reduces the signal to noise ratio. If we were to strobe the signal at a 50 % duty cycle, it would follow that the signal would last for twice as long. We test this hypothesis in figure 6.9. A probe beam is applied comprising of multiple square pulses of  $5\ \mu\text{s}$  separated by  $5\ \mu\text{s}$  and compared to a DC readout signal of the same peak amplitude. Note that the bandwidth of the APD is 100 kHz. A sinusoid with an exponential decay and a linear gradient offset is fitted to both data sets, but to the strobed probe data we also include a second higher frequency. From this we extract the decay times of  $69\ \mu\text{s}$  and  $140\ \mu\text{s}$  for the DC and strobed case respectively, which is in excellent agreement with our hypothesis. From this we conclude that the signal decay is due to the destructive readout process.

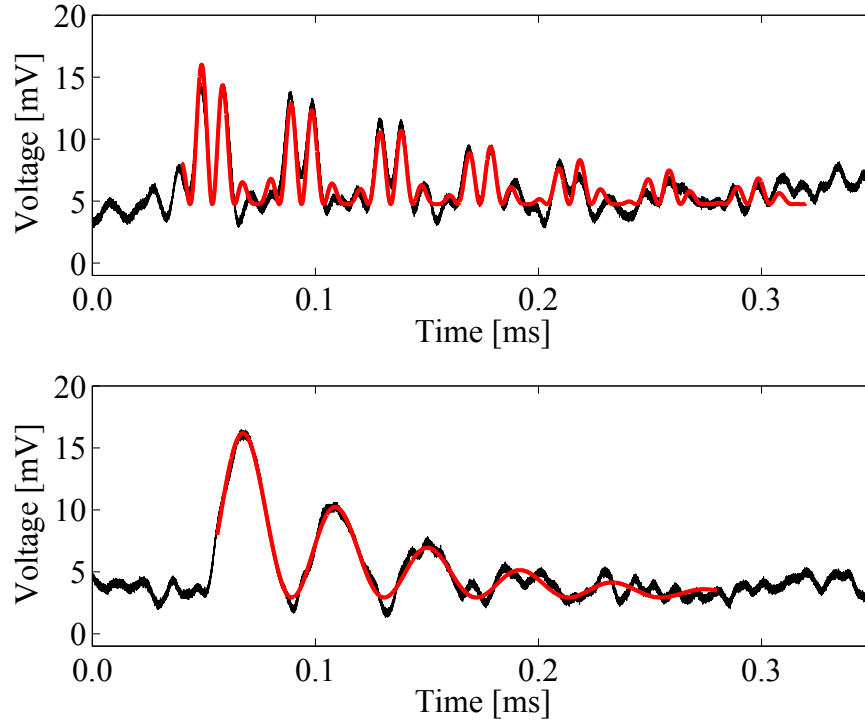


Figure 6.9: A strobbed probe with a 50 % duty should increase the decay constant of the data by a factor of 2. We fit decay constants of  $140 \mu\text{s}$  and  $69 \mu\text{s}$  to the strobbed (top) and DC (bottom) probe data respectively

### 6.2.3 APD Limitations

As shown above, the APD is functional, however it is not ideal. Firstly we were operating close to the signal to noise limit despite this particular model having amongst the highest sensitivity available (at our wavelength). A voltage amplifier was used in an attempt to improve the signal to noise but it was found that the noise was inherent to the APD module. Secondly, the bandwidth of the APD is only 100 kHz. The expected frequency of a second order momentum state CI ( $\pm 4\hbar k$ ) is 100 kHz and therefore if this is something we want to pursue then a higher bandwidth device may be needed. A photomultiplier tube may be sufficient for the task, however they can be expensive and easily damaged. Something more robust would be better suited and with this in mind, in the following section we use a single photon counting module (SPCM) for low level light detection.

## 6.3 Single Photon Counting Module (SPCM) Detection

### 6.3.1 Method of Detection

The experiments performed here are the same as those performed in the previous APD detection method section, and the differences arise in the signal acquisition and processing. The SPCM (Excelitas SPCM-AQRH-14-FC) is on continuously and we record the counts in LabVIEW via a National Instruments PCI-6713 interface card. Before we expect to detect our signal, we trigger the computer to start recording the SPCM counts, which arrive in the form of a pulse train. We also set a bin width on the computer, typically 4  $\mu\text{s}$ , giving  $\approx 10$  bins per period of the  $\approx 25$  kHz signal.

We assemble the apparatus as shown in figure 4.25. The APD is left in place and a single mirror is used to redirect the beam to the SPCM. This would allow us to quickly return to the previous APD setup. In addition to the SPCM, we also add two Uniblitz LS2T2 shutters: one in the telescope of beam B and a second in a telescope in the newer SPCM setup. We refer to these as ‘beam B blocking shutter’, and the ‘SPCM protection shutter’. The beam B blocking shutter is closed after the reflection pulse and prevents any leakage light from beam B reaching the SPCM, while the SPCM protection shutter prevents the splitting and reflection pulses from beam B entering the SPCM.

The SPCM counts are recorded in labVIEW and saved as a .csv file for analysis in MATLAB. We record the individual shots which allows us to average the data in post analysis.

### 6.3.2 Measurements

**Initial Measurements:** A BEC is created as described previously. After 2.1 ms of free expansion, the interferometer pulses are applied following the form of figure 6.6. The BEC is split into 3 with  $\approx 50\%$  in the  $\pm 2\hbar k$  modes, 50% in the  $0\hbar k$  mode, and negligible fraction in the higher orders. This is achieved using a pulse of 30  $\mu\text{s}$  duration and  $6.2 E_r$  amplitude. After  $T_1 = 600 \mu\text{s}$  a mirror pulse is applied. Finally the CI probe is applied for 500  $\mu\text{s}$  and the signal is recorded.

Figure 6.10 shows the data to which a sinusoid with a Gaussian envelope is fitted. This average of 10 shots returns a frequency of  $24.33 \pm 0.06$  kHz. Note that the larger uncertainty here compared to the data from figure 6.7 is due to fewer data points.

Given the counting nature of the SPCM, Poissonian counting statistics are used for the uncertainty calculations. The standard deviation of each data point is simply  $\sigma = \sqrt{\bar{C}}$ , where  $\bar{C}$  is the mean average of the number of counts. The standard error is then  $\sigma/\sqrt{N}$  where  $N$  is the number of samples [145].

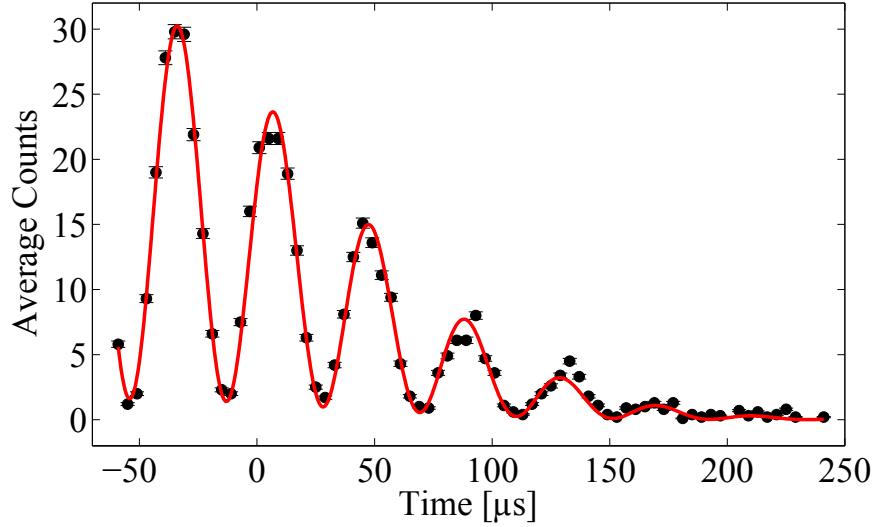


Figure 6.10: Contrast interferometry with SPCM detection. A sinusoid with a Gaussian envelope is fitted with a frequency of  $24.33 \pm 0.06$  kHz. Data is the average of 10 shots and the error bars are the standard error in each point.  $T = 0$  is the symmetrical interferometer time.

**Recent Measurements:** In our initial measurement we attributed the decay of the signal to the loss of atoms from the grating. This is supported by the data taken using the APD, specifically figure 6.9. From performing a 3-arm interferometer and using absorption images as the readout, we observe in figure 5.16 that the point of maximum contrast is  $\sim 30$   $\mu\text{s}$  before the symmetrical interferometer time. Thus we would expect that the CI data in figure 6.10 would include the time of peak contrast, although it may not be obvious as atom loss from the grating is assumed to be the dominant effect.

We therefore investigate the effect of moving the probe beam closer to the reflection pulse, and we observe some interesting results. From an interferometer sequence with a free expansion time of 2.1 ms and  $T_1 = 1$  ms we obtain the data in figure 6.11. A sinusoid with a Gaussian envelope is fitted and a frequency of  $24.42 \pm 0.05$  kHz is obtained, with a  $\chi^2 = 1.59$ . From the fit we determine the peak contrast to occur at  $-182$   $\mu\text{s}$  relative to the symmetrical interferometer time.

A reason for the discrepancy between symmetrical interferometer time and peak contrast time is most likely due to atomic interaction, which is discussed in a recent paper by Jamison *et al.* [88]. These interactions can be reduced by decreasing the density of the BEC. It is pointed out that increasing the BEC expansion time from 2 ms to 10 ms should decrease the interaction effects by at least a factor of 10. In order to characterise and quantify these interactions a three dimensional Gross-Pitaevskii model is performed in [44]. A full Gross-Pitaevskii equation simulation is currently being investigated in our group and will likely be reported on in the near future.

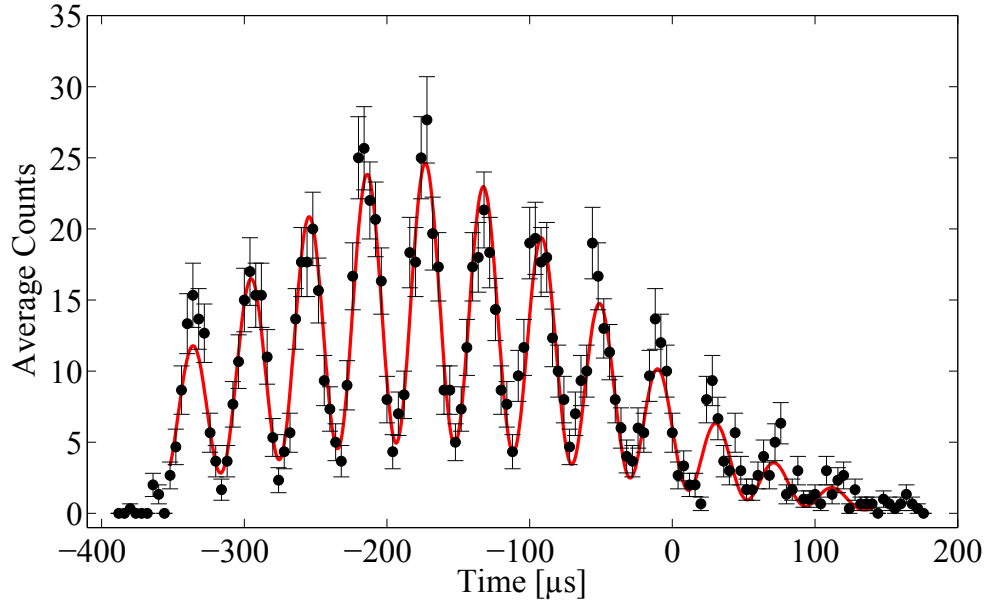


Figure 6.11: *Contrast interferometer with  $T_1=1$  ms. A sinusoid with Gaussian envelop is fitted and a frequency of  $24.42\pm 0.05$  kHz is returned. The time axis is relative to the symmetrical interferometer time. The peak contrast is found to occur  $182$   $\mu$ s before the symmetrical interferometer time. Fitting algorithm returns  $\chi^2=1.59$ . Data is average of three shots.*

In recent experiments the expansion time of the BEC is varied to investigate if this has an effect on the peak contrast position. For  $T_1=500$   $\mu$ s, we plot the peak contrast position relative to the symmetrical interferometer time as a function of expansion time in figure 6.12. An expansion time of 6.1 ms gives the smallest discrepancy (inset of figure 6.12). In future work it would be interesting to allow the BEC to expand further and observe the effect on discrepancy.

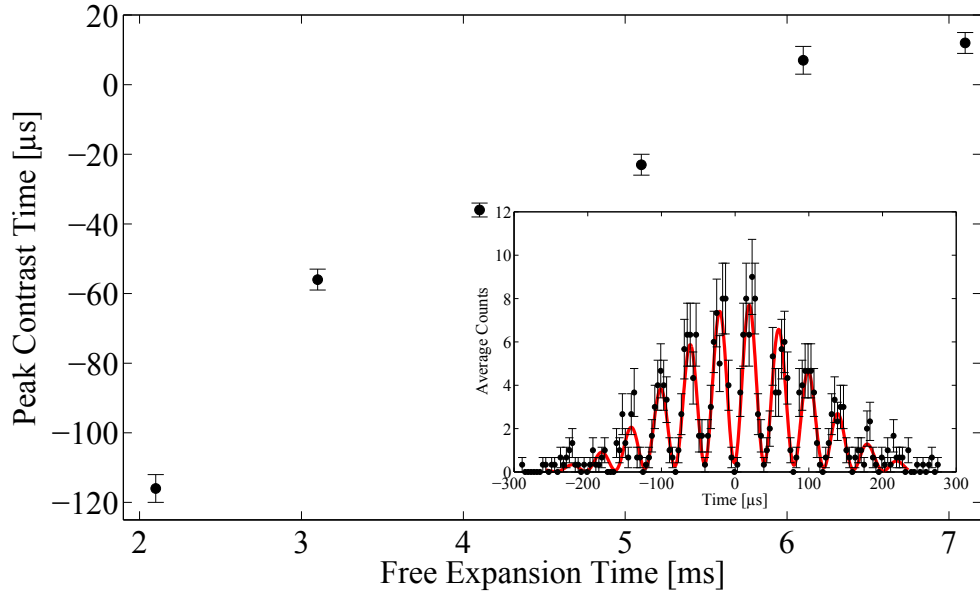


Figure 6.12: Time of peak contrast relative to the symmetrical interferometer time as a function of free expansion time. Inset shows the data from 6.1 ms expansion time with a fitted sinusoid with Gaussian envelope, and we find the peak contrast occurs at  $7 \pm 4 \mu\text{s}$ .

**Short CI:** An alternate method of performing contrast interferometry is what we refer to as ‘short CI’. As described in figure 6.13, the BEC is split then the CI probe beam is applied almost immediately after, and crucially, before the wave-packets spatially separate. The minimum delay that we can currently achieve between the splitting and probing pulse is  $120 \mu\text{s}$  which is limited by shutter opening and closing times.

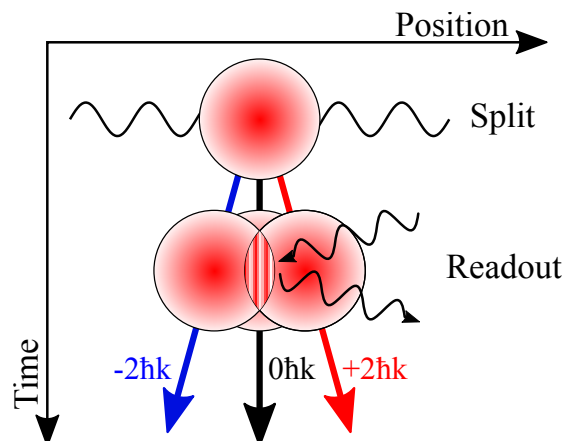


Figure 6.13: Short contrast interferometry scheme. A splitting pulse splits the BEC into three parts then the CI probe is applied before the wave-packets spatially separate.

Figure 6.14 shows data from a ‘short CI’ experiment. Given that we want to perform the interferometry sequence as quickly as possible, we split the BEC using a  $10 \mu\text{s}$  pulse of  $13 E_r$  amplitude. This results in  $\approx 60\%$  in the  $\pm 2\hbar k$  modes. After  $120 \mu\text{s}$ , the CI probe beam is applied in the SPCM signal recorded.

The average of 10 shots is fitted with a sinusoid with Gaussian envelope and the frequency is obtained. Figure 6.14 shows the data with a fitted frequency of  $25.91 \pm 0.10 \text{ kHz}$ . By performing the traditional interferometer (described in section 5.3) we predict a frequency of  $24.68 \text{ kHz}$ . The reason for this discrepancy is not yet fully understood and is under investigation at the time of writing, although we believe it is due to the mean field expansion of the BEC.

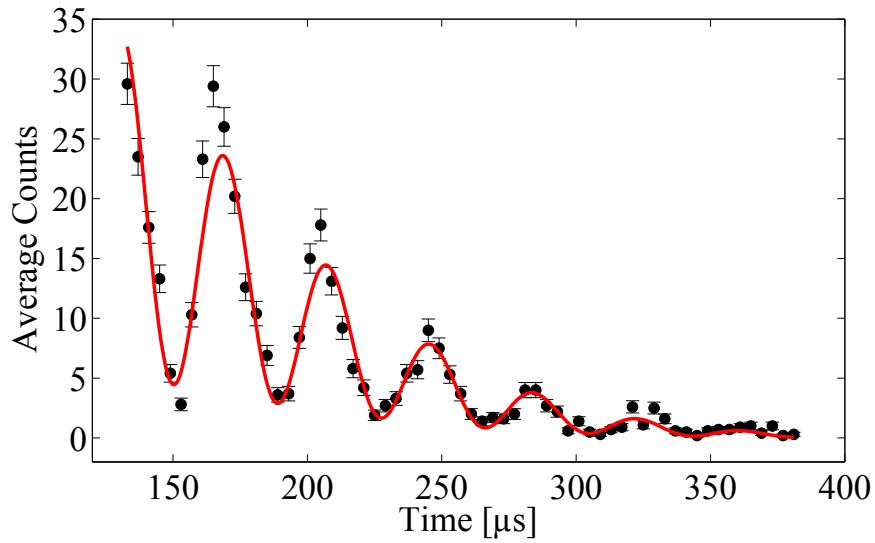


Figure 6.14: *Short contrast interferometry.* We perform a split, then we probe the matter-wave grating  $120 \mu\text{s}$  later, ie. we do not apply a reflection pulse. We fit a sinusoid with a Gaussian envelope and obtain a fitted frequency of  $25.91 \pm 0.10 \text{ kHz}$ . The time axis is relative to the start of the splitting pulse. Data is the average of 10 shots.

**Phase Stability:** Another discussion point which is common to all CI data sets is the reduced contrast, or the fact that the counts don’t go to zero in figure 6.14. Firstly, there is a resolution issue due to the finite bin width, which means that even in a perfect system the bin with the lowest counts would still have a non-zero value. Secondly, and more interestingly, we observe a slight phase drift between individual shots. This results in a slight loss of contrast, however the ‘true frequency’ of the signal is still observable. This phase drift is attributed to a variation in the intensity of the splitting and reflection pulses. Currently, this is most likely due to laboratory temperature fluctuations. In figure 6.15 we plot the phase of the interferometer as a function of temperature

### 6.3. SINGLE PHOTON COUNTING MODULE (SPCM) DETECTION

---

at the air conditioning inlet. Note that the temperature range at the interferometer is not expected to be this extreme.

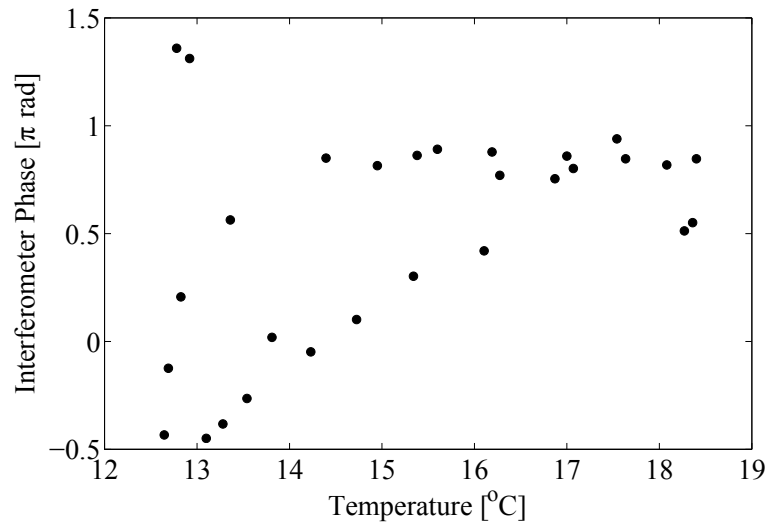


Figure 6.15: *Interferometer phase as function of temperature at the air conditioning inlet.*

# Chapter 7

## AC Coupled Ring Trap

Waveguides allow the interfering particles of an interferometer to be spatially confined. This leads to the advantage of increasing the interaction time which can lead to increased sensitivity. A popular geometry for atom (and light) interferometers is a ring shape. These typically come in three varieties: Optical, RF dressed, and magnetic. Optical ring traps are typically smaller and suited to the study of superflow, supercurrents, and vortices in BECs [49, 50, 51]. RF dressed traps have the advantage that their shape can be transformed adiabatically by the application of an RF field [57, 58]. Magnetic ring traps [2, 62, 65] are typically larger in size and are of particular interest for rotation sensing.

In order to create a magnetic ring trap, the use of current-carrying input and output wires is normally required to drive the coils that produce the magnetic field, which can result in the cylindrical symmetry of the ring trap being broken [63]. In order to suppress these end effects we have constructed a time-averaged trapping potential that results from the induced current in a copper ring generated via two external drive coils [6]. This is designed to limit the end-effects and maintain a smooth, cylindrically symmetric trapping potential. Moreover, the time varying nature of the current has the effect of averaging any roughness in the copper ring which further smooths the trapping potential [67].

The apparatus reported on here is a second generation experiment with the first generation comprising a larger, horizontal ring trap [7, 8]. The second generation ring trap is not the primary focus of this thesis, however its function has been demonstrated and some interesting results have been obtained which are promising for its future use as a waveguide for ultra-cold atoms and BECs.

In this chapter we will briefly discuss the theory of an AC coupled ring trap<sup>1</sup>, followed by an overview of recent results including the loading and Kapitza-Dirac splitting of a BEC in the ring trap. Finally we will discuss the current limitations of the system and future improvements.

---

<sup>1</sup>An in-depth explanation of the mechanisms of a AC coupled ring trap can be found in the thesis of Dinkelaker [8] and related publications [6, 7]

## 7.1 Theory

We start by describing the general mechanisms used in creating a ring trap. The ring trapping potential is created from the superposition of two magnetic fields, namely the *driving* AC magnetic field and the *induced* AC magnetic field. We start our description by considering a single straight wire through which current flows as shown in figure 7.1. This produces a cylindrically symmetric magnetic field, according to Ampère’s law, which decreases radially from the centre of the wire [102, 146]. If a magnetic bias field is then added orthogonally to the wire the magnetic field will cancel out at one radial position resulting in a line of magnetic zeros running parallel to the wire. To reduce Majorana losses, a magnetic bias field parallel to the wire can be applied to offset the magnetic zeros. This can then be used to trap atoms, and indeed this is how many atom chip traps operate, eg. [18].

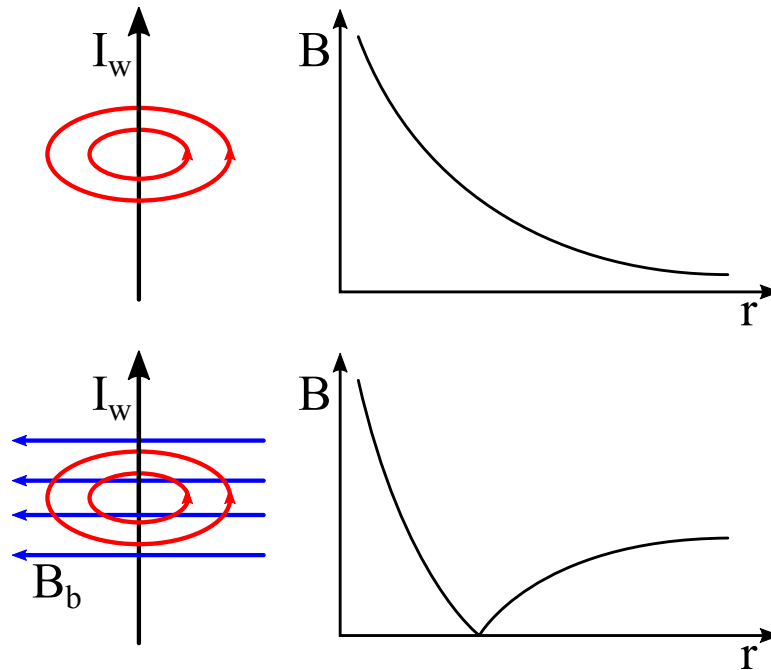


Figure 7.1: *Upper: A wire carrying current  $I_w$  produces a radially symmetric magnetic field (red ellipses) which falls off as  $1/r$ . Lower: By adding a DC bias field,  $B_b$ , the magnetic fields cancel at one radial position, which results in a trapping potential (for low field seeking atoms) running parallel to the wire.*

We can now take this wire and bend it such that it forms a ring with the potential minimum on the inside, thus creating a ring trap. However we need a way to get the electrical current into the wire, and without cutting the wire as this would introduce asymmetry from wire end effects. To achieve this we can induce a current in the wire by applying an alternating magnetic field to the ring. The induced current is proportional to the magnetic flux through the centre of the ring and from [6] can be

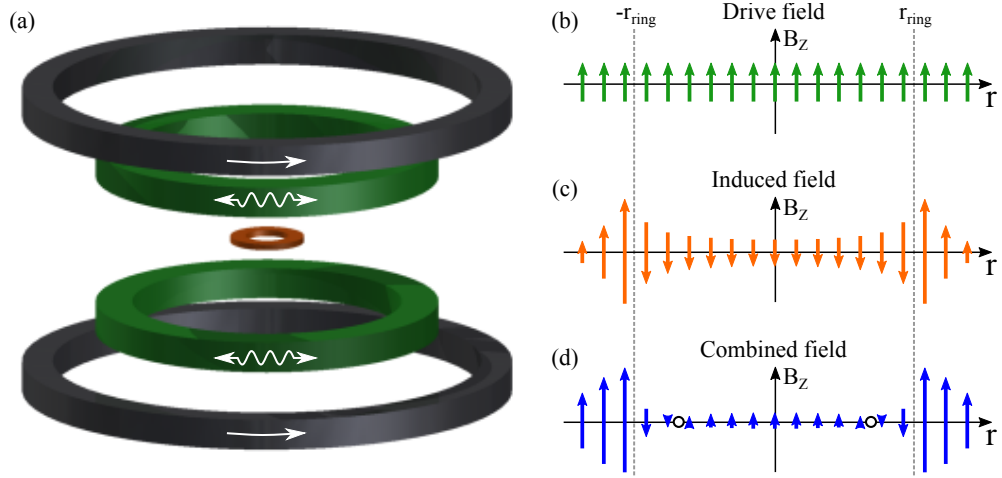


Figure 7.2: AC coupled ring trap (a) with green drive coils and black bias coils. The driving magnetic field (b) induces a magnetic field (c) from current in the copper ring resulting in a combined magnetic field (d). The circles in plot (d) plot indicate the potential minimum, which here is zero. Figure adapted from [7].

written as

$$I(r) = -\frac{\pi r_{\text{ring}}^2 B_0}{L\sqrt{1 + \Omega^{-2}}} \cos(\omega t + \delta_0), \quad (7.1)$$

where  $\Omega = \omega L/R$ ,  $\omega$  is the drive frequency,  $L$  and  $R$  are the coil inductance and resistance respectively, and  $\delta_0 = \tan^{-1}(1/\Omega)$  is the phase shift of the induced current relative to the drive field phase.

Conveniently, the induced magnetic field opposes the driving magnetic field within the ring according to Lenz's law, and as such a ring of magnetic zeros is produced inside the ring of wire. Figure 7.2 shows, for one instance in time, the driving magnetic field, the magnetic field resulting from the induced current, and the total combined field. The circles in the lower left plot indicate the position of the potential minimum, which here are zero.

Providing the drive frequency  $\omega$  is larger than the trap frequency, the atoms experience the time averaged trap potential, and it is this average potential that forms the basis of our ring trap. The shape of this radially symmetric potential can be likened to the bottom of a wine bottle (figure 7.3).

As described in section 2.1.4, the Larmor frequency  $\omega_L$  must be larger than the rate of change of the magnetic field in order that the atomic dipole adiabatically follows the trapping field, which is necessary to avoid Majorana losses. For the time-averaged potential it is the instantaneous field value that matters and as such  $|B(t)| > 0$  at all times.

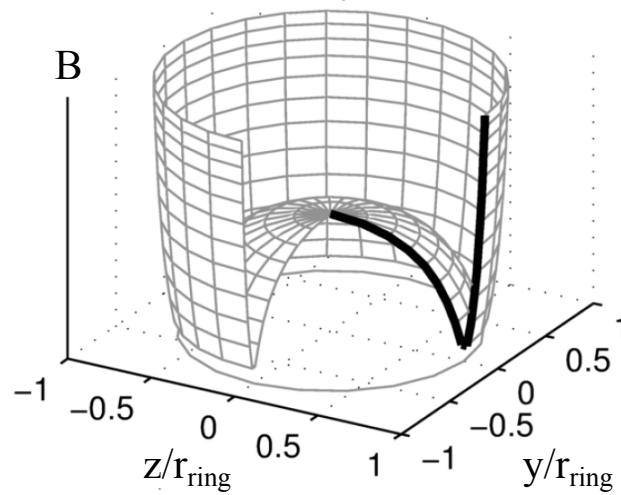


Figure 7.3: Ring trap potential (figure adapted from [8]).

To remove the ring of magnetic zeros we apply either a bias field orthogonal to the plane of the ring, or a quadrupole field with the axis of symmetry parallel to the plane of the ring. A bias field prevents the zero points sweeping radially through the potential minimum as the current alternates, and as a result ‘flattens’ the bottom of the trap and it becomes anharmonic (figure 7.4 centre plot). A quadrupole field shifts the magnetic zeros symmetrically out of the plane of the ring while keeping the time-averaged potential minimum in the centre (figure 7.4 right plot).

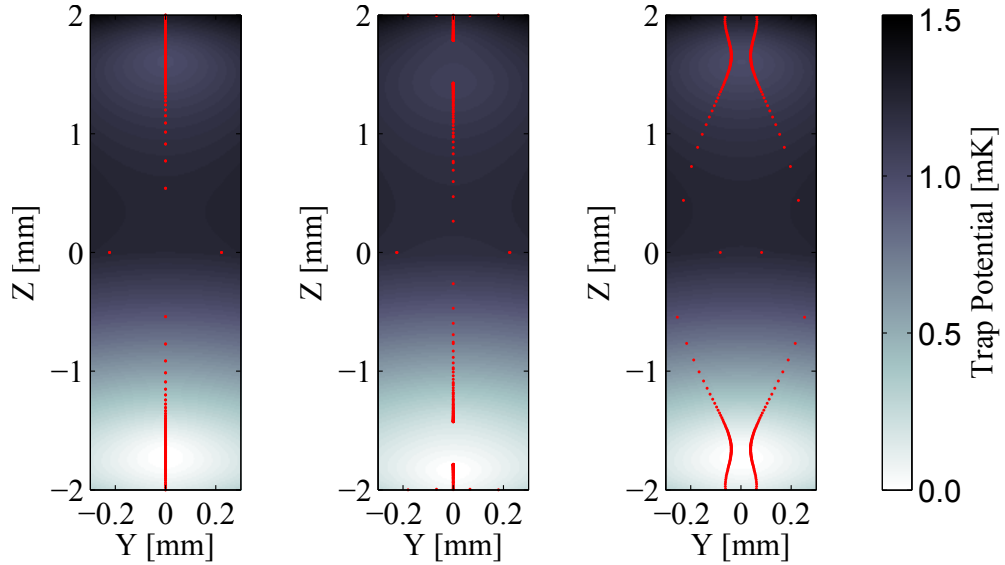


Figure 7.4: Vertical ring time-averaged trapping potentials with instantaneous zeros marked as red dots. Left: bare ring potential (drive field only). Centre: ring trap with  $Y$  bias field of 5 G. Right: ring trap with quadrupole field of 10 G/cm which pushes the zeros out of the plane of the ring.

The description above ignores the effects of gravity, which for a complete model we must include. In our second generation experiment we use a vertically orientated copper ring of 4 mm inner diameter to produce the trapping potential. The size of the ring was chosen for performing atom interferometry using the ring trap as a waveguide, and therefore the 4 mm diameter gives a significant area to accumulate a Sagnac phase. In order to account for the effects of gravity a MATLAB simulation was performed using code written by colleague Jonathan Pritchard. The simulation output is shown in figure 7.4. The plots show, from left to right, a vertical slice of the time averaged trapping potential formed by only applying the drive field, drive field plus a 5 G bias field, and drive field plus a 10 G/cm quadrupole field. In each case the driving field has a peak value of 100 G applied at a frequency of 44.7 kHz. We mark the instantaneous magnetic field zeros with red dots.

**Drive frequency:** The drive coil circuitry forms an LCR resonator, where  $L$  is the inductance of the coils,  $C$  is some load capacitor, and  $R$  is the total resistance. The total resistance is measured to be  $R = 1.96 \Omega$ , and we select a capacitance value of 247 nF such that the resonance frequency,  $f_0$ , given by  $1/(2\pi\sqrt{LC})$ , is 44.7 kHz (measured in figure 6.23 of [8]). This frequency allows us to use a high power (600 W) audio amplifier (Behringer Eurorack EP1500) with a peak frequency of 50 kHz to power the coils, but the frequency is still high enough that it is outside the limit of human hearing.

## 7.2 Thermal Atoms in the Ring Trap

Here we load atoms of around 35  $\mu\text{K}$  into the ring trap and let them expand to fill the potential. The experiment sequence up to RF evaporation follows the description in section 4.2. During the RF evaporation we apply a bias field of 37 G in the Z direction, ramped from 0 G in an s-curve over 2.5 s, which raises the centre of the quadrupole trap by 1.85 mm. At the end of this stage we are left with  $\sim 3 \times 10^7$  atoms in the quadrupole trap of 206 G/cm, at a temperature of 35  $\mu\text{K}$ . We then relax the quadrupole gradient to 15 G/cm over 200 ms whilst ramping the Z shim in an s-curve to 2.6 G. This keeps the centre of the magnetic trap at roughly the same position, and importantly overlapped with the ring trap potential. The Y and Z shim values are then tuned for optimal loading into the ring trap for the given ring trap parameters.

We then immediately turn on the ring trap by applying a driving field of 44.7 kHz with a maximum magnetic field of 130 G. We offset the magnetic zeros by applying a quadrupole field, which is ramped linearly from a starting value of 15 G/cm to 6 G/cm in 1 ms. The atoms in the ring trap can then be allowed to evolve for a variable time before some time-of-flight and an absorption image records their position. Ideally we want the time-of-flight to be as short as possible such that we see the atoms as close as possible to their ring trap position. The shortest we can manage is 0.8 ms and is limited by the probe shutter opening time.

Atoms are loaded into the ring trap at the top, slightly left of centre. At the time of running the experiment we did not have full control of the horizontal (X axis) position and this was the closest we could get the atoms to the centre. The hold time is then varied and we observe the cloud thermally expanding to fill the ring trap as well as a centre-of-mass motion analogous to the motion of a rigid pendulum. Figure 7.5 shows an example absorption image of the atoms having been in the ring trap for 42 ms. The fact that the ring of atoms has sagged slightly with respect to the copper is due to gravity and the fact that applying a quadrupole field loosens the trapping potential<sup>2</sup>.

---

<sup>2</sup>After 0.8 ms time-of-flight the atoms will have dropped only 3.1  $\mu\text{m}$

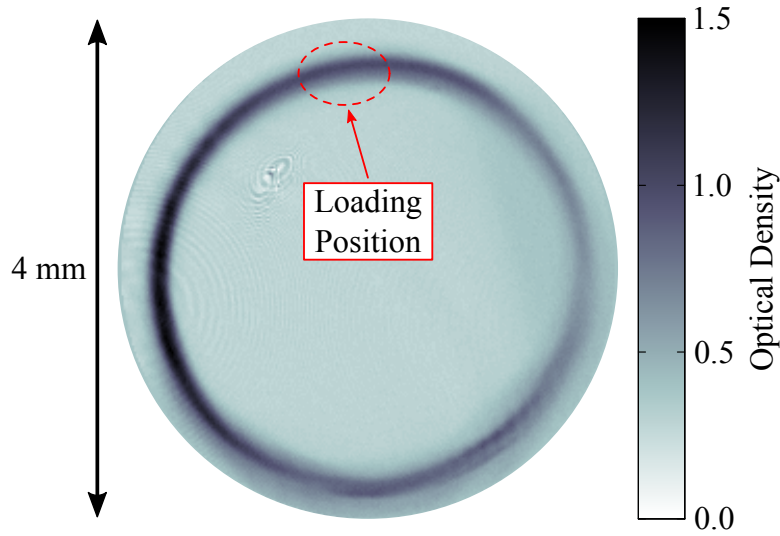


Figure 7.5: Atoms of  $\sim 35 \mu\text{K}$  loaded into the ring trap and allowed to evolve for 42 ms. Gravity acts downwards

In figure 7.6 we count the number of atoms in the ring trap by applying a background subtraction, masking the centre region of the ring where there are no atoms, then summing the pixel values. We plot the number of atoms as a function of ring trap hold time and fit an exponential decay to determine the trap lifetime which we find to be 60 ms. Note that we ignore the initial data points as the high optical density causes the image to saturate. The atom number is determined by pixel counting with a background subtraction applied.

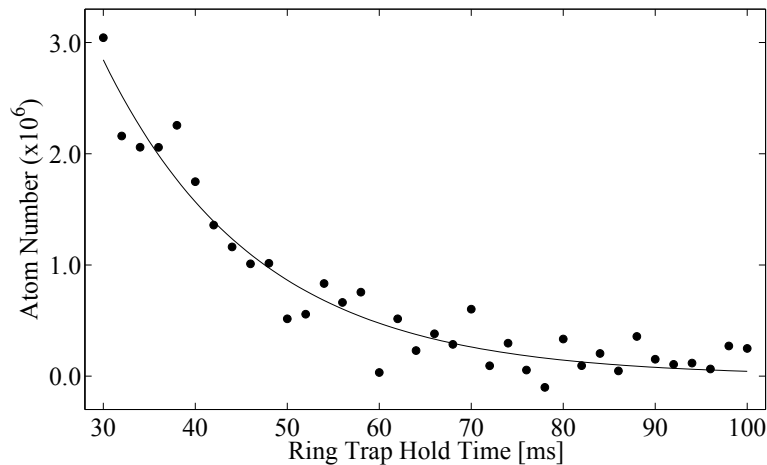


Figure 7.6: Ring trap lifetime. Atom number determined by pixel counting then exponential decay fitted to data and a lifetime of 60 ms obtained.

The short measured lifetime of 60 ms is primarily attributed to a possible loss mechanism located at roughly the ‘8 o’clock’ position of the ring trap. This loss is

further examined in the following section where we load ultra-cold atoms in the ring trap.

### 7.2.1 Loading from Dipole Trap

We now load the ring trap with ultra-cold atoms from the optical dipole trap. The vertical (Z axis) magnetic field shim is applied during RF evaporation as before such that the trap centre is approximately aligned with the ring trap. The relax trap stage loads the optical dipole trap as described in section 4.2, but this time the beams are crossed at the top of the ring trap, with the position of the beams adjusted for optimal atom loading into the ring trap. We then evaporatively cool the atoms using a typical power curve but it is stopped after 1.5 s when the beams have a power of around 0.9 W each. This leaves us with around  $10^6$  atoms at an estimated temperature of 1  $\mu$ K.

There is then a 1 ms transition time where the optical dipole trap is turned off and the ring trap is turned on. A quadrupole field of 27.2 G/cm is applied during the ring trap stage, and we vary the duration of this stage before recording an absorption image of the atoms. Again, a time-of-flight of 0.8 ms is used.

Figure 7.7 shows the evolution of the system as we vary the duration of the ring trap. The colour scale used is the logarithm of the optical density on order to that the atoms remain visible after longer durations. We see that the atoms are loaded off-centre and as such slosh around the ring trap, as well as expanding thermally. The interesting observation from these data can be seen from 28 ms onwards; the cloud of atoms starts to split at the ‘8 o’clock’ position. This splitting seems to be mirrored at the other side of the ring trap as well and is clear in images 40-45 ms.

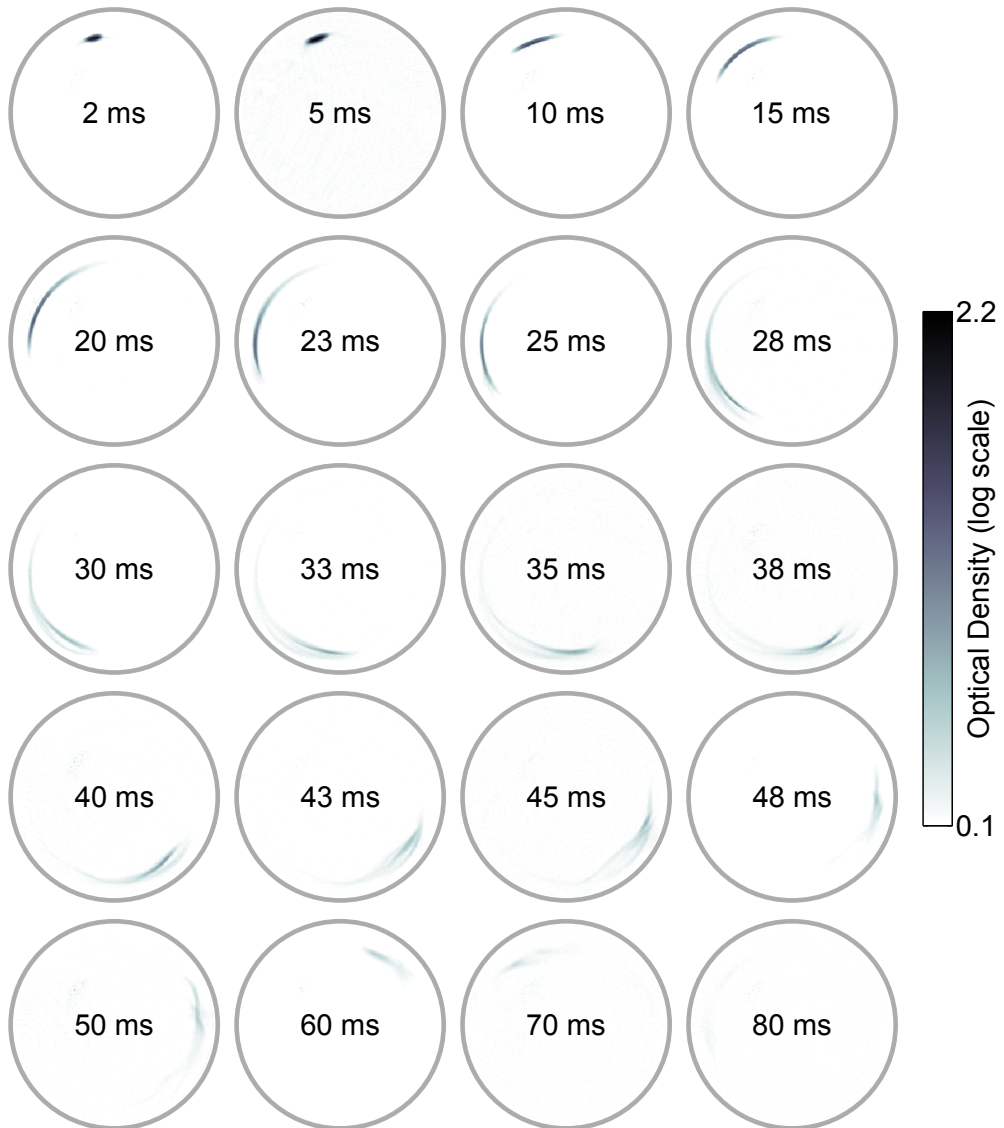


Figure 7.7: Ultra-cold atoms are loaded at the top of the ring trap and allowed to evolve for some time. We observe splitting of the atom cloud in the image labelled ‘28 ms’, and this seems to be mirrored in the image labelled ‘45 ms’.

It was postulated that the reason for this was end effects resulting from the input/output wires of the drive coils [147], which are positioned 4 cm from the copper ring for maximum coupling. The resultant perturbations in the local magnetic field may be causing an unexpected trap shape. To test this the drive coils were rotated by  $60^\circ$  and the experiment was repeated. We found that the position of the artefact also moved by  $60^\circ$  as shown in figure 7.8.

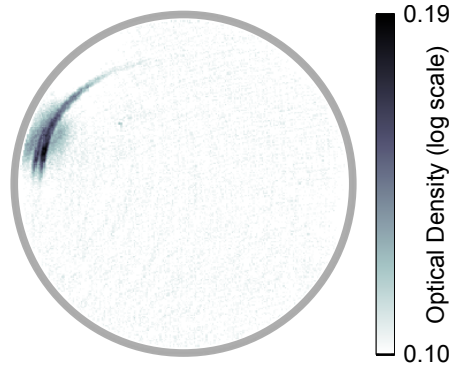


Figure 7.8: After rotating the AC drive coils by  $60^\circ$ , we see the position of the ring artefact shift by the same angle compared to the data in figure 7.7.

Another explanation for the splitting is that the kinetic energy of the atoms gained under the influence of gravity allows them to ride up the walls of the confining potential such that they reach the position of the magnetic field zeros as described in figure 7.4. Once at a point of zero magnetic field, the magnetic atomic sub-levels become degenerate and the atoms can freely fall into any of the 5 available  $m_F$  states, such that some of the atoms will no longer be trapped by the ring trap potential.

In this experiment we are applying a quadrupole field, which displaces the instantaneous magnetic zeros out of the plane of the ring (Y axis). This would indicate that the atoms are loaded outside the plane of the ring such that they then oscillate along the Y axis and encounter the magnetic field zeros. From the ring trap model used to generate figure 7.4, we estimate the magnetic zeros are displaced by a minimum of  $\approx 100 \mu\text{m}$ . Assuming a conservative harmonic potential in the Y direction, this would mean the loading position of the atoms would need to be only  $\approx 100 \mu\text{m}$  away from the ring plane in order for them to oscillate and reach the instantaneous zeros. However, we note that this hypothesis is not immediately concurrent with the ‘end-effect’ explanation which is supported by the data in figure 7.8.

## 7.2.2 Pendulum Modelling

Here we load thermal atoms into the bottom of the ring trap and allow them to oscillate azimuthally in the trapping potential. These oscillations can be likened to the motion of a rigid pendulum. The experimental sequence is similar to that of section 7.2.1 where we load ultra-cold atoms at the top of the ring, however here we apply a Z shim in the opposite direction such that the quadrupole trap centre is moved down during the RF evaporation stage. The atoms are then transferred to the optical dipole trap where they undergo evaporative cooling for 1 s.

The atoms are loaded into the ring trap slightly off-centre, and in this instance we do not apply a bias field or quadrupole field. A bias field would flatten out the trapping potential which would give the atoms less confinement in the radial direction and

## 7.2. THERMAL ATOMS IN THE RING TRAP

would lead to a less well defined pendulum length in the model. A quadrupole field would slightly distort the trap due to the cylindrical symmetry of the field<sup>3</sup>, and therefore the pendulum length would vary slightly depending on angular position. After some ring trap hold duration, the atoms are released and absorption images recorded.

We perform the experiment described above for both the original orientation of the AC drive coils and for the rotated orientation mentioned in the previous section, for which the location of the splitting of the atom cloud is shifted as shown in figure 7.8. From the data, we can then see if the orientation of the drive coils effects the frequency with which the atoms oscillate.

Analysis of the absorption images is performed in MATLAB. We first determine the centre of the ring trap from a calibration image containing no atoms, then apply a mask to exclude the central and outer regions of the ring where the outer mask has the radius of the copper ring (2 mm). The image pixels are then binned both radially and angularly around the ring centre and Gaussian profiles are fitted to the radial and angular position data to determine atom cloud centres. An example of this processing is shown in figure 7.9. We can then plot atom cloud angular position as a function of ring trap hold time, as shown in figures and 7.10a and 7.10b.

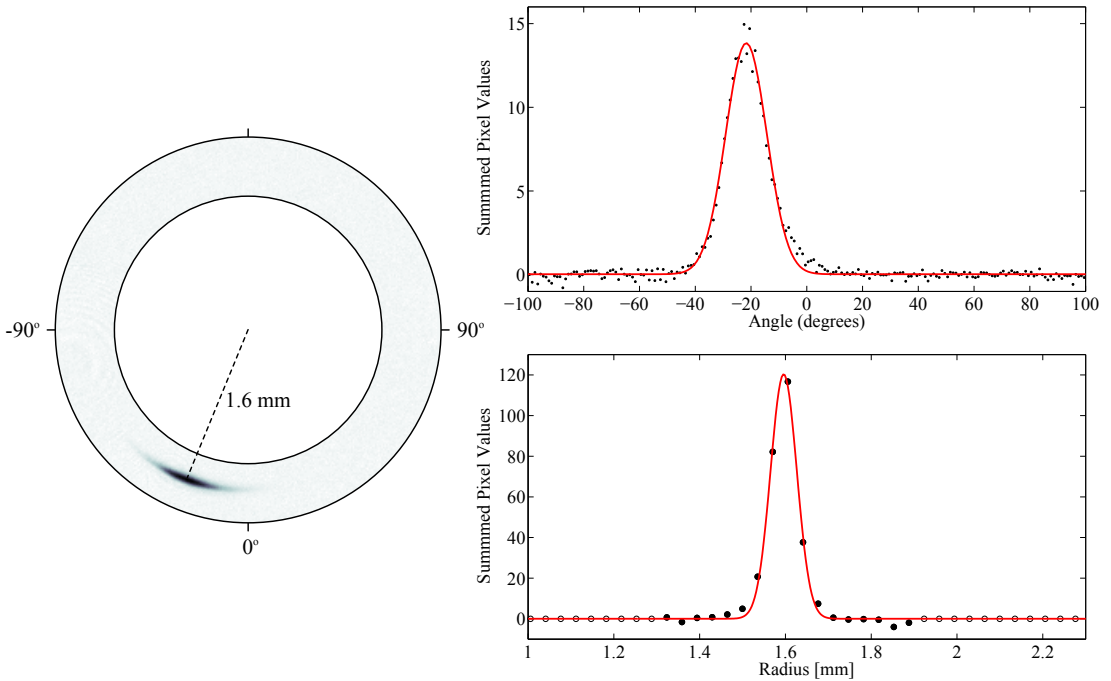


Figure 7.9: An example of the angular and radial binning of the (360 ms, rotated orientation) image of the atoms in the ring trap. In the lower plot the hollow data points indicate the radii where the image mask was applied.

<sup>3</sup>A field generated by our two coils has twice the gradient along the coil axis (Z) as it does in the radial directions (X,Y).

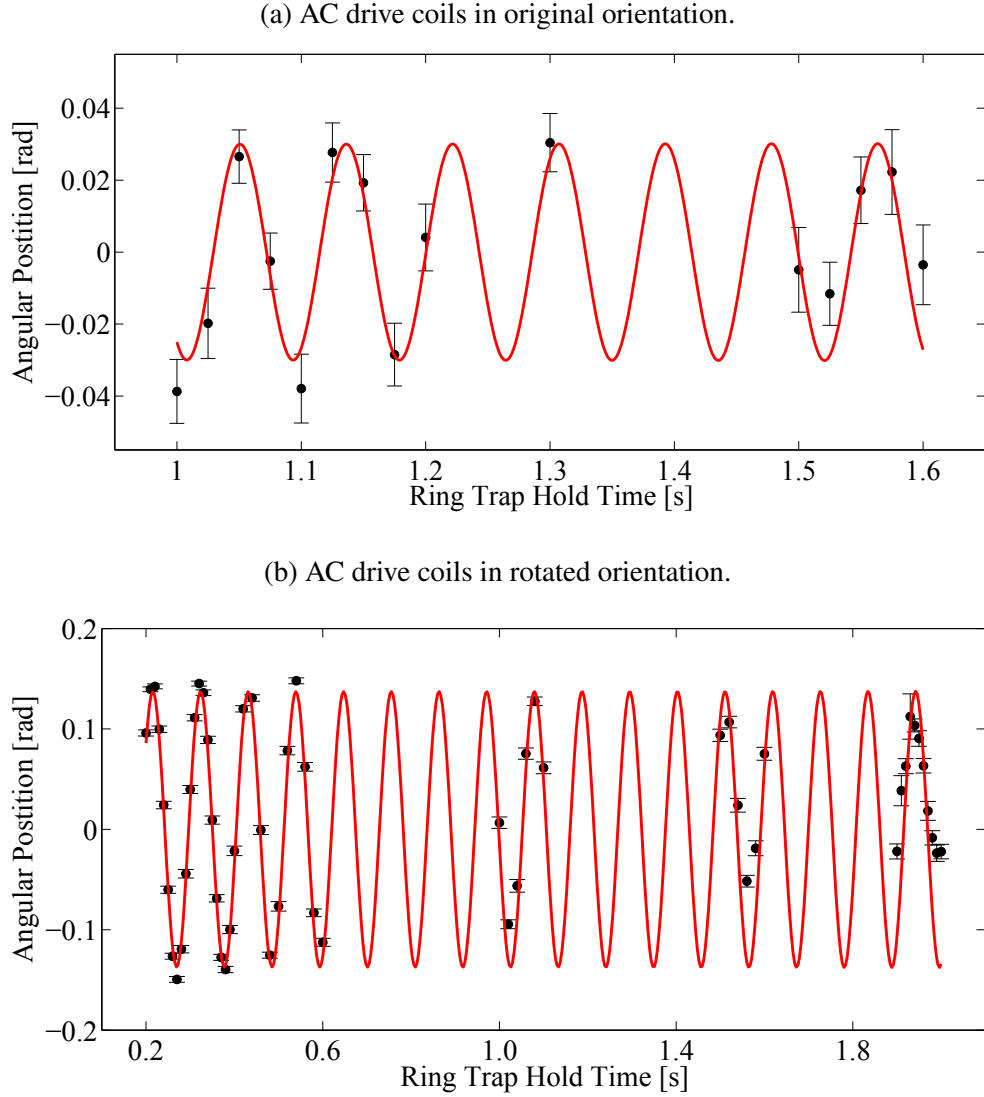


Figure 7.10: The angular position of ultra-cold atoms in the ring trap are recorded as a function of ring trap hold time. A rigid pendulum model is fitted to the data using equations 7.2 and we find an oscillation frequency of  $11.69 \pm 0.09$  Hz and  $9.266 \pm 0.002$  Hz for the upper and lower graphs respectively. In addition, there is an angular offset of  $-22^\circ$  and  $-18^\circ$  applied to the data in the upper and lower graphs respectively, meaning the pendulum stable point is to the left of centre in figure 7.9 in both cases.

The rigid pendulum model is calculated using numerical integration of the following equations:

$$\theta = \theta_0 + \frac{\partial\theta}{\partial t}t, \quad (7.2a)$$

$$\frac{\partial\theta}{\partial t} = v_0 + \frac{\partial^2\theta}{\partial t^2}t, \quad (7.2b)$$

$$\frac{\partial^2\theta}{\partial t^2} = -\frac{g'}{l}\sin(\theta), \quad (7.2c)$$

where  $\theta$  is position,  $t$  is time,  $v_0$  is initial velocity,  $g'$  is the total downward acceleration, and  $l$  is pendulum length. This model is then fitted to the data in figure 7.10b with a fixed pendulum length of 1.6 mm which is determined by the average centre position of the Gaussians fitted to the radially binned images.

The oscillation frequency of the atoms with the AC drive coils in their original orientation is determined to be  $11.69 \pm 0.09$  Hz from the fit to the data in figure 7.10a, and with the coils in their rotated orientation the oscillation frequency is found to be  $9.266 \pm 0.002$  Hz from figure 7.10b. In addition to the difference in frequency, there is also an angular offset observed in both data sets. The data presented in figures 7.10a and 7.10b have an applied offset of  $-22^\circ$  and  $-18^\circ$  respectively, meaning the pendulum stable point is to the left of centre in figure 7.9 in both cases. Therefore we conclude that there is a stray magnetic field, most probably from the AC drive coils [147], effecting the atoms within the ring trap.

**Trap lifetime:** The pendulum data allows for the determination of the trap lifetime via the data fitting method shown in figure 7.9. From figure 7.11, where the AC drive coils are in the rotated orientation, we observe a negligible decrease in atom number over the range of ring trap hold durations. Whilst we don't fit an exponential decay as we did in figure 7.6, it is clear that the trap lifetime is increased in this case. We attribute this increase to the fact that the atoms do not reach the point of the ring trap where we observe the splitting of the ultra-cold atom cloud (figure 7.8), as thus this loss mechanism is not present.

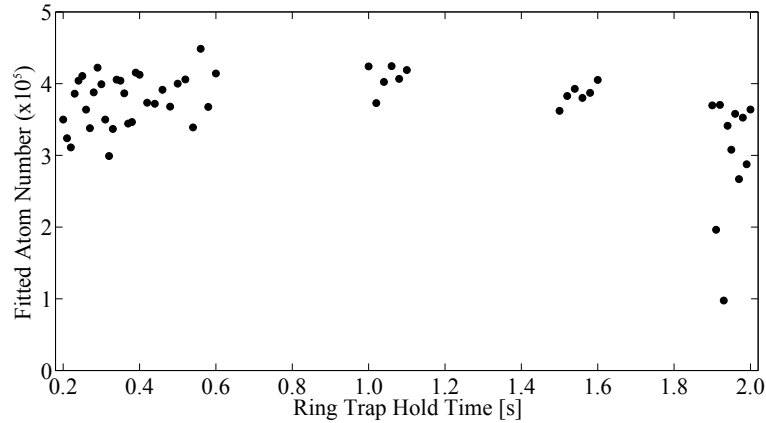


Figure 7.11: Atom number as a function of ring trap hold time, where the atoms are oscillating in the bottom of the ring trap, similar to a rigid pendulum.

### 7.2.3 Kapitza-Dirac Splitting

Whilst the dipole trapping beams were at the top of the ring trap, we also attempt to create a BEC and apply an interferometer splitting pulse. We use the same sequence used for loading ultra-cold atoms into the ring trap but this time we perform the full 4 s evaporation such that we are left with a BEC if  $1.2 \times 10^5$  atoms. This is checked by observing the characteristic bimodal distribution after some time-of-flight.

With the BEC loaded into the ring trap we apply a single square splitting pulse of 10  $\mu$ s duration to excite multiple momentum states. At this time we had not yet implemented our high efficiency interferometer pulses and were using an older optics setup. As a result the exact amplitude of the splitting pulse is unknown but we estimate  $\sim 60 E_r$  from the resultant populations.

Figure 7.12 shows an example image of such a split. Given that the atoms move out of the interferometer beams after the split, this is as far as we could go with an interferometer sequence. If the atoms were able to return to the interferometer region, in principle, we could apply a readout pulse and close the interferometer. For this to work we would also need to load the atoms closer to the top of the ring trap as in this system the momentum states are not travelling tangentially to the trapping potential and we would expect them to slosh radially as they travel around the ring. There are many more steps to performing a full interferometer sequence in the ring trap, but these data demonstrate a promising outlook.

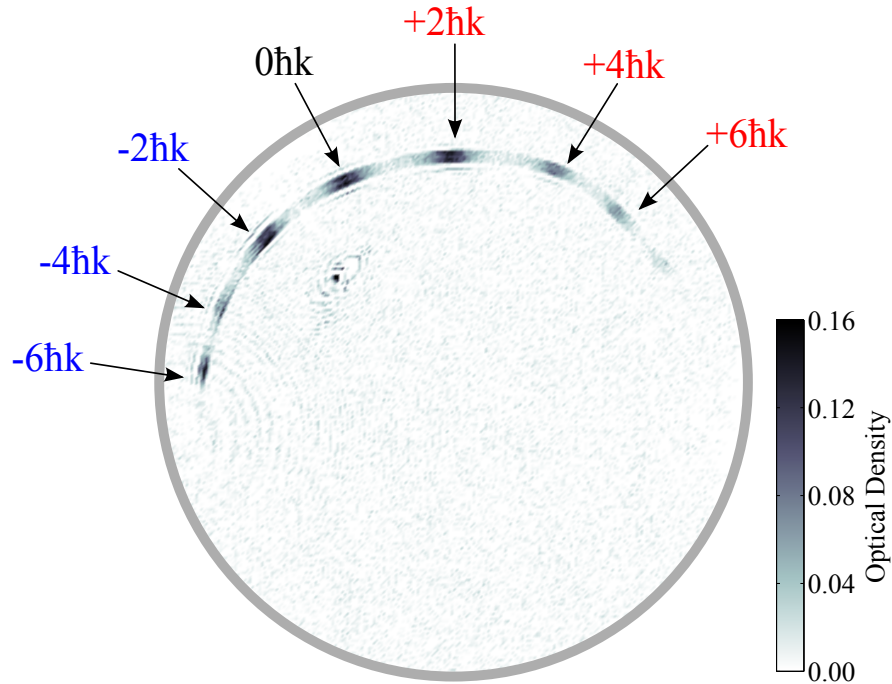


Figure 7.12: We load a BEC in the ring trap and apply a KD splitting pulse. An absorption image, taken after 20 ms in the ring trap, shows the resultant momentum mode populations.

### 7.3 Limitations

There are currently two main limitations to our AC coupled ring trap. Firstly, there is the perturbation in the smooth trapping potential as shown in figures 7.7 and 7.8. A potential fix would be to wind the drive coils such that the input and output wires are further away from the copper ring. However, this may lead to complications with regards to optical access as the coils would likely block the MOT beams in the current setup.

Secondly, whilst we can create a BEC at the top of the ring, we cannot create one at the bottom. This is because during the dipole loading stage the quadrupole field is relaxed but this causes some of the atoms to come into contact with the copper, which causes them to be lost from the atomic ensemble and this decrease in atom number prevents the creation of a BEC. A possible solution for this would be to load the dipole trap in the centre of the ring, then move the beams downwards during the 4 s dipole evaporation stage. This would require additional hardware such as stepper motors on the mirrors immediately before the chamber.

If we could load a BEC into the ring trap at the bottom, we could potentially remove the issue of the atom cloud splitting, as discussed in section 7.2.1, by having the input/output wires near the top of the ring and performing experiments using only the

### 7.3. LIMITATIONS

---

lower section of the ring. This is an attractive proposition as it would be possible to perform contrast interferometry (see section 6) in a wave guide which has yet to be experimentally demonstrated. However, the interferometer would not enclose an area<sup>4</sup> as it would if we started the atoms at the top, and therefore we would not be able to measure Sagnac effects.

---

<sup>4</sup>The plane of the ring is aligned approximately East-West to maximise the effect of the Earth's rotation

# Chapter 8

## Conclusions

### 8.1 Conclusions

The primary result of the work presented in the thesis is the construction of an atom interferometer. We have successfully used finely tuned optical pulses to excite and control momentum states of a BEC which were then used to make interferometric measurements of the recoil frequency of rubidium, as well as magnetic field gradients. From the measured recoil frequency in figure 5.16, an estimate of the fine-structure constant value was determined to be  $\alpha^{-1} = 137 \pm 10$ . These methods, used in chapter 5, whilst effective, were also time consuming. Therefore in chapter 6 we focussed our efforts on contrast interferometry; a faster method of obtaining essentially the same data. From figure 6.7 we calculate  $\alpha^{-1} = 137 \pm 5$ . In both methods the main uncertainty in the  $\alpha^{-1}$  calculation was the interferometer beam angle. By realigning our interferometer beams to be counter propagating, this uncertainty would be greatly reduced leading to a more precise measurement of  $\alpha$ .

We have demonstrated the first contrast interferometer using a BEC of  $^{87}\text{Rb}$ . Whilst the system is still in the process of being fully characterised, we have presented initial data containing the recoil frequency of  $^{87}\text{Rb}$ . This method is promising with regard to the precision measurement of the fine-structure constant as well as for rotation sensing, gravimetry, magnetometry, etc.

Another key result is the high efficiency control of the momentum states of our BEC using highly tuned optical pulses, which form the basis of the work presented in [9]. By substitution of the Hamiltonian in the Schrödinger equation we obtain a set of coupled differential equations describing the momentum state population evolution for a given pulse amplitude and duration. The equations can be numerically solved in MATLAB and we compare the model to experimental data and show excellent agreement.

Within the science chamber we have constructed an AC coupled ring trap for ultra-cold atoms and BECs. Whilst not the primary focus of the work presented, the principle has been demonstrated in chapter 7. Most encouragingly, we have demonstrated

the Kapitza-Dirac splitting of a BEC within the ring trap which forms the first step of an atom interferometer in a waveguide. We have also identified some issues with the current setup that will potentially inhibit us from performing a full interferometer sequence. By recognising these issues now we can rectify the problems in future designs.

## 8.2 Future Work

### 8.2.1 Magnetic Gradiometry using CI

The magnetic gradiometry presented in section 5.4 demonstrates that our atom interferometer is a valid measurement tool. In future work it would be interesting to use the contrast interferometer to make similar measurements, but with an increased readout rate. The current gradiometer uses a 2-arm configuration, which will not work with the CI probe beam. Therefore we would use a 3-arm system and the information about the magnetic field gradient would come from a phase shift in the signal.

### 8.2.2 Measurements of Gravity

As mentioned previously, atom interferometers are sensitive to gravity. Unfortunately, our interferometer is orientated horizontally and therefore we are insensitive to gravity. However, we can tilt our optics table slightly ( $\pm 0.3^\circ$ ) adding a slight vertical component to the atomic trajectory. For a typical 2 ms total interferometer duration the atoms would be separated by a maximum  $\sim 100$  nm in the vertical direction. We calculate that this small separation would give a phase shift of  $\sim 1$  rad in the interferometer output (see appendix A.8). In addition, the phase change is proportional to  $T^2$ , so a longer interferometer duration is very favourable.

### 8.2.3 Higher Order Interferometry

We have demonstrated excellent control of the first order momentum states and their use in interferometry. In the future we would like to construct an interferometer using higher order momentum states. The current limiting factor in our experiment is laser intensity control and in order to use higher orders successfully we need to maintain stable splitting and reflection pulses for extended periods of time. However we are optimistic that this is achievable with the current system, or at least with minimal changes to the interferometry laser setup.

# Appendix A

## A.1 Shutter Circuit Diagram

We construct homemade shutter circuits comprising Sunex SHT934 mechanical shutters and the circuit shown in figure A.1. The power supply operates in constant voltage mode and provides a maximum current of 250 mA when the shutters are held open. When a 5 V control voltage is applied to the base pin of the transistor it causes saturation and the shutter opens.

The shutters are typically placed at the foci of beams and therefore the timings of the shutter circuits are measured using a laser beam with a waist of  $\approx 30 \mu\text{m}$ . We measure an opening (closing) time of  $\approx 80 \mu\text{s}$  ( $\approx 80 \mu\text{s}$ ), with a delay of  $\approx 7 \text{ms}$  ( $\approx 4 \text{ms}$ ) and jitter of  $\approx 40 \mu\text{s}$  ( $\approx 70 \mu\text{s}$ ).

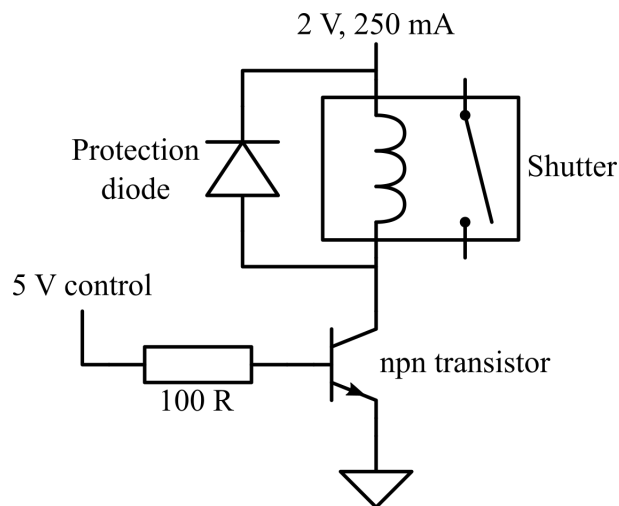


Figure A.1: *Homemade shutter circuit diagram.*

## A.2 LIAD Circuit Diagram

The circuit with which we control the Light Induced Atomic Desorption (LIAD) is shown in figure A.2. A 5 V control is applied to a relay switch to close the circuit and switch on the UV LEDs, and the  $4.7 \Omega$  power resistor sets the operating current.

A thermal cut-out is applied by way of a thermistor and FET; if a temperature of  $70^\circ\text{C}$  is reached, the voltage at the base pin of the FET decreases and the LEDs are switched off. We note that the circuit has never actually reached this temperature, even when the LEDs are on continuously.

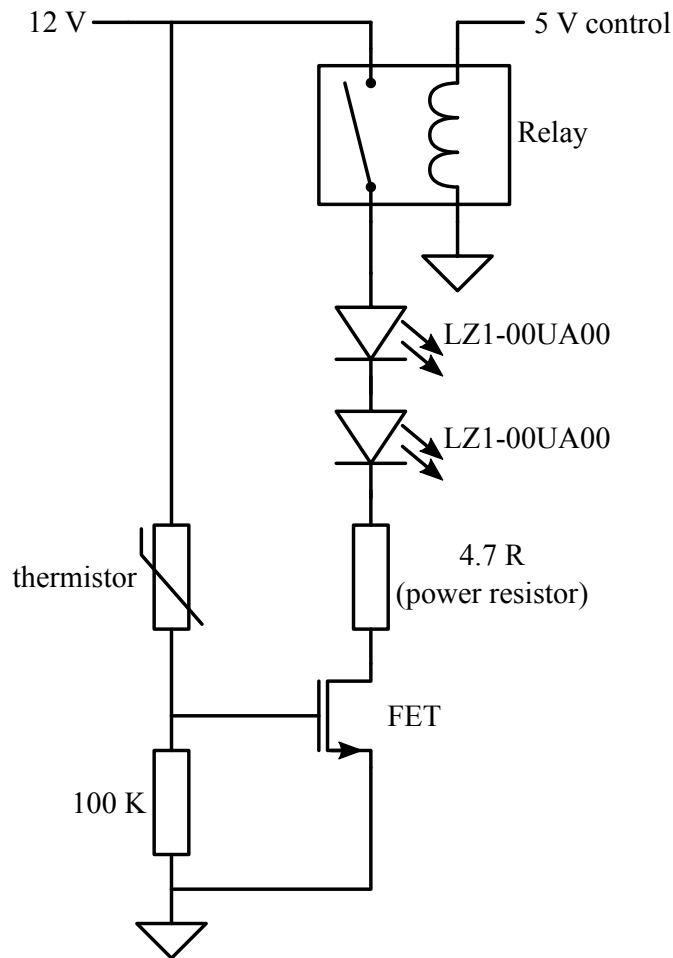


Figure A.2: LIAD circuit diagram.

### A.3 Magnetic Levitation

Zeeman energy can be written as

$$E = m_F g_F \mu_B B , \quad (\text{A.1})$$

where  $B$  is the magnetic field. Force can be written as

$$F = -\nabla E = -m_F g_F \mu_B \frac{dB}{ds} . \quad (\text{A.2})$$

Relating the gravitational and magnetic forces we find

$$mg = -m_F g_F \mu_B \frac{dB}{ds} . \quad (\text{A.3})$$

For  $^{87}\text{Rb}$ ,  $m_F=2, g_F=1/2$  giving

$$\frac{dB}{ds} = 15.4 \text{ G/cm} . \quad (\text{A.4})$$

Note, that according to our coil calibration data it would require quadrupole coil current of 12.7 A to achieve this magnetic field gradient. Experimentally we apply only 12.4 A, giving an expected field of 15.0 G/cm, and we find this current to be optimum in terms of supporting the atoms against gravity. Therefore it is likely that our coil calibration has changed slightly since it was first measured.

## A.4 AOM Driver Circuit Diagram

The AOM driver circuit shown in figure A.3 is used for all the AOMs in our optical setup. Both the amplitude and frequency control can be set to *internal* mode in which case the driver output is determined by the internal circuitry of the driver, or *external* mode in which case 0-10 V DC is used to control the amplitude and frequency via their respective inputs. Note that for the interferometry AOM drivers the frequency source is a Keysight N5138B which we fix at a frequency of 84 MHz. The frequency from the voltage controlled oscillator (VCO) is sent to an RF mixer (Minicircuits ZP-3LH-S+) along with the DC voltage to control the amplitude of the output.

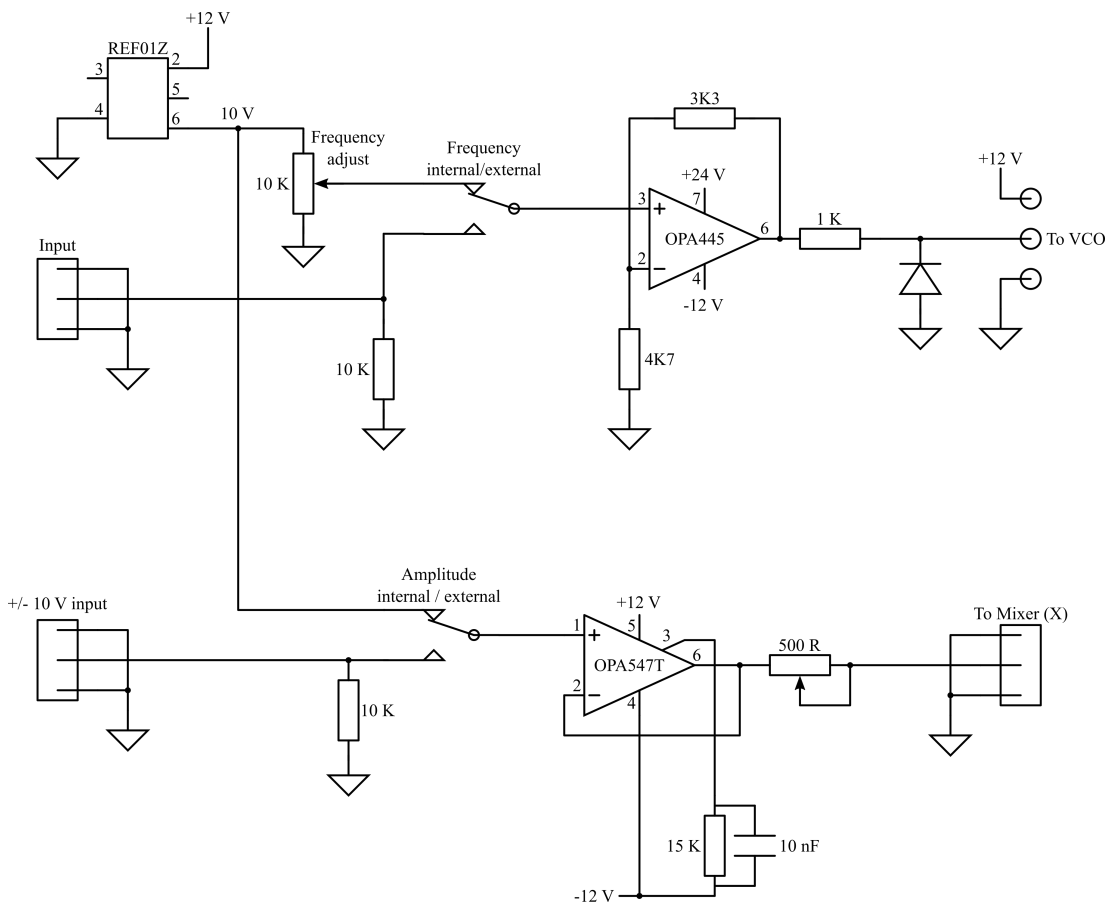


Figure A.3: AOM driver circuit diagram.

## A.5 Thermal Size Calculation

We start by considering the energy,  $E$ , of the atomic ensemble:

$$E = k_{\text{B}}T = \frac{1}{2}mv^2, \quad (\text{A.5})$$

where  $k_{\text{B}}$  is Boltzmann's constant,  $T$  is temperature,  $m$  is atomic mass, and  $v$  is atomic velocity. Now we equate velocity to the rate of change of displacement,

$$v = \frac{\partial\sigma}{\partial t}, \quad (\text{A.6})$$

where  $\sigma$  is displacement with respect to time  $t$ . By substitution of equation A.6 into equation A.5 we obtain

$$\frac{\partial\sigma}{\partial t} = \sqrt{\frac{2k_{\text{B}}T}{m}}. \quad (\text{A.7})$$

Displacement during the interval between time  $t_i$  to  $t_f$  can be written as the integral of velocity with respect to time such that

$$\sigma(t) = \int_{t_i}^{t_f} \frac{\partial\sigma}{\partial t} dt = \int_{t_i}^{t_f} \sqrt{\frac{2k_{\text{B}}T}{m}} dt. \quad (\text{A.8})$$

This then gives

$$\sigma(t) = \sqrt{\frac{2k_{\text{B}}T}{m}}t + \sigma_0, \quad (\text{A.9})$$

where  $\sigma_0$  is some initial displacement.

We can consider displacement in equation A.9 as the radius of a cloud of thermal atoms with temperature  $T$  after some free expansion time  $t$ , offset by some initial size  $\sigma_0$ .

## A.6 Calculation of $\alpha$

From figure 5.16 we fit a frequency of  $12.18 \pm 0.04$  kHz. We describe below the calculations to determine the value of  $\alpha$  and the associated uncertainty.

**Value of  $\alpha$ :** The angle of the interferometry beams  $\theta$  is measured to be  $26^\circ$ . This reduces the effective k-vector of the optical lattice and therefore the measured frequency of  $\omega$  relates to recoil frequency of rubidium  $\omega_r$  by

$$\omega_r = \frac{\omega}{4 \cos^2(\theta)} = \frac{12.18 \text{ kHz}}{4 \cos^2(26^\circ)} = 3.77 \text{ kHz} . \quad (\text{A.10})$$

By rearranging equation 1.9, the ratio of  $h/m_a$  is calculated from

$$\frac{h}{m_a} = \frac{4\pi\omega_r}{k^2} = \frac{4\pi \cdot 3.77 \text{ kHz}}{(8.05 \times 10^6 \text{ m}^{-1})^2} = 4.59 \times 10^{-9} \text{ m kg s}^{-1} , \quad (\text{A.11})$$

where  $k$  is  $2\pi/\lambda$ , and  $\lambda = 780.24$  nm (the beam angle has already be accounted for by altering the frequency).

Then by substitution into (equation 1.8)

$$\alpha^2 = \frac{2R_\infty m_a h}{c m_e m_a} , \quad (\text{A.12})$$

giving  $\alpha = 7.32 \times 10^{-3}$ , and  $1/\alpha = 136.63$ .

**Uncertainty in  $\alpha$ :** Firstly we deal with the uncertainty in the recoil frequency which, given the form of equation A.10, we write as

$$\delta\omega_r = \sqrt{\left(\frac{\partial\omega_r}{\partial\omega}\right)^2 (\delta\omega)^2 + \left(\frac{\partial\omega_r}{\partial\theta}\right)^2 (\delta\theta)^2} , \quad (\text{A.13})$$

where

$$\frac{\partial\omega_r}{\partial\omega} = \frac{\cos^2(\theta)}{2(\cos(2\theta) + 1)} , \quad (\text{A.14a})$$

$$\frac{\partial\omega_r}{\partial\theta} = \frac{2\omega \sin(\theta)}{3 \cos(\theta) + \cos(3\theta)} . \quad (\text{A.14b})$$

$$\delta\omega = 0.04 \text{ kHz} , \quad (\text{A.14c})$$

$$\delta\theta = 0.5^\circ . \quad (\text{A.14d})$$

Now we need an expression for the uncertainty in  $h/m_a$ :

$$\delta \frac{h}{m_a} = \sqrt{\left(\frac{\partial \frac{h}{m_a}}{\partial \omega_r}\right)^2 \delta \omega_r^2} , \quad (\text{A.15})$$

## A.6. CALCULATION OF $\alpha$

---

where

$$\frac{\partial \frac{h}{m_a}}{\partial \omega_r} = \frac{4\pi}{k^2}. \quad (\text{A.16})$$

and  $\delta\omega_r$  is given by equation A.13.

Finally, we assume the uncertainty in  $h/m_a$  is dominant in the expression for  $\alpha$  (equation A.12) and we define the constant

$$\beta = \frac{2R_\infty}{c} \frac{m}{m_e}. \quad (\text{A.17})$$

The uncertainty in  $\alpha^2$  can then be written as

$$\delta\alpha^2 = \sqrt{\left(\frac{\partial\alpha^2}{\partial\frac{h}{m_a}}\right)^2 \left(\delta\frac{h}{m_a}\right)^2}, \quad (\text{A.18})$$

where

$$\frac{\partial\alpha^2}{\partial\frac{h}{m_a}} = \beta. \quad (\text{A.19})$$

We can now calculate the uncertainty in  $\alpha^2$  by substitution of equation A.13 into equation A.15, then into equation A.18.

To convert the uncertainty in  $\alpha^2$  into an uncertainty in  $\alpha$  we use the following:

$$\alpha = \sqrt{\alpha^2}, \quad (\text{A.20})$$

and therefore

$$\delta\alpha = \sqrt{\left(\frac{\partial\alpha}{\partial\alpha^2}\right)^2 (\delta\alpha^2)^2} = \sqrt{\left(\frac{1}{2\sqrt{\alpha^2}}\right)^2 (\delta\alpha^2)^2}. \quad (\text{A.21})$$

From this we calculate  $\alpha = (7.3 \pm 0.6) \times 10^{-3}$ . Then to calculate the uncertainty in  $\alpha^{-1}$  we use the fractional uncertainty in  $\alpha$ , giving  $\alpha^{-1} = 136 \pm 10$ .

**Uncertainty in  $\alpha$  from contrast interferometry:** The uncertainty calculation for contrast interferometry data is similar to that outlined above with the exception of the following. Now the equation for  $\omega_r$  is

$$\omega_r = \frac{\omega}{8 \cos^2(\theta)}, \quad (\text{A.22})$$

and therefore the partial derivatives of equation A.14 become

$$\frac{\partial\omega_r}{\partial\omega} = \frac{\cos^2(\theta)}{4(\cos(2\theta) + 1)}, \quad (\text{A.23a})$$

$$\frac{\partial\omega_r}{\partial\theta} = \frac{\omega \sin(\theta)}{3 \cos(\theta) + \cos(3\theta)}. \quad (\text{A.23b})$$

## A.7 BEC Reflectivity

If a weak probe power ( $\ll I_{\text{sat}}$ ) is assumed, the refractive index of a BEC can be given by [108]

$$n_{\text{ref}} = 1 + \frac{\sigma_0 n \lambda}{4\pi} \left[ \frac{i}{1 + \delta^2} - \frac{\delta}{1 + \delta^2} \right], \quad (\text{A.24})$$

where  $\sigma_0 = 6\pi(\lambda/2\pi)^2$  is the resonant cross-section,  $n$  is the density,  $\lambda$  is the illuminating wavelength, and  $\delta$  is the detuning in half linewidths. In calculating the reflected power the imaginary term can be ignored so we obtain

$$n_{\text{ref}} = 1 - \frac{\sigma_0 n \lambda}{4\pi} \frac{\delta}{1 + \delta^2}. \quad (\text{A.25})$$

For a beam of normal incidence angle, the reflectivity of the interface of two mediums of differing refractive index is given by

$$R_{\text{int}} = \left( \frac{n_1 - n_2}{n_1 + n_2} \right)^2. \quad (\text{A.26})$$

In our case this give a reflectivity of  $\approx 0.02\%$ .

We typically apply a probe beam of  $\sim 100$  nW focussed to  $70 \mu\text{m}$  giving an intensity of  $13 \text{ W/m}^2$  at our matter-wave grating. Assuming the grating size is the same as the BEC radius of  $15 \mu\text{m}$ , the optical power incident on the BEC will be  $\approx 9$  nW. If the reflectivity is  $0.02\%$ , the reflected power is therefore  $\approx 2$  pW. Note that this calculation ignores the enhancement that would result from multiple layers of differing refractive index.

## A.8 Gravitational Phase Calculation

Here we calculate the expected phase difference in a tilted interferometer. We assume a simple model where the atoms travel out and then back in and ignore the phase accumulation during the splitting and reflection pulses.

The phase difference,  $\Delta\phi$ , can be written as

$$\Delta\phi = \int E dt = \int \frac{m g s(t)}{\hbar} dt = \frac{1}{2} \frac{m g s t}{\hbar}, \quad (\text{A.27})$$

where  $E$  is energy,  $m$  is atomic mass,  $g$  is gravitational acceleration, and  $s(t)$  is height which varies with time  $T$ .

We now need an expression for  $s$ . For an interferometer tilt angle  $\gamma$  the vertical displacement can be written as

$$s = \sin(\gamma) x, \quad (\text{A.28})$$

where the horizontal displacement  $x = vt$ , where  $v$  is velocity. The velocity of the atoms is determined by the wavevector of the interferometry beams,  $k = 2\pi/\lambda \cos(\theta)$ , where  $\theta$  is the beam angle (see figure 4.20). Since the splitting pulse is a two photon process:

$$k' = \frac{4\pi}{\lambda} \cos(\theta). \quad (\text{A.29})$$

The velocity is then given by

$$v = \frac{\hbar k'}{m} = \frac{\hbar 4\pi}{m\lambda} \cos(\theta). \quad (\text{A.30})$$

Equation A.28 then becomes

$$d = \sin(\gamma) \frac{\hbar 4\pi}{m\lambda} \cos(\theta) t. \quad (\text{A.31})$$

Finally, by substitution of equation A.31 into equation A.27 we obtain the phase difference for one arm making one outward journey:

$$\Delta\phi = \frac{2\pi g}{m\lambda} \sin(\gamma) \cos(\theta) t^2. \quad (\text{A.32})$$

Once we include the return journey and the phase difference from the other interferometer arm we get a final expression of

$$\Delta\phi = \frac{8\pi g}{m\lambda} \sin(\gamma) \cos(\theta) t^2. \quad (\text{A.33})$$

# Bibliography

- [1] A. S. Arnold and E. Riis, *Bose-Einstein condensates in ‘giant’ toroidal magnetic traps*, Journal of Modern Optics **49**, 959 (2002).
- [2] A. S. Arnold, C. S. Garvie, and E. Riis, *Large magnetic storage ring for Bose-Einstein condensates*, Physical Review A **73**, 041606 (2006).
- [3] M. E. Zawadzki, P. F. Griffin, E. Riis, and A. S. Arnold, *Spatial interference from well-separated split condensates*, Physical Review A **81**, 043608 (2010).
- [4] M. Zawadzki, *Bose-Einstein condensate manipulation and interferometry*, PhD thesis, Department of Physics, University of Stathclyde, 2010.
- [5] C. H. Carson, *High contrast interferometry and finite temperature coherence of Bose-Einstein condensates*, PhD thesis, Department of Physics and SUPA, University of Strathclyde, 2015.
- [6] P. F. Griffin, E. Riis, and A. S. Arnold, *Smooth inductively coupled ring trap for atoms*, Physical Review A **77**, 051402 (2008).
- [7] J. D. Pritchard, A. N. Dinkelaker, A. S. Arnold, P. F. Griffin, and E. Riis, *Demonstration of an inductively coupled ring trap for cold atoms*, New Journal of Physics **14**, 103047 (2012).
- [8] A. Dinkelaker, *Smooth inductively coupled ring trap for cold atom optics*, PhD thesis, Department of Physics and SUPA, University of Strathclyde, 2013.
- [9] A. R. MacKellar *et al.*, *An atom optics toolbox for atom interferometry*, In advanced preparation (2016).
- [10] H. Benson, *University physics* (John Wiley & Sons, 111 River Street, Hoboken, NJ, 1996).
- [11] K. U. Schreiber and J.-P. R. Wells, *Large ring lasers for rotation sensing*, Review of Scientific Instruments **84**, 041101 (2013).
- [12] G. Stedman, *Ring-laser tests of fundamental physics and geophysics*, Reports on Progress in Physics **60**, 615 (1997).

## BIBLIOGRAPHY

---

- [13] D. S. Durfee, Y. K. Shaham, and M. A. Kasevich, *Long-term stability of an area-reversible atom-interferometer Sagnac gyroscope*, Physical Review Letters **97**, 240801 (2006).
- [14] T. L. Gustavson, A. Landragin, and M. Kasevich, *Rotation sensing with a dual atom-interferometer Sagnac gyroscope*, Classical and Quantum Gravity **17**, 23852398 (2000).
- [15] T. L. Gustavson, P. Bouyer, and M. Kasevich, *Precision rotation measurements with an atom interferometer gyroscope*, Physical Review Letters **78**, 2046 (1997).
- [16] A. Lenef *et al.*, *Rotation sensing with an atom interferometer*, Physical Review Letters **78**, 760 (1997).
- [17] F. Riehle, T. Kisters, A. Witte, J. Helmcke, and C. J. Bordé, *Optical Ramsey spectroscopy in a rotating frames: Sagnac effect in a matter-wave interferometer*, Physical Review Letters **67**, 177 (1991).
- [18] Y.-J. Wang *et al.*, *Atom Michelson interferometer on a chip using a Bose-Einstein condensate*, Physical Review Letters **94**, 090405 (2005).
- [19] A. V. Rakholia, H. J. McGuinness, and G. W. Biedermann, *Dual-axis, high data-rate interferometer via cold ensemble exchange*, Physical Review Applied **2**, 054012 (2014).
- [20] G. Rosi *et al.*, *Measurement of the gravity-field curvature by atom interferometry*, Physical Review Letters **114**, 013001 (2015).
- [21] M. J. Snadden, J. M. McGuirk, P. Bouyer, K. G. Haritos, and M. A. Kasevich, *Measurement of the earth's gravity gradient with an atom interferometer-based gravity gradiometer*, Physical Review Letters **81**, 971 (1998).
- [22] B. Deissler, K. J. Hughes, J. H. T. Burke, and C. A. Sackett, *Measurement of the AC Stark shift with a guided matter-wave interferometer*, Physical Review A **77**, 031604 (2008).
- [23] P. L. Kapitza and P. A. M. Dirac, *The reflection of electrons from standing light waves*, Mathematical Proceedings of the Cambridge Philosophical Society **29**, 297 (1933).
- [24] D. L. Freidmund, K. Aflatooni, and H. Batelaan, *Observation of the Kapitza-Dirac effect*, Nature **413**, 142 (2001).
- [25] D. E. Keith, C. R. Eckstrom, Q. A. Turchette, and D. E. Pritchard, *An interferometer for atoms*, Physical Review Letters **66**, 2693 (1991).

## BIBLIOGRAPHY

---

- [26] O. Carnal and J. Mlynek, *Young's double-slit experiment with atoms: a simple atom interferometer*, Physical Review Letters **66**, 2689 (1991).
- [27] E. M. Rasel, M. K. Oberthaler, H. Batelaan, J. Schmiedmayer, and A. Zeilinger, *Atom wave interferometry with diffraction gratings of light*, Physical Review Letters **75**, 2633 (1995).
- [28] D. M. Giltner, R. W. McGowan, and S. A. Lee, *Atom interferometer based on Bragg scattering from standing light waves*, Physical Review Letters **75**, 2638 (1995).
- [29] L. Marton, *Electron interferometer*, Physical Review **85**, 1057 (1952).
- [30] L. Marton, J. A. Simpson, and J. A. Suddeth, *Electron beam interferometer*, Physical Review **90**, 490 (1953).
- [31] H. Rauch, W. Treimer, and U. Bonse, *Test of a single crystal neutron interferometer*, Physical Letters **47A**, 369 (1974).
- [32] R. Colella, A. W. Overhauser, and S. A. Werner, *Observation of gravitationally induced quantum interference*, Physical Review Letters **34**, 1472 (1975).
- [33] M. Kasevich and S. Chu, *Atomic interferometry using stimulated Raman transitions*, Physical Review Letters **67**, 181 (1991).
- [34] S. M. Dickerson, J. M. Hogan, A. Sugarbaker, D. M. S. Johnson, and M. A. Kasevich, *Multiaxis inertial sensing with long-time point source atom interferometry*, Physical Review Letters **111**, 083001 (2013).
- [35] B. Canuel *et al.*, *Six-axis inertial sensor using cold-atom interferometry*, Physical Review Letters **97**, 010402 (2006).
- [36] A. Arvanitaki, S. Dimopoulos, A. A. Geraci, J. Hogan, and M. Kasevich, *How to test atom and neutron neutrality with atom interferometry*, Physical Review Letters **100** (2008).
- [37] S. Gupta, K. Dieckmann, Z. Hadzibabic, and D. E. Pritchard, *Contrast interferometry using Bose-Einstein condensate to measure  $h/m$  and  $\alpha$* , Physical Review Letters **89**, 140401 (2002).
- [38] R. Bouchendira, P. Cladé, S. Guellati-Khélifa, F. Nez, and F. Biraben, *New determination of the fine structure constant and test of the quantum electrodynamics*, Physical Review Letters **106**, 080801 (2011).
- [39] L. de Broglie, *Waves and quanta*, Nature **112**, 2815 (1923).

## BIBLIOGRAPHY

---

- [40] A. D. Cronin, J. Schmiedmayer, and D. E. Pritchard, *Optics and interferometry with atoms and molecules*, *Reviews of Modern Physics* **81**, 1051 (1999).
- [41] D. Budker and M. Romalis, *Optical magnetometry*, *Nature Physics* **3**, 227 (2007).
- [42] O. Garcia, B. Deissler, K. J. Hughes, J. M. Reeves, and C. A. Sackett, *Bose-Einstein-condensate interferometer with macroscopic arm separation*, *Physical Review A* **74**, 031601 (2006).
- [43] M. Horikosji and K. Nakagawa, *Dephasing due to atom-atom interaction in a waveguide interferometer using a Bose-Einstein condensate*, *Physical Review A* **74**, 031602 (2006).
- [44] A. O. Jamison, J. N. Kutzg, and S. Gupta, *Atomic interactions in precision interferometry using Bose-Einstein condensates*, *Physical Review A* **84**, 043643 (2011).
- [45] F. Dalfovo, S. Giorgini, L. P. Pitaevskii, and S. Stringari, *Theory of Bose-Einstein condensation in trapped gases*, *Review of Modern Physics* **71**, 463 (1999).
- [46] W. Ketterle and M. W. Zwierlein, *Making, probing and understanding ultracold Fermi gases*, arXiv , 0801.2500v1 (2008).
- [47] G. Roati *et al.*, *Atom interferometry with trapped Fermi gases*, *Physical Review Letters* **92**, 23 (2004).
- [48] G. D. Bruce, J. Mayoh, G. Smirne, L. Torralbo-Campo, and D. Cassettari, *A smooth, holographically generated ring trap for the investigation of superfluidity in ultracold atoms*, *Physica Scripta* **T143**, 014008 (2011).
- [49] A. Ramanathan *et al.*, *Superflow in a toroidal Bose-Einstein condensate: an atom circuit with a tunable weak link*, *Physical Review Letters* **106**, 130401 (2011).
- [50] S. Moulder, S. Beattie, R. P. Smith, N. Tammuz, and Z. Hadzibabic, *Quantized supercurrent decay in an annular Bose-Einstein condensate*, *Physical Review A* **86**, 013629 (2012).
- [51] S. Beattie, S. Moulder, R. J. Fletcher, and Z. Hadzibabic, *Persistent currents in spinor condensates*, *Physical Review Letters* **110**, 025301 (2013).
- [52] G. E. Marti, R. Olf, and D. M. Stamper-Kurn, *Collective excitation interferometry with a toroidal Bose-Einstein condensate*, *Physical Review A* **91**, 013602 (2015).

## BIBLIOGRAPHY

---

- [53] V. A. Henderson, P. F. Griffin, E. Riis, and A. S. Arnold, *Comparative simulations of Fresnel holography methods for atomic waveguides*, New Journal of Physics **18**, 025007 (2016).
- [54] K. Henderson, C. Ryu, C. MacCormick, and M. G. Boshier, *Experimental demonstration of painting arbitrary and dynamic potentials for Bose-Einstein condensates*, New Journal of Physics **11**, 043030 (2009).
- [55] L. J. Garay, J. R. Anglin, J. I. Cirac, and P. Zoller, *Sonic analog of gravitational black holes in Bose-Einstein condensates*, Physical Review Letters **85**, 4643 (2000).
- [56] O. Zobay and B. M. Garraway, *Two-dimensional atom trapping in field-induced adiabatic potentials*, Physical Review Letters **86**, 1195 (2001).
- [57] I. Lesanovsky, S. Hofferberth, J. Schmiedmayer, and P. Schmelcher, *Manipulation of ultracold atoms in dressed adiabatic radio-frequency potentials*, Physical Review A **74**, 033619 (2006).
- [58] W. H. Heathcote, E. Nugent, B. T. Sheard, and C. J. Foot, *A ring trap for ultracold atoms in an RF-dressed state*, New Journal of Physics **10**, 043012 (2008).
- [59] W. Heathcote, *A toroidal trap for ultracold atoms in a RF-dressed state*, PhD thesis, Merton College, University of Oxford, 2007.
- [60] T. Schumm *et al.*, *Matter-wave interferometry in a double well on an atom chip*, Nature Physics **1**, 57 (2005).
- [61] M. Vangeleyn, B. M. Garraway, H. Perrin, and A. S. Arnold, *Inductive dressed ring traps for ultracold atoms*, New Journal of Physics B **47**, 071001 (2014).
- [62] J. A. Sauer, M. D. Barrett, and M. S. Chapman, *Storage ring for neutral atoms*, Physical Review Letters **87**, 270401 (2001).
- [63] M. B. Crookston, P. M. Baker, and M. P. Robinson, *A microchip ring trap for cold atoms*, Journal of Physics B **38**, 3289 (2005).
- [64] S. Wu, W. Rooijackers, P. Striehl, and M. Prentiss, *Bidirectional propagation of cold atoms in a “stadium”-shaped magnetic guide*, Physical Review A **70**, 013409 (2004).
- [65] S. Gupta, K. W. Murch, K. L. Moore, T. P. Purdy, and D. M. Stamper-Kurn, *Bose-Einstein condensation in a circular waveguide*, Physical Review Letters **95**, 143201 (2005).

## BIBLIOGRAPHY

---

- [66] C. Ryu *et al.*, *Observation of persistent flow of a Bose-Einstein condensate in a toroidal trap*, Physical Review Letters **99**, 260401 (2007).
- [67] J.-B. Trebbia, C. L. G. Alzar, R. Cornelussen, C. I. Westbrook, and I. Bouchoule, *Roughness suppression via rapid current modulation on an atom chip*, Physical Review Letters **98**, 263201 (2007).
- [68] T. Kinoshita, *The fine structure constant*, Reports on Progress in Physics **59**, 14591492 (1996).
- [69] N. Kolachevsky *et al.*, *Testing the stability of the fine-structure constant in the laboratory*, arXiv , 0904.1663v1 (2009).
- [70] B. Odom, D. Hanneke, B. D'Urso, and G. Gabrielse, *New measurement of the electron magnetic moment using a one-electron quantum cyclotron*, Physical Review Letters **97**, 030801 (2006).
- [71] P. A. M. Dirac, *The cosmological constants*, Nature , 323 (1937).
- [72] J. D. Barrow, H. B. Sandvik, and J. Magueijo, *Behaviour of varying-alpha cosmologies*, Physical Review D **65**, 063504 (2002).
- [73] R. M. Godun *et al.*, *Frequency ratio of two optical clock transitions in  $^{171}\text{Yb}^+$  and constraints on the time variation of fundamental constants*, Physical Review Letters **113**, 210801 (2014).
- [74] M. Acciarri *et al.*, *Measurement of the running of the fine-structure constant*, Physical Letters B **476**, 40 (2000).
- [75] F. Jegerlehner, *The running fine structure constant  $\alpha(E)$  via the Adler function*, arXiv , 0807.4206v1 (2008).
- [76] B. Odom, *The 64th Compton lecture series (2006): unsolved mysteries of the universe: looking for clues in surprising places: lecture 5*, Available at [http://kicp.uchicago.edu/~odom/compton\\_files/compton\\_lecture\\_05\\_handout.pdf](http://kicp.uchicago.edu/~odom/compton_files/compton_lecture_05_handout.pdf), Accessed: 2016-03-16.
- [77] D. Hanneke, S. Fogwell, and G. Gabrielse, *New measurement of the electron magnetic moment and the fine structure constant*, Physical Review Letters **100**, 120801 (2008).
- [78] *The NIST reference on constants, units, and uncertainty*, <http://physics.nist.gov/cgi-bin/cuu/Value?ryd>, Accessed: 2016-03-16.
- [79] B. J. Mount, M. Redshaw, and E. G. Myers, *Atomic masses of  $^6\text{Li}$ ,  $^{23}\text{Na}$ ,  $^{39,40}\text{K}$ ,  $^{85,87}\text{Rb}$ , and  $^{133}\text{Cs}$* , Physical Review A **82**, 042513 (2010).

## BIBLIOGRAPHY

---

- [80] *The NIST reference on constants, units, and uncertainty*, <http://physics.nist.gov/cgi-bin/cuu/Value?c>, Accessed: 2016-03-29.
- [81] *The NIST reference on constants, units, and uncertainty*, <http://physics.nist.gov/cgi-bin/cuu/Value?alphinv>, Accessed: 2016-01-26.
- [82] J. Robert S. Van Dyck, P. B. Schwinberg, and H. G. Dehmelt, *New high-precision comparison of electron and positron  $g$  factors*, *Physical Review Letters* **59**, 26 (1987).
- [83] A. Wicht, J. M. Hensley, E. Sarajlic, and S. Chu, *A preliminary measurement of the fine structure constant based on atom interferometry*, *Physica Scripta* **102**, 82 (2002).
- [84] P. Cladé *et al.*, *Precise measurement of  $h/m_{\text{Rb}}$  using Bloch oscillations in a vertical optical lattice: determination of the fine-structure constant*, *Physical Review A* **74**, 052109 (2006).
- [85] M. Cadoret *et al.*, *Combination of Bloch oscillations with a Ramsey-Bordé interferometer: new determination of the fine structure constant*, *Physical Review Letters* **101**, 230801 (2008).
- [86] G. Gabrielse, D. Hanneke, M. N. T. Kinoshita, and B. Odem, *Erratum: new determination of the fine structure constant from the electron  $g$  value and QED [Phys. Rev. Lett. 97, 030802 (2006)]*, *Physical Review Letters* **99**, 039902 (2007).
- [87] T. Aoyama, M. Hayakawa, T. Kinoshita, and M. Nio, *Revised value of the eighth-order contribution to the electron  $g - 2$* , *Physical Review Letters* **99**, 110406 (2007).
- [88] A. O. Jamison, B. Plotkin-Swing, and S. Gupta, *Advances in precision contrast interferometry with Yb-Bose-Einstein condensates*, *Physical Review A* **90**, 063606 (2014).
- [89] J. Klaers, J. Schmitt, F. Vewinger, and M. Weitz, *Bose-Einstein condensation of photons in an optical microcavity*, *Nature* **468**, 545 (2010).
- [90] A. Arnold, *Preparation and manipulation of an  $^{87}\text{Rb}$  Bose-Einstein condensate*, PhD thesis, University of Sussex, 1999.
- [91] S. Gupta, *Experiments with degenerate Bose and Fermi gases*, PhD thesis, Department of Physics, Massachusetts Institute of Technology, 2003.
- [92] T. Hänsch and A. Schawlow, *Cooling of gasses by laser radiation*, *Optics Communications* **13**, 68 (1975).

## BIBLIOGRAPHY

---

- [93] C. J. Foot, *Atomic physics* (Oxford University Press, Great Clarendon Street, Oxford, 2012).
- [94] S. Chu, L. Hollberg, J. Bjorkholm, A. Cable, and A. Ashkin, *Three-dimensional viscous confinement and cooling of atoms by resonance radiation pressure*, *Physical Review Letters* **55**, 48 (1985).
- [95] H. J. Metcalf and P. van der Straten, *Laser cooling and trapping* (Springer-Verlag, New York, 1999).
- [96] P. D. Lett, R. N. Watts, C. I. Westbrook, and W. D. Phillips, *Observation of atoms laser cooled below the Doppler limit*, *Physical Review Letters* **61**, 169 (1988).
- [97] C. Adams and E. Riis, *Laser cooling and manipulation of neutral particles*, *Progress in Quantum Electronics* **21** (1997).
- [98] D. A. Steck, *Rubidium 87 D line data*, Available at <http://steck.us/alkalidata>.
- [99] W. D. Phillips *et al.*, *Optical molasses: the coldest atoms ever*, *Physica Scripta* **T34**, 20 (1991).
- [100] E. L. Raab, M. Prentis, A. Cable, S. Chu, and D. Pritchard, *Trapping of neutral sodium atoms with radiation pressure*, *Physical Review Letters* **59**, 2631 (1987).
- [101] J. P. McGilligan, P. F. Griffin, E. Riis, and A. S. Arnold, *Phase-space properties of magneto-optical traps utilising micro-fabricated gratings*, *Optics Express* **23**, 8948 (2015).
- [102] J. Denschlag, D. Cassettari, and J. Schmiedmayer, *Guiding neutral atoms with a wire*, *Physical Review Letters* **82**, 2014 (1999).
- [103] D. Pritchard, *Cooling neutral atoms in a magnetic trap for precision spectroscopy*, *Physical Review Letters* **51**, 1336 (1983).
- [104] C. J. Pethick and H. Smith, *Bose-Einstein condensation in dilute gases* (Cambridge University Press, The Pitt Building, Trumpington Street, Cambridge, United Kingdom, 2002).
- [105] A. L. Migdall, J. V. Prodan, W. D. Phillips, T. H. Bergeman, and H. J. Metcalf, *First observation of magnetically trapped neutral atoms*, *Physical Review Letters* **54**, 2596 (1985).
- [106] D. J. Han, R. H. Wynar, P. Coueille, and D. J. Heinzen, *Bose-Einstein condensation of large numbers of atoms in a magnetic time-averaged orbiting potential trap*, *Physical Review A* **57**, R4114 (1998).

## BIBLIOGRAPHY

---

- [107] K. B. Davis *et al.*, *Bose-Einstein condensation in a gas of sodium atoms*, Physical Review Letters **75**, 3969 (1995).
- [108] W. Ketterle, D. S. Durfee, and D. M. Stamper-Kurn, *Making, probing and understanding Bose-Einstein condensates*, arXiv , 9904034v2 (1999).
- [109] A. L. Gaunt, T. F. Schmidutz, I. Gotlibovych, R. P. Smith, and Z. Hadzibabic, *Bose-Einstein condensation of atoms in a uniform potential*, Physical Review Letters **110**, 200406 (2013).
- [110] R. Grimm, M. Weidemüller, and Y. B. Ovchinnikov, *Optical dipole traps for neutral atoms*, arXiv , 990207v1 (1999).
- [111] D. L. Jenkin *et al.*, *Bose-Einstein condensation of a  $^{87}\text{Rb}$  in a levitated crossed dipole trap*, The European Physical Journal D **65** (2011).
- [112] A. Harsono, *Dipole trapping and manipulation of ultra-cold atoms*, PhD thesis, Merton College, University of Oxford, 2006.
- [113] M. D. Barrett, J. A. Sauer, and M. S. Chapman, *All-optical formation of an atomic Bose-Einstein condensate*, Physical Review Letters **87**, 010404 (2001).
- [114] I. Gotlibovych *et al.*, *A compact single-chamber apparatus for Bose-Einstein condensation of  $^{87}\text{Rb}$* , arXiv , 1212.4108v2 (2012).
- [115] Y.-J. Lin, A. R. Perry, R. L. Compton, I. B. Spielman, and J. V. Porto, *Rapid production of  $^{87}\text{Rb}$  Bose-Einstein condensates in a combined magnetic and optical potential*, Physical Review A **79**, 063631 (2009).
- [116] V. Bagnato, D. E. Pritchard, and D. Kleppner, *Bose-Einstein condensation in an external potential*, Physical Review A **35**, 4354 (1987).
- [117] M. Ueda, *Fundamentals and new frontiers of Bose-Einstein condensation* (World Scientific Publishing, Covent Garden, London, 2010).
- [118] S. Grossmann and M. Holthaus,  *$\lambda$ -transition to the Bose-Einstein condensate*, Z. Naturforsch **50**, 921 (1995).
- [119] S. Grossmann and M. Holthaus, *On Bose-Einstein condensation in harmonic traps*, Physical Review A **208**, 188 (1995).
- [120] J. R. Ensher, D. S. Jin, M. R. Matthews, C. E. Wieman, and E. A. Cornell, *Bose-Einstein condensation in a dilute gas: measurement of energy and ground-state occupation*, Physical Review Letters **77**, 4984 (1996).
- [121] T. L. Nicholson *et al.*, *Systematic evaluation of an atomic clock at  $2 \times 10^{-18}$  total uncertainty*, Nature Communications , 7896 (2015).

## BIBLIOGRAPHY

---

- [122] G. P. Barwood *et al.*, *Agreement between two  $^{88}\text{Sr}$  optical clocks to 4 parts in  $10^{17}$* , *Physical Review A* **89**, 050501 (2014).
- [123] K. J. Hughes, *Optical manipulation of atomic motion for a compact gravitational sensor with a Bose-Einstein condensate interferometer*, PhD thesis, Faculty of the School of Engineering and Applied Science, University of Virginia, 2008.
- [124] C. C. Gerry and P. L. Knight, *Introductory quantum optics* (Cambridge University Press, The Edinburgh Building, Cambridge, United Kingdom, 2004).
- [125] I. Bloch, T. W. Hänsch, and T. Esslinger, *Measurement of the spatial coherence of a trapped Bose gas at the phase transition*, *Nature* **403**, 166 (2000).
- [126] Y. Yamamoto, *Bose-Einstein condensation and matter-wave lasers: chapter 2: fundamental concepts of Bose-Einstein condensation*, Available at [http://www.nii.ac.jp/qis/first-quantum/e/forStudents/lecture/pdf/qis385/QIS385\\_chap2.pdf](http://www.nii.ac.jp/qis/first-quantum/e/forStudents/lecture/pdf/qis385/QIS385_chap2.pdf), Accessed: 2016-03-21.
- [127] S. Gupta, A. E. Leanhardt, A. D. Cronin, and D. E. Pritchard, *Coherent manipulation of atoms with standing light waves*, *C. R. Acad. Sci.* **2** (2001).
- [128] B. Gadway, D. Pertot, M. G. Cohen, and D. Schneble, *Analysis of Kapitza-Dirac diffraction patterns beyond the Raman-Nath regime*, *Optics Express* **17** (2009).
- [129] Y. B. Ovchinnikov *et al.*, *Diffraction of a released Bose-Einstein condensate by a pulsed standing light wave*, *Physical Review Letters* **83**, 284 (1999).
- [130] S. Wu, Y.-J. Wang, Q. Diot, and M. Prentiss, *Splitting matter waves using an optimised standing-wave light-pulse sequence*, *Physical Review A* **71** (2005).
- [131] F. J. Harris, *On the use of windows for harmonic analysis with the discrete Fourier transform*, *Proceedings of the IEEE* **66**, 51 (1978).
- [132] M. Kasevich and S. Chu, *Laser cooling below a photon recoil with three-level atoms*, *Physical Review Letters* **69**, 1741 (1992).
- [133] P. Berg *et al.*, *Composite-light-pulse technique for high-precision atom interferometry*, *Physical Review Letters* **114**, 063002 (2015).
- [134] P. Cladé *et al.*, *Determination of the fine structure constant based on Bloch oscillations of ultracold atoms in a vertical optical lattice*, *Physical Review Letters* **96**, 033001 (2006).

## BIBLIOGRAPHY

---

- [135] A. S. Arnold, J. S. Wilson, and M. G. Boshier, *A simple extended-cavity diode laser*, Review of Scientific Instruments **69**, 1236 (1998).
- [136] G. D. Bruce, *Alternative techniques for the production and manipulation of ultracold atoms*, PhD thesis, University of St. Andrews, 2012.
- [137] M. Greiner, I. Bloch, T. W. Hänsch, and T. Esslinger, *Magnetic transport of trapped cold atoms over a large distance*, Physical Review A **63**, 031401 (2001).
- [138] C.-L. Hung, X. Zhang, N. Gemelke, and C. Chin, *Accelerating evaporative cooling of atom into Bose-Einstein condensation in optical traps*, Physical Review A **78**, 011607 (2008).
- [139] A. E. Siegman, *LASERS* (Oxford University Press, Walton Street, Oxford).
- [140] *GaussianBeam*, <http://gaussianbeam.sourceforge.net>.
- [141] N. Keegan, *Light-pulse matter-wave interferometer in a magnetic waveguide*, University of Strathclyde, Department of Physics.
- [142] A. O. Jamison, *Precision Interferometry with Bose-Einstein Condensate*, PhD thesis, University of Washington, 2014.
- [143] B. P. Abbott *et al.*, *Observation of gravitational waves from a binary black hole merger*, Physical Review Letters **116**, 061102 (2016).
- [144] I. K. Kominis, T. W. Kornack, J. C. Allred, and M. V. Romalis, *A subfemtotesla multichannel atomic magnetometer*, Nature **422**, 596 (2003).
- [145] I. G. Hughes and T. P. A. Hase, *Measurements and their uncertainties* (Oxford University Press, Great Clarendon Street, Oxford, 2010).
- [146] A. Haase, D. Cassettari, B. Hessmo, and J. Schmiedmayer, *Trapping neutral atoms with a wire*, Physical Review A **64**, 043405 (2001).
- [147] *Private communication with Cass Sackett, University of Virginia.*